The Theory and Applications of Electrochemistry in Halidometallate Anion and Polyhalogen Monoanion Based Ionic Liquids:

Their Synthesis, Characterization, and Application

Inaugural-Dissertation
to obtain the academic degree
Doctor rerum naturalium (Dr. rer. nat.)

submitted to the
Department of Biology, Chemistry, Pharmacy
of Freie Universität Berlin

by

Tyler Andrew Gully

2021

The work for the present dissertation has been conducted between November 2017 and August 2021 under the guidance of Prof. Dr. Sebastian Hasenstab-Riedel at the Institute of Chemistry and Biochemistry (Department of Biology, Chemistry, Pharmacy) of the Freie Universität Berlin.

Statement of Authorship

I, Tyler Andrew Gully, assure that I of my own volition and by myself, with the assistance of the provided sources and resources, composed the following dissertation.

Subsequently, I assure that the following Dissertation has not been submitted for review elsewhere.

Selbstständigkeitserklärung

Hiermit versichere ich, Tyler Andrew Gully, dass ich die vorliegende Dissertation selbständig und lediglich unter Benutzung der angegebenen Quellen und Hilfsmittel verfasst habe.

Ich versichere außerdem, dass die vorliegende Dissertation noch nicht einem anderen Prüfungsverfahren zugrunde gelegen hat.

1st referee:	Prof. Dr. Sebastian Hasenstab-Riedel
2nd referee:	Prof. Dr. Christina Roth
Day of Disputation:	November 12th, 2021

Acknowledgements

The last months of my doctoral phase have been rather difficult for me, as my Mormor passed away at the end of October 2020 and her funeral at the end of February 2021. Additionally, my Nana died in the beginning of February 2021 and is around the time I am preoccupied with writing my dissertation. I have been thoroughly distracted and have had no time to properly mourn. I remember them both very well, and they were both very kind to my brother and me. May they rest in heaven. I love my Mormor and Grumpy and my Grandpa and Nana very much and remember that they helped me greatly with my life and education.

I acknowledge my high school chemistry teacher Mr. Dave Downs from Canyon High School - he was always a very wacky exciting teacher and made chemistry fun! I am very thankful that he taught me dimensional analysis, which I now teach to all of my first semester students! I wish there were more role models like you in school. Thank you Dr. Julia Bader for helping me correct and revise a lot of my scientific work, I have grown through this assistance. Thank you Prof. Dr. Christina Roth for teaching me and cultivating my interest in electrochemistry and of course being my second examiner. Last but not least, I thank my doctor father Prof. Dr. Sebastian Riedel for providing me an opportunity in a field that I have thoroughly enjoyed perusing: inorganic electrochemistry. The use of electrochemistry in inorganic chemistry is a highly useful analytic tool to further characterize substances and enhance innovative synthesis. The field has seen a small revival in the past decade, especially in light of the current energy and environmental revolution; I was proud to contribute.

I am thankful to my students Lena Moldenhauer, Max Höfler, Thomas Keilhack, Jan-Erik Fuhrmann, and Paul Bethge for allowing me to grow as an instructor and realize how to interconnect as to lead a project towards success. Your growth and success is apparent, and I am glad to have been a small part in this. Please remain thirsty for knowledge and success.

To my labmates in U406 and most suddenly in U306 I am very thankful for your past and continued support. Karsten Sonnenberg, I am thankful for your guidance during my master's degree. Dr. Karsten Sonnenberg and Dr. Benjamin Schmidt, a.k.a., "The Battery Boys," I am very grateful for having you in the BMBF project, being able to work together and enjoy a lot of time together. There is definitely a lot of understanding for each other after having completed this project and I hope to complete the trio with the "Dr." title! Thank you Patrick Voßnacker (Voßi) for your help and good friendship during our doctoral candidacy, you are unVossbar! Gene Senges, I had lots of fun working on the Simon's Process paper with you.

For anyone that came to visit in U406 I had a great time with you and lots of memories: Dr. Karsten Sonnenberg, Dr. Benjamin Schmidt, Patrick Voßnacker, Jonas Schmid, Marlon Winter, Gene Senges, Paul Golz, Sebastian Hämmerling, Sofiya Kotsyuda, Thomas Drews, Friederike Fuß, Dr. Jan Nissen and Luise Sander, Natallia Peschkur, and Dr. Yetsedaw Tsegaw. I thank all AG Riedel members, I gleaned significant amounts of information about interpersonal communication, project management, individual success, mental health, problem solving, and German culture. I enjoyed spending time with you.

Thanks go to Dr. Julia Bader, Dr. Benjamin Schmidt, Jonas R. Schmid, and Marlon Winter for help with correcting this manuscript.

Furthermore, after 12 years of tertiary education I am very grateful to my entire family for their support, without which I know I would not have been able to succeed in my endeavors. Additionally, my gratefulness extends to those that have supported me financially: My parents, Tim and Lauren Gully; my Grandpa (John Gully, deceased) and Nana (Cindy Gully, deceased); my Grandparents my Mormor (Inger Lawson, deceased) and Grumpy (Jim Ford, deceased); my Aunt Judy, Uncle Bill, cousin Jacob, and cousin Dara for allowing my to live with them for one year, it was very fun and I will never forget it!; my relatives in Sweden, my Great Aunt Kate Swegmark and my Aunts Ingrid, Karin, and Ebba; the United States of America government for providing financial aid; and the everyday German taxpayer for providing an educational system that pays for its tertiary education. Thank you Cameron, my brother, for being there and having a good relationship with me. I am also thankful to my Aunt Nancy and Uncle Mark Lebens for always being especially kind to me, and also to my Aunt Mary and Uncle Moti Motila for always going to Church with me, praising the Lord, and having chicken taco lunches afterwards. To all of you I am very grateful!

I would like to thank my girlfriend of the past 8 years, Nicola Ulsamer, for her involvement in my life and going on quite a few adventures with me. You have filled my life with some very exciting experiences. I also thank Klaus, Yvonne, Nina, and Noah Ulsamer for accepting me into your house and being a family in Germany for me, when I could not return home to the United States of America.

Abstract

Ionic liquids (IL) are increasingly used in electrochemical and battery applications due to their physicochemical properties, high conductivity, and large electrochemical windows compared to commonly used solvents. In this doctoral thesis the synthesis and characterization of the halidometallate anion and polyhalogen monoanion based ILs, the theoretical basis for the melt state of ILs, ion diffusion, and the practical electrochemical properties and considerations of ILs necessary for electrochemical applications have been explored. Specific attention was given to trihalogen monoanion based ILs (THMIL) of the type $[X_3]^-$ or $[XY_2]^-$ (X, Y = Cl, Br, I) for their oxidative strength and use in metal recycling, and the halidometallate anion based ILs $[SnBr_3]^-$, $[SnBr_5]^-$, $[MnCl_4]^{2-}$, and $[MnCl_5]^{2-}$ as the electroactive species. Together with ammonium, imidazolium, and pyrrolidinium ($[R_1R_2Pyrr]^+$ = alkylpyrrolidinium) based cations they were used in the development of a new competitive style of hybrid redox-flow battery . The conductivity, viscosity, as well as the redox potentials of the above species were determined. Raman and UV-*vis* spectroelectrochemistry techniques identified the electrochemically reduced and oxidized THMILs and halidometallate species. Using this information, THMILs were shown to be useful in a cyclical metal recycling process via the dissolution of metallic Sn, producing $[SnBr_3]^-$ and the subsequent reversible electroreduction of $[SnBr_3]^-$ to Sn and $[Br_3]^-$. Further, analysis of the relevant electrochemical and physicochemical characteristics of the various halidometallate based ILs showed that $[C_4C_1Pyrr]_2[MnCl_4]$ in γ-butyrolactone had the best physicochemical properties. It was subsequently used to make the all manganese redox-flow battery, consisting of the $Mn^0|[MnCl_4]^{2-}||[MnCl_4]^{2-}|[MnCl_5]^{2-}$ couple.

Kurzzusammenfassung

Ionische Flüssigkeiten (ILs) werden aufgrund ihrer physikochemischen Eigenschaften, ihrer hohen Leitfähigkeit und ihrer großen elektrochemischen Fenster im Vergleich zu den üblicherweise verwendeten Lösungsmitteln zunehmend in elektrochemischen und Batterieanwendungen eingesetzt. Diese Doktorarbeit befasst sich mit der Synthese und Charakterisierung von ILs auf Halidometallat-Anion- und Polyhalogen-Monoanion-Basis, die Untersuchung von den theoretischen Grundlagen für den Schmelzzustand von ILs, der Ionendiffusion, sowie den notwendigen elektrochemischen Eigenschaften für eine elektrochemische Anwendung von ILs. Aus großen Interesse wurden die Trihalogenmonoanionen-basierten ILs (THMIL) des Typs $[X_3]^-$ oder $[XY_2]^-$ (X, Y = Cl, Br, I) wegen ihrer Oxidationsstärke und ihrer Verwendung im Metallrecycling untersucht, sowie die Halidometallatanionen-basierten ILs $[SnBr_3]^-$, $[SnBr_5]^-$, $[MnCl_4]^{2-}$ und $[MnCl_5]^{2-}$ als elektroaktive Spezies. In Verbindung mit Kationen auf Ammonium-, Imidazolium- und Pyrrolidiniumbasis ($[R_1R_2Pyrr]^+$ = Alkylpyrrolidinium) wurden sie für die Entwicklung einer neuen wettbewerbsfähigen Art von Hybrid-Redox-Flow-Batterie eingesetzt. Die Leitfähigkeit, die Viskosität und die Redoxpotentiale der oben genannten Spezies wurden bestimmt. Durch Raman- und UV/Vis-Spektroelektrochemie wurden die elektrochemisch reduzierten und oxidierten THMILs und Halidometallat-Spezies identifiziert. Anhand dieser Informationen konnte gezeigt werden, dass die THMILs in einem zyklischen Metallrecyclingprozess durch die Auflösung von metallischem Sn und die anschließende reversible Elektroreduktion von $[SnBr_3]^-$ zu Sn und $[Br_3]^-$ nützlich sind. Bei der Analyse der relevanten elektrochemischen und physikalisch-chemischen Eigenschaften der verschiedenen ILs auf Halidometallatbasis zeigte $[C_4C_1Pyrr]_2[MnCl_4]$ in γ-Butyrolacton die besten physikochemischen Eigenschaften. Sie wurde anschließend für die Herstellung der All-Mangan-Redox-Flow-Batterieverwendet, die aus dem $Mn^0|[MnCl_4]^{2-}||[MnCl_4]^{2-}|[MnCl_5]^{2-}$ System besteht.

Abbreviations

List of Abbreviations

ABB	Aluminum-bromide redox-flow battery
Ag/Ag^+	Silver-silver chloride electrode
aSSB	All-solid-state battery
C	Chemical mechanism
CA	Chronoamperometry
CCDC	Cambridge Crystallographic Data Centre
CE	Counter electrode
CHE	Computational hydrogen electrode
CHN	Elemental analysis
CPCA	Controlled-potential chronoamperometry
Cu/Cu^{2+}	Copper-copper sulfate electrode
CV	Cyclic voltammetry
DSC	Differential scanning calorimetry
DSSC	Dye-sensitized solar cell
E	Electrochemical mechanism
ECF	Electrochemical fluorination
ESI-MS	Electrospray ionization mass spectroscopy
Fc/Fc^+	Ferrocene-ferrocenium internal reference electrode
HRFB	Hybrid redox-flow battery
IL	Ionic liquid
IR	Infrared spectroscopy
LCO	$LiCoO_2$; positive electrode material in a Li-ion battery
LIB	Li-ion battery
Li-NMC	$LiNiMnCoO_2$; positive electrode material in a Li-ion battery
LSV	Linear sweep voltammetry
MSBR	Molten salt fast breeder reactor
NARFB	Non-aqueous redox-flow battery
NE	Nernst-Einstein
NMR	Nuclear magnetic resonance
OTTL	Optically transparent thin-layer cell
qSSB	Quasi-solid-state battery
r.t.	Room temperature
RE	Reference electrode
RFB	Redox-flow battery
RTIL	Room temperature ionic liquid
SCE	Saturated calomel electrode
SERS	Surface enhanced Raman spectroscopy

SHE	Standard hydrogen electrode
SSB	Solid-state battery
WE	Working electrode
VFT	Vogel-Fulcher-Tamman equation
VRFB	Vanadium redox-flow battery
UV-*vis*	Ultraviolet-visible spectroscopy
ZBB	Zinc-bromide redox-flow battery

List of Equation Variables

B	The thermodynamic probability of an ion moving into an unoccupied "hole" or interstitial void
c	Concentration of the electroactive species
c_i	Concentration of a given ion
C	Constant
D	Linear diffusion
D_i	Diffusion of ions
$E°$	Cell potential
f	Slipperiness of an ion
F	Faraday constant
$\vec{F}$	Frictional force of molecules upon each other in a liquid
G	(Gibbs) free energy
G_{fus}	(Gibbs) free energy of fusion
G_{latt}	(Gibbs) free energy of lattice formation
G_{solv}	(Gibbs) free energy of solvation
H	Enthalpy
i	Current
j_i	Flux density of a particle
k_B	Boltzmann constant
n	Moles of electrons transferred
Q	Reaction quotient
r	Radius of an ion
R	Gas constant
S	Entropy
S_A	Surface area of a planar electrode
t	Time
T	Temperature
T_g	Glassy transition temperature
Y	Ionicity
z	Directional axis on the *xyz* coordinate plane

α	Ion decoupling factor
α_{ox}	Chemical activity of the oxidized species
α_{red}	Chemical activity of the reduced species
η	Dynamic viscosity
Λ_m	Molar conductivity
Λ_{NE}	Equivalent molar conductivity
μ_i	Ion mobility
σ	Conductivity
ν_i	Ion stoichiometry

List of Chemical Abbreviations

aHF	Anhydrous hydrogen fluoride
$[AlCl_4]^-$	Tetrachloridoaluminate(III)
AlF_3	Aluminum(III) fluoride
$[AsPh_4]^+$	Tetraphenylarsonium(I)
$[AuCl_4]^-$	Tetrachloridoaurate(III)
$[BF_4]^-$	Tetrafluoridoborate
Br^-	Bromide
$[Br_3]^-$	Tribromine monoanion
$[Cat.]^+$	Cation
Cl^-	Chloride
$C_{\#}$	Alkyl chain length of "#" number of carbon atoms
$[C_4C_1C_1IM]^+$	1-butyl-(2,)3-(di)methylimidazolium)
$[Cl_3]^-$	Trichlorine monoanion
$[C_{12}SO_3]^-$	Dodecal sulfonate
Fc	Ferrocene
$[FeCl_4]^-$	Tetrachloridoferrate(III)
$[FSA]^-$	Bis(fluorosulfonyl)amide
GBA	Gamma-butyrolactone
I^-	Iodide
$[I_3]^-$	Triiodine monoanion
Li	Lithium
$[MBr_6]^- \cdot (Br_2)$	Bromine-rich halidometallates
M	Metal
MeCN	Acetonitrile
Mg	Magnesium
Mn	Manganese
$[MnBr_4]^{2-}$	Tetrabromidomanganate(II)
$[Mn(btc)]^-$	Benzene-1,3,5-tricaboxilic acid manganate(II)

$[MnCl_4]^{2-}$	Tetrachloridomanganate(II)
$[MnCl_5]^{2-}$	Pentachloridomanganate(III)
$[Mn(NCO)_4]^{2-}$	Cyanatidomanganate(II)
$[Mn(NCS)_4]^{2-}$	Thiocyanidomanganate(II)
$[Mn_4(OCOCH_3)_{10}]^{2-}$	Acidomanganate(II)
MX_n	Metal halide
$[MX_n]^-$	Halidometallate
Na	Sodium
NaCl	Sodium chloride
NaF	Sodium fluoride
$[NTf_2]^-$	Bis(trifluoromethanesulfonyl)amide
$[N_{R1R2R3R4}]^+$	Quaternary alkylammonium
$[N_{2221}]^+$	Triethylmethyl ammonium
$[N_{22.(3O1)2}]^+$	*N*,*N*-diethyl-3-di(methoxypropyl) ammonium
$[OTf]^-$	Trifluoromethanesulfonate
PHM	Polyhalogen monoanion
PHMIL	Polyhalogen monoanion ionic liquid
$[PF_6]^-$	Hexafluoridophosphate
$[PPh_4]^+$	Tetraphenylphosphonium
$[PNP]^+$	Tetraphenylphosphonium undecachloride
$[P_{R1R2R3R4}]^+$	Quaternary alkylphoshonium
$[R_1R_2IM]^+$	1,3-alkylimidazolium
ROTf	alkyltriflate
$[R_1R_2Pyrr]^+$	*N*,*N*-alkylpyrrolidinium
Sn	Tin
$[SnBr_3]^-$	Tribromidostannate(II)
$[SnBr_6]^{2-}$	Hexabromidostannate(IV)
$[SnCl_3]^-$	Trichloridostannate(II)
$[SnCl_4]^{2-}$	Tetrachloridostannate(II)
$[Sn_2Cl_5]^-$	Pentachloridostannate(II)
$[SnCl_6]^{2-}$	Hexachloridostannate(IV)
$[S_{R1R2R3}]^+$	Tertiary alkylsulfonium
$[Sn(NTf_2)_3]^-$	Bis(trifluoromethanesulfonyl)amidostannate
THM	Trihalogen monoanion
THMIL	Trihalogen monoanion ionic liquid
V	Vanadium
X^-	Halide
$[X_n]^-$	Polyhalogen monoanion
$[X_3]^-$	Trihalogen monoanion
$[XF_4]^-$	Tetrafluoridohalogenate(III) monoanions

$[XY_2]^-$	Tri-interhalogen monoanion

Table of Contents

1. Introduction

In 2019, the Swedish Royal Academy of Sciences granted the Nobel Prize in chemistry to Goodenough, Whittingham, and Yoshino for their work on Li-ion batteries (LIBs). The reasoning behind the decision was the widespread use of Li-ion batteries (LIBs) in consumer electronics, especially electronic vehicles,[1] and the hope for solving future energy and environmental problems. The development of LIBs will not only help to store the excess energy from wind and solar energy sources but will also support a "fossil fuel-free society."[1]

As early as the 1950's various effects on the environment, due to the then acceptable chemical practices from industry and government, resulted in a variety of disasters in local environments and made the public consciousness aware to problems caused by poor industrial practices, resulting in various environmental regulations.[2] In 1982 the company Exxon[3] and later in 1988 the company Shell,[4] both fossil fuel companies, had commissioned studies documenting and predicting the negative consequences of climate change due to carbon based fossil fuel sources and CO_2 release. The results indicated a variety of detrimental environmental effects and the studies were first distributed publicly in 2018.[3,4] Despite this knowledge, many companies engaged and still to this day engage in misleading information campaigns and continued economic practices regarding chemical processes and fuel sources that lead to ineffectual climate policy.[5,6] Positively, the damages caused by chemical industrial processes enabling climate change and the necessary changes required to stabilize the climate are becoming common knowledge due to the publication of international reports such as that of the International Panel on Climate Change's recent Sixth Assessment Report.[7] Innovative research, design, and implementation of new and existing technologies in combination with social change will help to stabilize and repair previous harmful changes to the environment.[6,8]

Scientists occupy a key position of power and authority in "the how and the why" of climate change and its stabilization. On an individual level, an average scientist can rely on the principles of green chemistry to produce new technologies, materials, and synthesis routes or identify new power sources less harmful to the environment. On a communal level as a group, influence could be used to drive decision making and best practices in the private sector, public sector with legislation similar to "The Green New Deal" in the United States of America[9] or international agreements such as "The Paris Agreement."[10] Public outreach can be advocated for programs that model the "Fridays for Future"[11] movement to focus on transparency concerning chemical and energy sustainability.

As part of the transition towards climate stability, non-carbon based fuel sources have been suggested, hydrogen,[12] nuclear fusion and fission,[13] wind,[14] solar photovoltaics,[15] geothermal,[16] or wave energy.[17] In order to utilize all the excess or intermittent energy produced by alternate fuel sources, batteries present themselves as part of the solution. Implementing redox-flow batteries, such as the all-vanadium battery,[18] zinc-bromide battery,[19] or recently non-aqueous versions based on V, Mn, Fe, or Al IL batteries that can store the excess energy in electricity grids for cities and industrial use is a productive step towards integrating alternative energy sources into everyday life. Mobile batteries such as Li-ion, Mg-ion, Na-ion,[20] or inorganic solid-state batteries[21] could be used in mobile consumer electronics or in electronic vehicles.

As a byproduct of a changing climate the search for cleaner, better synthesis routes, new materials, energy sources, and green chemicals has fueled the growth of ionic liquids research in the past two decades. Ionic liquids (ILs) stem from molten salt chemistry and are defined as salt melt below 100 °C.[22] Often called designer chemicals, ILs are very appealing because their properties can be easily modified in the initial synthesis to be matched to the necessary requirements and applications. Over the past decade ILs have been increasingly used by chemists and material scientists in electrochemical applications[23] for their low vapor pressure and desirable electrochemical properties in regards to diffusion and charge transport phenomena.

The following body of work aims to highlight ionic liquids, especially ILs based on inorganic halidometallates and polyhalogen monoanions, and guides the reader through their initial discovery, synthesis, defining physical and electrochemical characteristics, and finally how to apply the given knowledge about ILs in electrochemical applications, such as metal recycling or battery technologies.

1.1 Molten salt chemistry: A precursor to ionic liquids

Derived from traditional molten salt chemistry, ionic liquids are molten salts or ionic media in the liquid state, with melting temperatures below 100 °C.[22] Given that molten salts and ionic liquids are the same from a physical perspective, except for the lowered melting point, it is therefore of some small interest to look at several examples of prior and modern molten salt chemistry, before investigating ILs further.

Traditional molten salt chemistry is difficult to perform and energy intensive due to the relatively high temperatures necessary to facilitate reactions. Take the example of sodium chloride, NaCl, simple to dissolve in an aqueous solution and seen in every first-year chemistry curriculum from testing the solubility of ions in water to separating halogens. However, when heated to its melting point of 801 °C[24] a variety of new properties occur: for instance, due to the ionic bonds that held the solid together being disrupted, the specific conductance of the melt increases significantly to 3.09 $S \cdot cm^{-1}$ at 802.3 °C.[25] The conductance is utilized in an industrial process known as the Downs' Process, see **Figure 1**, whereby a 1:2 mixture of NaCl and $CaCl_2$ (to reduce the melting point temperature) is heated to 600 °C and subsequent electrolysis at 10 – 125 $mA \cdot cm^{-2}$ generates liquid sodium metal at the iron cathode and chlorine gas at the carbon anode.[26,27] The calcium has a significantly lower anodic potential ($E°$ = –3.8 V)[28] than sodium ($E°$ = –2.71 V),[28] therefore no liquid calcium is generated. The liquid sodium is less dense than the surrounding electrolyte solution and is collected at the surface in a separate reservoir. The process generates the majority of high purity sodium metal used around the world.[26] The entire reason for performing the reduction process as a molten salt as opposed to in aqueous solution stems from the large reduction potential of Na metal being greater than the electrochemical window of water, whereby the hydrogen evolution reaction would occur.[28] Additionally, the viscosity of molten NaCl (1.029 mPa·s, 1082.3 °C)[29] is similar to water (0.89 mPa·s, 25 °C).[30]

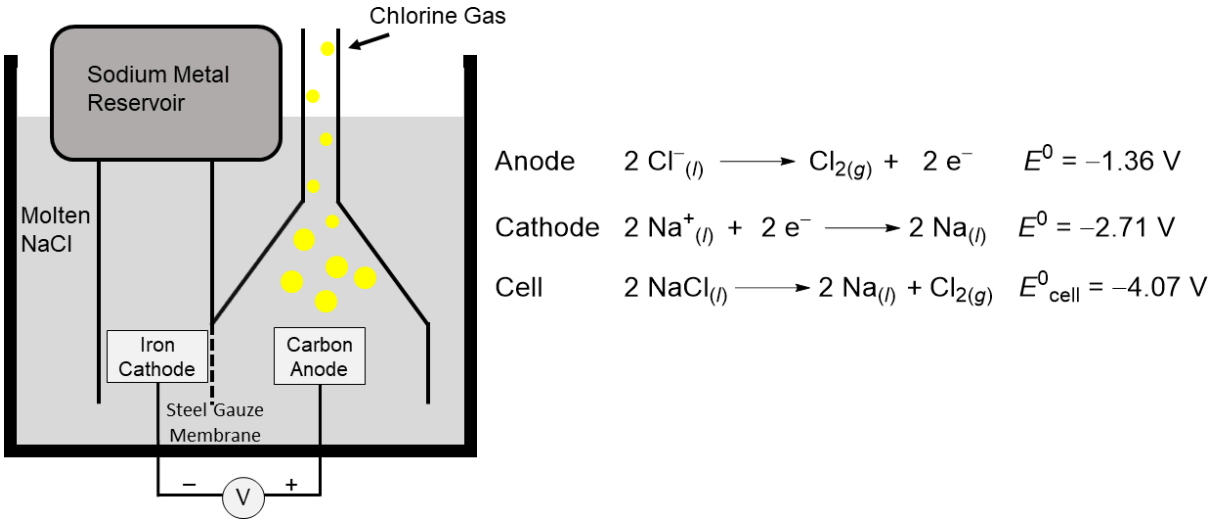

Figure 1. Representation of a Downs' Cell for the electrolysis of molten NaCl to produce $Na_{(l)}$ and $Cl_{(g)}$, including the half-cell and cell potentials.[28] Picture made by author.

A second example of molten salts used to procure pure metals due to the large negative potential of metal reduction in aqueous solutions is the electrolysis of alumina, Al_2O_3, to

metallic Al. The industrial process is two-fold: first the synthesis of Al_2O_3 from bauxite ore and caustic soda, NaOH, via the Bayer process,[31] and subsequent reduction thereof to Al in the Hall-Héroult process or more commonly referred to as the Cryolite process.[32,33] The reason for the name Cryolite process is due to the additive electrolyte salt cryolite, which is a complex salt of sodium hexafluoridoaluminate, $Na_3[AlF_6]$. When combined with alumina or bauxite in an 85 % to 15 % ratio, a eutectic mixture forms lowering the total melting temperature to 935 °C which can save significant amounts of energy when compared to the melting point of the pure substance at 2054 °C.[32] The anode is constructed from pure carbon and is oxidized in the presence of freed oxygen from the alumina, resulting in carbon dioxide as driving force of the reaction. The cathode material is similar to the anode, but contains a larger amount of ash, and is built directly into the bottom and sides of the cell housing, such that liquid aluminum, being denser (Al, 2.39 $g \cdot mL^{-1}$ at 950 °C)[32] than the cryolite mixture, is reduced at the electrode surface producing Al with purities greater than 99.5 % and CO_2, see **Equation (1).**

$$2\ Al_2O_3 + 3\ C \longrightarrow 4\ Al + 3\ CO_2 \quad (1)$$

Modern facilities have an energy usage of 14 – 15 $kW \cdot h \cdot kg^{-1}$ Al produced[32,33] with theoretical thermodynamic minima being obtained without inefficiencies at 6.232 $kW \cdot h \cdot (kg\ Al)^{-1}$.[34] The total environmental costs of using the Hall-Héroult process are rather large and result in a total exergy equivalent of 152.05 MJ and 6.96 kg of CO_2 all in respect to 1 kg of Al produced.[34] The energy expenditure in this industrial process and other electrolytic smelting processes is one reason why alternatives are being sought in ionic liquids that have considerably lower energy demands.

A final example of molten salt chemistry is the formation of useful materials in Li-ion batteries. By mixing LiCl and Mn_2O_3 at 900 °C for 7 h results in the formation of $LiMn_2O_4$ nanoparticles.[35] $LiMn_2O_4$ is a common cathode material in LIBs with a discharge specific capacity of 123 $mA \cdot h \cdot g^{-1}$[36] and can be increased by doping with Na and Mg and adding a graphene sheet layer to 146 $mA \cdot h \cdot g^{-1}$ ($Li_{0.94}Na_{0.06}Mg_{0.08}Mn_{1.92}O_4$).[37] For the anode materials, SnO_2 nanorods can be synthesized by heating Sn nanoparticles with NaCl and KCl in air at 720 °C for 1 d.[38] The SnO_2 nanorods are then intercalated with Li during discharge to $LiSnO_2$ and have a higher theoretical energy density (782 $mA \cdot h \cdot g^{-1}$)[38] than intercalated graphite electrodes (372 $mA \cdot h \cdot g^{-1}$).[39] Despite the high theoretical energy density, the downside to using SnO_2 electrodes is their increase in volume during delithiation as opposed to graphite

electrodes. As an alternative, SnS_2 retains the high theoretical energy density and has a comparably limited volume change.[40]

1.2 What are ionic liquids?

The first characterized ionic liquids were ethanolammonium nitrate from Gabriel in 1888[41] and ethylammonium nitrate from Walden in 1914.[42] These simple molten salts were some of the first low melting or ambient temperature ionic liquid compounds, but only later received the moniker '*ionic liquid*' near the 1970's with the term molten salt being reserved for salts with higher temperature melting points. During the 1970's the true advancement and popularity in the field of ILs started and was broadened by expanding upon the organic cation and use of a chloridometallate anion in basic research performed by Osteryoung,[43] and Wilkes and Hussey.[44] In the 1990's and 2000's interest was further increased with common discussions of organic anions, and catalysis and synthesis by Fuller et al.[45,46] and Bonhôte,[47] which led to further research by Wasserscheid[48–50] and expanding the theoretical and experimental understanding by Abbott et al.[51,52] The last decade also had several advancements in the application of ILs towards energy storage systems[19,53,54] and green chemistry,[55–59] and will likely remain of scientific interest in industrial and scientific applications in the coming decade.

Based on the previous introduction to molten salts the usefulness of ionic liquids becomes apparent. Why wouldn't the average chemist want to have access to a high thermally[60] and electrically conductive,[61,62] moderately viscous,[63] robust ionic compound that can be a substitute solvents,[51,64] engage in synthesis,[65,66] exhibits a large energy density,[54] and has a variety of applications without the large energy and safety demands imposed by traditional molten salt chemistry?[26,67] ILs are often referred to as designer chemicals,[68] due to the rather large amount of physical properties that can be easily altered given a change in cation or anion, and can be used in many applications. Arguably the first of the modern ILs was the organic cation – inorganic anion combination with the tetrachloridoaluminate anion or historically called tetrachloroaluminate, $[AlCl_4]^-$.[43,44] In 1951 this compound was of great interest to Hurley and Wler[69] as an alternative to the Hall-Héroult aluminum smelting technique, and will be discussed further in a later section, see **Section 1.5.2.1 Metal** recycling and electrodeposition.

When developing, characterizing, or applying ILs there is typically a wide variation in the cation, with specifics aimed towards analyzing the anion.[44,46,70–72] Several common classes of

cations have emerged in the literature based on ammonium cations:[63] quaternary ammonium ($[N_{R_1R_2R_3R_4}]^+$)[73,74] ($_{R_n}$ = length of carbon chain, periods in between numbers indicate an independent chain) and more recently amphiphilic compounds with two charge centers,[74] imidazolium ($[R_1R_2IM]^+$),[44,71,75] (R_n = length of a carbon chain), piperidinium ($[R_1R_2Pip]^+$),[76] pyrrolidinium ($[R_1R_2Pyrr]^+$),[77] or partial perfluorinated triazolium cations,[78,79] see **Figure 2**. Other common cations are the quaternary phosphonium ($[P_{R_1R_2R_3R_4}]^+$)[80] or tertiary sulfonium cations ($[S_{R_1R_2R_3}]^+$).[81] The size of the alkyl chains can change the density, miscibility in water, or lower the melting temperature;[51,82,83] additionally, the electrochemical window can be adjusted to the active species.[82,84] By changing the alkyl chain length a destabilization of the Coulomb packing occurs, resulting in lowering the energy necessary to melt, despite the increase in stability via increased van der Waals forces in chains of $n > 7$.[85]

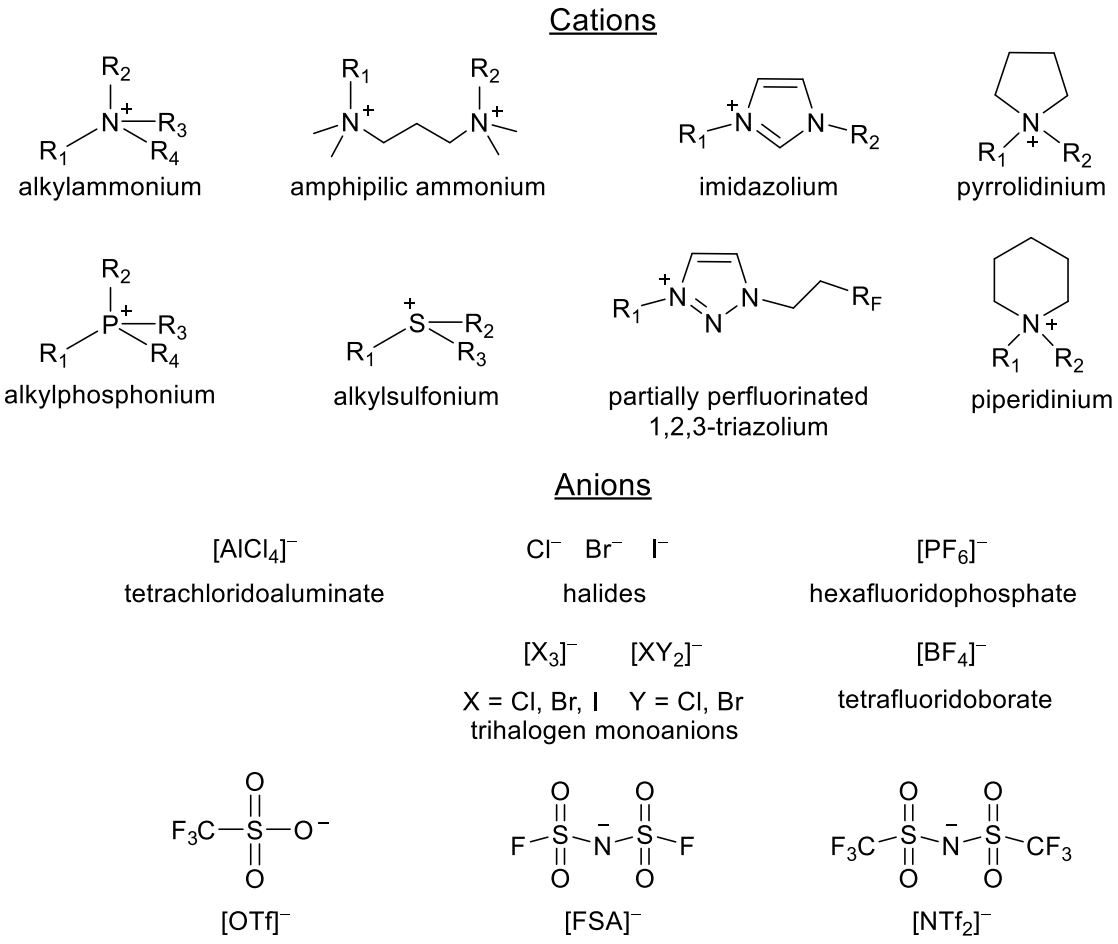

Figure 2. Commonly used cations and anions in ionic liquids.

The commonly used anions include $[NO_3]^-$,[42] halidometallates of similar form to $[M(X)Cl_{x+1}]^-$ (X = II, III, IV) for but not limited to the following metals Al^{III},[43] Ga^{III},[86] In^{III},[86] Fe^{III},[87] Co^{II},[87] Zn^{II},[86,88] Mn^{II},[89] Sn^{II} and Sn^{IV},[90] and Hf^{IV}.[86] Changing the anion is useful

to adjust the density, conductivity, or viscosity of the IL,[83] and can play a role as the active species in electrochemical or catalytic reactions.[68] Polyhalogen monoanions $[X_n]^-$ (n = odd) or halides X^-, where X = Cl, Br, I, are also used often to increase conductivity,[61,73,91] as sequestering agent for dihalogen gases,[92,93] and in energy producing systems.[59,93,94] Perfluorinated species like $[BF_4]^-$[83] or $[PF_6]^-$,[83] organic (compounds containing carbon) perfluorinated trifluoromethanesulfonate ($[OTf]^-$, $[SO_3CF_3]^-$),[74,95,96] bis(fluorosulfonyl)amide ($[FSA]^-$, $[N(SO_2F)_2]^-$),[74] or bis(trifluoromethanesulfonyl)amide ($[NTf_2]^-$, $[N(SO_2CF_3)_2]^-$) [74] are, due to the non-polarizability of fluorine electrons, especially valued for their viscosity lowering effects via the van der Waals interactions, and destabilization effects towards the solid state lattice.[97] Additionally, $[NTf_2]^-$ has two isoenergetic forms that increase the number of modes of configurational entropy and thus stabilization of the liquid state, or stated differently, destabilization of the packing structure.[98]

1.3 Synthesis of common ionic liquids

There is large variety in ionic liquids and they can be tailor synthesized for the required chemical property. However, many syntheses can be broadly grouped into categories. Of particular interest for all ILs is the resulting purity after synthesis, because the physicochemical characteristics can vary significantly based on the contaminant. It has been suggested that without a proper water or contaminant analysis, that collected data can be deemed unreliable.[66] The water content can for some ILs be determined by Karl-Fischer titration.[80] However, it is to be noted that the majority of current studies do not specify water content or impurities, rather they list one of the following purification methods.[66]

To reduce the impurity levels within ILs, several methods of purification exist. Starting with synthesis, the precursors should be properly distilled or purified,[99] the product should be preferentially recrystallized from an organic solvent, e.g., hexane, methanol, or ethanol.[74] To remove the water impurity and to some extent remaining organic impurities, the IL is subjected to vacuum, 10^{-3} – 10^{-6} mbar, at temperatures between 50 – 110 °C for a period of 3 h to several days.[44,80,100] The compound is analyzed for impurities via ^1H and ^{13}C NMR analysis and Raman spectroscopy or mass spectroscopy (MS). Another method to remove contaminants, especially the halides from *n*-RX or MgRX (X = Cl, Br, I) precursors in the synthesis of organic cations, is addition of A3 size molecular sieves. A3 size molecular sieves have been shown to reduce the impurity concentration within $[C_4C_1IM][PF_6]$ ($[C_4C_1IM]$ = 1-butyl-3-methyl-

imidazolium) leading to greater electrochemical windows, whereas as A4 increased contamination.[100]

Given that the purity of commercially available ionic liquids typically ranges from 97 to 99 % and their availability has increased in the last 15 years, it is reasonable to purchase a variety of commonly available ILs. The purchase of ILs instead of synthesizing can save time and provides the chemist with a catalogue of readily accessible ILs with varied chemical properties. The purity of these ILs should still be strictly controlled before reporting in any literature. For more unique ILs that are not commercially available, they can be synthesized in the laboratory.[101,102]

Another interesting use of ILs is in ionothermal synthesis, where the cation and anion act simultaneously as the solvent and act as the framework for further synthesis products.[103] Ionothermal synthesis can be used to generate polycationic and polyanionic species, zeolites, and metal organic frameworks.[103,104] The synthesis method can be used to dissolve metals within $[Cl_3]^-$ or $[Br_3]^-$ based ILs,[57] but during the synthesis process the original physicochemical properties of the IL change, e.g., conductivity, viscosity, dissolving capacity, and diffusion rates.[105,106]

While not many studies on the detailed mechanism of ionothermal synthesis exist,[107] one that is being currently investigated is that of fluorination with $[BF_4]^-$ and $[PF_6]^-$ anion based ILs. An example of an ionothermal fluorination synthesis is that of MnF_2 nanoparticles. By adding the IL $[C_4C_1IM][BF_4]$ to $Mn(CH_3COO)_2$ at 150 °C for 35 h, MnF_2 nanoparticles were synthesized.[108] The proposed fluorination mechanism involves residual H_2O within the IL hydrolyzing the $[BF_4]^-$ anion upon heating into $BF_3{\cdot}H_2O$ and F^-.[108,109] The F^- acts as the fluorinating agent, and the method is proposed to be less dangerous than direct fluorination via HF or F_2.[109] The resulting MnF_2 is useful as an anode material in Li-ion batteries and has shown to have reversible electrochemical activity with Li, resulting in a specific capacity of 237 $mA{\cdot}h{\cdot}g^{-1}$ at 10 °C over a period of 5000 cycles.[108]

A final example of ionothermal synthesis is in the formation of large discrete anionic species, for instance $[PNP][Cl_{13}]^-$[110] ($[PNP]^+$ = tetraphenylphosphonium undecachloride) or $[AsPh_4][Cl(BrCl)_6]$.[111] At the time of writing, the largest known discrete polyanionic species are the spherical shaped zeolites $[C_4C_1C_1IM]_{24}[Sn_{36}Ge_{24}Se_{132}]$ ($[C_4C_1C_1IM]^+$ = 1-butyl-(2,)3-(di)methylimidazolium) and $[C_4C_1IM]_{24}[Sn_{32.5}Ge_{27.5}Se_{132}]$ with an outer diameter of 2.83 nm and inner diameter of 1.16 nm.[112] They are synthesized by the synthesized using the ILs

$[C_4C_1C_1IM][BF_4]$ and $[C_4C_1IM][BF_4]$, respectively, and reacting with $[K_4(H_2O)_3][Ge_4Se_{10}]$ and $SnCl_4 \cdot 5\,H_2O$ with a small amount of 2,6-dimethylmorpholine.[112] Of interest is the interaction between the cations as a stabilizing forces for the polyanionic species.[112]

The following section will briefly describe a general synthesis and the relevance of the most commonly used ions in recent years. The primary emphasis is placed on inorganic anions but should not detract the reader from the usefulness or attempting to study the other ionic species in the current literature.

1.3.1 Inorganic anions

Ionic liquids, as are currently known, follow one of three systems: organic-inorganic, organic-organic, or inorganic-inorganic salts. The first salts of interest were organic-inorganic systems of the chloridometallates and remain the most prevalent. With time additional anions were introduced for different chemical properties. The perfluorinated anions $[PF_6]^-$ and $[BF_4]^-$ were important as their chemical properties made use of biphasic systems.[83] Later, polyhalogen monoanion ionic liquids (PHMIL) became the focus of anionic research in the 2010's for their relatively large conductivities,[61] sequestering properties,[93] and metal dissolution properties.[56–58]

Metal-ligand anion based ILs are a subgroup of ILs and have recently received an increase in attention within literature due to their luminescence, catalytic, and magnetic properties.[113] These properties stem from the liquid phase and the unique influence on chemical and physicochemical characteristics granted by the metal.[106] Within this body of work the halidometallate anion based ILs ($[MX_n]^-$, M = metal, X = Cl, Br, or I) with the metals manganese and tin were of great importance due to their relative natural abundance,[24] electrochemical properties,[114,115] and similarity in redox chemistry to the zinc-bromide redox-flow battery[115,116] A variety of Mn and Sn anion based ionic liquids are found in the literature[90,117–129] and are a small listing is presented in **Table 1**.

Table 1. Manganese and tin-ligand anion based ionic liquids.

Mn based Ionic Liquid	Refs.	Sn based ionic liquids	Refs.
$[C_4C_1IM]_2[MnCl_4]$	[117]	$[C_8C_1IM][SnCl_3]$	[118,119]
$[C_6C_1IM]_3[MnCl_4][C_{12}SO_3]$	[120]	$[C_2C1_1IM][SnCl_3][AuCl_4]$	[121]
$[C_2C_1]_3[MnCl_4][AlCl_4]$	[122]	$[C_4C_1Pyrr]_2[SnCl_3][NTf_2]$	[123]
$[C_4C_1IM]_2[MnBr_4]$	[124]	$[C_8C_1IM]_2[SnCl_4]$	[118]
$[N_{4222}]_2[Mn(NCS)_4]$	[125]	$[C_8C_1IM][Sn_2Cl_5]$	[118]
$[N(PPh_3)_2]_2[Mn(NCO)_4]$	[125]	$[C_8C_1IM]_2[SnCl_6]$	[118]
$[C_2C_1IM]_2[Mn_4(OCOCH_3)_{10}]$	[126]	$[PPh_4][SnBr_3]$	[127]
$[C_2C_1IM][Mn(btc)]$	[128]	$[C_4C_1IM]_2[SnBr_6]\cdot Br_2$	[90]
		$[C_4C_1Pyrr][Sn(NTf_2)_3]$	[129]

1) btc = benzene-1,3,5-tricarboxylic acid

The synthesis of different halidometallate anion based ILs and an in depth discussion of their analysis is presented in the next section, followed by a look at polyhalogen anion based ILs, and finally, how the two merge in the formation of halogen-rich halidometallates anions.

1.3.1.2 Halidometallates and their speciation, $[MX_n]^-$ (M = Metal, X = Cl, Br, I)

For a long time, ionic liquids were akin to ambient or near ambient temperature chloridoaluminate salt melts. This perception was to first change in literature around the 2000's when perfluorinated anions became more prevalent,[49,68,130] and electrochemical application of ILs utilized more non-metallic supporting electrolytes.[67,131] While a wealth of study has been performed with halidometallate ILs, there is still room for innovation. Typically, halidometallate salts are synthesized by dissolving the metal halide, MX_n, in the halide ionic liquid, [Cat.]Y. The coordination sphere of the metal envelops the additional ligand and can form an equilibrium of multiple metallate anions, see **Equation (2).**

$$MX_n \xrightarrow{[Cat.]Y} [Cat.][MX_nY] \xrightleftharpoons{[Cat.]Y} [Cat.][MY_2] + [Cat.]X_n \quad (2)$$

The speciation of metallates into distinct binary ILs was observed by Welton et al. by dissolving a metal salt in $[C_4MPy]I$ and subsequent dissociation into two distinct cations and anions.[132] By changing the metal, metal salt concentration, and Cl to Br or I the chemical properties can be altered.[118,133] For instance, in halidoaluminate(III) salts ($[AlX_4]^-$) the melting temperature increases going from Cl,[43] Br,[134] to I.[43]

Complete speciation studies are rather limited and typically require multiple methods of analysis across multiple scientific publications. Currently, the following species may be considered relatively well studied based on the amount of literature available: bromidoaluminate(III),[54,134] chloridoaluminate(III),[44,135] chloridogallate(III),[119,136] chloridoindate(III),[119,137] chloridostannate(II),[118] and chloridozincate(II).[138] Current literature is still developing evidence for speciation in the many IL species including chloridoferrate(III) or chloridocobaltate(II), or ILs with Br and I based ligands, for instance bromidostannate(II/IV).[139]

Given the importance of speciation in understanding halidometallate synthesis, it is important to acquire the proper tools of analysis. Due to the ionic state the following basic methods of analysis are mandatory: vibrational and UV-*vis* spectroscopy, NMR analysis of the metal species, and thermodynamic and electrochemical analysis. Some other techniques that are helpful, but not necessary include: electron paramagnetic resonance spectroscopy or X-ray photoelectron spectroscopy.

1.3.1.5.1 Vibrational spectroscopy

Both IR and Raman spectroscopy are important techniques in determining the primary species in the halidometallates and examining the M–X vibrational modes. Primarily Raman spectroscopy is used to monitor metal ligand vibrational modes between 600 – 100 cm^{-1}.[118,138,140,141] A simple method to demonstrate speciation is to analyze the vibrational intensity at varying amounts of metal halide salts. By utilizing Raman spectroscopy on $[AlX_4]^-$ (X = Cl, Br, or I) systems the formation and equilibrium between $[AlX_4]^-$ and $[Al_2X_7]^-$ could be confirmed for varying amounts of χ_{AlX_3}, see **Table 2**.

Table 2. Raman frequencies of $[AlX_4]^-/[Al_2X_7]^-$ systems (X = Cl, Br, or I) at varying amounts of AlX_3.

Halide, X^-	Refs.	χ_{AlX_3}	$[AlX_4]^-$ / cm^{-1}	$[Al_2X_7]^-$ / cm^{-1}
Cl^-	[43]	0.50	351	-
		0.60	351	315
		0.67	-	315
Br^-	[134]	0.50	211	-
		0.60	211	200
		0.67	-	200
I^-	[142]	0.50	146	140

Mixed-halide systems are rather rare, but have been studied for $[N_{111.16}][InBr_xCl_{(4-x)}]$ systems. The resulting vibrational bands were in agreement with the statistical variation for $\chi_{InCl_3} = 0.50$ and could be assigned to previous literature values.

One downside to Raman spectroscopy is that it cannot or only with difficulty resolve spectra of species with concentrations less than 5 – 10 mol%. Therefore, the dominant species in the ionic phase is identifiable, but non-dominant species will be less likely registered.[68] Another problem that may occur is fluorescence caused by organic impurities or increasing χ_{MX_Y} concentrations.[141,143] It was suggested for the $[FeCl_4]^-$ system to use a Nd:YAG laser (1064 nm) excitation source instead of a 785 nm excitation source to reduce fluorescence caused by impurities.[144]

Overall, Raman spectroscopy is a valuable tool to identify the primary species of a given melt and can be used in a variety of halidometallate systems.

1.3.1.5.2 NMR spectroscopy of metal species

NMR spectroscopy is a good complementary analysis method to vibrational spectroscopy because it can help identify secondary species. Due to the liquid nature of the IL they can be measured directly without dilution in a deuterated solvent, rather an external deuterium lock is used for ^1H and ^{13}C NMR analysis. Additionally, and more importantly for halidometallate systems, NMR spectroscopy of metals has been used successfully to track speciation in IL systems. However, the observed chemical shift in neat ionic media may differ markedly from their solution counterpart.[145]

Minor shifts in speciation around the metal nuclei can result in significant variation to NMR signals and can be observed in the width and shape of the signal. The NMR signals and their full width at half maximum ($\Delta\nu_{1/2}$) can be dependent on a variety of factors including the sample viscosity, molecular symmetry of the metal species, temperature, or a dynamic equilibrium between multiple species.[68] Samples with high viscosities, quite common amongst ILs, require longer reorientation correlation times, which reduces the quadrupolar relaxation rate and results in broad NMR signals.[145] The lower the symmetry around the metal center, the broader are the signals.[68,145]

The $[C_4C_1IM][SnCl_3]$[146] and $[C_8C_1IM][SnCl_3]$[118] systems and their speciation were analyzed by ^{119}Sn NMR spectroscopy. Originally based on ^{119}Sn NMR chemical shifts and varying χ_{SnCl_2}, three different stannate species were proposed, $[SnCl_3]^-$, $[SnCl_4]^{2-}$,

and $[Sn_2Cl_5]^-$.[146] However, a later more comprehensive study utilized Raman spectroscopy, XPS, and viscometric data in tandem with ^{119}Sn NMR to identify only two species, $[SnCl_3]^-$ (δ = –68 pPHM) and $[Sn_2Cl_5]^-$ (δ = –245 pPHM).[118] The $[SnCl_3]^-$ speciation could only be determined in combination with other techniques as the ^{119}Sn NMR was not sufficient. This system of investigation can be further applied to $[SnBr_3]^-$ or $[SnI_3]^-$ in the future.

Thus, NMR analysis helped determine the speciation of $[C_8C_1IM][SnCl_3]$. However, it is best used together with vibrational spectroscopy to help determine the dominant species in phase equilibrium.

1.3.1.5.3 UV-*vis* spectroscopy

UV-*vis* spectroscopy can be useful for halidometallates that absorb ultraviolet or visible light. The measurement times are fast and useful for testing larger amounts of samples. The limiting factor in UV-*vis* spectroscopy are the high extinction coefficients for neat systems. ILs, such as $[C_2C_1IM][AlCl_4]$,[147] reach the extinction coefficient in larger cuvettes due to their concentration resulting in detector saturation. Therefore, to reduce the extinction coefficient cuvettes with a path length less than 0.1 mm should be used and dilution should be considered, although a change in speciation may occur, due to the cuvette geometry.[148]

Recently, Lahiri, and Das performed a series of electrodeposition experiments of aluminum and aluminum-titanium alloy with a $[C_2C_1IM][AlCl_4]$ electrolyte and a sacrificial titanium anode.[147] The speciation within the electrolyte was analyzed via UV-*vis* spectroscopy and NMR analysis, indicating formation of a titanium-aluminum complex within the IL electrolyte.

A couple other chloridometallates have been analyzed via UV-*vis* spectroscopy including $[C_4C_1IM][FeCl_4]$ after exposure to γ radiation,[149] $[P_{666.14}]_2[CoCl_4]$ in the selective extraction of Co and Ni from 8 M HCl solutions between the aqueous and ionic liquid phase,[150] or a mixture of d-block metals in the form of $[C_4Py][M_1M_2Cl_4]$ (M = Co, Cu, Mn; χ_M = 0.25, 0.50, 0.75) in combination with their electrochemical conductance (10^{-1} – 10^{-4} mS·cm^{-1}) and stability windows (2.5 – 3 V).[151]

1.3.1.5.4 Thermal properties and differential scanning calorimetry

Other defining physical characteristics of ILs are their melting, solidification, and glassy transition temperatures. By using differential scanning calorimetry (DSC) the key physical characteristics can be determined.[68,138] The thermal properties can be compiled into a phase diagram to confirm the IL species and whether it has contaminants, changing its overall

chemical composition. However, as a reference method, this only works if the IL has been previously identified and catalogued.[68]

1.3.1.5.5 The influence of the cation upon the anion

Until this point the differing spectroscopic techniques have been discussed in the determination of anionic speciation without consideration towards the cation. However, the cation by way of functionalizing groups, hydrogen bonding, and steric can affect the formation of the anion.[118,152]

One example of the cation effecting the anion are the chloridoplumbate(II) ILs. Given $[P_{666.14}][PbCl_3]$ a slightly distorted trigonal planar structure (D_{3h}) was proposed for $[PbCl_3]^-$ based on Raman spectroscopy and ^{207}Pb NMR analysis. However, with the counter ion $[C_2C_1IM]^+$, $[PbCl_3]^-$ has a *pseudo*-tetrahedral configuration (C_{3v}).[152] The proposed difference is attributed to the stereochemically active lone pair electrons on Pb, comparable to $[C_2C_1IM][SnCl_3]$.[118,152]

1.3.1.5.6 Analysis of the solid, solvated, and gas states

Ionic liquids are salts in the liquid state. Methods of analysis in the gas phase, solid state, or in solvent are useful, but do not always represent a complete chemical analysis of the neat liquid phase. Analysis techniques that observe the solid state via X-ray diffraction analysis, the gas phase via mass spectroscopy, or ILs dissolved in solvent can lead to misleading results, and the analysis techniques have been corrected multiple times years after initial publication.[68]

1.3.1.5.6.1 X-ray diffraction analysis and the solid state

X-ray diffraction analysis (XRD) can help identify species in the ionic phase. However, single crystals cannot be assumed to represent the constitution of the ionic liquid. One example is of $[C_4C_1IM][AuCl_4]$, where several examples exist of crystallography confirming the structure of square planar for $[AuCl_4]^-$,[153,154] but was further confirmed with additional Raman spectroscopy and *ab initio* calculations.[68]

$[C_4C_1IM][SnCl_3]$ ILs and their anion speciation as neat ILs were only found to exist as $[SnCl_3]^-$ or $[Sn_2Cl_5]^{2-}$ via Raman spectroscopy and ^{119}Sn NMR analysis. However, the structural evidence suggested single crystal of $[SnCl_3]^-$ or $[SnCl_4]^{2-}$.[117] Furthermore, crystals grown from MeCN produced $[SnCl_4]^{2-}$ moieties and those grown directly from the melt $[SnCl_3]^-$. Therefore, for the $[SnCl_3]^-$ system, XRD analysis while helpful, did not properly identify the speciation within the neat melt.[117]

1.3.1.3 The polyhalogen monoanion, $[X_n]^-$ (n = odd, X = F, Cl, Br, I)

Within the last 10 years a significant amount of fundamental discovery occurred within the field of polyhalogen monoanion (PHM) chemistry. The fundamental areas of study elucidated the very interesting structural diversity of PHMs of the form $[X_{2n+1}]^-$ (X = F, Cl, Br, I; n = 1, 3, 5, 7) based on a synthesis of X_2 and [Cat.]X,[91,111,155,156–158] see **Equation (3).** The formation of these PHMs benefitted by using larger organic cations, as opposed to alkali salts, to form ionic liquids (PHMIL). These PHMILs have subsequently been characterization via Raman spectroscopy, XRD analysis, or electrochemical analysis.[61,73,115,159,160] Based on the fundamental chemistry, an increasing number of applications are being found for PHMILs including metal dissolution and recycling experiments,[55,57] gas sequestration,[93,161] battery applications,[19,93,162] and halogenation reactions in organic systems.[158]

$$[\text{Cat.}]X + n\,X_2 \longrightarrow [\text{Cat.}][X_{2n+1}] \quad (3)$$

At the time of writing, the most highly coordinated discrete PHMs that have been experimentally obtained are $[F_5]^-$,[157,163] in a 4 K argon matrix-isolation experiments, $[Br_{11}]^-$[156] or $[Cl_{13}]^-$,[110] being determined in the solid state, and $[I_{15}]^-$,[164] suggested with ESI-MS data, and the interhalogen species $[Cl(BrCl)_6]^-$ [111] in the solid state. Halogen bonding has differing bond strengths depending on the complex (5 – 180 kJ·mol^{-1})[165] and can be primarily attributed to the σ-hole effect. The σ-hole effect is possible to calculate via the electrostatic potential of polyhalogen species, and is defined in a recent review on polyhalogen chemistry: "*A belt of charge accumulation perpendicular to the molecule's main axis is observed, and a region of more positive electrostatic potential on the bonding axis is revealed*."[91] Whereby, the σ-hole is smallest in fluorine and increases to iodine by F < Cl < Br < I.[91]

The above PHMs have been examined primarily outside of ionic liquids. However, many polychlorine and polybromine monoanion RTILs can be synthesized given the correct organic cation. The most commonly discussed PHMIL is the trihalogen monoanion,[91] and it will be discussed in the next section.

1.3.1.3.1 Trihalogen monoanions, $[X_3]^-$ (X = Cl, Br, I)

The most commonly studied PHMILs are the trihalogen monoanions (THM), with Chattaway and Hoyle analyzing the first interhalogen THMs in 1923.[166] THM based ionic liquids (THMIL) come in two distinct forms, as the homonuclear species, $[X_3]^-$ (X = Cl, Br, I),

and the interhalogen species $[XY_2]^-$ (X, Y = Cl, Br, I). For triinterhalogen monoanions the preferred central atom is typically the more electropositive halogen atom surrounded by the more electronegative halogen atoms, e.g., $[ICl_2]^-$.[167,168] However, when the halogen ratio is reversed, e.g., more I than Cl, then the central atom is the more electronegative species (Cl) surrounded by more electropositive species (I), e.g., $[ClI_2]^-$.[167,169] In solution, currently not known in ionic media, the preferred structure for THMs with a single heavier atom is $[Y–X–Y]^-$ and with a lighter single atom is $[Y–X–X]^-$.[170,171]

Useful methods of analyzing THMILs include Raman spectroscopy, UV-*vis* spectroscopy, conductometry, viscometry, X-ray diffraction analysis or electrochemical analysis.[91] NMR analysis can be used to observe the cation component in THMILs, but $^{35/37}$Cl, $^{79/81}$Br, and ^{127}I NMR spectroscopy has not been useful in identifying the anionic species, due to quadrupolar effects yielding broad signals and unresolved spectra for all but the simplest of haloorganic molecules.[172]

1.3.1.3.2 Interhalogen tetrafluoridohalogenate(III) monoanions, $[XF_4]^-$ (X = Cl, Br, I)

While not yet ionic liquids, the interhalogen tetrafluoridochlorate(III) monoanions ($[ClF_4]^-$) have recently been prepared with the organic cation $[N_{2221}]^+$[173] in acetonitrile and propionitrile. Previously, alkali salts were used in the synthesis of $[ClF_4]^-$, due to the high reactivity of the reactant ClF_3. However, the alkali cation can be exchanged for an ammonium cation by addition of fluorine in argon to the $[N_{2221}]Cl$ salt in acetonitrile at –40 °C. Via ^{19}F NMR analysis of $[N_{2221}]^+$ at 0 °C the cation stability was demonstrated at room temperature for one month before fluorination of the alkyl groups.[173] Utilization of the organic cation is an important step closer to a neat IL. Future research could then make use of the IL and the oxidizing strength of the fluoridohalogenate(III) species based on Cl, Br or I.

1.3.3 Halogen-rich halidometallates: Combining halidometallates anions and halogen networks, $[MX_6]^-·X_2$ (X = Cl, Br)

The current trend in recent literature concerning PHMILs is to dissolve metals in them[55–58] thus forming halidometallates, or the synthesis of bromine-rich halidometallates of the general form $[Cat.][MBr_6]·Br_2$ by Adonin et al.[174–181] and Feldmann et al.[88,90,182]

Binnemans et al. demonstrated that $[Cl_3]^-$[55,57,58] and $[Br_3]^-$[55] PHMILs could dissolve metals for possible recycling purposes. However, within their studies no characterization of the products was obtained, but a halidometallate species was likely produced.

In the solid state, polyhalogen monoanions of type $[Br_{2n+1}]^-$[181,183] or $[Cl_{2n+1}]^-$[110,184] (n = 1 – 6) form networks of 1-, 2-, and 3-D structures. By combining polyhalogen monoanions in slight excess with various halidometallate ionic liquids, networks between the halidometallates and polyhalogen monoanions are formed. Several known species include $[Pt_2Br_{10}]^-$,[182] $[SbBr_6]^{3-}$,[175–177] $[BiBr_5]^{2-}$,[178] or $[TeBr_6]^{2-}$[180,185] and are connected via $[Br_3]^-$ or Br_2 units to form 3-D networks. In $[C_4C_1IM]_2[SnBr_6]\cdot Br_2$, discrete $[SnBr_6]^{2-}$ units form a series of 3-D networks connected by Br_2 units,[90] and are similar to those in $[ZnBr_5]\cdot Br_2$.[88] The compound was highlighted for its stability: Br_2 was only released at 250 °C.[90] Additionally, interhalogen networks between $[TeCl_6]^{2-}$ and Br_2 were demonstrated to be feasible.[179,185]

The current halide-rich systems have been primarily analyzed the solid state, and it would be interesting to see such systems extended to the liquid state. The combination of properties from halidometallate ILs and PHMILs would be beneficial, as the polyhalogen component could provide increased specific conductivity,[61,73] and benefit from the energy density with an active metal species[54] in electrochemical applications.

1.3.2 Organic anions

Organic anions, anions that contain carbon components within IL ion pairs, are useful alternatives to the chloride salts, as they are not as reactive, do not absorb as much water, and can be dried to a relatively low water content.[59,83] The organic anion when paired with an organic cation in an IL has an electrochemical window between 4 and 6 V[186,187] but can be significantly larger given certain ILs, e.g., $[C_4C_1IM][OTf]$ (9.0 V),[158] being significantly larger to water, making electrochemical applications more feasible.[188] The commonly occurring anions $[OTf]^-$ and $[NTf_2]^-$ typically find use in lithium ion batteries with or without carbonate solvents as additional conductive supporting electrolytes for the transport of ions.[131,186]

1.3.2.1 Trifluoromethanesulfonate, triflate anion, $[OTf]^-$

The synthesis of trifluoromethanesulfonate or its common name triflate anions ($[OTf]^-$ or $[CF_3SO_3]^-$) proceeds by mixing trifluoromethanesulfonic acid (triflic acid) and a metal chloride,[96,189] typically Ag.[190] The reaction is strongly exothermic and produces $HCl_{(g)}$. Subsequently, through alkylation via alkyliodide and triflic acid the alkyltriflate (CF_3SO_2OR or ROTf) is synthesized. Mixing $CF_3SO_2OCH_3$ and methylimidazol results in the IL $[RC_1IM][OTf]$, see **Scheme 1**.[95] In order to avoid contaminants in the precursors an

alternative halide and metal free synthesis of $CF_3SO_2OCH_3$ was developed via mixing triflic anhydride and dimethylcarbonate, with CO_2 as the byproduct.[95,191]

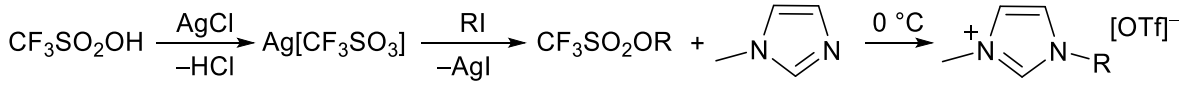

Scheme 1. Preparation of $[RC_1IM][OTf]$ starting from triflic acid via the metal triflate.[190,191]

1.3.2.2 Bis(trifluoromethanesulfonyl)amide anion, $[NTf_2]^-$

Bis(trifluoromethanesulfonyl)amide ($[NTf_2]^-$ or $[(CF_3SO_2)_2N]^-$) is a commonly occurring anion in the literature and is especially desirable for its electrochemical stability and aprotic nature caused by the CF_3 groups and their polarizability.[83] The IL, $[IM][NTf_2]$, is therefore often used in non-aqueous systems for battery applications.[67,131,192] Typically, $[NTf_2]^-$ is purchased as an alkali metal[193] or Ag salt[47,193] and an ion exchange reaction is performed.

The synthesis of $[NTf_2]^-$, similar to $[OTf]^-$, requiring multiple steps and specialized knowledge and equipment that can be used with anhydrous HF (aHF). By mixing CH_3SO_2Cl and KF an exothermic reaction occurs and produces CH_3SO_2F. Subsequently, via the Simons process,[194] selective electrochemically fluorinated (ECF) CF_3SO_2F is formed by dissolving CH_3SO_2F in aHF and applying a voltage of 4 – 6 V and 6 – 9 A for 46 h, see **Scheme 2**.[195,196] After several steps and heating to 110 °C the alkali salt precursor $Na[NTf_2]$ is formed.[195]

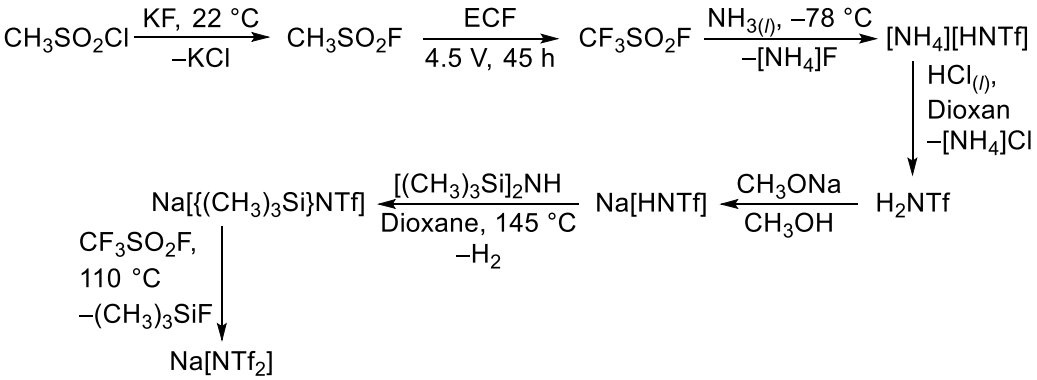

Scheme 2. Synthesis of $Na[NTf_2]$ from CH_3SO_2Cl.[195,196] With Tf = CF_3SO_2.

1.3.3 Synthesis of cations

The research on cations in ILs is more prolific than that of anions in ILs and is centered around organic rather than inorganic cations. Variation of organic cations typically occurs in the alkyl tail length, with more asymmetric cations such as $[N_{3221}]^+$, while good at lowering the

melting point, hinder crystallization leading to a larger glass phase. Whereas more symmetric cations such $[N_{2222}]^+$ typically generate solid state structures.[66,197]

1.3.3.1 Inorganic cations

Inorganic cations, within IL systems, are not as well researched in current scientific literature compared to organic cations in ILs. Additionally, most inorganic cations within ILs are found in inorganic-inorganic systems. However, when inorganic cations are used they typically consist of an alkali salt and a relatively large inorganic anion with a large ionic radius and low charge density, for example, $Na_{13}[La(TiW_{11}O_{39})_2]$.[198] The lanthanide (Ln) based ILs ($Na_{13}[Ln(TiW_{11}O_{39})_2]$) were synthesized for biphasic catalysis and separation techniques.[198] By varying the lanthanide species within $Na_{13}[Ln(TiW_{11}O_{39})_2]$ the conductivity ranged from 1.1 – 2.0 $mS \cdot cm^{-1}$.[170]

The synthesis of $Na_{13}[Ln(TiW_{11}O_{39})_2]$ was carried out by mixing sodium tungstate with $TiCl_4$ in glacial acetic acid, before adding $LnNO_3$ and heating for 3 h at 75 °C.[198] Another recently determined RTIL with an inorganic cation system was $[PBr_4][Al_2Br_7]$ and the compound's ionicity was confirmed via the Walden plot.[199] Some other cations include $[PCl_4]^+$,[200] $[SCl_3]^+$,[201] or $[ClSO_2NH_3]^+$ when paired with a weakly basic anion.[97]

1.3.3.2 Organic cations

Arguably the most commonly used cations for ILs in the current literature are ammonium based. Of the multitude of ammonium based organic cations the 1,3-dialkylammonium[50,90,130,202] and 1,1-dialkylpyrrolidinium[59,60,67,73] salts appear significantly more than other salts. The reason for their desirability is a well-known synthesis,[47,130] and a wide variety of chemical characteristics can be changed by increasing the alkyl chain length, or by adding alkyl groups with additional substituents such as ether groups[102] or perfluorinated alkyl chains.[78,79]

1.3.3.2.1 1,3-Dialkylimidazolium cation, $[R_1R_2IM]^+$

The synthesis of 1,3-dialkylimidazolium ($[R_1R_2IM]^+$) salts is common in the literature. Bonhôte proposed a synthesis by using methylimidazole and adding an equivalent of *n*-BuCl, forming $[C_4C_1IM]Cl$,[47] see **Scheme 3**. After synthesis of the halide salt, it can be further reacted with X_2 or MX_3 to form PHMILs or halidometallate salts as previously described. The halide salt can then undergo an anion exchange reaction via silver halide.[47]

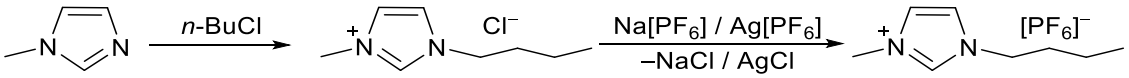

Scheme 3. Synthesis of $[C_4C_1IM]Cl$ and subsequent anion exchange reaction to $[C_4C_1IM][PF_6]$.[47,130]

One downside to Bonhôte's synthesis is the potential contamination of halides during or after the ion exchange.[203] An IL can be checked for halide impurities via an $AgNO_3$ test or X-ray fluorescence spectroscopy.[193] To reduce the amount of contamination, halide free syntheses with non-halide counterions have been proposed by Dupont et al. with $[OTf]^-$.[130] Alternatively, phase separation can be used another form of ion exchange instead of AgX, for example with Li[OTf] or $Na[PF_6]$.[47,102,130]

1.3.3.2.1 1,1-Dialkylpyrrolidinium cation, $[R_1R_2Pyrr]^+$

One of the benefits of the pyrrolidinium salts ($[R_1R_2Pyrr]^+$) in comparison to the imidazolium salts is their greater chemical stability against halogenation reactions[73,204] and on average larger electrochemical windows.[67,205] Forsyth and MacFarlane first proposed the synthesis of pyrrolidinium salts $[R_1R_2Pyrr]^+$ (R_1 = Me, Et, Pr, Bu) from the quaternization reaction of methylpyrrolidine with an $[OTf]^-$ counterion, see **Scheme 4**.[77] The methylpyrrolidinium precursor is very common in literature and can be synthesized from butanediol and methylamine with a Cu/Ni catalyst.[206] Further they determined typical physicochemical characteristics with the conductivity being 1.4 $mS \cdot cm^{-1}$ for $[C_3C_1Pyrr][OTf]$ and 2.2 $mS \cdot cm^{-1}$ for $[C_4C_1Pyrr][OTf]$.[77] Since then, a variety of synthesis alterations have been performed for electrochemical applications.[205,207]

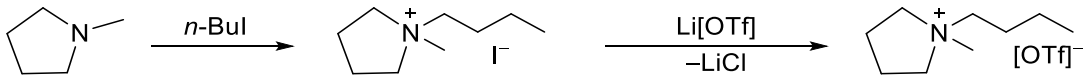

Scheme 4. Synthesis of $[C_4C_1Pyrr]I$ and subsequent anion exchange reaction to $[C_4C_1Pyrr][OTf]$.[77]

1.4 Thermodynamics, diffusion, Walden's rule, and cyclic voltammetry

Ionic liquids have a variety of desirable chemical and physical characteristics due to their ionic media and chemical composition. However, the most widely discussed points for comprehension are the liquid state,[51,52] ion migration and its influence upon viscosity,[97,208] and electrochemical conductance.[67,209]

Thermodynamically, the process of a solid melting into a liquid is called fusion. The energy required for this process at any given temperature (T) results from changes to enthalpy (H) and

entropy (S) resulting in the Gibbs free energy of fusion (G), see **Equation (4)**. At the melting temperature the value of G is zero, negative values correspond to the liquid state, and positive values to the solid state.[82]

$$\Delta G = \Delta H - T\Delta S \qquad (4)$$

For ILs, ΔG_{fus} has been calculated via volume-based thermodynamics.[82,210] Whereby utilizing a Born-Fajans-Haber cycle the energy of fusion for a given temperature is equivalent to the difference between the lattice energy (ΔG_{latt}) and the solvation energy (ΔG_{solv}) of a system, see **Equation (5)**.[82]

$$\Delta G^{T}_{fus} = \Delta G^{T}_{latt} - \Delta G^{T}_{solv} \qquad (5)$$

The diffusion of individual ions within ILs is related to charge transfer and the conductivity within the ionic liquid. Abbott modified Hole theory to explain the ion mobility, not just for dilute solutions, but also aptly to ILs.[51,52,211,212] Hole theory postulates that ion migration through a melt occurs via a set probability of individual ions entering into an interstitial void as a result of the thermal fluctuations. The "holes" or interstitial voids and ions, their locations and size are considered random and constantly changing.[51]

In experimental terms, Hole theory can help explain the temperature dependent conductivity and viscosity. The Vogel-Fulcher-Tamman equation (VFT) is a semi-empirical derivative of the Arrhenius equation used to predict the temperature dependent dynamic viscosity (η), which is the viscosity developed by an external force acting on particles in a fluid, and the specific conductivity (σ), see **Equations (6)** and **(7)**.[51,52,213]

$$\eta(T) = \eta_0 \exp\left(\frac{B}{(T - T_g)}\right) \qquad (6)$$

$$\sigma(T) = \sigma_0 \exp\left(-\frac{B'}{(T - T_g')}\right) \qquad (7)$$

The terms η_0 and σ_0 are the dynamic viscosity and specific conductivity at infinite temperature, respectively, B and B' are related to the thermodynamic probability of an ion moving into an unoccupied "hole" or interstitial void, and T_g and T_g' are the glassy transition temperatures. The VFT equation describes ILs, however, it can be expanded to use when the ILs are diluted as well. The difference in T_g and T_g' as well as B and B' stems from conductivity

measurements containing a measure of temperature-dependent ion association that is lacking in viscosity measurements.[214]

The movement of ions through the various holes leads to a local change in concentration. The translational movement and diffusion of ions (D_i), given isothermal and isobaric systems, result in a local concentration gradient that can be explained by Fick's first and second laws, see **Equations (8)** and **(10)**, respectively.[215] Fick's first law relates the flux density of the particle (j_i) to the proportionality of the diffusion constant and concentration gradient for some concentration (c_i) and along a one-dimensional directional axis (z):[215]

$$\vec{j_i} = -D_i \frac{\delta c_i}{\delta z_i} \qquad (8)$$

Combining the first law, **Equation (8)**, with the law of mass conservation with a given change in concentration over time (t),

$$\frac{\delta c_i}{\delta t} + \frac{\delta\left(D_i \delta c_i / \delta z_i\right)}{\delta z_i} = 0 \qquad (9)$$

then results in Fick's second law.[215]

$$\frac{\delta c_i}{\delta t} = D_i \frac{\delta^2 c_i}{\delta z_i^2} \qquad (10)$$

When considering a fluid under an applied force, the diffusion of ILs can be determined by the Stokes-Einstein equation. Stokes recognized the relation between the internal frictional force enacted upon the migration of spherical particles in liquids ($\vec{F}$). The force is proportional to the volume of a sphere with radius (r), but is also influenced by the "slipperiness" of ions to pass one another (f) ($f = 6$ for perfect stick or $f = 4$ for perfect slip), the viscosity, and the velocity of the sphere within the fluid ($\vec{v}$),[216] see **Equation (11)**. The relation bears his name, Stokes' law.

$$\vec{F} = f\pi\eta r\vec{v} \qquad (11)$$

In 1905, Einstein proposed what is now known as the Einstein relation, based upon Brownian motion, or the random movement of particles. The diffusion of a particle is proportional to ion mobility under a force (μ_i), and the temperature (T), with k_B being the Boltzmann constant,[217] see **Equation (12)**.

$$D_i = \mu_i k_B T \qquad (12)$$

The general ion mobility can be replaced with the internal frictional force. The Stokes-Einstein equation follows for the diffusion of a particle through a liquid, see **Equation (13)**.[209]

$$D_i = \frac{k_B T}{f \pi \eta r} \qquad (13)$$

The ion migration and therefore diffusion properties of ILs can be represented by the Stokes-Einstein equation.[51,52] If $D\eta/T$ is constant for all T, then the liquid may be considered to have Stokesian behavior, and if not, then non-Stokesian behavior is said to occur. The case of non-Stokesian behavior in ILs will be examined in more detail for PHMILs in a following section, see **Section 1.4.2**.

1.4.1 Walden's rule

As first noted by Walden in 1906 in his empirical study of $[N_{2222}]I$[218] and subsequent work on binary salts in 1920,[219] the dynamic viscosity, and the equivalent molar conductivity (Λ_{NE}) of salts are proportional to a constant at all temperatures (C). The mathematical result of the empirical relation is Walden's rule.

Through further empiricism the early German school of electrochemists (1890 – 1930) soon realized that Walden's rule was non-ideal for certain silver iodide salts and thus modified it to become the fractional Walden's rule.[220] The discrepancy stems from cation-anion size differences and diffusion in relation to one another, thus a decoupling factor, α, was added to the viscosity term, see **Equation (14)** and **(15)**.[97,213,214,220,221] The result is typically plotted on a logarithmic scale in the Walden plot.

$$\Lambda_{NE} \eta^{\alpha} = C = \text{constant} \qquad (14)$$

$$\log \Lambda_{NE} = \log C + \alpha \log \eta^{-1} \qquad (15)$$

The ideal solution for a Walden plot is a 1 M KCl aqueous solution resulting in a slope of 1 and y-intercept of 0. ILs follow non-ideal behavior and thus obey the fractional Walden rule. Angell[222,223] was one of the first to compare IL ionicity based on the Walden plot, see **Figure 3**. Typically, values that are above the ideal KCl line indicate a fluid with "superionicity," dissociated ion pairs that follows the Grotthuss mechanism; those directly below the ideal KCl line are considered to be "good" ILs with minor ion association; or even

lower as "poor" ILs with aggregates of ions.[214] The Walden plot has become a common base of comparison between ILs to quickly screen for their electrochemical applicability.[224]

However, it is important to note that Schreiner et al.[214] in 2009 and Harris[225] in 2020 have criticized the Angell-Walden analysis for molten media based upon high temperature melts of alkali chlorides and of various ionic liquids and the resulting inaccuracies in determining whether a substance is superionic or not. The primary critiques correspond to the decoupling factor yielding varying slopes in ILs.[214] Primarily, as a failure of the Nernst-Einstein equation being valid for infinitely dilute electrolyte solutions,[225] system size, and the previously unrecognized consequences of viscosity.[226] The proposed alternative is to utilize non-equilibrium thermodynamic quantities called Laity resistance coefficients, with the base assumption that the substance is a salt melt.[225]

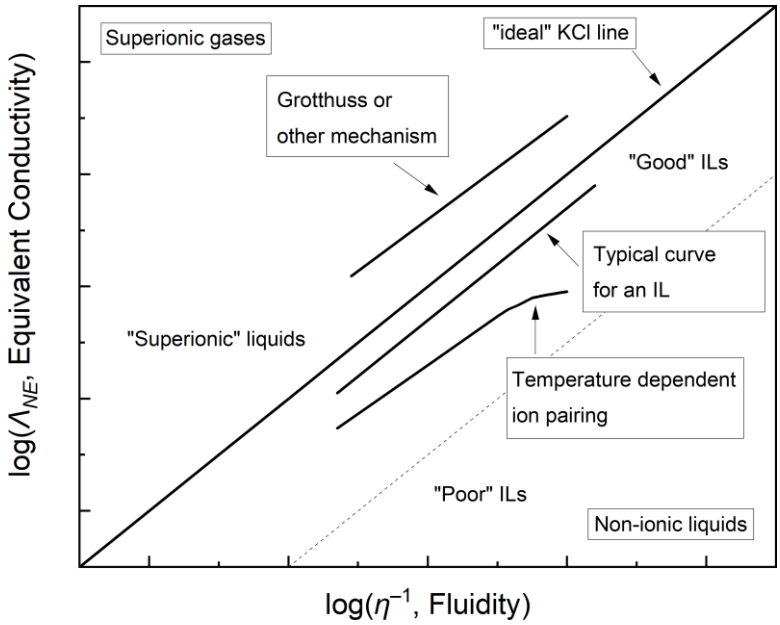

Figure 3. Classification diagram of a Walden plot for ionic liquids. The ideal KCl line is an 1 M KCl aqueous solution represented by a solid line with a slope of 1, and the dashed line is an arbitrary delimiter between "good" and "poor" ionic liquids. Picture made by author, adapted from literature[222,223]

To address Harris' criticism it is important to understand the Nernst equation and its limitations. The Gibbs Free energy ($G°$) is related to the cell potential ($E°$), and energy per charge transferred, with moles of electrons transferred (n), and Faraday's constant, (F), see **Equation (16)**.[28]

$$\Delta G° = -nFE° \qquad (16)$$

Given a chemical reaction there exists an equilibrium between species yielding the reaction quotient (Q). The Gibbs Free energy of a chemical system with the gas constant (R) can be written as follows.[28]

$$\Delta G° = RT\ln Q \qquad (17)$$

Then inserting the cell potential and replacing the reaction quotient with the chemical activities of the electrochemically oxidized species, α_{ox}, and the reduced species, α_{red}, yields the Nernst equation, see **Equation (18)**.[28]

$$E = E° - \frac{RT}{nF}\ln\frac{\alpha_{red}}{\alpha_{ox}} \qquad (18)$$

The Nernst equation is valid for all concentration ranges. However, in a laboratory setting it is difficult or unpractical to determine the activity coefficients. Therefore, for dilute solutions, experimentally (10^{-4} – 10^{-5} M), or preferably for infinitely dilute solutions, the activity coefficients can be approximated for the reduced and oxidized species to be the same, resulting in unity.[220]

In comparison, as the concentration increases and for purely ionic substances the chemical activity coefficients start to differ from one another and reduce the usefulness of the Nernst equation, as the experimental chemical activity cannot be easily obtained. While Debye and Hückel proposed a theory for dealing with semi-dilute solutions,[227] the activity coefficients of pure molten salts cannot currently be accurately determined.[228] Therefore, in practical, experimental terms the Nernst equation applies to dilute solutions, but fails for concentrated solutions or for ILs.[225]

By combining the Nernst equation and the Einstein relation the Nernst-Einstein equation is formed, see **Equation (19)**. It relates the self-diffusion coefficient to the individual ionic species (D_{Si}), based on individual ion stoichiometries (ν_i), and the species charge (z_i) to the equivalent molar conductivity (Λ_{NE}). Furthermore, the equivalent molar conductivity is equal to the specific conductivity (σ) divided by the concentration of the electroactive species (c) and species' charge.[225]

$$\Lambda_{NE} = \frac{\sigma}{cz_i} = \left(\frac{F^2}{RT}\right)(\nu_+ z_+^2 D_{S+} + \nu_- z_-^2 D_{S-}) \qquad (19)$$

The ionicity of the ionic liquid (Y) is the ratio between the molar conductivity (Λ_m) and equivalent molar conductivity, see **Equation (20)**. If the ionicity is unity, 1, then perfect

ionicity occurs and an equal distribution of anions and cations is present in the system. If $Y < 1$ then aggregates of cation-anion pairs form, and if $Y > 1$ then non-Stokesian behavior occurs.[225]

$$Y = \frac{\Lambda_m}{\Lambda_{NE}} \qquad (20)$$

The Nernst-Einstein equation, as a result of being formulated for one extreme (infinitely dilute solutions), cannot adequately describe the other extreme (pure substances).[229] ILs are pure substances, the extreme, and are not properly described via electrochemical laboratory experiments. Furthermore, Watanabe et al. demonstrated that the path length of finite particles and friction caused via dynamic viscosity required for ion migration was the key physical discrepancy.[226] They found a correlation was demonstrated between low viscosity ILs deviating more significantly and high viscosity ILs deviating less from the Nernst-Einstein equation.[226]

At this current point in time more studies are required to provoke thought, create new hypothesis, and provide a clear theoretical and experimental framework for ionic movement within pure electrolyte systems. Overall, the Walden plot has been and will likely remain an extremely important factor for scientists screening certain ILs over others for battery applications based solely on the conductivity and diffusion properties.[59,97,229,230]

1.4.2 Non-Stokesian charge transport, Grotthuss mechanism, and polyhalogen monoanion ionic liquids

The Stokesian case of diffusion has been thoroughly explored within IL systems, and describes ion diffusion related to the viscosity and conductivity of an IL in conjunction with Walden's rule. Deviation from Stokesian behavior was first reported by Grotthuss in his study of the high mobility of protons in water.[231] The protons simultaneously make and break hydrogen bonds with oxygen atoms, resulting in the rapid diffusion of protons.[231] For most ILs, the ions diffuse past one another according to Stokesian behavior, but in PHMILs non-Stokesian diffusion is postulated.[94,159,231–234]

Watanabe and Kawano had investigated mixtures of $[C_2C_1IM][BF_4]$ and $[C_3C_1IM]I/[I_3]$ ILs in dye-sensitized solar cells (DSSC) and came to the conclusion that the higher conductivity and lower viscosity values were directly caused by the higher concentration and diffusion of $[I_3]^-$ moieties.[94,234] They postulated a Grotthuss style mechanism of diffusion for the $I^-/[I_3]^-$ system, based on the dissociation equilibrium of $[I_3]^-$. Generally, the diffusion of

PHMILs and the Grotthuss mechanism depends upon the formation of an intermediate $[X_n]^-$ (n = odd) and its dissociation into X_{n-1} and $[X^- \cdots X_{n-1}]^-$, see **Scheme 5**. The Grotthuss mechanism can also be further extended to interhalogen systems such as $[ICl_2]^-$.[71]

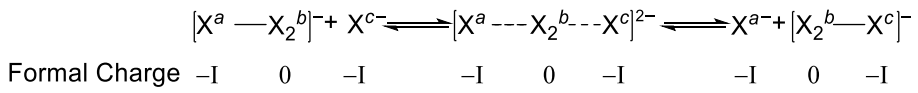

Scheme 5. Proposed Grotthuss mechanism via bond dissociation and formation in halide-trihalogen monoanion $X^-/[X_3]^-$ systems.

The apparent diffusion (D_{app}) of the system is represented by a combination of Grotthuss style diffusion with the exchange reaction of halogen atoms (D_{ex}) contributing the most and diffusion consistent with Stokesian behavior regarding the physical transport of ions (D_{phys}) as per the Dahms-Ruff equation, see **Equation (21)**. The exchange reaction term can be broken down into the rate constant of the exchange reaction (k_{ex}), the center-to-center intersite distance (δ), and the concentration of the electroactive species. Zhang and Bentley et al. recently determined the apparent diffusion of several dual salt RTILs of $I^-/[I_3]^-$ (6 – 15 mM I^-) with a D_{app} ranging between 0.7 and $4.4 \cdot 10^{-7}$ $cm^2 \cdot s^{-1}$.[72,159] The range in diffusion coefficients can be attributed to the varying concentration of I^- and the choice of IL solvent. The diffusion is relatively high compared to other ILs due to the Grotthuss style mechanism. In comparison, the diffusion of I^- in common molecular solvents was two orders of magnitude greater in water ($1.6 \cdot 10^{-5}$ $cm^2 \cdot s^{-1}$) or in acetonitrile ($2.1 \cdot 10^{-5}$ $cm^2 \cdot s^{-1}$).[72]

$$D_{app} = D_{ex} + D_{phys} = \frac{1}{6} k_{ex} \delta^2 c + D_{phys} \qquad (21)$$

Grossi et al. performed solid state electrochemical and computational studies of $[C_2C_1IM]I/[I_3]$ and proposed the formation of $[I_3]^- \cdots I \cdots I \cdots [I_3]^-$, or formally $[I_8]^{2-}$ as an octaiodine dianion, chains that transfer charge via a Grotthuss mechanism.[235] The formation of $[X_8]^{2-}$ for Cl,[236] Br,[171] and I[237] is well known and further PHMILs can form 2-D or 3-D networks in the solid state. The studies by Grossi and others demonstrated that the equilibrium of the Grotthuss mechanism in the solid state is uncertain.[231,235] Furthermore, in the liquid phase ion dissociation energies,[238] Coulombic effects,[212] ion transport,[94,232,235,239] Stokesian diffusion[159,235] and the Grotthuss mechanism[94,234] within PHMILs make it difficult to precisely determine the species equilibrium. Given the current knowledge of the solid and liquid state of PHMs, determining the actual species equilibrium in the liquid phase is currently non-trivial.

1.4.3 The basics of cyclic voltammetry in conjunction with ionic liquids

Typically, when ILs are investigated in terms of electrochemical characteristics their diffusivity, conductivity and ionicity, as described above, and their window of electrochemical stability are of importance. Cyclic voltammetry (CV), linear sweep voltammetry (LSV), and other electrochemical scanning techniques can determine the diffusion constants, specific conductivity of ILs, and the region of electrochemical stability.

The cyclic voltammetry experiment is particularly important as the redox potentials of a given substance can be confirmed. The resulting redox activity obeys the Nernst equation,[240,241] see **Equation (18)**, and the oxidative potential of a substance in a given solvent is quantified. Additionally, the electronic energy required of a single electron related to the thermal energy of an oxidation or reduction is called the thermal voltage (25.693 mV at 25.0 °C).[28] It is derived from (k_bT/q) within the Nernst-Einstein equation, with q being the charge of a species. To perform CV measurements, typically a three-electrode set-up consisting of a working electrode (WE) and counter or "auxiliary" electrode (CE) made out of an inert material such as Pt, Au, Ni, carbon or glassy carbon (GC), and a reference electrode (RE) is used, see **Figure 4**. For electroanalytic measurements the WE and CE are typically planar electrodes, with the surface area of the CE being slightly larger to enable greater current changes. Additionally, the RE is typically located physically closer to the WE than the CE.[28,67]

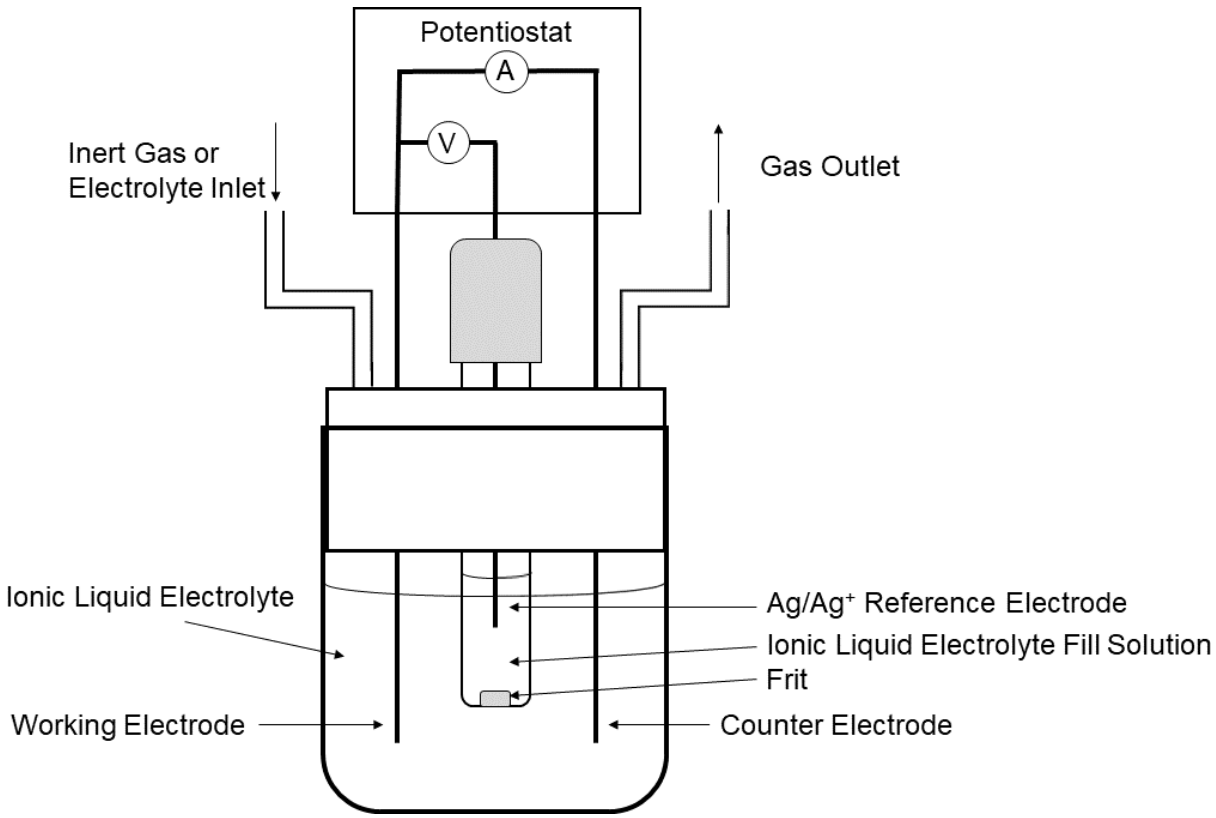

Figure 4. Three-electrode cell designed for inert electrochemical measurements. Picture made by author.

In regards to the electrolyte solution, RTILs can be measured directly as neat substances without further treatment. However, they can be diluted with a supporting electrolyte such as another IL with lower viscosity to assist in transporting the electroactive species.[72] Additionally, in cases where organic molecular solvents such as acetonitrile (MeCN) or tetrahydrofuran (THF) have high vapor pressures or are inflammable and they can be replaced with an ionic solvent, e.g., $[C_4C_1Pyrr][NTf_2]$, to negate these effects.[209,242]

1.4.3.1 Reference Electrodes

The potential of redox reactions should be reported against a stable reference electrode. In aqueous systems the standard hydrogen electrode (SHE) is the standard with $[Pt\text{-}Pd||H^+||H_2]$ at $E = 0$ V, but other REs are commonly used, such as the saturated calomel electrode (SCE) ($[Hg|Hg_2Cl_2|KCl]$, $E = +0.242$ V vs SHE), the silver–silver chloride (Ag/Ag+) ($[Ag|AgCl|KCl]$, $E = +0.197$ V vs SHE), or the copper–copper(II) sulfate (Cu/Cu^{2+}) ($[Cu|CuSO_4]$, $E = +0.314$ V vs SHE).[28]

Typically, the reference electrode solution is separated from the bulk electrolyte solution via a frit, leading to a liquid-junction potential in the tens of millivolts. The fill solution in the RE could also leak into the IL, this can occur in non-aqueous electrodes such as with Ag/Ag^+ in acetonitrile.[243] To avoid the problem it is preferred to use an RE of Ag wire in the desired IL separated by a glass housing and frit.[71–73,159] For instance, an Ag wire in 10 mM Ag[OTf] in $[C_3C_1Pyrr][NTf_2]$ during electrochemical studies of $[NTf_2]^-$ based ILs has been shown to reduce the liquid-junction potential due to the similarity between the electrolyte and the fill solution.[244]

Two general alternatives exist for REs: ferrocene and metallocene derivatives as an internal standard or the *pseudo*- or *quasi*-reference electrode. The use of ferrocene (Fc) as an internal standard with its single electron reduction-oxidation step to ferrocenium (Fc^+/Fc) was first reported by Gagne, Koval, and Lisensky for non-aqueous acetonitrile solutions.[245] Other metallocenes such as decamethyl ferrocene and ferrocene derivatives,[246] ruthenocene,[247] or cobaltocene[248] are used to determine the redox potential, if the redox waves of Fc and the active species overlap. Thus, the off-shifted potential of the other metallocenes does not interfere with interpretation of the redox potential. The problem with metallocenes is their poor solubility in ILs[249] and possible shift in redox potential of the active species IL.[250] The resulting redox potential can then be referenced based on ferrocene back to aqueous systems

via indirect means,[251] and thus the redox potential of any measured electrolyte species can be compared to one another.

The *quasi*-reference electrode is to be used when the above methods fail. Typically, a wire of chemically inert metal, Ag, Au, or Pt is chosen and a one-electrode reaction occurs resulting in M^+/M, but the thermodynamics of the system are not well defined. Therefore, the current is referenced and the potential at the CE properly adjusted to manipulate the WE voltage or current, but the redox potential cannot be referenced to any chemical reaction.[67]

1.4.3.2 Electrochemical stability and diffusion

The CV can be especially important in determining the purity of known ILs and the stability of newly synthesized ones. Typically ILs vary in their electrochemical stability with their electrochemical windows between 2 and 5.5 V,[67,100,242,252] for instance, $[C_2C_1IM][NTf_2]$ has an electrochemical window of 4.5 V.[47] CV is also good at identifying trace impurities within the known IL, especially halides ($> 10^{-5}$ M).[100]

As an example, for this dissertation, of displaying impurities in a known IL, **Figure 5** displays unpublished results produced of a CV of $[C_4C_1Pyrr][OTf]$ that was vacuum dried for 12 h (10^{-3} mbar, 100 °C) with no further purification after purchase from the manufacturer (Pt planar 1 mm diameter WE and CE; Fc^+/Fc internal RE; scan rate 100 $mV \cdot s^{-1}$). The reduction and oxidation waves between –1 and 2 V are indications of impurities, probably from chloride impurities caused by synthesis, see **Section 1.3.3.2 Organic** cations. The chloride is oxidized in two steps from Cl^- to $[Cl_3]^-$ followed by subsequent oxidation to Cl_2.[253,254] If the impurities are removed, then the electrochemical window is between –1.5 and 2.5 V.

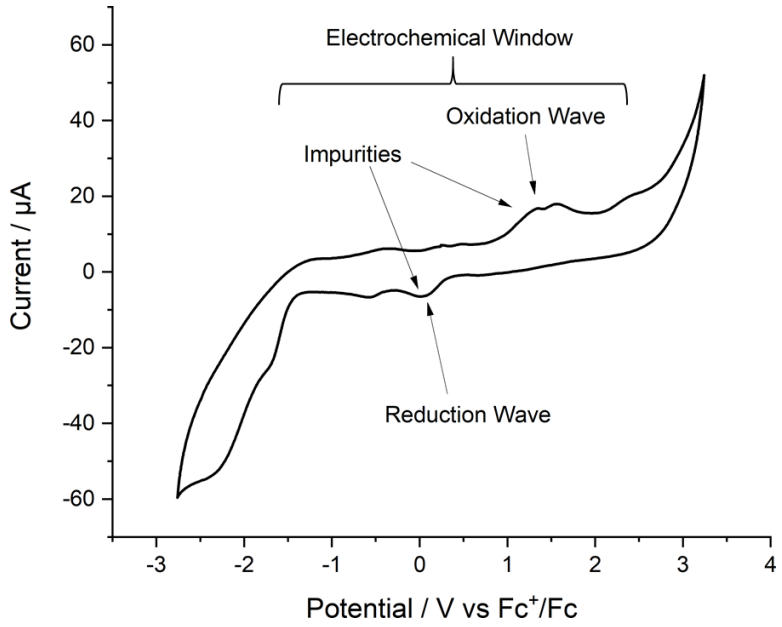

Figure 5. Cyclic voltammogram of $[C_4C_1Pyrr][OTf]$ after drying under vacuum. Impurities are probably halides from synthesis. Scan rate of 100 $mV \cdot s^{-1}$. Cyclic voltammogram recorded by author.

As previously discussed, the diffusion in ILs is a very important factor in their electrochemical applicability. The diffusion coefficient of a substance can be determined via chronoamperometric (CA) measurements and the Cottrell equation, as mentioned earlier with $I^-/[I_3]^-$.[72,159] Whereby, the current varies based upon stepwise changes in the applied WE potential, and drops over time (t) once the concentration (c) through diffusion of the electroactive species reaches equilibrium between the WE and the bulk solution. The current (i) is proportional to the square root of linear diffusion (D) between planar electrodes with a surface area (S_A). This results in the Cottrell equation,[28] see **Equation (22)**.

$$i = \frac{nFS_A c\sqrt{D}}{\sqrt{\pi t}} \qquad (22)$$

1.4.3.3 Spectroelectrochemistry

By combining electrochemical and spectroscopy techniques a greater degree of information can be won than from the individual techniques. Typically, a CV or linear sweep voltammogram (LSV) scan determines the point of electrochemical activity and subsequently a CA at the relevant potential reduces or oxidizes the electroactive species; this procedure is called controlled-potential chronoamperometry (CPCA).[255] During the electrochemical reduction-oxidation process (mostly in the CA, but also sometimes during the CV) Raman or UV-*vis* spectroscopy is employed to determine, *in situ*, the change in the vibrational or electronic structure of the electroactive species at the surface of the working electrode.[255,256]

The standard procedure is to use an optically transparent thin-layer cell (OTTL cell) to perform Raman,[255,256] IR,[256] or UV-*vis*[255,257] spectroscopy in tandem with CPCA. The WE is positioned in the middle and close to the cell windows. During UV-*vis* spectroscopy, the WE is typically a fine mesh electrode so that the light source is unhindered in passing through the OTTL cell into the detector. In comparison, the set-up for Raman spectroscopy uses a solid mirror electrode made of Pt, Ag, or Au to reflect light into the detector, and can take advantage of the surface enhanced Raman spectroscopy effect (SERS) to increase the signal intensity fourfold.[258]

The cell configuration inhibits diffusion past the diffusion layer from the WE to the bulk solution, thus creating a region of near complete electrolyte electrolysis near the WE. The drop in current on the current-potential plot is indicative of complete electrolysis in OTTL cells. The increase in local concentration is beneficial for Raman spectroscopy to identify the main species but may result in a molar extinction coefficient too large for a UV-*vis* spectrometer. Due to limited diffusion, scan rates should be lowered ($1 – 5\ mV \cdot s^{-1}$) to allow for electrolyte homogenization within the bulk solution. As a final consideration to diffusion properties and cell design, the scanning techniques may be either galvanostatic or potentiostat, but the diffusion remains quantitively the same.[255]

Spectroelectrochemistry does not need to be only in dilute solutions but has been used in combination with molten salt chemistry. For instance, the molten salts of K_2TaF_7-LiF-NaF-Na_2O were melted and electrolysis was performed with varying Ta/O ratios to synthesize various oxide salts.[259] Due to the chemical reactivity of evolved fluorine gas, the molten salt had to be cooled to a solid before *ex-situ* Raman spectroelectrochemical measurements. Unfortunately, due to speciation effects within the molten salt the *ex-situ* measurements lacked information concerning the liquid phase that *in-situ* measurements would have recorded, and possibly were missed during the experiment.[256]

1.5 Modern electrochemical applications of ionic liquids

Due to the unique chemical properties of ionic liquids and their “designer” qualities, they have found prevalent use in a variety of chemical applications. The IL mostly does not act alone but performs a supporting role to a known process and increases efficiency. The following is a non-exhaustive list of various applications that ILs have been used for: supported IL gel polymer membranes,[205,260] magnetic liquids,[261,262] bi-phasic separation and

extraction,[76,263] increasing material resistance towards radiation,[149,264] catalysis,[154,265] coupling reactions such as Diels-Alder cycloaddition[266] or Friedel-Crafts alkylation,[158,261] biocatalytic processes,[267] pharmaceuticals,[268] or gas separation.[269] There is a wealth of literature on various applications which is worth reading to understand the scope and relevance of ionic liquids. Rather than discussing the myriad of applications, the following section focuses on the current standing of ILs in regard to the electrochemical applications of metal recycling, electrosynthesis, and energy storage and collection systems.

1.5.1 Green chemistry and ionic liquids

Before the applications can be discussed in full, it is important to recognize that up to this day, ionic liquids are often described and marketed as "green" solvents. Their introduction as such was due to their low vapor pressure, relative non-flammability, and large temperature range compared to molecular solvents.[270,271,272,273] The classification of ILs as a green solvent creates an important relation to their application in catalysis, as a supporting electrolyte in battery or other electrochemical technologies, because the implication is that the application becomes "greener" by association to the IL.

Ironically, due to the designer nature of ILs, they can be produced to have properties that are inflammable[274] or toxic.[273,275] Additionally, the purification and extraction processes to remove contaminants from the IL can result in the use of additional solvents. In light of environmental concerns, Anastas and Warner developed the "twelve principles of green chemistry" to evaluate the greenness of a chemical process.[276] For ILs typically two relevant rules are applied: number 5, the use of benign solvents and auxiliaries; and number 12, use of inherently benign chemistry to prevent accidents. However, this should be relativized for each individual IL and its properties. Deetlefs and Seddon critically evaluated the synthesis of $[C_nC_1IM][X]/[NTf]$ (X = Cl, Br, I) and its purification process based on total laboratory synthesis.[270] Their conclusions indicate more focus should be given on an individual basis to each IL based on the twelve principles of green chemistry, and a good synthesis will have an *E*-factor, the ratio between waste and product produced, close to zero.

In 2011, the editorial to the journal *Green Chemistry* announced that they would no longer continue publishing any synthesis of new ionic liquids, unless specific insights were gained about cleaner methodologies.[272] The paradigm shift towards greener IL synthesis also changes how some researchers view ILs as solvents. A current trend in research is to move away from ILs and towards using deep eutectic solvents.[277]

Overall, ILs have beneficial physicochemical characteristics making them ideal in various applications. Caution is advised when making blanket statements about ILs and their processes becoming more environmentally friendly as a result of their use. Rather, an individual assessment based on the total experimental design should determine how green a process is.

1.5.2 Constant current techniques: Electrodeposition and Electrolysis

Controlled potential chronoamperometry is useful in the production of metals and plated materials through electrochemical deposition. Additionally, electrosynthesis of organic and inorganic species can be performed with the CPCA technique.[67,209] The large electrochemical window of ILs is of great benefit here in addition to their conductive properties, allowing for a wide range of reductive and oxidative reactions. Not only the electrochemical properties are desirable, but the reusability of ILs is of great importance in developing a more sustainable or energy efficient process. The use of ILs should enhance current electrosynthesis techniques and be made viable for larger industrial application.[209]

1.5.2.1 Metal recycling and electrodeposition

As discussed in the opening material on molten salt chemistry, a large amount of resources is expended every year towards the production of pure metals such as aluminum or sodium via electrodeposition from molten salt baths. A large portion of the energy requirement stems from the heat necessary to raise the salt temperature to the melting point during the electroreduction process.[34] Additionally, with an increased demand for Li-ion batteries for electronic vehicles, methods to reuse or recycle rare metals from the batteries including Li, Ni, Mn, and Co are highly sought after.[278,279]

The most studied IL system for electroreduction is that of $[AlCl_4]^-$ melts based on $[IM]^+$ and $[Pyrr]^+$ cations as an alternative to the Halt-Héroult process.[280] The use of low temperature melts in aluminum production would significantly lessen the overall cost and energy expenditures. Another benefit of electroreduction in ILs is the high active species concentration (c > 1 M), contributing to a greater amount of recoverable material. Typically, a buffer using NaCl is used to maintain the 1:1 ratio between $AlCl_3$ and Cl^-, resulting in a neutral solution. When the solution is more Lewis acidic the equilibrium shifts towards $[Al_2Cl_7]^{2-}$ and if the cathodic current is shifted to more positive currents, then alloying occurs.[281]

Metal deposition from ILs has been observed for Li,[282] Na,[283] Ga,[284] Sn,[284] or Te.[285] Pt is very interesting for recycling purposes, due to its relative chemical inertness. Recently, a biphasic extraction and electrodeposition process was developed using the binary salt

$[C_{14}C_3IM]Br/[C_8C_1IM][PF_6]$ and $[PtCl_6]^{2-}$ in $HCl_{(aq.)}$. The report indicated a 97 % yield of electroreduced Pt(IV) to Pt(0) and that Pt was selectively separated from Fe, Ni, Cu, and Zn.[286]

Typically, the electroreduction process assumes the synthesis of the halidometallate via mixture of the halide IL and a metal halide MX_n. This implies that the MX_n species must first be synthesized from the metal and the respective halide species, or more rarely from the metal oxide.[287] A better method for metal recycling would be to use an RTIL to dissolve the metal into the melt and subsequent formation of $[MX_{n+1}]^-$.

One of the first mentions of ILs dissolving metals is the anodic dissolution of Ag, Au, Cu, Fe, Co, Sn, Zn, Ni, and Pb in a mixture of $[C_4C_1IM]Cl$ and the deep eutectic solvent choline chloride and ethylene glycol (1:2 molar ratio choline chloride to ethylene glycol).[288] The natural progression was the work of Binnemans et al. and their use of THMILs [Cat.][Cl_3] and [Cat.][Br_3] ([Cat.]$^+$ = imidazolium and pyrrolidinium) to dissolve a variety of precious metals.[55–58] The idea generated from this is metal recycling involving the redox couple between metal, polyhalogen monoanion, and halidometallate ($M/[X_3]^-/[MX_4]^-$).

Metal recycling is a two-step process. The metal reacts with [Cat.][X_3] and forms the respective halidometallate IL [Cat.][MX_n] (n = 3 – 5). The second step is the electroreduction of the active species, $[MX_n]^-$, into metal (M) at the cathode and electrooxidation of $[X_3]^-$ at the anode to higher order PHMILs or X_2 that would coordinate to the [Cat.]X salt, thus replenishing the original $[X_3]^-$ stock.

The goal and the hope of metal recycling with ILs is to create a circular process. Whereby PHMILs leach metals from waste electronics or other materials and form halidometallates, followed by a selective electroreduction of the metal species produces the desired metal and the PHMILs are regenerated, see **Scheme 6**.

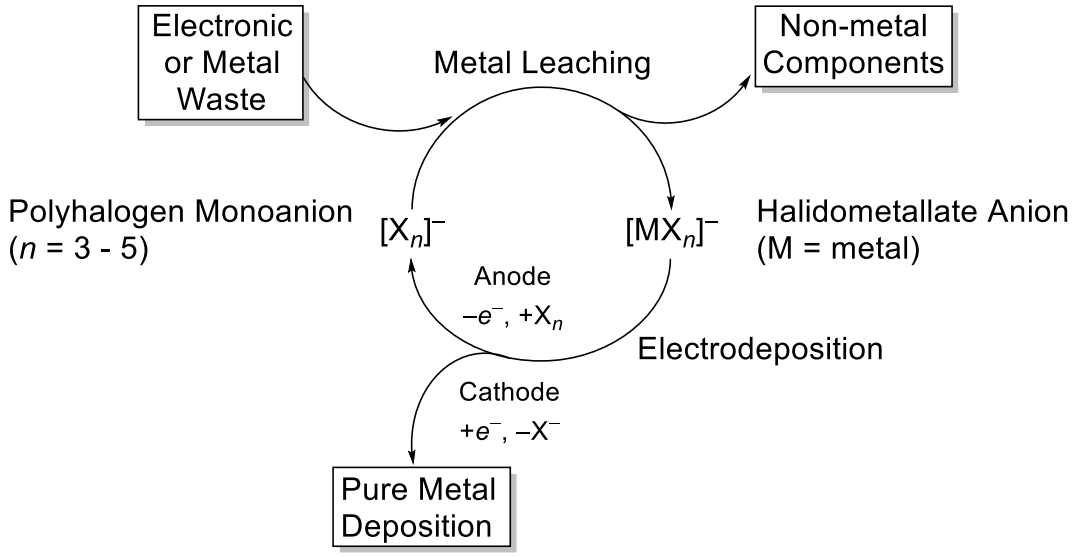

Scheme 6. Proposed metal recycling based upon the electrodeposition process for various metals using polyhalogen monoanions. Scheme made by author.

The electrodes would constantly be exposed to the corrosive environment of the PHMIL, therefore the proper electrode material should be used. The suggestion for the anode would be a carbon graphite based electrode, because the intercalation of halides into the electrode would not drastically hinder the formation of X_2 or $[X_n]^-$, similar to a Downs cell.[26,27] The use of a metal sacrificial electrode of Zn[289] or Fe[290] could be considered, but advised against as the anode material. The cathode material does not have the same constraint as the anode and will be under constant negative and therefore reductive potential. Using an inexpensive metal electrode made from Fe, Ni, or Zn, similar to metal deposition in aqueous solution,[291] should suffice.

However, future endeavors should focus on the selective electrodeposition of lanthanide[83] and transition metal halidometallates,[68] as there is already plentiful literature on their preparation and properties, and comparison to current aqueous methods. The use of ILs in metal recycling is a promising alternative to the current molten salt electrochemistry.

1.5.2 Energy storage and conversion systems – Batteries and photovoltaics

Ionic liquids are playing an ever-increasing role in energy based applications. The increase to conductivity and therefore current flow is especially useful in energy storage systems such as batteries to facilitate the movement of ions and electrons. An increase in the reaction and diffusion speed positively influences the charge and discharge cycling rate in batteries.[230]

Generally speaking, batteries are two thermodynamic systems separated by a membrane interacting via an exchange of ions trying to reach chemical equilibrium. Two redox systems are governed by the Nernst equation and are separated by a membrane that allows the transfer of protons or other ions depending upon the system, forming a Galvanic cell, see **Figure 6**.[18,53,116] As the system exchanges ions through the membrane, an electric gradient forms between the half-cells and the drawn current can be used for a variety of mechanical applications, from powering a cell phone or a car to other household appliances. Depending on battery type their voltage range is anywhere from 2.1 to 5.5 V.[18,53] On a theoretical basis a higher voltage of E_{cell} = 7.15 V could yet still be obtained if using $Sr^{+}|Sr_{(s)}$ ($E°$ = –4.10 V)[24] and H^{+}, $F_{2(g)}|HF_{(s)}$ ($E°$ = +3.05 V)[28] although the result would be very difficult to control from a safety perspective.

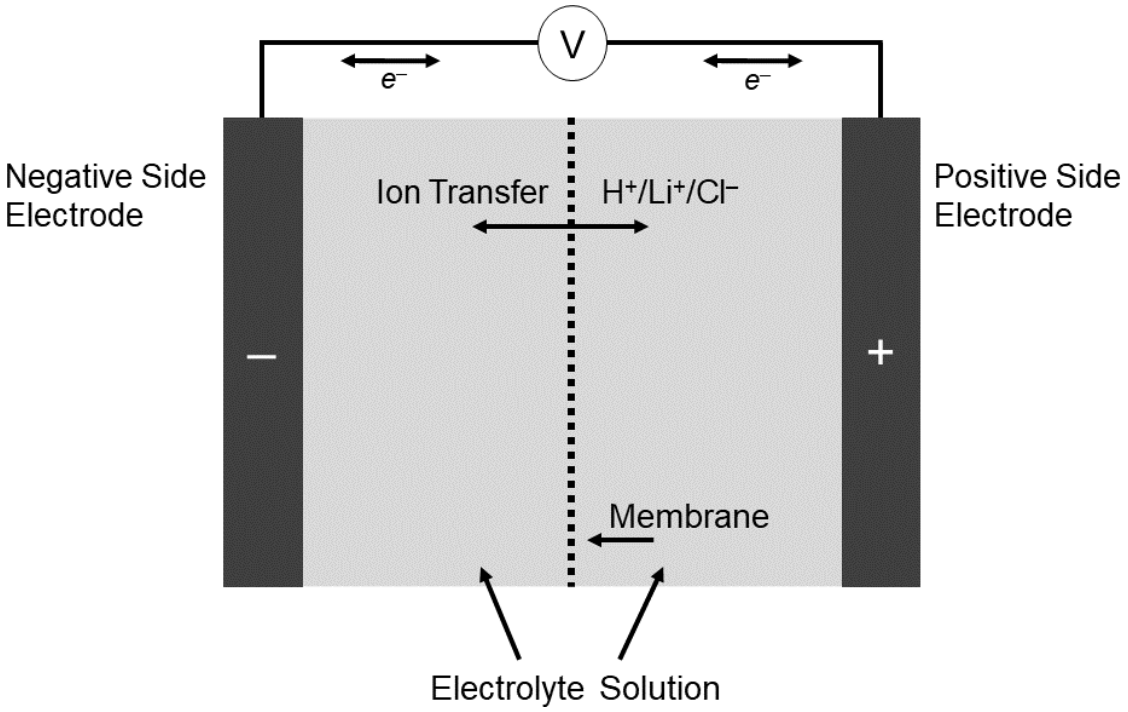

Figure 6. Diagram of a typical battery. Picture made by author.

In comparison to electrolysis where the electroreduction-oxidation process is defined for the electrodes, the anode and cathode of a battery change based upon the charge or discharge cycle. Therefore, a convention has been set. During the spontaneous discharge of a system, the reduction at the cathode indicates the positive side, and the oxidation at the anode indicates the negative side. Then when the non-spontaneous charging of a system occurs, the pole flips and reduction occurs at the negative side and oxidation at the positive side.[292]

The use of ionic liquids in DSSCs and the most common battery systems (redox-flow, Li-ion, solid state batteries) and their effects on these systems will be discussed briefly in the next section.

1.5.2.1 Redox-flow batteries

Redox flow batteries (RFBs) are an increasingly viable option for the storage of intermittent renewable energy in medium to large-scale applications. Compared to other batteries, RFBs contain a distinct advantage to decoupling energy and power densities via the scaling of electrolyte. Liquid electrolyte is stored in external tanks and flows through the cell stack, resulting in reversible redox reactions between the electroactive species and converting chemical energy into electricity, see **Figure 7**. Currently, RFBs are just starting to be commercialized.[116] Therefore, a variety of improvements to the electrolyte and the active species are underway. ILs are versatile due to their "designer" properties and can be readily used in RFBs. The application of IL materials in RFBs falls into two general categories: supporting electrolytes and additives, or the redox-active species and media.[230]

The current standard for RFBs is the vanadium RFB (VRFB). The vanadium electrolyte is typically 1.6 M with the positive side electrolyte consisting of a V^{+II}/V^{+III} and the negative side $V^{+IV}O_2/V^{+V}O^{2+}$ aqueous solution in 2.5 – 5 M sulfuric acid.[293] Typically the operating voltages are between 1.1 and 1.6 V[294] with a theoretical energy density of 25 to 35 $W \cdot h \cdot L^{-1}$.[116] Current trends in VRFB research produce non-aqueous redox-flow batteries (NARFB) that incorporate organic solvents and RTILs to benefit from the increased electrochemical window potentials. [116,230]

An example of vanadium as the electroactive species in a non-aqueous RFB (NARFB) with ILs as supporting electrolytes is the redox media vanadyl(III)acetylacetonate ($V(acac)_3$). $[C_4C_1IM][NTf_2]$ and $[C_4C_1Pyrr][NTf_2]$ act as the supporting electrolyte, leading to an increase in the operating voltage to 2.2 V and increased the diffusion rates.[295] Additionally, the negative couple was changed to V^{+III}/V^{+IV}, but was only quasi-reversible with an 88 % coulombic efficiency.[296] A further alteration to the system was later undertaken to the active species instead utilizing $Cr(acac)_3$ and $Mn(acac)_3$ and full system reversibility was observed.[297]

A current alternative to the VRFB is the zinc-bromide battery (ZBB) which is classified as a hybrid redox-flow battery (HRFB) because Zn deposition occurs at the positive electrode and a semi-flow state is achieved upon discharge. In comparison to the VRFB, the ZBB has a larger

operating voltage (1.85 V) with a theoretical capacity of 60 to 85 mA·h·g^{-1}.[116] IL additives have found use in the ZBB in the form of ammonium bromide salts to form $[Br_n]^-$ (n = 3 – 9) species that sequester the evolving Br_2 gas.[19,93,298]

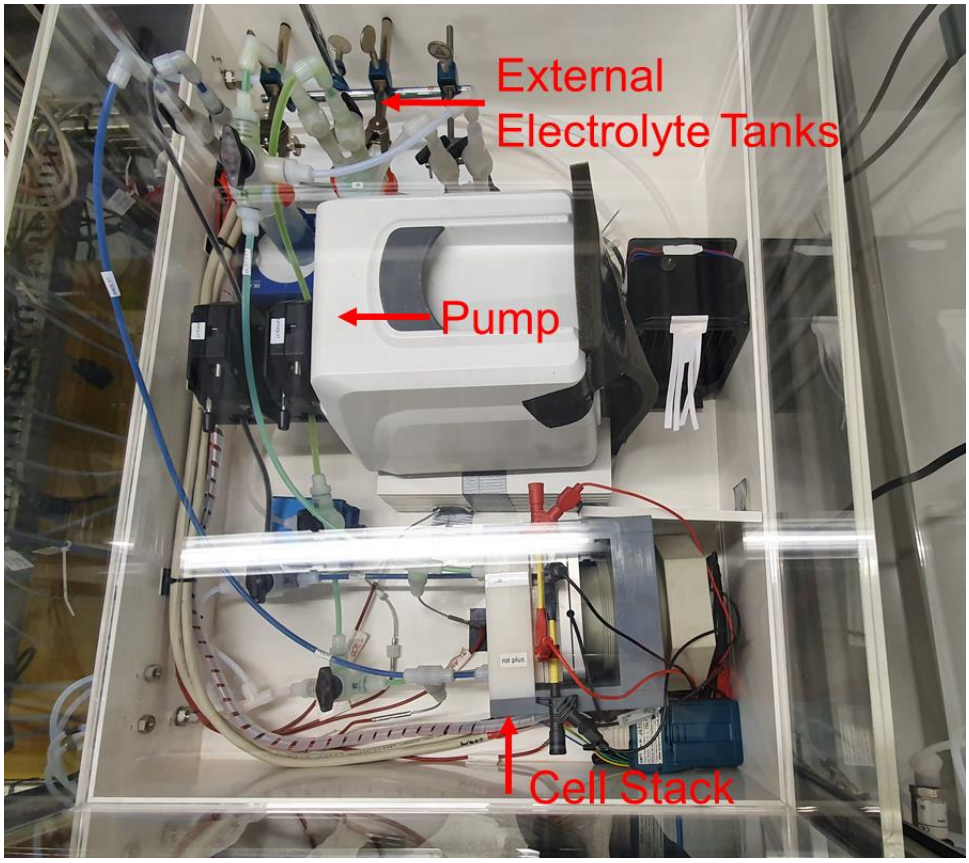

Figure 7. Picture of laboratory test set-ups for an all-manganese redox-flow battery within an inert gas temperature regulated chamber. Photo taken by author.

When examining the active species, recent research has turned to halidometallate based ionic liquids. A recent example is the aluminum-bromide[54] HRFB (ABB) with the electrochemical cell $Al^0/[Al^{+III}Br_4]^-||Br^-/Br_2$ and is similar to the ZBB.[116] The ABB had an operating voltage of 1.9 V and theoretical specific capacity of 22 mA·h·g^{-1}.[54] The benefit of the ABB and future IL-based NARFBs is the use of other metal centers, Mn or Cr, so that the variable concentration of the active species in the electrolyte can be increased significantly (>1 M) to further increase the specific capacity.

Overall, the inclusion of ILs into RFB systems in the last four years has started to shift focus away from aqueous systems towards non-aqueous ones.[230] Further, ILs as the active species have proven to increase the operating voltage and the specific capacity.[116] The new NARFBs based on ILs are state of the art, but still need further development and research to

be competitive. NARFBs based on ILs can become a serious contender to the standard VRFB in the future.

1.5.2.2 Lithium-ion batteries

Lithium-ion batteries (LIB) are high-performance rechargeable batteries that found use in a variety of consumer electronics and more recently electronic vehicles. The predecessors of the LIB were Ni metal hydride or lead-acid batteries, both having comparatively low energy densities and a smaller electrochemical window due to using an aqueous electrolyte.[53] LIBs have larger voltage windows due to the organic electrolyte such as carbonates, the reductive potential of Li/Li^+ (–3.04 V vs SHE),[28] and the small atomic radius and atomic mass, resulting in higher energy densities. LIBs are composed of four primary components: a positive electrode containing Li typically intercalated in an oxide, a negative electrode such as carbon/graphite, a membrane, and an organic solvent with dissolved Li electrolyte.[53] ILs are used in LIBs primarily as an additive to help in the intercalation process during charge-discharge, or as a supporting electrolyte to increase the conductivity and diffusion of Li^+ in the electrolyte solution.[59]

The positive electrode material is typically a high voltage metal oxide such as $LiCoO_2$ (LCO)[53] or in newer models a mixed oxide containing $LiNiMnCoO_2$ (Li-NMC).[278,279] LCO has a theoretical capacity of 274 $mA \cdot h \cdot g^{-1}$ and requires 5 V vs Li/Li^+ for complete delithiation of the electrode.[299] An alternative system is that of lithium-sulfur batteries that have a high theoretical capacity of 1672 $mA \cdot h \cdot g^{-1}$.[300] During the discharge process, deintercalation of Li occurs at the negative carbon electrode, the Li^+ carries current and Li is intercalated into the LCO or Li-NMC positive electrode.[53] Three primary problems can occur during the charge-discharge process: firstly, inhomogeneous Li intercalation at the positive electrode can occur after complete delithiation during the prior discharge;[53] secondly, high reductive current at the negative electrode can lead to Li-platting and dendrite growth;[53] and thirdly, the high voltages required lead to oxidation of the organic electrolyte.[59] Each of these effects can lead to irreversible capacity losses of up to 5 % in the case of dendrite growth,[301] or physical catastrophic failure due to a dendrite burr puncturing the membrane separator.[53]

The organic cation and perfluorinated organic anion style ILs are commonly used in LIBs. This is due to their large electrochemical windows. Of the perfluorinated anions, $[FSA]^-$ and $[NTf_2]^-$ are frequently used due to anodic stability and weak interactions in the liquid.[302,303] Li salt/IL electrolytes are known to have intercalation of the IL-cation[302] or organic solvent[304]

into the graphite electrode and its destruction via physical peeling or exfoliation. By using $[FSA]^-$ based ILs the reversible intercalation of Li is unhindered by the organic cation and facilitates charge transfer at the electrode-electrolyte interface.[303]

Dendrite formation has been shown to be dependent upon the Li salt cathode material and IL additive. Basile, Bhatt, and O'Mullane observed the changes in anodic surface morphology for several systems of Li salts and ILs, Li[$FePO_4$]/[C_3C_1Pyrr][NTf_2], Li[PF_6]/[C_3C_1Pyrr][NTf_2], and Li[AsF_6]/[C_3C_1Pyrr][NTf_2].[305] They determined the topology of the anode to remain relatively unchanged using Li[$FePO_4$]/[C_3C_1Pyrr][NTf_2] after 1000 cycles, whereas with the other Li salts, Li-platting occurred within 225 cycles.

While ILs have helped increase LIB stability and performance, liquid electrolytes do however have their limitations, being less energy dense than solids and the inclusion of organic solvents allows for inflammability. Further developments in LIBs move away from liquid electrolytes and towards solid polymer electrolytes and the creation of a solid-state battery.

1.5.2.3 Solid-state batteries

Solid-state batteries (SSB) are currently being researched intensely to use the fledgling technology in electronic vehicles, utilizing considerably higher energy densities, and longer overall lifetimes,[306] and increased safety due to the lack of inflammable solvents,[307] compared to liquid electrolyte based LIBs. SSBs are inorganic in their chemistry using either Li^+, Na^+, or Mg^{2+} as their primary energy source with operating voltages over 5 V and capacities over 120 $mA \cdot h \cdot g^{-1}$.[21,306,308] The primary downsides to this technology are irregularities or cracks in the electrode/electrolyte formation caused by physical stresses leading to contact gaps or dendrite growth resulting in gas evolution of CO_2 or O_2 at the cathode.[309] However, the ease of modelling and designing solid electrolytes is beneficial in future battery design.

There are two types of SSBs, the all-solid-state battery (aSSB) and the quasi-solid-state battery (qSSB). ILs have been used in aSSBs to increase the ion diffusion and create a Li-IL conductive network. The aSSBs with a mixture containing Li[NTf_2], and [C_2C_1IM][NTf_2] and polyethylene reached energy capacities of 136.2 $mA \cdot h \cdot g^{-1}$.[310] Whereas qSSBs reach a middle ground between aSSBs and LIBs, with ILs featuring comparatively prominently in the qSSB. Forsyth et al. demonstrated the usefulness of a carbon-coated sodium vanadium phosphate gel $Na_3[V_2(PO_4)_3]$ as a catholyte and membrane, in a Na-based qSSB reaching specific capacity (117 $mA \cdot h \cdot g^{-1}$) retentions of 92 % after 150 cycles.[260]

Additionally, within SSBs supported gel ionic liquid membranes can be used as conductive physically resilient membranes. The supported gel ionic liquid membrane is composed of long alkyl chains and mixtures of various ILs, e.g., Na[OTf] with $[C_2C_1IM][OTf]$ immobilized in poly(vinylidene) fluoride-co-hexafluoropropylene.[311]

Overall, SSBs benefit from the use of ILs and research in this field has been limited due to the newness of the technology. Again, due to ILs being so versatile, they will likely find use in SSB technology and their presence will advance with time.

1.5.2.4 Dye-Sensitized Solar Cells

Based on photovoltaics, dye-sensitized solar cells (DSSC) utilize the p-n gap of solid semi-conductors to harness UV light from the sun and produce electricity through subsequent redox reactions in the liquid electrolyte. DSSCs are constructed from four components: the working electrode, photosensitizer (dye), redox-mediator (electrolyte), and the counter electrode.[15]

The WE is a semi-conductor metal oxide compound such as TiO_2, Nb_2O, ZnO, SnO_2 (n-Type) or NiO (p-type).[15] These materials typically have relatively high band gaps of 3.0 – 3.2 V.[312] Additionally, they are attached to a UV light transparent glass. The photosensitizer or dye, e.g., zinc porphyrin,[313] is placed on the WE on the opposite side of the glass and the primary function is to absorb the incidence light, resulting in an electron excitation from the highest occupied molecular orbital (HOMO) to the lowest unoccupied molecular orbital (LUMO). The dye should have a similar HOMO to the metal oxide and a LUMO slightly lower than the electrolyte.[15]

The most commonly used electrolyte is the triiodine monoanion ($[I_3]^-$) ionic liquid. The reasons for this are its well-known redox chemistry, relatively low reduction potential in the $I^-/[I_3]^-$ redox couple, and the high conductivity of polyhalogen monoanions caused by the Grotthuss mechanism, see **Section 1.4.2 Non-Stokesian** charge transport, Grotthuss mechanism, and polyhalogen monoanion ionic liquids. In 1958, Popov and Geske determined the electrochemical redox system for $[X_3]^-$ systems having two individual redox couples: $X^-/[X_3]^-$ and $[X_3]/X_2$.[253,254] The redox potentials of $I^-/[I_3]^-$ ILs were determined against Fc^+/Fc for the IL $[C_2C_1IM]I$ in $MeCN/[C_2C_1IM][NTf_2]$ (0.2 M I^-, $T = 25$ °C, $E_{1/2} = -0.32$ V).[72] This information is valuable in determining which IL mixture given common solvents produces the lowest reductive potential.

The CE is typically made of platinum or of carbon. Pt currently demonstrates the best efficiencies over other electrode materials, because Pt catalyzes the $I^-/[I_3]^-$ reduction via the surface-electrolyte interface inducing formation of conductive holes at the electrode surface.[15] The physical deformation of the electrode allows for $[I_3]^-$ molecules to orient themselves optimally in relation to other I atoms and engage more efficiently in the Grotthuss based charge transfer.[235] The downside to $[I_3]^-$ ILs is their corrosiveness leading to battery leakage.[314] Alternative electrolytes such as the pseudohalogen $[SCN]^-/(SCN)_2$[315] or Co(II)/Co(III),[316] and the CE materials carbon,[317] carbonylsulfide,[314] or alloys of FeSe[313] have been proposed to deal with the corrosiveness of the electrolyte.

Instead of the $I^-/[I_3]^-$ redox mediator, two halogen based redox couple alternatives are currently being investigated in the literature, $Br^-/[Br_3]^-$[318,319] and the binary system $I^-,Br^-/[BrI_2]^-$,[320,321] with the system $Cl^-,Br^-/[ClBr_2]^-$ being theoretically possible based on equilibrium constants obtained through pulse radiolysis experiments.[322] The alternative combinations of $Cl^-/[Cl_3]^-$ and $I^-,Cl^-/[ClI_2]^-$ are unfeasible, due to the facile irreversible electrooxidation of Cl^- to Cl_2 in aqueous solution.[323] The first benefit of using $Br^-/[Br_3]^-$ and the binary $I^-,Br^-/[BrI_2]^-$ include a decrease in the absorption of visible light, leading to more effective dye regeneration.[320,323] The second benefit is in the increased redox potential difference between species from 0.54 V ($I^-/[I_3]^-$)[324] to 0.64 V and 0.81 V for $I^-,Br^-/[BrI_2]^-$[320] and $Br^-/[Br_3]^-$,[318] respectively.

1.6 Outlook

As discussed in this introduction, ionic liquids are valuable due to their unique chemical characteristics that can be tuned during synthesis in either the cation or anion for the desired chemical property. While much variation is typically focused on organic cations,[240] by expanding upon trihalogen monoanion and halidometallate RTILs instead, a variety of useful electrochemical applications including metal recycling of rare metals or higher voltage batteries can be developed. The benefit of using trihalogen monoanion RTILs is their conductivity, due to non-Stokesian diffusion properties,[234] and their oxidative potential,[57] which can be combined for more efficient metal recycling. Whereas halidometallates can find use in redox-flow batteries making use of cheaper metals, such as Mn,[297] and demonstrate larger potential ranges than aqueous vanadium RFBs. Overall, the investigation and synthesis of new and existing trihalogen monoanion and halidometallate RTILs leads to the improvement of current electrochemical technologies.

References

[1] J. B. Goodenough, M. S. Whittingham, A. Yoshino, *Nobel Prize 2019: Chemistry*, Stockholm, Sweden, **2019**.

[2] M. Amiero, L. Sedrez, *A history of environmentalism*. *Local struggles, global histories*, Bloomsbury, London, **2014**.

[3] Coordination and Planning Division Exxon Research and Engineering Company, *CO_2 "Greenhouse" Effect: A Technical Review*, Exxon Research and Engineering Company, Florham Park, New Jersey, USA, **1982**.

[4] R. H. Jacobs, M. H. P. Griffiths, P.E. Bright, J.B. Homer, J.A.C.M. van Oudenhoven, J. M. Waller, *The Greenhouse Effect*, Shell Internationale Petroleum Maatschappij B.V., The Hague, Netherlands: Health, Safety and Environment Division (HSE), **1988**.

[5] a) M. Phillips, *J Bus Ethics* **2019**, *156*, 1151; b) K. Maiti, S. Chakraborty (Eds.) *Environment and society*, Lexington books, Lanham, Maryland, **2020**.

[6] J. T. Park, *J. Sust. Dev.* **2015**, *14*, 189.

[7] IPCC, 2021, *Climate Change 2021: The Physical Science Basis. Contribution of Working Group I to the*
Sixth Assessment Report of the Intergovernmental Panel on Climate Change, eds. Masson-Delmotte, V., P. Zhai, A. Pirani, S. L. Connors, C. Péan, S. Berger, N. Caud, Y. Chen, L. Goldfarb, M. I. Gomis, M. Huang, K. Leitzell, E. Lonnoy, J. B. R. Matthews, T. K. Maycock, T. Waterfield, O. Yelekçi, R. Yu and B. Zhou. Cambridge University Press. In Press.

[8] a) R. Bellamy, S. Osaka, *Nat. Clim. Change* **2020**, *10*, 98; b) N. Seddon, B. Turner, P. Berry, A. Chausson, C. A. J. Girardin, *Nat. Clim. Change* **2019**, *9*, 84.

[9] a) 116th United States Congress (Ed.) *Green New Deal: H. Res. 109*, USA, **2019**; b) K. Goh, *J. Am Plan. Ass.* **2020**, *86*, 188.

[10] a) A. Ollila, *IJCCSM* **2019**, *11*, 18; b) *7. d Paris Agreement*. *Paris Agreement*, **2015**.

[11] Fridays For Future, "Who We Are", can be found under https://fridaysforfuture.org/what-we-do/who-we-are/, **2018**.

[12] I. Staffell, D. Scamman, A. Velazquez Abad, P. Balcombe, P. E. Dodds, P. Ekins, N. Shah, K. R. Ward, *Energ. Environ. Sci.* **2019**, *12*, 463.

[13] B. R. Betzler, A. Rykhlevskii, A. Worrall, K. Huff, *Impacts of Fast-Spectrum Molten Salt Reactor Characteristics on Fuel Cycle Performance*, Oak Ridge Laboratories, Oak Ridge, Tennessee, USA, **2019**.

[14] M. Child, C. Kemfert, D. Bogdanov, C. Breyer, *Ren. Energ.* **2019**, *139*, 80.

[15] K. Sharma, V. Sharma, S. S. Sharma, *Nano. Res. Lett.* **2018**, *13*, 381.

[16] Y. Zhang, G.-F. Zhao, *Geomech. Geophys. Geo-energ. Geo-resour.* **2020**, *6*.

[17] I. López, J. Andreu, S. Ceballos, I. Martínez de Alegría, I. Kortabarria, *Ren. Sust. Energ. Rev.* **2013**, *27*, 413.

[18] J. Winsberg, T. Hagemann, T. Janoschka, M. D. Hager, U. S. Schubert, *Angew. Chem. Int. Ed.* **2017**, *56*, 686.

[19] M. E. Easton, P. Turner, A. F. Masters, T. Maschmeyer, *RSC Adv.* **2015**, *5*, 83674.

[20] A. Bhide, J. Hofmann, A. K. Dürr, J. Janek, P. Adelhelm, *Phys. Chem. Chem. Phys.* **2014**, *16*, 1987.

[21] J. Janek, W. G. Zeier, *Nat. Energ.* **2016**, *1*.

[22] G. A. O. Tiago, I. A. S. Matias, A. P. C. Ribeiro, L. M. D. R. S. Martins, *Molec.* **2020**, *25*.

[23] K. E. Johnson, *Electrochem. Soc. Inter.* **2007**, *16*.

[24] R.C. Weast, *CRC Handbook of Chemistry and Physics*, CRC Press LLC, Cleveland, OH, **1972**.

[25] a) E. R. van Artsdalen, I. S. Yaffe, *J. Phys. Chem.* **1955**, *59*, 118; b) A.R. Allnat, P. Pantelis, S.J. Sime, *J. Phys. C* **1971**, *4*, 1778.

[26] K. S. Mohandas, N. Sanil, P. Rodriguez, *J. Appl. Electrochem.* **2002**, *32*, 1383.

[27] J.C. Downs, *Electrolytic Process and Cell*, **1922,** USP 1,501,756.

[28] A. J. Bard, L. R. Faulkner, *Electrochemical methods*. *Fundamentals and applications*, Wiley, New York, **2001**.

[29] T. Ito, N. Kojima, A. Nagashima, *Int. J. Thermophys.* **1989**, *10*, 819.

[30] R.W. Bradshaw, *Viscosity of Multi-component Molten Nitrate Salts—Liquidus to 200°C*, U.S. Department of Commerce **2010**, 1.

[31] A. R. Hind, S. K. Bhargava, S. C. Grocott, *Coll.Surf. A* **1999**, *146*, 359.

[32] A. Schmidt, *Elektrochemie*, Eds.: G. Milazzo, R. Defay, I. Epelboin, P. Gallone, M. Garreau, F. Hilbert, S. Hjertén, N. Ibl, K. M. Oesterle, E. Pungor et al., Birkhäuser Basel, Basel, **1983**, pp. 174–203.

[33] N.W.F. Phillips, R.H. Singleton, E.A. Hollingshead, *J. Electrochem. Soc.* **1955**, *102*, 690.

[34] M. Obaidat, A. Al-Ghandoor, P. Phelan, R. Villalobos, A. Alkhalidi, *Sust.* **2018**, *10*, 1216.

[35] M. Helan, L. J. Berchmans, A. Z. Hussain, *Ionics* **2010**, *16*, 227.

[36] M.-J. Lee, S. Lee, P. Oh, Y. Kim, J. Cho, *Nano. Lett.* **2014**, *14*, 993.

[37] X. Liu, Q. Chen, Y. Li, C. Chen, X. Xing, B. Huang, J. Yang, S. Xiao, S. Chen, R. Wang, *J. Phys. Chem. C* **2020**, *124*, 26106.

[38] Y. Wang, J. Y. Lee, *J. Phys. Chem. B* **2004**, *108*, 17832.

[39] A. S. Hassan, K. Moyer, B. R. Ramachandran, C. D. Wick, *J. Phys. Chem. C* **2016**, *120*, 2036.

[40] Z. Liu, H. Deng, P. P. Mukherjee, *ACS Appl. Mater. Inter.* **2015**, *7*, 4000.

[41] S. Gabriel, J. Weiner, *Ber. Dtsch. Chem. Ges.* **1888**, *21*, 2669.

[42] P. Walden, *Bull. Acad. Imper. Sci. St. Petersbourg* **1914**, 405.

[43] R. J. Gale, B. Gilbert, R. A. Osteryoung, *Inorg. Chem.* **1978**, *17*, 2728.

[44] J. S. Wilkes, J. A. Levisky, R. A. Wilson, C. L. Hussey, *Inorg. Chem.* **1982**, *21*, 1263.

[45] R. T. Carlin, J. Fuller, *Chem. Commun.* **1997**, 1345.

[46] J. Fuller, R. T. Carlin, H. C. de Long, D. Haworth, *J. Chem. Soc., Chem. Commun.* **1994**, 299.

[47] P. Bonhôte, A.-P. Dias, N. Papageorgiou, K. Kalyanasundaram, M. Grätzel, *Inorg. Chem.* **1996**, *35*, 1168.

[48] P. Wasserscheid, T. Welton (Eds.) *Ionic Liquids in Synthesis*, 2nd Ed., Weinheim, Germany, **2008**.

[49] P. Wasserscheid, *Nature* **2006**, *439*, 797.

[50] P. Wasserscheid, W. Keim, *Angew. Chem.* **2000**, *39*, 3772.

[51] A. P. Abbott, *Eur. J. Chem. Phys. Chem.* **2004**, *5*, 1242.

[52] A. P. Abbott, *Eur. J. Chem. Phys. Chem* **2005**, *6*, 2502.

[53] M. Li, J. Lu, Z. Chen, K. Amine, *Adv. Mater.* **2018**, e1800561.

[54] M. Hog, B. Burgenmeister, K. Bromberger, M. Schuster, S. Riedel, I. Krossing, *Chem. Electro. Chem.* **2017**, *4*, 2934.

[55] A. van den Bossche, E. de Witte, W. Dehaen, K. Binnemans, *Green Chem.* **2018**, *20*, 3327.

[56] A. van den Bossche, W. Vereycken, T. Vander Hoogerstraete, W. Dehaen, K. Binnemans, *ACS Sustain. Chem. Eng.* **2019**, *7*, 14451.

[57] X. Li, A. van den Bossche, T. Vander Hoogerstraete, K. Binnemans, *Chem. Commun.* **2018**, *54*, 475.

[58] X. Li, Z. Li, M. Orefice, K. Binnemans, *ACS Sustain. Chem. Eng.* **2019**, *7*, 2578.

[59] M. Watanabe, M. L. Thomas, S. Zhang, K. Ueno, T. Yasuda, K. Dokko, *Chem. Rev.* **2017**, *117*, 7190.

[60] M. Musiał, K. Malarz, A. Mrozek-Wilczkiewicz, R. Musiol, E. Zorębski, M. Dzida, *ACS Sust. Chem. Eng.* **2017**, *5*, 11024.

[61] H. Haller, M. Hog, F. Scholz, H. Scherer, I. Krossing, S. Riedel, *Z. Naturforsch.* **2013**, *68b*, 1103.

[62] M. Kar, O. Tutusaus, D. R. MacFarlane, R. Mohtadi, *Energ. Environ. Sci.* **2019**, *12*, 566.

[63] S. Zhang, N. Sun, X. He, X. Lu, X. Zhang, *J. Phys. Chem. Ref. Data* **2006**, *35*, 1475.

[64] T. Welton, *Chem. Rev.* **1999**, *99*, 2071.

[65] P. Wasserscheid, T. Welton, *Ionic Liquids in Synthesis, Vol. 1*, Wiley-VCH Verlag GmbH & Co. KGaA, Weinheim, Germany **2003**.

[66] N. V. Plechkova, K. R. Seddon, *Chem. Soc. Rev.* **2008**, *37*, 123.

[67] D. R. MacFarlane, M. Forsyth, P. C. Howlett, J. M. Pringle, J. Sun, G. Annat, W. Neil, E. I. Izgorodina, *Acc. Chem. Res.* **2007**, *40*, 1165.

[68] J. Estager, J. D. Holbrey, M. Swadźba-Kwaśny, *Chem. Soc. Rev.* **2014**, *43*, 847.

[69] F. H. Hurley, T. P. WIer, *J. Electrochem. Soc.* **1951**, *98*, 203.

[70] C. J. Dymek, Wilkes, J. S., M.-A. Einarsrud, H. A. Øye, *Polyhedron* **1988**, *7*, 1139.

[71] C. L. Bentley, A. M. Bond, A. F. Hollenkamp, P. J. Mahon, J. Zhang, *Anal. Chem.* **2016**, *88*, 1915.

[72] C. L. Bentley, A. M. Bond, A. F. Hollenkamp, P. J. Mahon, J. Zhang, *J. Phys. Chem. C* **2015**, *119*, 22392.

[73] T. A. Gully, P. Voßnacker, J. R. Schmid, H. Beckers, S. Riedel, *ChemistryOpen* **2021**, 255.

[74] R. Kawai, S. Yada, T. Yoshimura, *ACS Omega* **2019**, *4*, 14242.

[75] M. E. Hirschberg, N. V. Ignat'ev, A. Wenda, H. Willner, *J. Fluorine Chem.* **2012**, *137*, 50.

[76] A. O. Ezzat, H. A. Al-Lohedan, A. M. Atta, *ACS Omega* **2021**, *6*, 5061.

[77] D. R. MacFarlane, P. Meakin, J. Sun, N. Amini, M. Forsyth, *J. Phys. Chem. B* **1999**, *103*, 4164.

[78] T. Alpers, T. W. T. Muesmann, O. Temme, J. Christoffers, *Eur. J. Org. Chem.* **2018**, *2018*, 4331.

[79] H. Xue, B. Twamley, J. M. Shreeve, *J. Org. Chem.* **2004**, *69*, 1397.

[80] G. Adamová, R. L. Gardas, M. Nieuwenhuyzen, A. V. Puga, L. P. N. Rebelo, A. J. Robertson, K. R. Seddon, *Dalton Trans.* **2012**, *41*, 8316.

[81] D. Freudenmann, S. Wolf, M. Wolff, C. Feldmann, *Angew. Chem. Int. Ed.* **2011**, *50*, 11050.

[82] I. Krossing, J. M. Slattery, C. Daguenet, P. J. Dyson, A. Oleinikova, H. Weingärtner, *J. Am. Chem. Soc.* **2006**, *128*, 13427.

[83] K. Binnemans, *Chem. Rev.* **2007**, *107*, 2592.

[84] J. F. Vélez, M. B. Vazquez-Santos, J. M. Amarilla, P. Tartaj, B. Herradón, E. Mann, C. del Río, E. Morales, *Electrochimica Acta* **2018**, *280*, 171.

[85] F. Endres, D. MacFarlane, A. Abbott, *Electrodeposition from ionic liquids*, Wiley-VCH, Weinheim, Germany, **2008**.

[86] L. C. Brown, J. M. Hogg, M. Swadźba-Kwaśny, *Top. Current Chem.* **2017**, *375*, 78.

[87] M. A. Zakharov, Y. V. Filatova, M. A. Bykov, N. V. Avramenko, L. A. Aslanov, *Russ. J. Coord. Chem.* **2020**, *46*, 268.

[88] D. Hausmann, C. Feldmann, *Inorg. Chem.* **2016**, *55*, 6141.

[89] S. Pitula, A.-V. Mudring, *Eur. J. Chem.* **2010**, *16*, 3355.

[90] A. Eich, R. Köppe, P. W. Roesky, C. Feldmann, *Eur. J. Inorg. Chem.* **2019**, *2019*, 1292.

[91] K. Sonnenberg, L. Mann, F. A. Redeker, B. Schmidt, S. Riedel, *Angew. Chem. Int. Ed.* **2020**, *59*, 5464.

[92] a) E. Lancry, B.-Z. Magnes, I. Ben-David, M. Freiberg, *ECS Trans.* **2013**, *53*, 107; b) G. P. Rajarathnam, A. M. Vasallo, *The Zinc/Bromine Flow Battery Material Challenges and Practical Solutions for Technological Advancement*, Springer, XXI, **2016**.

[93] M. Schneider, G. P. Rajarathnam, M. E. Easton, A. F. Masters, T. Maschmeyer, A. M. Vassallo, *RSC Adv.* **2016**, *6*, 110548.

[94] R. Kawano, M. Watanabe, *Chem. Commun.* **2005**, 2107.

[95] N. V. Ignat'ev, P. Barthen, A. Kucheryna, H. Willner, P. Sartori, *Molec.* **2012**, *17*, 5319.

[96] N. E. Dixon, G. A. Lawrance, P. A. Lay, A. M. Sargeson, H. Taube in *Inorganic Synthesis,* (Eds.: R. J. Angelici, F. Basolo), John Wiley & Sons, New York, **1990**, *28*, pp. 70–76.

[97] C. A. Angell, Y. Ansari, Z. Zhao, *Faraday Disc.* **2012**, *154*, 9-27.

[98] L. F. O. Faria, T. A. Lima, M. C. C. Ribeiro, *Cryst. Growth Des.* **2017**, *17*, 5384.

[99] A. K. Burrell, R. E. Del Sesto, S. N. Baker, T. M. McCleskey, G. A. Baker, *Green Chem.* **2007**, *9*, 449.

[100] M. Gnahm, D. M. Kolb, *J. Electroanal. Chem.* **2011**, *651*, 250.

[101] a) M. Wempe, *J. Mol. Struct.* **2001**, *562*, 63; b) J. Gao, G. Wang, Z. Wang, Y. Wang, J. Liu, W. Liu, Z. Zou, *J. Mater. Chem. A* **2014**, *2*, 19275.

[102] H. S. Schrekker, D. O. Silva, M. A. Gelesky, M. P. Stracke, C. M. L. Schrekker, R. S. Gonçalves, J. Dupont, *J. Brazil. Chem. Soc.* **2008**, *19*, 426.

[103] E. R. Parnham, R. E. Morris, *Acc. Chem. Res.* **2007**, *40*, 1005.

[104] a) M. F. Groh, A. Wolff, M. A. Grasser, M. Ruck, *Int. J. Molec. Sci.* **2016**, *17*; b) T. P. Vaid, S. P. Kelley, R. D. Rogers, *Int. U. Cryst. J.* **2017**, *4*, 380.

[105] B. Wang, L. Qin, T. Mu, Z. Xue, G. Gao, *Chem. Rev.* **2017**, *117*, 7113.

[106] T. Zhang, T. Doert, H. Wang, S. Zhang, M. Ruck, *, Angew. Chem. Int. Ed.* **2021**. DOI: 10.1002/anie.202104035

[107] a) M. F. Groh, S. Paasch, A. Weiz, M. Ruck, E. Brunner, *Eur. J. Inorg. Chem.* **2015**, *2015*, 3991; b) M. A. Grasser, T. Pietsch, E. Brunner, T. Doert, M. Ruck, *ChemistryOpen* **2021**, *10*, 117.

[108] K. Rui, Z. Wen, Y. Lu, J. Jin, C. Shen, *Adv. Energy Mater.* **2015**, *5*, 1401716.

[109] N. Zhang, X. Xiao, H. Pang, *Nanoscale horizons* **2019**, *4*, 99.

[110] K. Sonnenberg, P. Pröhm, N. Schwarze, C. Müller, H. Beckers, S. Riedel, *Angew. Chem. Int. Ed.* **2018**, *57*, 9136.

[111] B. Schmidt, K. Sonnenberg, H. Beckers, S. Steinhauer, S. Riedel, *Angew. Chem. Int. Ed.* **2018**, *57*, 9141.

[112] Y. Lin, W. Massa, S. Dehnen, *J. Am. Chem. Soc.* **2012**, *134*, 4497.

[113] A. G. Zazybin, K. Rafikova, V. Yu, D. Zolotareva, V. M. Dembitsky, T. Sasaki, *Rus. Chem. Rev.* **2017**, *86*, 1254.

[114] W. D. Sides, Q. Huang, *Electrochimica Acta* **2018**, *266*, 185.

[115] B. Bennett, J. Chang, A. J. Bard, *Electrochimica Acta* **2016**, *219*, 1.

[116] E. Sánchez-Díez, E. Ventosa, M. Guarnieri, A. Trovò, C. Flox, R. Marcilla, F. Soavi, P. Mazur, E. Aranzabe, R. Ferret, *J. Pow. Sourc.* **2021**, *481*, 228804.

[117] C. Zhong, T. Sasaki, A. Jimbo-Kobayashi, E. Fujiwara, A. Kobayashi, M. Tada, Y. Iwasawa, *Bull. Chem. Soc. Jpn.* **2007**, *80*, 2365.

[118] M. Currie, J. Estager, P. Licence, S. Men, P. Nockemann, K. R. Seddon, M. Swadźba-Kwaśny, C. Terrade, *Inorg. Chem.* **2013**, *52*, 1710.

[119] J. Estager, A. A. Oliferenko, K. R. Seddon, M. Swadźba-Kwaśny, *Dalton Trans.* **2010**, *39*, 11375.

[120] P. D. Ola, M. Matsumoto, *Chem. Biochem. Eng. Q. (Online)* **2019**, *33*, 229.

[121] X. H. Xu, C. L. Hussey, *J. Electrochem. Soc.* **1993**, 3095.

[122] F. Endres, M. Bukowski, R. Hempelmann, H. Natter, *Angew. Chem. Int. Ed* **2003**, *42*, 3428.

[123] M. Sano, N. Tachikawa, K. Yoshii, N. Serizawa, Katayama Yasushi, *Electrochem.* **2018**, *86*, 260.

[124] R. E. Del Sesto, T. M. McCleskey, A. K. Burrell, G. A. Baker, J. D. Thompson, B. L. Scott, J. S. Wilkes, P. Williams, *Chem. Comm.* **2008**, 447.

[125] T. Peppel, M. Geppert-Rybczyńska, C. Neise, U. Kragl, M. Köckerling, *Mater.* **2019**, *12*.

[126] P. Dera, E. Bruffey, G. J. Finkelstein, C. Kelly, A. Gigante, H. Hagemann, G. Severa, *ACS Omega* **2020**, *5*, 15592.

[127] U. Müller, N. Mronga, C. Schumacher, K. Dehnicke, *Z. Naturforsch.* **1982**, *37B*, 1122.

[128] L. Xu, Y.-U. Kwon, B. de Castro, L. Cunha-Silva, *Crys. Growth Des.* **2013**, *13*, 1260.

[129] N. Tachikawa, N. Serizawa, Y. Katayama, T. Miura, *Electrochimica Acta* **2008**, *53*, 6530.

[130] C. C. Cassol, G. Ebeling, B. Ferrera, J. Dupont, *Adv. Syn. Catal.* **2006**, *348*, 243.

[131] J. C. Forgie, S. El Khakani, D. D. MacNeil, D. Rochefort, *Phys. Chem. Chem. Phys.* **2013**, *15*, 7713.

[132] M. Y. Lui, L. Crowhurst, J. P. Hallett, P. A. Hunt, H. Niedermeyer, T. Welton, *Chem. Sci.* **2011**, *2*, 1491.

[133] L. A. Bischoff, J. A. P. Sprenger, P. T. Hennig, N. V. Ignat'ev, M. Finze, *Z. Anorg. Allg. Chem.* **2018**, *177*, 46.

[134] M. Hog, M. Schneider, I. Krossing, *Eur. J. Chem.* **2017**, *23*, 9821.

[135] C. L. Hussey, *Proceedings Electrochem. Soc.* **1981**, *1981-10*, 220.

[136] a) S. P. Wicelinski, R. J. Gale, Wilkes, J. S., *Thermochimica Acta* **1988**, *126*, 255; b) K. R. Seddon, G. Srinivasan, M. Swadźba-Kwaśny, A. R. Wilson, *Phys. Chem. Chem. Phys.* **2013**, *15*, 4518.

[137] J.-Z. Yang, P. Tian, W.-G. Xu, B. Xu, S.-Z. Liu, *Thermochimica Acta* **2004**, *412*, 1.

[138] J. Estager, P. Nockemann, K. R. Seddon, M. Swadźba-Kwaśny, S. Tyrrell, *Inorg. Chem.* **2011**, *50*, 5258.

[139] K. Sonnenberg, *Investigation of Polyhalides: Synthesis, Characterization, and Application Possibilities of Polybromides, Polychlorides, and Bromostannates*, Freie Universität Berlin, *Dissertation*, **2018,** Berlin, Germany.

[140] R. W. Berg, *Monatshefte Chem.* **2007**, *138*, 1045.

[141] S. P. Wicelinski, R. J. Gale, S. D. Williams, G. Mamantov, *Spectrochim. Acta A* **1989**, *45*, 759.

[142] F. Bertasi, F. Sepehr, G. Pagot, S. J. Paddison, V. Di Noto, *Adv. Funct. Mater.* **2016**, *26*, 4860.

[143] M. S. Sitze, E. R. Schreiter, E. V. Patterson, R. G. Freeman, *Inorg. Chem.* **2001**, *40*, 2298.

[144] S. Hayashi, S. Saha, H. Hamaguchi, *IEEE Trans. Magn.* **2006**, *42*, 12.

[145] J. Mason (Ed.) *Multinuclear NMR*, Springer US, Boston, MA, **1987**.

[146] P. Illner, A. Zahl, R. Puchta, N. van Eikema Hommes, P. Wasserscheid, R. van Eldik, *J. Organomet. Chem.* **2005**, *690*, 3567.

[147] A. Lahiri, R. Das, *Mater. Chem. Phys.* **2012**, *132*, 34.

[148] E. N. Golubeva, A. I. Kokorin, D. I. Kochubei, V. I. Pergushov, V. V. Kriventsov, *Kin. Catal.* **2002**, *43*, 408.

[149] W. Huang, S. Chen, H. Fu, G. Wu, *Rad. Res.* **2010**, *174*, 650.

[150] S. Wellens, B. Thijs, K. Binnemans, *Green Chem.* **2012**, *14*, 1657.

[151] C. Balischewski, K. Behrens, K. Zehbe, C. Günter, S. Mies, E. Sperlich, A. Kelling, A. Taubert, *Eur. J. Chem.* **2020**, *26*, 17504.

[152] F. Coleman, G. Feng, R. W. Murphy, P. Nockemann, K. R. Seddon, M. Swadźba-Kwaśny, *Dalton Trans.* **2013**, *42*, 5025.

[153] M. Hasan, I. V. Kozhevnikov, M. R. H. Siddiqui, A. Steiner, N. Winterton, *Inorg. Chem.* **1999**, *38*, 5637.

[154] C. J. Serpell, J. Cookson, A. L. Thompson, C. M. Brown, P. D. Beer, *Dalton Trans.* **2013**, *42*, 1385.

[155] a) H. Haller, S. Riedel, *Nachr. Chem.* **2012**, *60*, 865; b) H. Haller, *Dissertation*, Albert-Ludwigs-Universität Freiburg, Freiburg, **2014**.

[156] H. Haller, J. Schröder, S. Riedel, *Angew. Chem. Int. Ed.* **2013**, *52*, 4937.

[157] L. Andrews, X. Wang, *Phys. Chem. Chem. Phys.* **2018**, *20*, 23378.

[158] B. Schmidt, B. Schröder, K. Sonnenberg, S. Steinhauer, S. Riedel, *Angew. Chem. Int. Ed.* **2019**, *58*, 10340.

[159] C. L. Bentley, A. M. Bond, A. F. Hollenkamp, P. J. Mahon, J. Zhang, *J. Phys. Chem. C* **2014**, *118*, 22439.

[160] a) M. R. Ciumag, T. Tzedakis, C. A. Barrès, *Electrochimica Acta* **2012**, *70*, 142; b) J. G. Vos, A. Venugopal, W. A. Smith, M. T. M. Koper, *J. Electrochem. Soc.* **2020**, *167*, 46505.

[161] P. Voßnacker, T. Keilhack, N. Schwarze, K. Sonnenberg, K. Seppelt, M. Malischewski, S. Riedel, *J. Eur. Inorg. Chem.* **2021**, *2021*, 1034.

[162] V. K. Davis, C. M. Bates, K. Omichi, B. M. Savoie, N. Momčilović, Q. Xu, W. J. Wolf, M. A. Webb, K. J. Billings, N. H. Chou et al., *Science* **2018**, *362*, 1144.

[163] a) T. Vent-Schmidt, F. Brosi, J. Metzger, T. Schlöder, X. Wang, L. Andrews, C. Müller, H. Beckers, S. Riedel, *Angew. Chem.* **2015**, *127*, 8397; b) F. Brosi, T. Vent-Schmidt, S. Kieninger, T. Schlöder, H.

Beckers, S. Riedel, *Chem. Eur. J.* **2015**, *21*, 16455; c) S. Riedel, T. Köchner, X. Wang, L. Andrews, *Inorg. Chem.* **2010**, *49*, 7156.

[164] M. Groessl, Z. Fei, P. J. Dyson, S. A. Katsyuba, K. L. Vikse, J. S. McIndoe, *Inorg. Chem.* **2011**, *50*, 9728.

[165] P. Metrangolo, H. Neukirch, T. Pilati, G. Resnati, *Acc. Chem. Res.* **2005**, *38*, 386.

[166] F. D. Chattaway, G. Hoyle, *J. Chem. Soc. Trans.* **1923**, *123*, 654.

[167] L. F. Olsson, *Inorg. Chem.* **1985**, *24*, 1398.

[168] R. W. G. Wyckoff, *J. Am. Chem. Soc.* **1920**, *42*, 1100.

[169] Y.-Q. Wang, Z.-M. Wang, C.-S. Liao, C.-H. Yan, *Acta Cryst. C* **1999**, *55*, 1503.

[170] J. H. Miller, L. Andrews, *Inorg. Chem.* **1979**, *18*, 988.

[171] K. Sonnenberg, P. Pröhm, S. Steinhauer, A. Wiesner, C. Müller, S. Riedel, *Z. Anorg. Allg. Chem.* **2017**, *643*, 101.

[172] C. Hall, *Q. Rev., Chem. Soc.* **1971**, *25*, 87.

[173] P. Pröhm, J. R. Schmid, K. Sonnenberg, S. Steinhauer, C. J. Schattenberg, R. Müller, M. Kaupp, P. Voßnacker, S. Riedel, *Angew. Chem. Int. Ed.* **2020**, 16002.

[174] S. A. Adonin, M. A. Bondarenko, P. A. Abramov, A. S. Novikov, P. E. Plyusnin, M. N. Sokolov, V. P. Fedin, *Eur. J. Chem.* **2018**.

[175] S. A. Adonin, M. A. Bondarenko, A. S. Novikov, P. A. Abramov, P. E. Plyusnin, M. N. Sokolov, V. P. Fedin, *Z. Anorg. Allg. Chem.* **2019**, *645*, 1141.

[176] S. A. Adonin, M. A. Bondarenko, A. S. Novikov, P. A. Abramov, P. E. Plyusnin, M. N. Sokolov, V. P. Fedin, *Cryst. Eng. Comm.* **2019**, *21*, 850.

[177] S. A. Adonin, M. A. Bondarenko, A. S. Novikov, P. E. Plyusnin, I. V. Korolkov, M. N. Sokolov, V. P. Fedin, *Inorg. Chim. Acta* **2020**, *502*, 119278.

[178] S. A. Adonin, I. D. Gorokh, A. S. Novikov, D. G. Samsonenko, P. E. Plyusnin, M. N. Sokolov, V. P. Fedin, *Dalton Trans.* **2018**, *47*, 2683.

[179] A. N. Usoltsev, S. A. Adonin, A. S. Novikov, P. A. Abramov, M. N. Sokolov, V. P. Fedin, *Cryst. Eng. Comm.* **2020**, *22*, 1985.

[180] A. N. Usoltsev, S. A. Adonin, A. S. Novikov, M. N. Sokolov, V. P. Fedin, *J. Coord. Chem.* **2019**, *72*, 1890.

[181] S. A. Adonin, M. N. Sokolov, V. P. Fedin, *Coord. Chem. Rev.* **2018**, *367*, 1.

[182] A. Eich, R. Köppe, P. W. Roesky, C. Feldmann, *Z. Anorg. Allg. Chem.* **2018**, *644*, 275.

[183] I. D. Gorokh, S. A. Adonin, M. N. Sokolov, P. A. Abramov, I. V. Korolkov, E. Y. Semitut, V. P. Fedin, *Inorg. Chim. Acta* **2018**, *469*, 583.

[184] a) R. Brückner, H. Haller, S. Steinhauer, C. Müller, S. Riedel, *Angew. Chem. Int. Ed.* **2015**, *54*, 15579; b) R. Brückner, H. Haller, S. Steinhauer, C. Müller, S. Riedel, *Angew. Chem.* **2015**, *127*, 15800.

[185] A. N. Usoltsev, S. A. Adonin, A. S. Novikov, D. G. Samsonenko, M. N. Sokolov, V. P. Fedin, *Cryst. Eng. Comm* **2017**, *19*, 5934.

[186] D. S. Silvester, R. G. Compton, *Z. Phys. Chem.* **2006**, *220*, 1247.

[187] M. Lipsztajn, R. A. Osteryoung, *J. Electrochem. Soc.* **1983**, *130*, 1968.

[188] K. Larsson, K. Binnemans, *Green Chem.* **2014**, *16*, 4595.

[189] a) A. M. Bond, G. A. Lawrance, P. A. Lay, A. M. Sargeson, *Inorg. Chem.* **1983**, *22*, 2010; b) R. J. Batchelor, J. N. R. Ruddick, J. R. Sams, F. Aubke, *Inorg. Chem.* **1977**, *16*, 1414.

[190] T. Gramstad, R. N. Haszeldine, *J. Chem. Soc.* **1957**, 4069.

[191] N. V. Ignatyev, M. Schmidt, U. Heider, P. Sartori, A. Kucheryna, *Method for Producing Perfluoroalkanesulfonic Acid Esters*, Merck Patents, **2002**, EP 1 399 417 B1.

[192] a) A. S. Shaplov, E. I. Lozinskaya, D. O. Ponkratov, I. A. Malyshkina, F. Vidal, P.-H. Aubert, O. V. Okatova, G. M. Pavlov, L. I. Komarova, C. Wandrey et al., *Electrochimica Acta* **2011**, *57*, 74; b) S. Kazemiabnavi, Z. Zhang, K. Thornton, S. Banerjee, *J. Phys. Chem. B* **2016**, *120*, 5691.

[193] T. Vander Hoogerstraete, S. Jamar, S. Wellens, K. Binnemans, *Anal. Chem.* **2014**, *86*, 3931.

[194] a) S. Mattsson, G. Senges, S. Riedel, B. Paulus, *Chem. Eur. J.* **2020**, *26*, 10781; b) A. Dimitrov, S. Rüdiger, N. V. Ignatyev, S. Datcenko, *J. Fluorine Chem.* **1990**, *50*, 197.

[195] J. Foropoulos, D. D. Desmarteau, *Inorg. Chem.* **1984**, *23*, 3720.

[196] T. Gramstad, R. N. Haszeldine, *J. Chem. Soc.* **1956**, 173.

[197] J. D. Holbrey, W. M. Reichert, M. Nieuwenhuyzen, S. Johnson, K. R. Seddon, R. D. Rogers, *Chem. Commun.* **2003**, 1636.

[198] L. Dai, S. Yu, Y. Shan, M. He, *Eur. J. Inorg. Chem.* **2004**, *2004*, 237.

[199] T. G. Tucker, S. K. Davidowski, C. A. Angell, *J. Electrochem. Soc.* **2017**, *164*, H153-H158.

[200] D. Hausmann, R. Köppe, S. Wolf, P. W. Roesky, C. Feldmann, *Dalton Trans.* **2016**, *45*, 16526.

[201] G. Mamantov, R. Marassi, F. W. Poulsen, S. E. Springer, J. P. Wiaux, R. Huglen, N. R. Smyrl, *J. Inorg. Nucl. Chem.* **1979**, *41*, 260.

[202] a) S. Bulut, P. Klose, M.-M. Huang, H. Weingärtner, P. J. Dyson, G. Laurenczy, C. Friedrich, J. Menz, K. Kümmerer, I. Krossing, *Eur. J. Chem.* **2010**, *16*, 13139; b) R. Jarosova, G. M. Swain, *J. Electrochem. Soc.* **2015**, *162*, H507-H511; c) C. Müller, K. Németh, S. Vesztergom, T. Pajkossy, T. Jacob, *Phys. Chem. Chem. Phys.* **2016**, *18*, 916.

[203] a) C. Villagrán, M. Deetlefs, W. R. Pitner, C. Hardacre, *Anal. Chem.* **2004**, *76*, 2118; b) K. R. Seddon, A. Stark, M.-J. Torres, *Pure App. Chem.* **2000**, *72*, 2275.

[204] R. Brückner, H. Haller, M. Ellwanger, S. Riedel, *Eur. J. Chem.* **2012**, *18*, 5741.

[205] E. Abitelli, S. Ferrari, E. Quartarone, P. Mustarelli, A. Magistris, M. Fagnoni, A. Albini, C. Gerbaldi, *Electrochimica Acta* **2010**, *55*, 5478.

[206] Y. Long, P. Wang, Y. Fei, D. Zhou, S. Liu, Y. Deng, *Green Chem.* **2019**, *21*, 141.

[207] M. Döbbelin, I. Azcune, M. Bedu, A. Ruiz de Luzuriaga, A. Genua, V. Jovanovski, G. Cabañero, I. Odriozola, *Chem. Mater.* **2012**, *24*, 1583.

[208] J. G. McDaniel, A. Yethiraj, *J. Phys. Chem. B* **2018**, *122*, 250.

[209] H. Ohno (Ed.) *Electrochemical aspects of ionic liquids*, Wiley, Hoboken, USA, **2011**.

[210] a) L. Glasser, H. D. B. Jenkins, *Chem. Soc. Rev.* **2005**, *34*, 866; b) H. D. B. Jenkins, D. Tudela, L. Glasser, *Inorg. Chem.* **2002**, *41*, 2364.

[211] M. H. Cohen, G. S. Grest, *Phys. Rev. B* **1979**, *20*, 1077.

[212] M. K. Nagarajan, J. O. Bockris, *J. Phys. Chem.* **1966**, *70*, 1854.

[213] P. Wachter, M. Zistler, C. Schreiner, M. Fleischmann, D. Gerhard, P. Wasserscheid, J. Barthel, H. J. Gores, *J. Chem. Eng. Data* **2009**, *54*, 491.

[214] C. Schreiner, S. Zugmann, R. Hartl, H. J. Gores, *J. Chem. Eng. Data* **2010**, *55*, 1784.

[215] A. Fick, *Ann. Phys.* **1855**, *170*, 59.

[216] G. G. Stokes, *Trans. Cambridge Phil. Soc.* **1851**, *9*, 8.

[217] A. Einstein, *Ann. Phys.* **1905**, *322*, 549.

[218] P. Walden, *Z. Phys. Chem.* **1906**, *55U*.

[219] P. Walden, *Z. Anorg. Allg. Chem.* **1920**, *113*, 85.

[220] M. P. Longinotti, H. R. Corti, *J. Phys. Chem. B* **2009**, *113*, 5500.

[221] M. Musiał, S. Bair, S. Cheng, Z. Wojnarowska, M. Paluch, *J. Molec. Liq.* **2021**, *331*, 115772.

[222] W. Xu, E. I. Cooper, C. A. Angell, *J. Phys. Chem. B* **2003**, *107*, 6170.

[223] M. Yoshizawa, W. Xu, C. A. Angell, *J. Am. Chem. Soc.* **2003**, *125*, 15411.

[224] S.-Y. Lee, K. Ueno, C. A. Angell, *J. Phys. Chem. C* **2012**, *116*, 23915.

[225] K. R. Harris, *J. Phys. Chem. B* **2019**, *123*, 7014.

[226] Y. Shao, K. Shigenobu, M. Watanabe, C. Zhang, *J. Phys. Chem. B* **2020**, *124*, 4774.

[227] P. Debye, E. Hückel, *Physik. Zeit.* **1923**, *24*, 185.

[228] J. Richter (Ed.) *Ionic Liquids*. *Molten Salts and Electrolyte Solution-Some Aspects of Their Transport Properties with Respect to a Common Theory of Liquids*, New York, USA, **1981**.

[229] K. R. Harris, *J. Phys. Chem. B* **2018**, *122*, 10964.

[230] V. M. Ortiz-Martínez, L. Gómez-Coma, G. Pérez, A. Ortiz, I. Ortiz, *Sep. Purif. Tech.* **2020**, *252*, 117436.

[231] T. Ogawa, K. Kamiguchi, T. Tamaki, H. Imai, T. Yamaguchi, *Anal. Chem.* **2014**, *86*, 9362.

[232] I. Rubinstein, M. Bixon, E. Gileadi, *J. Phys. Chem.* **1980**, *84*, 715.

[233] S. Park, D. H. Han, J. G. Lee, T. D. Chung, *ACS Appl. Energ. Mater.* **2020**, *3*, 5285.

[234] R. Kawano, M. Watanabe, *Chem. Comm.* **2003**, 330.

[235] J. Grossi, J. J. Kohanoff, N. J. English, E. M. Bringa, M. G. Del Pópolo, *J. Phys. Chem. B* **2017**, *121*, 6436.

[236] R. Brückner, P. Pröhm, A. Wiesner, S. Steinhauer, C. Müller, S. Riedel, *Angew. Chem. Int. Ed.* **2016**, *55*, 10904.

[237] a) E. E. Havinga, K. H. Boswijk, E. H. Wiebenga, *Acta Cryst. A* **1954**, *7*, 487; b) K. N. Robertson, P. K. Bakshi, T. S. Cameron, O. Knop, *Z. Anorg. Allg. Chem.* **1997**, *623*, 104; c) A. Gräfe-Kavoosian, S. Nafepour, K. Nagel, K.-F. Tebbe, *Z. Naturforsch. B* **1998**, *53*, 641.

[238] F. A. Redeker, A. Kropman, C. Müller, S. E. Zewge, H. Beckers, B. Paulus, S. Riedel, *J. Fluorine Chem.* **2018**, *216*, 81.

[239] I. Rubinstein, E. Gileadi, *J. Electroanal. Chem. Inter. Electrochem.* **1980**, *108*, 191.

[240] D. MacFarlane, M. Kar, J. M. Pringle, *Fundamentals of ionic liquids*. *From chemistry to applications*, John Wiley & Sons, Incorporated, Newark, USA, **2017**.

[241] a) J. Heinze, *Angew. Chem.* **1984**, *96*, 823; b) V. Radtke, A. Ermantraut, D. Himmel, T. Koslowski, I. Leito, I. Krossing, *Angew. Chem. Int. Ed.* **2018**, *57*, 2344; c) N. Elgrishi, K. J. Rountree, B. D. McCarthy, E. S. Rountree, T. T. Eisenhart, J. L. Dempsey, *J. Chem. Educ.* **2018**, *95*, 197.

[242] M. Armand, F. Endres, D. R. MacFarlane, H. Ohno, B. Scrosati, *Nat. Mater.* **2009**, *8*, 621.

[243] a) P. Singh, K. White, A. J. Parker, *J. Power Sources* **1983**, *10*, 309; b) B. Kratochvil, E. Lorah, C. Garber, *Anal. Chem.* **1969**, *41*, 1793.

[244] G. A. Snook, A. S. Best, A. G. Pandolfo, A. F. Hollenkamp, *Electrochem. Commun.* **2006**, *8*, 1405.

[245] R. R. Gagne, C. A. Koval, G. C. Lisensky, *Inorg. Chem.* **1980**, *19*, 2854.

[246] S. M. Batterjee, M. I. Marzouk, M. E. Aazab, M. A. El-Hashash, *Appl. Organometal. Chem.* **2003**, *17*, 291.

[247] J. C. Swarts, A. Nafady, J. H. Roudebush, S. Trupia, W. E. Geiger, *Inorg. Chem.* **2009**, *48*, 2156.

[248] N. G. Connelly, W. E. Geiger, *Chem. Rev.* **1996**, *96*, 877.

[249] S. Yousefinejad, F. Honarasa, A. Solhjoo, *J. Chem. Eng. Data* **2016**, *61*, 614.

[250] E. H. B. Anari, M. Romano, W. X. Teh, J. J. Black, E. Jiang, J. Chen, T. Q. To, J. Panchompoo, L. Aldous, *Chem. Commun.* **2016**, *52*, 745.

[251] a) V. V. Pavlishchuk, A. W. Addison, *Inorg. Chim. Acta* **2000**, *298*, 97; b) G. Gritzner, J. Kuta, *Pure and Applied Chemistry* **1984**, *56*, 461.

[252] S. Zang, *Ionic liquids: physicochemical properties*, Elsevier, Amsterdam, **2009**.

[253] A. I. Popov, D. H. Geske, *J. Am. Chem. Soc.* **1958**, *80*, 5346.

[254] A. I. Popov, D. H. Geske, *J. Am. Chem. Soc.* **1958**, *80*, 1340.

[255] T. Jarosz, P. Data, M. Lapkowski, *Display and Imaging* **2016**, *2016*, 229.

[256] A. Blacha-Grzechnik, K. Karon, P. Data, *J. Vis. Exp.* **2018**.

[257] T. H. Le, A. Nafady, X. Qu, A. M. Bond, L. L. Martin, *Anal. Chem.* **2012**, *84*, 2343.

[258] a) D. L. Jeanmaire, R. P. van Duyne, *J. Electroanal. Chem. Inter. Electrochem.* **1977**, *84*, 1; b) K. S. Joya, X. Sala, *Phys. Chem. Chem. Phys.* **2015**, *17*, 21094; c) J. R. Lombardi, R. L. Birke, *J. Phys. Chem. C* **2014**, *118*, 11120.

[259] E. Robert, E. Christensen, B. Gilbert, N. Bjerrum, *Electrochimica Acta* **1999**, *44*, 1689.

[260] T. C. Mendes, X. Zhang, Y. Wu, P. C. Howlett, M. Forsyth, D. R. MacFarlane, *ACS Sust. Chem. Eng.* **2019**, *7*, 3722.

[261] A. Saha, S. Payra, D. Dutta, S. Banerjee, *ChemPlusChem* **2017**, *82*, 1129.

[262] a) E. Santos, J. Albo, A. Irabien, *RSC Adv* **2014**, *4*, 40008; b) K. Wu, X. Shen, *New J. Chem.* **2019**, *43*, 15857.

[263] S. K. Shukla, S. Pandey, S. Pandey, *J. Chromatog. A* **2018**, *1559*, 44.

[264] B. J. Mincher, J. F. Wishart, *Solv. Extrac. Ion Exch.* **2014**, *32*, 563.

[265] S.-M. Xia, K.-H. Chen, H.-C. Fu, L.-N. He, *Frontiers Chem.* **2018**, *6*, 462.

[266] a) C. Chiappe, M. Malvaldi, C. S. Pomelli, *Green Chem.* **2010**, *12*, 1330; b) G. Aridoss, K. K. Laali, *Curr. Org. Synth.* **2017**, *14*; c) C. Velez, B. Doherty, O. Acevedo, *Int. J. Molec. Sci.* **2020**, *21*.

[267] a) F. van Rantwijk, R. A. Sheldon, *Chem. Rev.* **2007**, *107*, 2757; b) P. Xu, S. Liang, M.-H. Zong, W.-Y. Lou, *Biotech. Adv.* **2021**, 107702; c) M. Yang, H. Wu, Y. Lian, X. Li, Y. Ren, F. Lai, G. Zhao, *Microbial Cell Factories* **2014**, *13*, 143.

[268] a) I. M. Marrucho, L. C. Branco, L. P. N. Rebelo, *Ann. Rev. Chem. Biomolec. Eng.* **2014**, *5*, 527; b) S. N. Pedro, C. S. R Freire, A. J. D. Silvestre, M. G. Freire, *In. J. Molec. Sci.* **2020**, *21*.

[269] a) Y.-F. Hu, Z.-C. Liu, C.-M. Xu, X.-M. Zhang, *Chem. Soc. Rev.* **2011**, *40*, 3802; b) S. Elhenawy, M. Khraisheh, F. AlMomani, M. Hassan, *Molec.* **2020**, *25*; c) D. Shang, X. Liu, L. Bai, S. Zeng, Q. Xu, H. Gao, X. Zhang, *Curr. Op. Green Sust. Chem.* **2017**, *5*, 74.

[270] M. Deetlefs, K. R. Seddon, *Green Chem.* **2010**, *12*, 17.

[271] a) D. Appleby, C. L. Hussey, K. R. Seddon, J. E. Turp, *Nature* **1986**, *323*, 614; b) A. Mohammad, D. Inamuddin, *Green Solvents II*, Springer Dordrecht, Netherlands, **2012**.

[271] T. Welton, *Green Chem.* **2011**, *13*, 225.

[273] R. Sanghi, V. Singh, *Green chemistry for environmental remediation*, Scrivener Pub.; Co-published by John Wiley & Sons, Salem, Mass., Hoboken, USA, **2012**.

[274] a) M. Smiglak, W. M. Reichert, J. D. Holbrey, J. S. Wilkes, L. Sun, J. S. Thrasher, K. Kirichenko, S. Singh, A. R. Katritzky, R. D. Rogers, *Chem. Comm.* **2006**, 2554; b) Y. Li, Y. Pan, G. Huang, Q. Wang, Q. Wei, J. Jiang, *J. Loss Prev. Proc. Ind.* **2020**, *64*, 104081; c) A.-O. Diallo, A. B. Morgan, C. Len, G. Marlair, *Energ. Environ. Sci.* **2013**, *6*, 699.

[275] X.-D. Hou, Q.-P. Liu, T. J. Smith, N. Li, M.-H. Zong, *PloS one* **2013**, *8*, e59145.

[276] P. T. Anastas, J. C. Warner, *Green chemistry*. *Theory and practice*, Oxford University Press, Oxford, **2000**.

[277] E. L. Smith, A. P. Abbott, K. S. Ryder, *Chem. Rev.* **2014**, *114*, 11060.

[278] W. Xuan, A. Otsuki, A. Chagnes, *RSC Adv.* **2019**, *9*, 38612.

[279] K. H. Chan, J. Anawati, M. Malik, G. Azimi, *ACS Sust. Chem. Eng.* **2021**, *9*, 4398.

[280] a) F. Endres, A. Abbott, D. MacFarlane (Eds.) *Electrodeposition from Ionic Liquids*, Wiley-VCH Verlag GmbH & Co. KGaA, Weinheim, Germany, **2017**; b) T. J. Melton, J. Joyce, J. T. Maloy, J. A. Boon, J. S. Wilkes, *J. Electrochem. Soc.* **1990**, *137*, 3865.

[281] I.-W. Sun, P.-Y. Chen in *Electrodeposition from Ionic Liquids* (Eds.: F. Endres, A. Abbott, D. MacFarlane), Wiley-VCH Verlag GmbH & Co. KGaA, Weinheim, Germany, **2017**, pp. 157–186.

[282] M. Lipsztajn, R. A. Osteryoung, *Inorg. Chem.* **1985**, *24*, 716.

[283] G. E. Gray, P. A. Kohl, J. Winnick, *J. Electrochem. Soc.* **1995**, *142*, 3636.

[284] P.-Y. Chen, Y.-F. Lin, I.-W. Sun, *J. Electrochem. Soc.* **1999**, *146*, 3290.

[285] E. G.-S. Jeng, I.-W. Sun, *J. Electrochem. Soc.* **1997**, *144*, 2369.

[286] M. Chen, S. Li, C. Jin, M. Shao, Z. Huang, *Separ. Purif. Tech.* **2021**, *259*, 118204.

[287] a) J. Richter, M. Ruck, *Molec.* **2019**, *25*; b) A. Yao, F. Qu, Y. Liu, G. Qu, H. Lin, S. Hu, X. Wang, T. Chu, *Dalton Trans.* **2019**, *48*, 16249.

[288] A. P. Abbott, G. Frisch, J. Hartley, W. O. Karim, K. S. Ryder, *Prog. Nat. Sci. Mater. Int.* **2015**, *25*, 595.

[289] A. Farooq, M. Hamza, Q. Ahmed, K. M. Deen, *Electrochimica Acta* **2019**, *314*, 135.

[290] X. Tian, D. Y. Ding, *Mater. Sci. Forum* **2016**, *852*, 49.

[291] A. C. Hegde, K. Venkatakrishna, N. Eliaz, *Surf. Coat. Tech.* **2010**, *205*, 2031.

[292] D. Linden, T. B. Reddy, *Handbook of Batteries*, McGraw-Hill, **2002**. Web: Aug 09, 2021.

[293] L. Li, S. Kim, W. Wang, M. Vijayakumar, Z. Nie, B. Chen, J. Zhang, G. Xia, J. Hu, G. Graff et al., *Adv. Energ. Mater.* **2011**, *1*, 394.

[294] K. W. Knehr, E. C. Kumbur, *Electrochem. Commun.* **2011**, *13*, 342.

[295] L. Bahadori, R. Boyd, A. Warrington, M. S. Shafeeyan, P. Nockemann, *J. Molec. Liq.* **2020**, *317*, 114017.

[296] X. Wu, J. Liu, X. Xiang, J. Zhang, J. Hu, Y. Wu, *Pure App. Chem.* **2014**, *86*, 661.

[297] A. Ejigu, P. A. Greatorex-Davies, D. A. Walsh, *Electrochem. Comm.* **2015**, *54*, 55.

[298] D. Bryans, B. G. McMillan, M. Spicer, A. Wark, L. Berlouis, *J. Electrochem. Soc.* **2017**, *164*, A3342-A3348.

[299] a) K. Mizushima, P. C. Jones, P. J. Wiseman, J. B. Goodenough, *Mat. Res. Bull.* **1980**, *15*, 783; b) N. A. Godshall, I. D. Raistrick, R. A. Huggins, *Mater. Res. Bull.* **1980**, *15*, 561.

[300] P. G. Bruce, S. A. Freunberger, L. J. Hardwick, J.-M. Tarascon, *Nat. Mater.* **2011**, *11*, 19.

[301] G. G. Amatucci, J. M. Tarascon, L. C. Klein, *J. Electrochem. Soc.* **1996**, *143*, 1114.

[302] M. Holzapfel, C. Jost, P. Novák, *Chem. Comm.* **2004**, 2098.

[303] M. Ishikawa, T. Sugimoto, M. Kikuta, E. Ishiko, M. Kono, *J. Pow. Sourc.* **2006**, *162*, 658.

[304] Z. X. Shu, R. S. McMillan, J. J. Murray, *J. Electrochem. Soc.* **1993**, *140*, 922.

[305] A. Basile, A. I. Bhatt, A. P. O'Mullane, *Nat. Comm.* **2016**, *7*, ncomms11794.

[306] J. Li, C. Ma, M. Chi, C. Liang, N. J. Dudney, *Adv. Energ. Mater.* **2015**, *5*, 1401408.

[307] T. Famprikis, P. Canepa, J. A. Dawson, M. S. Islam, C. Masquelier, *Nat. Mater.* **2019**.

[308] P. Albertus, S. Babinec, S. Litzelman, A. Newman, *Nat. Energ.* **2018**, *3*, 16.

[309] a) T. Bartsch, F. Strauss, T. Hatsukade, A. Schiele, A.-Y. Kim, P. Hartmann, J. Janek, T. Brezesinski, *ACS Energ. Lett.* **2018**, *3*, 2539; b) T. Inoue, K. Mukai, *ACS Appl. Mater. Inter.* **2017**, *9*, 1507.

[310] Z. Wang, H. Zhou, C. Meng, W. Xiong, Y. Cai, P. Hu, H. Pang, A. Yuan, *ACS Appl. Energ. Mater.* **2020**, *3*, 4265.

[311] D. Kumar, S. A. Hashmi, *Solid State Ionics* **2010**, *181*, 416.

[312] a) F. A. GRANT, *Rev. Mod. Phys.* **1959**, *31*, 646; b) P. Hotsenpiller, Bolt J.D., Farneth W.E., Lowekamp
J.B., G. S. Rohrer, *J. Phys. Chem. B* **1998**, *102*, 3216.

[313] H. Cai, Q. Tang, B. He, R. Li, L. Yu, *Nano.* **2014**, *6*, 15127.

[314] M. Wang, A. M. Anghel, B. Marsan, N.-L. Cevey Ha, N. Pootrakulchote, S. M. Zakeeruddin, M. Grätzel, *J. Am. Chem. Soc.* **2009**, *131*, 15976.

[315] G. Oskam, B. V. Bergeron, G. J. Meyer, P. C. Searson, *J. Phys. Chem. B* **2001**, *105*, 6867.

[316] S. Sasi, A. Sajeev, S. K. Sugunan, P. R. Nair, S. Mathew, *Micro Nanosys.* **2021**, *13*.

[317] H.-J. Wang, C.-P. Chen, R.-J. Jeng, *Mater.* **2014**, *7*, 2411.

[318] Z.-S. Wang, K. Sayama, H. Sugihara, *J. Phys. Chem. B* **2005**, *109*, 22449.

[319] K. Kakiage, E. Fujimura, Y. Nakada, T. Ogino, T. Kyomen, M. Hanaya, *Key Eng. Mater.* **2014**, *596*, 35.

[320] K. Yoo, N. C. Deb Nath, H. C. Kang, S. Muthu, J.-J. Lee, *ECS J. Solid State Sci. Technol.* **2021**, *10*, 25007.

[321] Ershov, B. G., E. Janata, Gordeeva, A. V., *Russ. Chem. Bull.* **2008**, *57*, 1821.

[322] Ershov, B. G., M. Kelm, A. V. Gordeev, E. Janata, *Phys. Chem. Chem. Phys.* **2002**, *4*, 1872.

[323] L. Troian-Gautier, M. D. Turlington, S. A. M. Wehlin, A. B. Maurer, M. D. Brady, W. B. Swords, G. J. Meyer, *Chem. Rev.* **2019**, *119*, 4628.

[324] P. Wardman, *J. Phys. Chem. Ref. Data* **1989**, *18*, 1637.

2. Objective

The current energy transition from fossil fuels to alternative energy sources has created a demand from public, government, and industrial interests to invent and refine technologies that will aid in the energy transition. A key component of this change, as highlighted by the Nobel Prize in chemistry in 2019, is the use of batteries as a form of saving excess energy. The most common batteries are the Li-ion battery and the vanadium redox-flow battery. Ionic liquids are often seen in the current scientific literature as additives or electroactive components in battery technologies.

The Li-ion battery utilizes a variety of rare metals including Li and Co, and with increasing demand, new chemical methods are being researched to recycle these precious metals. Recently, the trihalogen monoanion ionic liquids [Cat.][Cl_3] and [Cat.][Br_3] ([Cat.]$^+$= imidazolium or pyrrolidinium) have been demonstrated to dissolve a variety of precious metals. To demonstrate the applicability of metal dissolution, the synthesis products and electrochemical characterization need to be analyzed.

In this work, the trihalogen monoanion based ionic liquids [N_{2221}][X_3] and [N_{2221}][XY_2] (X = Cl, Br, I, Y = Cl, Br) will have their physicochemical and electrochemical properties analyzed, and oxidative strength quantified. Further, the chemistry of chloridometallate anion based room temperature ionic liquids [$SnCl_3$]$^-$ and other [MCl_n]$^-$ (M = metals) are well known, but not that of the [C_8C_1IM][$SnBr_3$] or [C_8C_1IM][$SnBr_5$] ([IM]$^+$ = imidazolium). Therefore, the potential of the trihalogen monoanion ionic liquids as metal recycling agents will be tested by dissolving Sn in [C_8C_1IM][Br_3] to synthesize [C_8C_1IM][$SnBr_3$] and performing cyclic voltammetry experiments to analyze the active species bromidostannate anions ([$SnBr_3$]$^-$ and [$SnBr_5$]$^-$) as a first principles approach towards metal recycling in a closed system.

In regard to vanadium redox-flow batteries, they have been proposed to service electrical grids in the storage and distribution of electricity from intermittent energy sources. The downside is that vanadium is costly, toxic, and the potential output is limited due to the electrochemical window of water. Alternatives are metal halide and halidometallate based ionic liquids as the electroactive species, because they are non-aqueous, have larger potential windows and theoretical energy densities. An all-manganese non-aqueous redox-flow battery with the electrolyte [C_4C_1Pyrr][$MnCl_4$] ([Pyrr]$^+$ = pyrrolidinium) is considered. The proposed benefits to the battery stem from manganese being rather common and economical, having a large potential window, and Mn-crossover through the membrane is non-disruptive to battery performance.

3. Publications

The scientific publications are presented in first author and second author contributions and represent the tangible scientific progress achieved during the doctoral candidacy phase.

Each scientific entry is precluded by the table of contents graphic, list of authors, the digital object identifier (DOI), copyright permissions, and author contributions. The supporting information of each article as well as any full characterization of unpublished compounds are located in the appendix sections D and E, respectively.

3.1. Conductivity and Redox Potentials of Ionic Liquid Trihalogen Monoanions $[X_3]^-$, $[XY_2]^-$, and $[BrF_4]^-$ (X=Cl, Br, I and Y=Cl, Br)

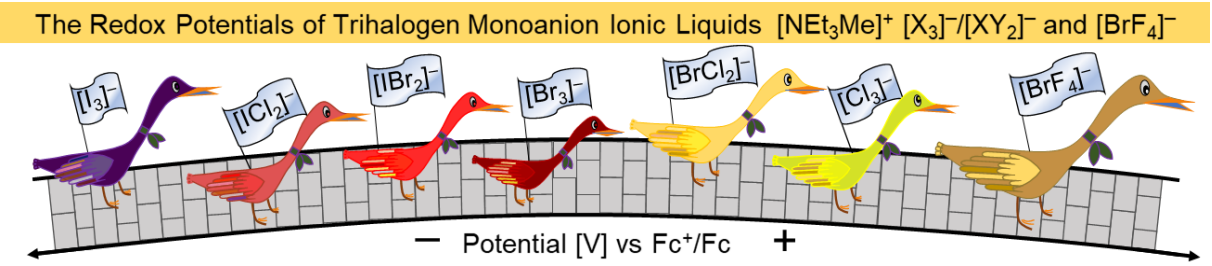

Tyler A. Gully, Patrick Voßnacker, Jonas R. Schmid, Helmut Beckers, and Sebastian Riedel*

ChemistryOpen **2021**, *10*, 255-264.
DOI: https://doi.org/10.1002/open.202000263

This is an invited contribution to a Special Issue dedicated to Material Synthesis in Ionic Liquids.

Author contributions

M.Sc. Tyler A. Gully designed the project, performed the experiments, characterized the products, and analyzed the physicochemical, electrochemical, and spectroscopy data. Additionally, he wrote the original manuscript.

M.Sc. Patrick Voßnacker synthesized the various trihalogen monoanion salts and provided NMR analysis of $[N_{2221}]I$. Additionally, he corrected the original manuscript.

M.Sc. Jonas R. Schmid synthesized $[N_{2221}][BrF_4]$ for electrochemical experiments and provided the NMR analysis thereof. Additionally, he corrected the original manuscript.

Dr. habil. Helmut Beckers provided scientific guidance and helped write the original manuscript.

Prof. Dr. Sebastian Riedel supervised the project and was responsible for conceptualization and the acquisition of the financial support for the project leading to this publication. He was also responsible for reviewing and editing the original draft of this publication.

Special Issue

Conductivity and Redox Potentials of Ionic Liquid Trihalogen Monoanions $[X_3]^-$, $[XY_2]^-$, and $[BrF_4]^-$ (X = Cl, Br, I and Y = Cl, Br)

Tyler A. Gully, Patrick Voßnacker, Jonas R. Schmid, Helmut Beckers, and Sebastian Riedel*[a]

The ionic liquid (IL) trihalogen monoanions $[N_{2221}][X_3]^-$ and $[N_{2221}][XY_2]^-$ ($[N_{2221}]^+$ = triethylmethylammonium, X = Cl, Br, I, Y = Cl, Br) were investigated electrochemically via temperature dependent conductance and cyclic voltammetry (CV) measurements. The polyhalogen monoanions were measured both as neat salts and as double salts in 1-butyl-1-methyl-pyrrolidinium trifluoromethane-sulfonate ([BMP][OTf], $[X_3]^-/[XY_2]^-$ 0.5 M). Lighter IL trihalogen monoanions displayed higher conductivities than their heavier homologues, with $[Cl_3]^-$ being 1.1 and 3.7 times greater than $[Br_3]^-$ and $[I_3]^-$, respectively. The addition of [BMP][OTf] reduced the conductivity significantly. Within the group of polyhalogen monoanions, the oxidation potential develops in the series $[Cl_3]^- > [BrCl_2]^- > [Br_3]^- > [IBr_2]^- > [ICl_2]^- > [I_3]^-$. The redox potential of the interhalogen monoanions was found to be primarily determined by the central halogen, I in $[ICl_2]^-$ and $[IBr_2]^-$, and Br in $[BrCl_2]^-$. Additionally, tetrafluorobromate(III) ($[N_{2221}]^+[BrF_4]^-$) was analyzed via CV in MeCN at 0 °C, yielding a single reversible redox process ($[BrF_2]^-/[BrF_4]^-$).

1. Introduction

In 1923 Chattaway and Hoyle performed the first thorough characterization of polybromides and polychlorides monoanions.[1] Since then, the trihalogen monoanions of the general form $[X_3]^-$[2,3,4] and $[XY_2]^-$[4–9] (X = Cl, Br, I, Y = F, Cl, Br, and I) have been extensively studied, and higher polyhalogen monoanions such as $[Cl_{13}]^-$[10] or $[Cl(BrCl)_6]^-$[11] have become well established. Amongst the existing interhalogen monoanions two classifications exist, the classical and non-classical variety.[12] Classical interhalogens have a more electropositive center being surrounded by electronegative halogen atoms as found in $[ICl_2]^-$.[9,13] In comparison, in non-classical interhalogens an electronegative center is surrounded by more electropositive dihalogen molecules such as in $[Cl(I_2)_4]^-$, or $[ClI_2]^-$.[9,14] Another point of comparison between the homonuclear $[X_3]^-$ and interhalogen monoanions $[XY_2]^-$ is the solution equilibrium. Due to the variety in halogen atoms, a more complex equilibrium in solution for $[XY_2]^-$ exists compared to that of the homonuclear species.[15–18]

In the solid state, polyhalogens of type $[Br_x]^-$[19] or $[Cl_x]^-$[20] (x = 3–5) are known to form network structures joined by halogen bonds through a so-called sigma-hole.[11] The sigma hole is a region of greater electron density and more positive electrostatic potential located perpendicular to the bonding axis. The use of halogen bonding can be extended to hybrid polyhalogen-halometalate networks. Whereby halometalates, such as $[SbBr_6]^{2-}$,[21] $[BiBr_5]^{2-}$,[22] or $[TeBr_6]^{2-}$[23] are coordinated via $[Br_3]^-$ or Br_2 units. Additionally, interhalogen networks can form between $[TeCl_6]^{2-}$ and Br_2.[24]

The recent advancements in the polyhalogen monoanion structural characterization were due to stabilization of the anion in the solid state by using more bulky organic cations such as $[NR_4]^+$ (R = methyl, ethyl, propyl)[25] $[PPh_2Cl_2]^+$,[2] or $[HMIM]^+$ (1-methyl-1-hexylimadazolium).[26] As a consequence of using these cations to stabilize the polyhalogen anions, ionic liquids (IL) and sometimes room temperature ionic liquids (RT-IL) were formed.[20,26,27] In addition to forming larger polyhalogen monoanions, their conductivity, melting points, and electrochemical properties can be selectively tuned by variation of the cation.[25,28,29] Some typical cations in IL synthesis are the imidazolium,[26,29–31] pyrrolidinium,[31] and alkyl ammonium[27,31] cations, for a list of ions depicted in this work see Scheme 1.

Within the last 10 years a variety of uses concerning polyhalogens were established. For instance, the interhalogen anion in the non-classical salt $[N_{2221}][Cl(BrCl)_2]$ ($[N_{2221}]^+$ = triethylmethyl-ammonium) acts as a halogenating reagent towards alkenes, alkynes, and Michael systems.[32] It was demonstrated that by using $[N_{2221}]^+Cl^-$ gaseous Cl_2 could be sequestered in the salt as a liquid, making it safer and easier to use in the laboratory as a chlorinating agent compared to Cl_2.[27] Very recently, the bonding situation of symmetrical and asymmetrical $[Cl_3]^-$ has been investigated by experimental and computed electron density experiments.[33] In the case of liquid

[a] T. A. Gully, P. Voßnacker, J. R. Schmid, H. Beckers, Prof. Dr. S. Riedel
Freie Universität Berlin
Fachbereich Biologie, Chemie, Pharmazie
Institut für Chemie und Biochemie – Anorganische Chemie
Fabeckstr. 34/36
14195 Berlin (Germany)
E-mail: s.riedel@fu-berlin.de

Supporting information for this article is available on the WWW under https://doi.org/10.1002/open.202000263

Special Issue

An invited contribution to a Special Issue dedicated to Material Synthesis in Ionic Liquids.

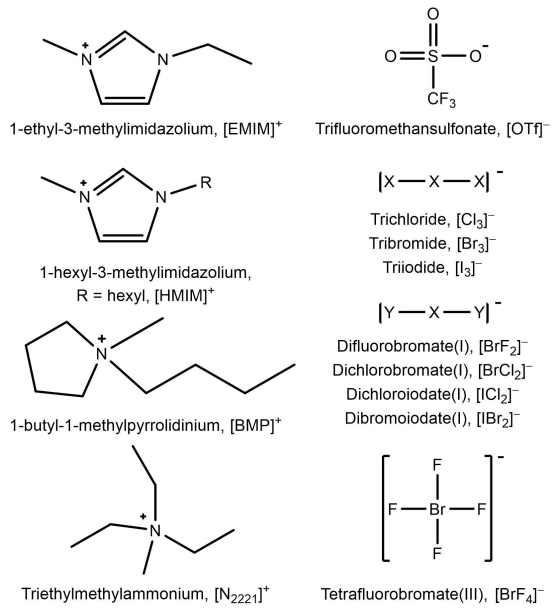

Scheme 1. List of cations and anions used in this work.

Br_2, a solid, $[NBu_4][Br_3]$ or $[NPr_3][Br_9]$,[34] was synthesized to directly perform halogenation reactions.

A significant portion of modern polyhalogen IL applications are based around their electrochemistry, primarily battery technologies. The primary examples are the zinc bromide battery[35,36] and in dye sensitized solar cells.[37,38] In the zinc bromide battery, the purpose of $[Cat]^+Br^-/[Br_3]^-$ is to react with Br_2 and form higher order polyhalogen monoanions that will not gas out of the cell, and as an added benefit increase the conductivity of the electrolyte.[35,36] In dye sensitized solar cells, $[Cat][I_3]$ monoanions act as charge transfer agents.[37,38]

The use of polyhalogens in batteries as charge carriers can be related to their conductance and relationship to the Grotthuss mechanism.[37,39,40] The Grotthuss-like hopping mechanism shuttles X^- moieties within the polyhalogens enabling higher conductivity values in contrast to traditional diffusion based ion transport.[16,38,39,41–43]

The reactive IL can also be further used for the dissolution of UO_2 in $[Cl_3]^-$,[44] recycling of nickel hydride batteries,[45] and the dissolution of rare metals such as Au[11,46,47], Ga,[48] or magnets made of Sm[49] with $[Cl_3]^-$ and $[Br_3]^-$ ILs. Whereby, the determination of the polyhalogen standard potentials could lead to an expedited screening process of determining which metals could be selectively dissolved or chemicals that are readily oxidized into their respective halogenation product.

The electrochemistry of the trihalogen monoanions in non-aqueous media was well studied by Popov in 1958, who did experiments to determine the electrochemical mechanisms of $[I_3]^-$,[50] $[Br_3]^-$[51] and $[ICl_2]^-$[51] and $[IBr_2]^-$[51] in acetonitrile (MeCN) solutions. The other trihalogen monoanions have since been thoroughly characterized in a variety of solvents.[16,18,30,40,52–54] The electrochemistry of molten halogen anions is limited to GaI/$[ICl_2]$, which was investigated at 300 °C.[53]

Bentley *et al.* reexamined the redox chemistry of trihalogen monoanions ILs as double salt ionic liquids (DSIL) via cyclic voltammetry (CV).[15,30] Their purpose was to describe how traces of I^- in ILs were able to etch and dissolve gold electrode surfaces by providing the potentials and redox mechanism of $[I_3]^-$ IL monoanions.[30] By using 1-ethyl-1-methyl-imadazolium bis(trifluoromethanesulfonyl)imide, $[EMIM][NTf_2]$, or trifluoromethanesulfonate, $[OTf]^-$, in combination with the iodide polyhalogens, DSIL salts were formed and studied via CV. The redox mechanism and potential of $[I_3]^-$, and the classical and non-classical interhalogen monoanions, $[ICl_2]^-$ and $[ClI_2]^-$, respectively, were determined.[30]

Subsequently, Bard proposed an electrochemical (E) chemical (C) style mechanism as an ECEC mechanism for the two step oxidation of $Br^-/[Br_3]^-/Br_2$ in nitrobenzene.[55] The mechanism is contrary to previously postulated mechanisms of Allen et al. for Br^-,[56,57] Yu et al. for Br^- and Cl^-,[58] or Bentley et al. for I^-,[30] who propose a CECE style mechanism with the initial step being dependent on the dissociation of X^- and X_2 to $[X_3]^-$. The downside to modeling the CECE mechanism being the high stability of the trihalide monoanion ($K_{eq} > 10^6$ M^{-1}).[30]

Here we present a systematic approach to the electrochemical characterization via conductance and CV measurements of the trihalogen monoanion ILs based on $[N_{2221}][X_3]$ (X = Cl, Br, and I) and classical interhalogen monoanions $[N_{2221}][XY_2]$, (X,Y = Cl, Br, and I) both as neat salts and as DSILs using [BMP][OTf] ($[BMP]^+$ = 1-bu-1-methyl-pyrrolidinium) and [EMIM][OTf] ($[EMIM]^+$ = 1-ethyl-3-methylimidazolium) supporting electrolytes, see Scheme 1. Additionally, the stable interhalogen monoanion $[BrF_4]^-$[5] was characterized via CV in MeCN at 0 °C.

2. Results and Discussion

The homonuclear $[N_{2221}][X_3]$ (X = Cl, Br, and I) and heteronuclear trihalogen monoanions $[N_{2221}][X_3]$ (X = Cl, Br, and I) were synthesized, and their composition confirmed by Raman spectroscopy (see supporting information). The trihalogen monoanion salts display a variety of colors, ranging from yellow $[Cl_3]^-$, yellow-orange $[BrCl_2]^-$, red $[Br_3]^-$, bright red $[IBr_2]^-$, to dark brown-red $[ICl_2]^-$ and dark brown $[I_3]^-$, as shown in Figure 1. The addition of [BMP][OTf] to the neat compounds results in the formation of a DSIL that is liquid at room temperature, yielding an optimal system for electrochemical measurements.

All compounds were analyzed by means of UV-visible spectroscopy (Figure 2), which can also be employed for reaction monitoring. The use of the UV-*vis* spectra as an identifier for chemical reactions will be useful and described in a later section studying the chemical oxidation of metallocenes. A shift in the absorption wavelengths to higher wavelengths is noticeable for the $[X_3]^-$ monoanions from $[Cl_3]^-$ (407 nm), via $[Br_3]^-$ (440 nm), to $[I_3]^-$ (492, 558 nm), whereas the interhalogen monoanions ($[XY_2]^-$) have similar absorptions ranging around 400 nm.

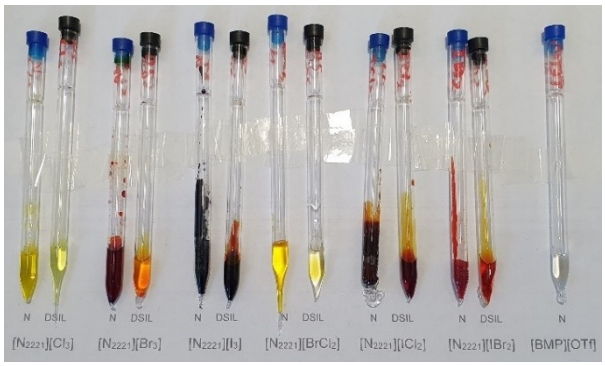

Figure 1. $[N_{2221}][X_3]$ and $[N_{2221}][XY_2]$ as neat liquid (N, left) and mixed with [BMP][OTf] (DSIL, right) ($[X_3]^-$ and $[XY_2]^-$ 0.5 M). The samples from left to right: $[Cl_3]^-$, $[Br_3]^-$, $[I_3]^-$, $[BrCl_2]^-$, $[ICl_2]^-$, $[IBr_2]^-$, $[Cl_3]^-$, [BMP][OTf].

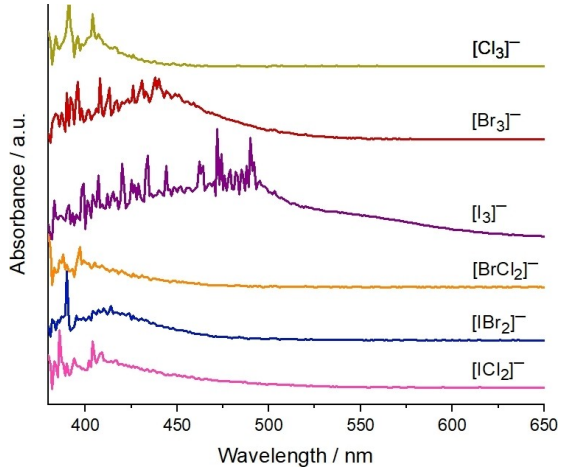

Figure 2. UV-*vis* of $[N_{2221}][X_3]$ and $[N_{2221}][XY_2]$ (X, Y = Cl, Br, I) in MeCN.

2.1. Conductivity

The comparison of physicochemical characteristics, conductivity and viscosity between different ionic liquids is well established in the literature. Polyhalogen anions, however, have relatively large conductivities that are attributable to a Grotthuss-like hopping mechanism.[16,38,39,41–43] Grossi proposed a mechanism based on $[I_3]^-$ in the solid structure. Two $[X_3]^-$ moieties come into contact forming a temporary $[X_6]^-$ molecule ($X_2\cdots X^-\cdots X_3^-$) and subsequently eject a X^- that "hops" to the next $[X_3]^-$ moiety.[16] Based upon their calculations, the insertion of the X^- and the resulting conductivity is heavily dependent on the angle of the incoming $[X_3]^-$ moiety.[16] However, the actual situation in a polyhalogen ILs relating to the Grotthuss-like mechanism are dependent on a variety of other factors including the direction of the mutual intermolecular attack,[16] solvent sheath,[41,42] Coulombic interactions,[59] charge transport,[38,41] diffusion phenomena,[39,43] and halogen dissociation energies.[60]

The temperature dependent conductivity of ILs and DSILs can be modelled by the semi-empirical Vogel-Fulcher-Tamman equation (VFT).[59] The following equation describes the conductivity based VFT equation:

$$\sigma(T) = \sigma_0 exp\left(-\frac{B}{(T - T_g)}\right) \quad (1)$$

Where σ is the conductivity at a given temperature, σ_0 is the conductivity at infinite temperature, B is the thermodynamic probability of particles to interact with each other, and T_g is the glassy transition temperatures. The VFT describes ILs and is valid in IL mixtures of salts and solvents.[59]

$[N_{2221}][Cl_3]^-$ is the only room temperature IL. The other trihalogen monoanions were solid at room temperature, part liquid and solid ($[N_{2221}][Br_3]$), or at the glassy transition phase ($[N_{2221}][BrCl_2]$). The mixture of liquid and solid occurred for $[N_{2221}][IBr_2]$ and $[N_{2221}][ICl_2]$ during the melting process and only the conductivities obtained from a homogeneous melt are presented.

The temperature dependent conductivity of the neat $[N_{2221}][X_3]$ display a clear trend with the lighter halogens having greater conductivity than their heavier homologues ($[Cl_3]^- > [Br_3]^- > [I_3]^-$). Interestingly, $[N_{2221}][Cl_3]$ (44.8 $mS\cdot cm^{-1}$) and $[N_{2221}][Br_3]$ (39.5 $mS\cdot cm^{-1}$) were significantly closer than that of $[N_{2221}][I_3]$ (12.0 $mS\cdot cm^{-1}$) at 55.0 °C, see Figure 3.

In comparison to the $[N_{2221}][X_3]$ salts, the $[N_{2221}][XY_2]$ salts have conductivities that were lower than the conductivity of $[N_{2221}][Br_3]$ but larger than those of $[N_{2221}][I_3]$. The most conductive interhalogen salt contains $[BrCl_2]^-$ (46.5 $mS\cdot cm^{-1}$), followed by $[IBr_2]^-$ (32.4 $mS\cdot cm^{-1}$) and $[ICl_2]^-$ (28.5 $mS\cdot cm^{-1}$). In the range of 70–75 °C, the conductivity of $[ICl_2]^-$ becomes larger than $[IBr_2]^-$, see Table 1.

The addition of the second salt [BMP][OTf] reduced the conductivity of trihalogen monoanions to values similar to [BMP][OTf] compared to their neat salt counterparts, see Figure 4. The [BMP][OTf] will interact with $[N_{2221}][X_3]$ through increased Coulombic interactions caused by the mixing of two

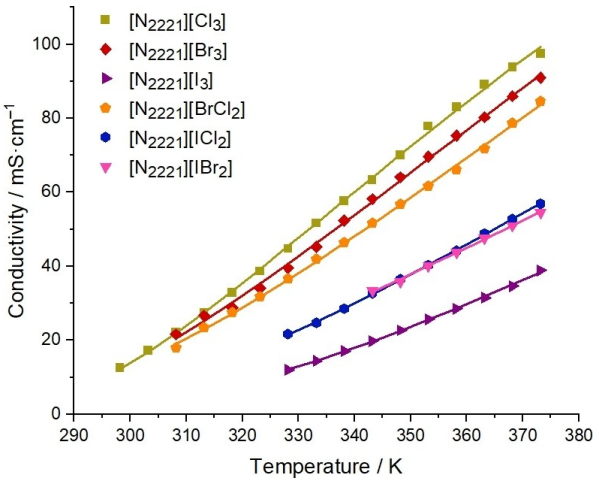

Figure 3. Temperature dependent conductivity of neat $[N_{2221}][X_3]$ and $[N_{2221}][XY_2]$ salts (X,Y = Cl, Br, and I).

Table 1. Conductivity of neat $[N_{2221}][X_3]$ and $[N_{2221}][XY_2]$ (X, Y = Cl, Br, and I) ILs and DSILs in [BMP][OTf] ($[X_3]^-/[XY_2]^-$, 0.5 M) at select temperatures.

Compound	Ionic Liquid	T [°C] and σ [mS·cm^{-1}] 25.0 °C	65.0 °C	100.0 °C
$[Cl_3]^-$	Neat	12.5	57.6	97.5
	[BMP][OTf]	2.5	15.5	34.5
$[Br_3]^-$	Neat	–	52.4	91.0
	[BMP][OTf]	2.2	12.5	29.4
$[I_3]^-$	Neat	–	17.0	38.9
	[BMP][OTf]	1.5	8.2	19.1
$[BrCl_2]^-$	Neat	–	46.5	84.6
	[BMP][OTf]	2.1	13.1	30.2
$[ICl_2]^-$	Neat	–	28.5	56.9
	[BMP][OTf]	2.4	12.4	27.4
$[IBr_2]^-$	Neat	–	32.4	54.6
	[BMP][OTf]	2.3	13.2	28.1
[BMP][OTf]	Neat	1.6	12.2	28.1

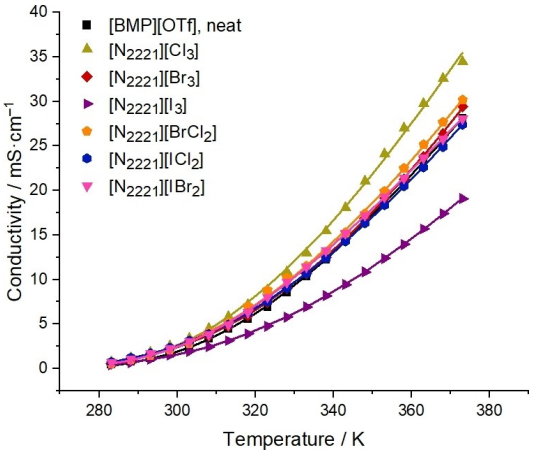

Figure 4. Temperature dependent conductivity of the DSILs $[N_{2221}][X_3]$ and $[N_{2221}][XY_2]$ (X, Y = Cl, Br, I) mixed with [BMP][OTf] ($[X_3]^-/[XY_2]^-$ 0.5 M). [BMP][OTf] is overlapped by the interhalogen monoanions.

ILs,[61] which lead to significantly reduced conductivities in the trihalogen monoanion salts.

The conductivity of the $[X_3]^-$ salts have the same conductivity trends as in the neat trihalogen monoanion ILs. At 25.0 °C, $[Cl_3]^-$ (2.5 mS·cm^{-1}) had the largest conductivity followed by $[Br_3]^-$ (2.2 mS·cm^{-1}) and $[I_3]^-$ (1.5 mS·cm^{-1}), which mirrors the neat $[X_3]^-$ ILs.

By increasing the temperature, the order of the most conductive trihalogen monoanion salts changes. Initially, at T = 25.0 °C, the conductivities are greatest as follows: $[Cl_3]^- > [ICl_2]^- > [IBr_2]^- > [Br_3]^- > [BrCl_2]^- >$ [BMP][OTf] $> [I_3]^-$. In comparison, at higher temperatures, T = 100.0 °C, the order changes slightly: $[Cl_3]^- > [BrCl_2]^- > [Br_3]^- > [IBr_2]^-$ = [BMP][OTf] $> [ICl_2]^- > [I_3]^-$.

2.2. Cyclic Voltammetry

To examine the redox behavior of the trihalogen monoanions under conditions reflecting their use for further applications[32,46] the neat ILs as well as DSILs were investigated.

The cyclic voltammograms of the neat $[Cl_3]^-$, $[Br_3]^-$, and $[I_3]^-$ ILs exhibit under anodic conditions relative to open circuit two redox processes, see Figure 5. We assign the first I, which either occurs as a wave (Br) or a shoulder (Cl, I), to the oxidation of X^- (Eq. 3) being in equilibrium with $[X_3]^-$ (Eq. 2). The second II appears as a current increase denoting the anodic end of the electrochemical window of the respective IL; we assign it to the oxidation of $[X_3]^-$ to X_2 (Eq. 4). This is in accordance to the processes, which have been thoroughly studied in a variety of solvents for X^-, and is observed in Cl^-, Br^-, and I^-:[16,18,30,40,51–53,62]

$$[X_3]^- \rightleftharpoons X^- + X_2 \quad (2)$$

$$3\,X^- \longrightarrow [X_3]^- + 2\,e^- \quad (3)$$

$$[X_3]^- \longrightarrow 1.5\,X_2 + e^- \quad (4)$$

The $E_{1/2}$ potential for the redox process I is given as the following approximation:

$$E_{1/2} = E_{c,p} + \frac{E_{a,p} - E_{c,p}}{2} \quad (5)$$

where $E_{c,p}$ and $E_{a,p}$ are the peak or shoulder (inflection point) potentials of the cathodic and anodic waves. In the Figures 5–9, $E_{c,p}$ and $E_{a,p}$ are displayed as their respective wave, I_c or I_a, respectively. The potential of the redox process II was set at 85 % of current relative to the baseline current of process I. This potential clearly is not comparable to $E_{1/2}$ values, for this reason we call this value E_{II}. The potentials of the redox processes are summarized in Table 2.

Due to the highly concentrated nature of the neat ILs, the observed potentials vary compared to the CVs in nonaqueous solvents,[30,50,51,55] or in other IL salt electrolyte solutions,[30,56] as discussed below.

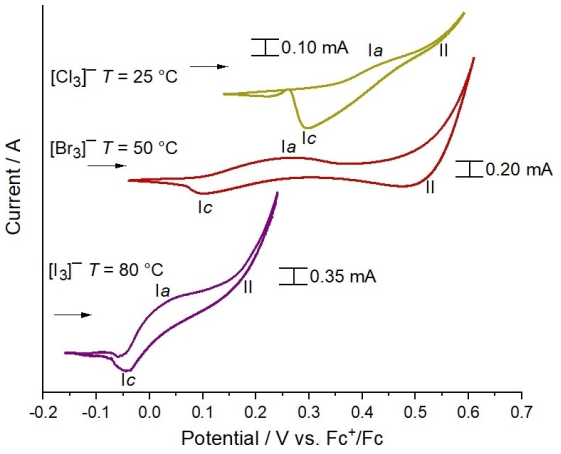

Figure 5. Cyclic voltammograms of neat $[N_{2221}][X_3]$ (X = Cl, Br, I). Scan rate of 10 mV·s^{-1}; the arrow represents scan direction and the zero current; second cycle.

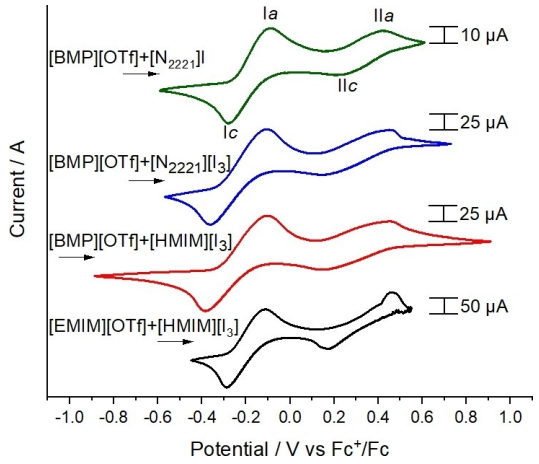

Figure 6. Cyclic voltammograms of [HMIM][I_3] in [EMIM][OTf] ($[I_3]^-$ 0.3 M), in [BMP][OTf] ($[I_3]^-$ 0.34 M), and [N_{2221}][I_3] (0.5 M) and [N_{2221}]I (0.5 M) in [BMP][OTf]. Scan rate of 10 mV·s^{-1}; the arrow represents scan direction and the zero current, second cycle.

Cyclic Voltammetry of DSIL $[N_{2221}]^+[X_3]^-/[XY_2]^-$ in [BMP][OTf]:

Recently, Bentley et al. had determined the standard potentials of $[I_3]^-$ and $[ICl_2]^-$ in a variety of ILs, specifically [EMIM][I_3] in [EMP][OTf].[15,30] The $[EMIM]^+$ cation is stable in combination with the $[I_3]^-$ monoanion, whereas the $[Cl_3]^-$ monoanion was found to chlorinate the alkyl chains of such cations due to a higher oxidation potential.[20]

Therefore, the $[N_{2221}]^+$ cation and supporting electrolyte [BMP][OTf] was used to determine the trihalogen monoanion potentials. A comparison of the CV results between the imidazolium class cation $[HMIM]^+$ and $[N_{2221}]^+$ with I^- and the $[I_3]^-$ monoanion in the supporting electrolytes $[EMIM]^+/[BMP]^+[OTf]^-$ is shown in Figure 6.

Starting from the imidazolium salt [HMIM][I_3] in [EMIM][OTf] two redox processes belonging to the $I^-/[I_3]^-$ (I, −0.20 V) and $[I_3]^-/I_2$ (II, 0.24 V) were observed and the curve characteristic is comparable to previous studies.[30] [HMIM][I_3] in [BMP][OTf] and [N_{2221}][I_3] also have similar redox potentials varying up to 0.04 V.

The CV of [N_{2221}]I in [BMP][OTf] indicates due to its similarity to that of [N_{2221}][I_3] in [BMP][OTf] two issues. First, the equilibrium between $[I_3]^-$ and $I^- + I_2$ according to Eq. 2. Second, the dependence of the I-content in the solution on the curve shape. The peaks of both waves Ia and Ic as well as IIa and IIc is by about 0.1 V more separated in case of solutions containing more I ($[I_3]^-$).

With regards to the two wave mechanism of $X^-/[X_3]^-/X_2$, two complete mechanisms have been proposed recently, a 4 step CECE mechanism from Bentley et al. (X = I)[30] and an 11 step ECEC mechanism from Bard et al. (X = Br).[55] The proposed mechanisms of Bard and Bentley were simulated to the CV of [N_{2221}][I_3] in [BMP][OTf]. However, while the resulting simulated curves were similar in shape, the simulations were not detailed enough to form a sufficient statement about the mechanism. The rather high concentration of the electrolyte solution or of the neat substance likely, make the measurement unfeasible.

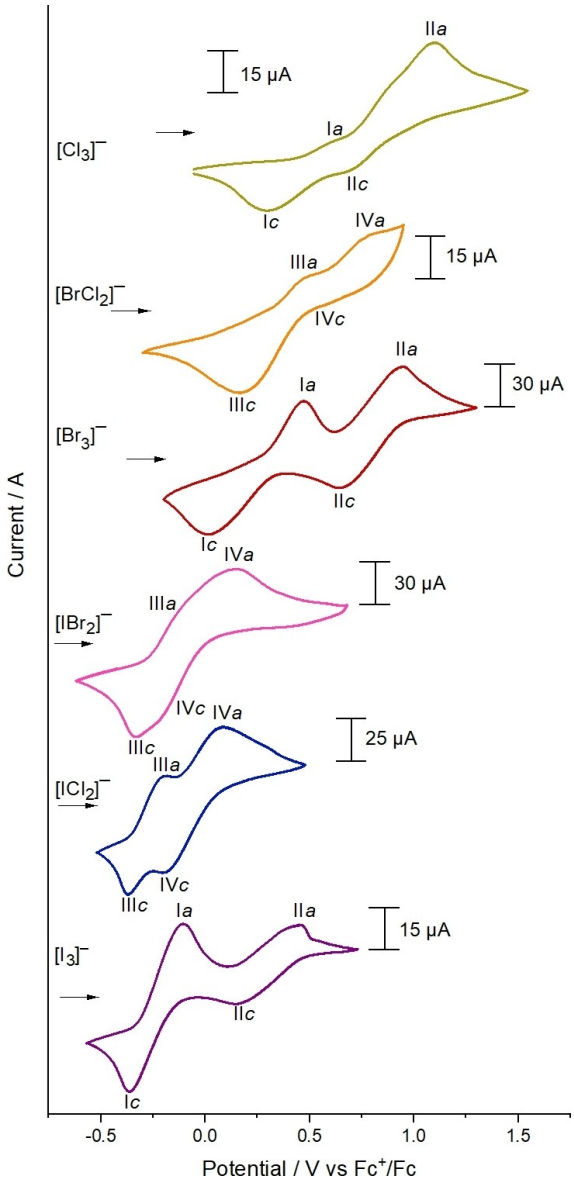

Figure 7. Cyclic voltammograms of [N_{2221}][X_3] and [N_{2221}][XY_2] (X, Y = Cl, Br, I) in [BMP][OTf] ($[X_3]^-/[XY_2]^-$ 0.5 M). Scan rate of 10 mV·s^{-1}; the arrow represents scan direction and the zero current, second cycle.

Table 2. The redox potentials of neat [N_{2221}][X_3] (X = Cl, Br, I). Explanations see text.

Ionic Liquid	Temperature [°C]	$E_{1/2}$ or E_{II} (V vs Fc^+/Fc) **I** ($X^-/[X_3]^-$)	**II** ($[X_3]^-/X_2$)
[N_{2221}][Cl_3]	25	0.37	0.55
[N_{2221}][Br_3]	50	0.18	0.52
[N_{2221}][I_3]	80	−0.02	0.18

Therefore, in this work, only the general mechanism that has been agreed upon in literature[30,56,58] and presented in Eq. 3 and 4 are presented. The focus will be placed on the oxidative power of the concentrates $[X_3]^-$ species in the [BMP][OTf] IL electrolyte solution.

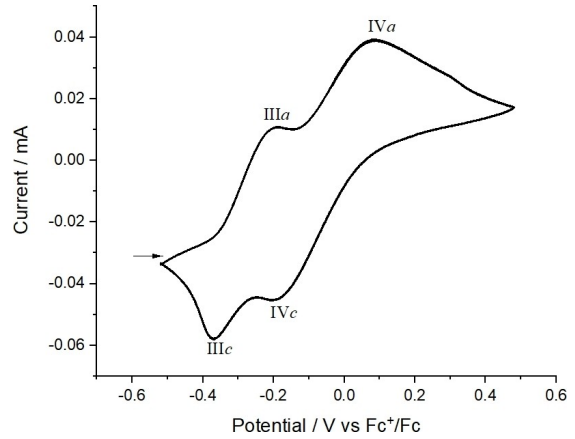

Figure 8. Cyclic voltammogram of $[N_{2221}][ICl_2]$ in [BMP][OTf] ($[ICl_2]^-$ 0.5 M). Scan rate of 10 mV·s^{-1}; the arrow represents scan direction, second cycle.

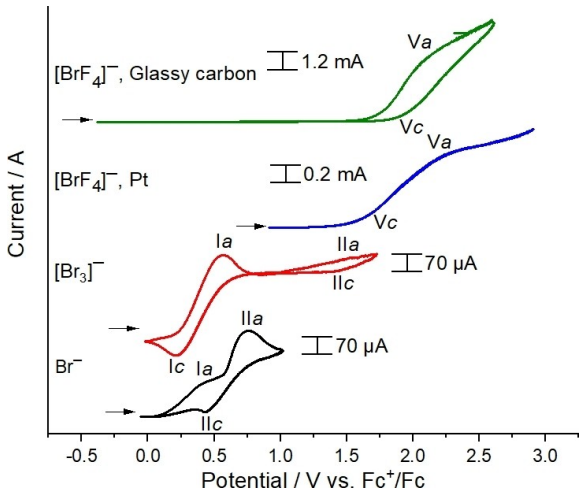

Figure 9. Cyclic voltammogram of $[N_{2221}]^+Br^-/[Br_3]^-/[BrF_4]^-$ (50 mM) in MeCN. The working electrodes are a planar Pt electrode (1 mm diameter) and a planar glassy carbon electrode (2 mm diameter) Measured at a temperature of 0 °C; scan rate of 100 mV s$^-$; and the arrow represents scan direction and the zero current, second cycle.

Due to $[N_{2221}][I_3]$ in [BMP][OTf] displaying similar redox potentials independent of the cation and the supporting electrolyte, the cation $[N_{2221}]^+$ and the supporting electrolyte [BMP][OTf] will be used for the other trihalogen monoanions.

Based upon the trihalogen monoanion, the redox potential for wave **I** varies significantly. The strongest oxidizing agent, based on $X^-/[X_3]^-$, being $[Cl_3]^-$ (0.46 V) followed by $[Br_3]^-$ (0.25 V) then $[I_3]^-$ (−0.24 V) (Figure 7, Table 3).

For $[Cl_3]^-$ two observable oxidation steps for the $[Cl_3]^-/Cl_2$ occurred for the scan rate of 10 mV·s^{-1}. The initial shoulder at 0.86 V disappears at scan rates of 1000 m V·s^{-1} (Figure S23). The resulting shoulder at 0.86 V likely results due to the influence of the redox couples **I** and **II** on each other. The calculated $E_{1/2}$ value for wave **II** of $[Cl_3]^-$ should therefore be used with caution.

The interhalogen monoanions have differing electrochemistry compared to $[X_3]^-$, as seen in the CVs of $[ICl_2]^-$, $[IBr_2]^-$, and $[BrCl_2]^-$. $[ICl_2]^-$ in [BMP][OTf] has 2 different quasi-irreversible redox processes, see Figure 8. The liquid phase equilibrium of interhalogen monoanions and the electrochemical products concerning them has been continually investigated since Popov in 1958.[15,17,51,63] A recently reported mechanism for the electrochemical oxidation of the I^- and Cl^- in $[EMIM]^+$ bis (trifluoromethanesulfonyl)imide consists of a combination of electrochemical-chemical (EC) mechanisms and the production of several interhalogen monoanion species.[15,30]

Despite, $[ICl_2]^-$ being a molecule composed of two halogens, the possible resulting mixtures due to the various chemical rearrangements and electron transfer reactions lead to a complex mechanism. Since the variety of synthesized interhalogens of type XY, XY_3, XY_5, or $[X_aY_b]^-$ (a = 1–5, b = 2–6)[13,64] is rather large and the determination of the mechanism becomes complicated. Therefore, in the present work, we postulate a simplified mechanism for the interhalogens of type $[XY_2]^-$. In a future work we will perform Raman spectroelectrochemical measurements to help elucidate the electrochemical mechanism of the $[XY_2]^-$ species.

On the basis of $[XY_2]^-$ two redox processes where observed. The proposed oxidation of III starts with the equilibrium between $[XY_2]^-$ and I^- and Cl^- (Eq. 6) followed by the oxidation of X^- to $[X_3]^-$ (Eq. 7). The reasoning for this oxidation stems from the comparison between trihalogen monoanions. The redox potentials of I are very similar to the shoulder of III, based upon the central halogen atom, see Figure 7. The species $[N_{2221}][I_3]$ for I has a similar potential (−0.24 V) to those of III for $[N_{2221}][ICl_2]$ (−0.28 V) and $[N_{2221}][IBr_2]$ (−0.24 V). This can also be expanded to $[Br_3]^-$ (0.25 V) and $[BrCl_2]^-$ (0.33 V).

$$[XY_2]^- \rightleftharpoons X^- + 2\,Y^- \quad (6)$$

$$3\,X^- \longrightarrow [X_3]^- + 2\,e^- \quad (7)$$

However, the second redox couple of $[ICl_2]^-$ and $[IBr_2]^-$ (IV) differed significantly from $[I_3]^-$ (II).

The subsequent oxidation at IV, is also analogous to $[X_3]^-$, with the oxidation of the trihalide species $[XY_2]^-$ to $[XY_4]^-$ and

Table 3. The $E_{1/2}$ redox potentials of DSILs $[Cat][X_3]$ and $[Cat][XY_2]$ (X and Y = Cl, Br, I) in [BMP][OTf] or [EMP][OTf] ($[X_3]^-/[XY_2]^-$ 0.5 M).

Ionic Liquid	Additive Salt	$E_{1/2}$ (V vs Fc^+/Fc) **I** ($X^-/[X_3]^-$)	**II** ($[X_3]^-/X_2$)
$[N_{2221}][Cl_3]$	[BMP][OTf]	0.46	0.90
$[N_{2221}][Br_3]$	[BMP][OTf]	0.25	0.81
$[N_{2221}][I_3]$	[BMP][OTf]	−0.24	0.31
$[N_{2221}]I$	[BMP][OTf]	−0.18	0.33
$[HMIM][I_3]^a$	[BMP][OTf]	−0.24	0.31
$[HMIM][I_3]^b$	[EMIM][OTf]	−0.20	0.32
		III ($X^-/[X_3]^-$)	**IV** ($[ICl_2]^-/ICl_3 + [Cl(ICl)_2]^-$)
$[N_{2221}][BrCl_2]$	[BMP][OTf]	0.33	0.70
$[N_{2221}][IBr_2]$	[BMP][OTf]	−0.24	−0.02
$[N_{2221}][ICl_2]$	[BMP][OTf]	−0.28	−0.05

[a] $[I_3]^-$ 0.34 M, [b] $[I_3]^-$ 0.3 M

X_2 (Eq 8). With the oxidation IV_a of $[XY_2]^-$ occurring at lower potentials than $[X_3]^-$. In the case of $[ICl_2]^-$ and $[IBr_2]^-$ the formation of I_2 at the WE could explain the drop in the anodic current.

$$2\,[XY_2]^- \longrightarrow [XY_4]^- + 0.5\,X_2 + e^- \quad (8)$$

Both CVs of the trihalogen monoanions as neat and DSIL salts were measured and found to undergo the same redox processes, although at slightly differing potentials. The difference in potential between the neat IL and DSIL is caused by difference between electrolyte solution of the trihalogen monoanions. The addition of [BMP][OTf] likely influences the Coulombic interactions between trihalogen monoanions, resulting in shifted potentials from the neat salt to potentials similar to previous reports.[30]

Chemical oxidation of metallocenes with trihalogen monoanions: To determine the oxidation strength of the trihalogen monoanions based upon chemical means, and not to elucidate the electrochemical mechanism, a variety of metallocenes ($TiCp_2Cl_2$, $RuCp_2$, AcFc (acetylferrocene), Fc, $FcCp^*_2$ (decamethylferrocene), and $CoCp_2$) with differing potentials,[65–69] see Table 4, were added to $[N_{2221}][X_3]$ and $[N_{2221}][XY_2]$ (X,Y = Cl, Br, I) in MeCN. The benefit to metallocenes is that the potential is tunable based upon the metal center and the substituents on the cyclopentadienyl ring.[66] Addition of the polyhalogen will act as an oxidizing agent, a one electron process should occur.[68]

A visible color change will be observed, if the diluted (MeCN) trihalogen monoanion oxidizes the metallocene. When no reaction occurred the color remained unchanged. The absorption and change of absorption wavelengths were further examined via UV-*vis* spectroscopy to monitor the metallocene oxidation, see SI Figures S9–15 and Table S1 in the Supporting Information. The following series displays the oxidation power of the investigated trihalogen monoanions, where any trihalogen monoanion will oxidize the species to its left: $CoCp_2 < FcCp^*_2 < Fc < [I_3]^- < [ICl_2]^- < [IBr_2]^- < [Br_3]^- < AcFc < RuCp_2 < [BrCl_2]^- < [Cl_3]^-$.

According to the recorded UV-vis spectra $CoCp_2$, $FcCp^*_2$, and Fc were oxidized by all trihalogen monoanions. Only $[BrCl_2]^-$ and $[Cl_3]^-$ had sufficient oxidation strength to oxidize $RuCp_2$ and AcFc. Lastly, $TiCp_2Cl_2$ did not react with any of the trihalogen monoanions.[69]

The $[ClF_4]^-/[BrF_4]^-/[IF_4]^-$ species are well known structurally,[5–7,70] but the electrochemical characterization is currently lacking in the literature. Therefore, the CVs of $[N_{2221}]Br$ and $[N_{2221}][Br_3]$ were measured under the same conditions (50 mM, MeCN, $T = 0\,^\circ C$) to adequately compare other known bromide monoanions to the redox processes of $[N_{2221}][BrF_4]$, see Figure 9.

The redox processes of Br^- and $[Br_3]^-$ undergo the same redox processes as in the previously described (see Equations 2 and 3). In regards to Br^- for I ($Br^-/[Br_3]^-$), only the anodic wave was visible as a shoulder at 0.40 V. The second wave was irreversible with the anodic II*a* ($[Br_3]^-/Br_2$) occurring at 0.75 V and cathodic wave II*b* at 0.43 V, see Table 5.

The $[Br_3]^-$ species also undergoes the an irreversible reaction from wave **I** ($Br^-/[Br_3]^-$) with a peak separation of 350 mV. The second redox couple ($[Br_3]^-/Br^-$) is only quasi-reversible at 1.47 V. The results for Br^- and $[Br_3]^-$ yielded similar results to Popov and Geske's original study of Br^- and $[Br_3]^-$ in MeCN.[51]

The fluoride based $[BrF_4]^-$ is a strong oxidizing agent and can be used as a brominating agent in organic reactions,[71] and can oxidize Pt to form $[PtF_4]^{2-}$ or $[PtF_6]^{2-}$ at $T > 400\,^\circ C$.[72] Using the Pt WE, a single irreversible redox couple was observed, V. The change in current slope forming two shoulders are denoted as V*c* (1.71 V) and V*a* (2.21 V), and were used to determine the $E_{1/2}$ potential (1.96 V). Based on the CV a first postulate was the oxidation of Pt to $[PtF_4]^{2-}$ or $[PtF_6]^{2-}$. However, upon changing the WE to glassy carbon (GC), the two shoulders V*a* (1.93 V) and V*c* (2.05 V) were measured with similar potentials to the Pt electrode. Therefore, Pt is unlikely oxidized during V, rather a different redox couple exists.

To the redox couple of $[BrF_4]^-$, we postulate two separate mechanisms, one based on a CEC mechanism and the other on an CECC mechanism. Both mechanisms yield BrF_5.

The CEC mechanism starts with the equilibrium between $[BrF_4]^-$ to BrF_3 and F^- (Eq. 9). The dissociation of $[I_3]^-$ and $[Br_3]^-$ have been proposed previously,[30,56,57] and could therefore be applied to the interhalogen $[BrF_4]^-$ mechanism. The second step is the subsequent oxidation of F^- to F_2 (Eq. 10) at 2.21 V (Va) at the Pt WE surface. Barrès et al. have demonstrated that the oxidation of F^- to F_2 from $NEt_3 \cdot 3HF$ in MeCN occurs at 2.2 and 3 V vs SCE depending on if the F^- is adsorbed at a Pt electrode or in solution, respectively.[73] The anodic shoulder is at a relatively large potential, so the oxidation to F_2 is possible. The last step is the chemical reaction between F_2 and BrF_3 to BrF_5 (Eq. 11). Gross and Meinert have demonstrated that BrF_5 is stable in acetonitrile,[74] thus the end product seems possible.

$$[BrF_4]^- \rightleftharpoons BrF_3 + F^- \quad (9)$$

Table 4. Redox potentials of various metallocenes (V vs Fc).

Half-reaction	Electrolyte solution	$E^{o\prime}$ [V]
$RuCp_2 \rightleftharpoons [RuCp_2]^+ + e^-$	CH_2Cl_2/0.05 M $BArF_{24}$	0.56[68]
$RuCp_2 \rightleftharpoons [RuCp_2]^+ + e^-$	CH_2Cl_2/0.1 M TFAB	0.41[68]
$AcFc \rightleftharpoons [AcFc]^+ + e^-$	MeCN	0.26[66,67]
$Fc \rightleftharpoons [Fc]^+ + e^-$	MeCN	0[65]
$FcCp^*_2 \rightleftharpoons [FcCp^*_2]^+ + e^-$	MeCN	−0.59[65]
$TiCp_2Cl + Cl^- \rightleftharpoons TiCp_2Cl_2 + e^-$	THF/0.2 M Bu_4NPF_6	−1.27[69]
$CoCp_2 \rightleftharpoons [CoCp_2]^+ + e^-$	CH_2Cl_2	−1.33[65]

Table 5. The $E_{1/2}$ redox potentials of $[N_{2221}]^+Br^-/[Br_3]^-/[BrF_4]^-$ (50 mM) in MeCN.

Ionic Liquid	Working Electrode	$E_{1/2}$ (V vs Fc^+/Fc) **I** ($Br^-/[Br_3]^-$)	**II** ($[Br_3]^-/Br_2$)	**V** ($[BrF_4]^-/BrF_5$)
$[N_{2221}]Br$	Pt	0.40[a]	0.59	–
$[N_{2221}][Br_3]$	Pt	0.39	1.47	–
$[N_{2221}][BrF_4]$	Pt	–	–	1.96
$[N_{2221}][BrF_4]$	GC	–	–	1.99

[a] $E_{a,p}$

$$2\,F^- \longrightarrow F_2 + 2\,e^- \quad (10)$$

$$F_2 + BrF_3 \longrightarrow BrF_5 \quad (11)$$

The CECC mechanism also starts with the dissociation of $[BrF_4]^-$ to BrF_3 and F^- (Eq. 9) followed by the oxidation of F^- to F_2 (Eq. 10). However the F_2 would subsequently react with $[BrF_4]^-$ to form $[BrF_6]^-$ (Eq. 12). The electrochemically produced species $[BrF_6]^-$ is stable in MeCN when prepared with $[N(CH_3)_4]^+$ F^- and $CsBrF_4$.[5] Thus, the species formation seems logic. The last step is the dissociation of F^- from $[BrF_6]^-$ to form BrF_5 (Eq. 13).

$$F_2 + [BrF_4]^- \longrightarrow [BrF_6]^- \quad (12)$$

$$[BrF_6]^- \rightleftharpoons BrF_5 + F^- \quad (13)$$

The reduction of the newly generated BrF_5 would proceed in reverse of either the proposed mechanisms. Comparing the CVs between the GC and Pt WEs indicates the reduction step occurs independently of the electrode material.

After the CV a ^{19}F NMR was measured and the strongest signal ($\delta = -35.54$ ppm) was assigned to $[BrF_4]^-$, concurring with a previous report.[5]

As an interesting aside, the introduction of Fc to the solution as an external redox couple did not result in the chemical destruction of Fc. Rather, Fc was oxidized to Fc^+ in solution turning a dark blue-green color, forming the salt $[Fc]^+$ $[BrF_4]^-$. Other metallocenes may also form stable ionic compounds with $[BrF_4]^-$.

3. Conclusions

Conductivities and redox potentials of the $[N_{2221}][X_3]$ and $[XY_2]^-$ trihalogen monoanions were determined. The conductivity of the neat salts indicates a clear trend of the respective homologues, with lighter $[Cl_3]^-$ having the largest and heavier $[I_3]^-$ the lowest conductivity. The interhalogen monoanions conductivities of $[ICl_2]^-$, $[IBr_2]^-$, and $[BrCl_2]^-$ were found to range between $[Br_3]^-$ and $[I_3]^-$. The DSIL mixtures with [BMP][OTf] displayed significantly reduced conductivity for all salts. Interestingly, the conductivity measurements of the DSIL salts revealed a different temperature dependence for the trihalogen monoanions. For instance, $[ICl_2]^-$ was more conductive than $[IBr_2]^-$ at 25 °C, but the reverse is true at 100 °C.

The experimental potentials for the neat polyhalogen monoanions were measured via cyclic voltammetry and containing useful information for the oxidation of various compounds. Of the homohalogens $[Cl_3]^-$ is the strongest oxidizing agent followed by $[Br_3]^-$ and $[I_3]^-$. The mechanism regarding the interhalogen system is not well known and a simple mechanism is proposed. However, the mechanism for the interhalogen system is complex due to the formation of various interhalogen compounds. Future work using Raman spectroelectrochemical techniques will be used to further identify the mechanism.

The interhalogen oxidation strength was also compared chemically by reacting the trihalogen monoanions with various metallocenes in acetonitrile. $[Cl_3]^-$ and $[BrCl_2]^-$ were able to oxidize all tested metallocenes, including $RuCp_2$. In comparison, Fc was oxidized by all investigated trihalogen monoanions.

A first look into the electrochemistry of the fluorobromate monoanion, $[BrF_4]^-$, was examined via cyclic voltammetry in acetonitrile. One quasi-reversible redox couple was found, which is proposed to be associated with $[BrF_4]^-/BrF_5$. Two separate mechanisms for the redox couple have been proposed both based on the dissociation of $[BrF_4]^-$ to F^- and subsequent oxidation to F_2. Additionally, the oxidation potential of $[BrF_4]^-$ is significantly greater than that of both $[Br_3]^-$ and Br^-. Based on the proposed redox couple in $[BrF_4]^-$ a similar redox couple could exist in $[ClF_4]^-$ and $[IF_4]^-$.

Experimental Section

Reagents

All experiments were performed using standard Schlenk techniques using argon gas. The following chemicals were purchased [HMIM]I (*Io-li-tec*, 99%), [BMP][OTf] (*Merck*, TH_Geyer CM, 99%), [EMIM][OTf] (*Solvent Innovations*, 99%), $[N_{2221}]Cl$ (*TCI*, 98.0%), $[N_{2221}]Br$ (*Fluorochem*, 95%), Cl_2 (*Linde Gas*, 2.5 purity), Br_2 (*Acros Organics*, 99+%) subsequently condensed onto activated A3 molecular sieves, I_2 (*Riedel-de Haën*, 99.8%), ferrocene (Fc, *Fluorochem*, 99.9%), ruthenocene ($RuCp_2$) (*Abcr*, 99.9%-Ru), acetyl ferrocene (AcFc, *Fluka*, 95% CHN), cobaltecene ($CoCp_2$, *Sigma*), decamethylferrocene (FcCp*2, Sigma, 97%). $[N_{2221}]I$ was prepared according to literature.[75]

Preparation of the trihalogen monoanion ILs occurred by adding (I_2) or condensing (Cl_2, Br_2) one equiv. of X_2 (Cl, Br, or I) to one equiv. of their respective halogen salt $[N_{2221}]X$. To obtain the homogeneous salt ($[N_{2221}][X_3]/[XY_2]$), the mixture was liquified at temperatures not exceeding 120 °C. For exact preparation of the trihalogen monoanion ILs, please see supporting information. The double salt ionic liquid mixtures (DSIL) of [Cat.][X_3] and [Cat.][XY_2] with [BMP][OTf] have a concentration of 0.5 M, except where noted.

UV/Vis and Raman Spectroscopy and Conductivity Methods

The UV-*vis* spectra were recorded using a Perkin Elmer Lambda 465 photometer with deuterium and tungsten lamps. A quartz cuvette with a Rydberg-Schlenk attachment was used to maintain an argon atmosphere. Raman-spectra were measured at −40 °C or *r.t.* using a MultiRAM FT-Raman-Spectrometer by Bruker, equipped with a Nd:YAG-laser and a Ge-detector cooled with liquid nitrogen (1064 nm, 30–450 mW, 64–256 scans, resolution: 2 cm). The temperature dependent conductivity was measured using the *Mettler Toledo AG* SevenCompact S230 Conductivity Meter and INLAB® 710 sensor. Measurements were performed under argon counter flow. The temperature was gradually raised $T = 8$–100 °C in an oil bath.

Electrochemistry

A three electrode configuration and *Bio-Logic* SP-300 potentiostat was used. The working electrode (WE) and counter electrode (CE)

were planar Pt electrodes (1 mm diameter). The electrodes were rinsed with HNO_3, isopropanol, acetone and ethyl acetate. Subsequent Pt electrode activation occurred by polishing with 0.1 μm diamond polish (*Zimmer and Peacock*) rinsed with distilled water followed by 0.05 μm alumina polish (*Zimmer and Peacock*) and rinsed with distilled water. Excess alumina was removed in a sonication bath in distilled water. The electrode was subsequently cycled between the oxygen and hydrogen evolution potentials in 0.1 M H_2SO_4 as described in literature.[76] The Ag reference electrode (RE) was prepared based on literature,[15,30] by taking a Ag wire dipped into the IL or DSIL electrolyte fill solution in a fritted RE (alumina frit, *Ionode*, EChem-Ref-R-SR). The REs were allowed an equilibrium time of 12 h to 5 d, depending on the salt. All experiments were performed under argon. All CVs presented are of the second cycle, as negligible deviation from the first cycle was recorded.

To measure the CVs of neat $[N_{2221}][Br_3]$ and $[N_{2221}][I_3]$ the temperature was raised to 50 °C and 80 °C, respectively, to keep the salt as a melt. The DSILs were all in the liquid phase at room temperature, making the measurement of all trihalogen monoanions feasible.

$[N_{2221}][BrF_4]$ (50 mM) was prepared in MeCN at −40 °C and the cyclic voltammogram (CV) measured at 0 °C. The electrochemical cell was a three electrode set-up with the WE, CE and RE being planar Pt electrodes (1 mm diameter) and a planar glassy carbon WE (2 mm diameter, *HTW*, Sigradur G) coated in perfluoroalkoxy alkanes (PFA). The transfer of solution was performed at −40 °C by placing a PFA tube into the solution and applying a slight overpressure via argon gas. Thus, pumping the liquid into the cell. The cell design and inert transfer of solution to the cell is based on literature.[77]

CV simulations performed using DigiElch-Professional v8.F (ElchSoft.com).

Safety Precautions

Addition of sufficient amounts of Fc to neat $[N_{2221}][Cl_3]$ under Ar is strongly exothermic and produces smoke. If exposed to air, the mixture ignites at *r.t.* Additionally, higher concentrations of $[BrF_4]^-$ than given in this paper can lead to gas evolution of F_2, leading to explosions. At higher concentrations of $[BrF_4]^-$ it probably reacts vigorously upon contact with Fc in a similar fashion to neat $[Cl_3]^-$.

Acknowledgements

We thank the priority program SPP 1708 for financial support and Dr. Valentin Radtke for scientific discourse.

Conflict of Interest

The authors declare no conflict of interest.

Keywords: polyhalogen monoanions · cyclic voltammetry · ionic liquids · conductivit · tetrafluorobromate

[1] F. D. Chattaway, G. Hoyle, *J. Chem. Soc. Trans.* **1923**, *123*, 654.
[2] J. Taraba, Z. Zak, *Inorg. Chem.* **2003**, *42*, 3591.
[3] a) Z. Sun, K. B. Moore, J. G. Hill, K. A. Peterson, H. F. Schaefer, R. Hoffmann, *J. Phys. Chem. B* **2018**, ; b) A. W. Coleman, C. M. Means, S. G. Bott, J. L. Atwood, *J. Crystallogr. Spectrosc. Res.* **1990**, *20*, 199; c) T. Bernstein, F. H. Herbstein, *Acta Crystallogr. B* **1968**, *24*, 1640.
[4] A. I. Popov, in: *Halogen Chemistry* (Ed.: V. Gutmann), Academic Press, New York, **1967**, pp. 225–264.
[5] W. W. Wilson, K. O. Christe, *Inorg. Chem.* **1989**, *28*, 4172.
[6] X. Zhang, K. Seppelt, *Z. Anorg. Allg. Chem.* **1997**, *623*, 491.
[7] S. Ivlev, P. Woidy, V. Sobolev, I. Gerin, R. Ostvald, F. Kraus, *Z. Anorg. Allg. Chem.* **2013**, *639*, 2846.
[8] a) B. S. Ault, L. Andrews, *Inorg. Chem.* **1977**, *16*, 2024; b) G. L. Breneman, R. D. Willett, *Acta Crystallogr.* **1967**, *23*, 334.
[9] L. F. Olsson, *Inorg. Chem.* **1985**, *24*, 1398.
[10] K. Sonnenberg, P. Pröhm, N. Schwarze, C. Müller, H. Beckers, S. Riedel, *Angew. Chem. Int. Ed.* **2018**, *57*, 9136.
[11] B. Schmidt, K. Sonnenberg, H. Beckers, S. Steinhauer, S. Riedel, *Angew. Chem. Int. Ed.* **2018**, *57*, 9141.
[12] H. Haller, S. Riedel, *Z. Anorg. Allg. Chem.* **2014**, *640*, 1281.
[13] R. W. G. Wyckoff, *J. Am. Chem. Soc.* **1920**, *42*, 1100.
[14] Y.-Q. Wang, Z.-M. Wang, C.-S. Liao, C.-H. Yan, *Acta Crystallogr. C* **1999**, *55*, 1503.
[15] C. L. Bentley, A. M. Bond, A. F. Hollenkamp, P. J. Mahon, J. Zhang, *Anal. Chem.* **2016**, *88*, 1915.
[16] J. Grossi, J. J. Kohanoff, N. J. English, E. M. Bringa, M. G. Del Pópolo, *J. Phys. Chem. B* **2017**, *121*, 6436.
[17] T. X. Wang, M. D. Kelley, J. N. Cooper, R. C. Beckwith, D. W. Margerum, *Inorg. Chem.* **1994**, *33*, 5872.
[18] J. Xu, N. S. Georgescu, D. A. Scherson, *J. Electrochem. Soc.* **2014**, *161*, H392–H398.
[19] a) I. D. Gorokh, S. A. Adonin, A. S. Novikov, M. N. Sokolov, D. G. Samsonenko, V. P. Fedin, *J. Mol. Struct.* **2019**, *1179*, 725; b) I. D. Gorokh, S. A. Adonin, M. N. Sokolov, P. A. Abramov, I. V. Korolkov, E. Y. Semitut, V. P. Fedin, *Inorg. Chim. Acta* **2018**, *469*, 583.
[20] R. Brückner, H. Haller, S. Steinhauer, C. Müller, S. Riedel, *Angew. Chem. Int. Ed.* **2015**, *54*, 15579.
[21] a) S. A. Adonin, M. A. Bondarenko, A. S. Novikov, P. A. Abramov, P. E. Plyusnin, M. N. Sokolov, V. P. Fedin, *Z. Anorg. Allg. Chem.* **2019**, *645*, 1141; b) S. A. Adonin, M. A. Bondarenko, A. S. Novikov, P. E. Plyusnin, I. V. Korolkov, M. N. Sokolov, V. P. Fedin, *Inorg. Chim. Acta* **2020**, *502*, 119278; c) S. A. Adonin, M. A. Bondarenko, A. S. Novikov, P. A. Abramov, P. E. Plyusnin, M. N. Sokolov, V. P. Fedin, *CrystEngComm* **2019**, *21*, 850.
[22] S. A. Adonin, I. D. Gorokh, A. S. Novikov, D. G. Samsonenko, P. E. Plyusnin, M. N. Sokolov, V. P. Fedin, *Dalton Trans.* **2018**, *47*, 2683.
[23] A. N. Usoltsev, S. A. Adonin, A. S. Novikov, M. N. Sokolov, V. P. Fedin, *J. Coord. Chem.* **2019**, *72*, 1890.
[24] A. N. Usoltsev, S. A. Adonin, A. S. Novikov, P. A. Abramov, M. N. Sokolov, V. P. Fedin, *CrystEngComm* **2020**, *22*, 1985.
[25] H. Haller, M. Ellwanger, A. Higelin, S. Riedel, *Z. Anorg. Allg. Chem.* **2012**, *638*, 553.
[26] H. Haller, M. Hog, F. Scholz, H. Scherer, I. Krossing, S. Riedel, *Z. Naturforsch.* **2013**, *68b*, 1103.
[27] H. Haller, *Dissertation*, Albert-Ludwigs-Universität Freiburg, Freiburg, **2014**.
[28] a) D. S. Silvester, R. G. Compton, *Z. Phys. Chem.* **2006**, *220*, 1247; b) G. Adamová, R. L. Gardas, M. Nieuwenhuyzen, A. V. Puga, L. P. N. Rebelo, A. J. Robertson, K. R. Seddon, *Dalton Trans.* **2012**, *41*, 8316.
[29] J. S. Wilkes, J. A. Levisky, R. A. Wilson, C. L. Hussey, *Inorg. Chem.* **1982**, *21*, 1263.
[30] C. L. Bentley, A. M. Bond, A. F. Hollenkamp, P. J. Mahon, J. Zhang, *J. Phys. Chem. C* **2015**, *119*, 22392.
[31] S. Zhang, N. Sun, X. He, X. Lu, X. Zhang, *J. Phys. Chem. Ref. Data* **2006**, *35*, 1475.
[32] B. Schmidt, S. Ponath, J. Hannemann, P. Voßnacker, K. Sonnenberg, M. Christmann, S. Riedel, *Chem. Eur. J.* **2020**, *25*, 15183.
[33] H. Keil, K. Sonnenberg, C. Müller, R. Herbst-Irmer, H. Beckers, S. Riedel, D. Stalke, *Angew. Chem. Int. Ed.* **2021**, *60*, 2569, 132, 1.
[34] T. M. Beck, H. Haller, J. Streuff, S. Riedel, *Synthesis* **2014**, *46*, 740.
[35] M. E. Easton, P. Turner, A. F. Masters, T. Maschmeyer, *RSC Adv.* **2015**, *5*, 83674.
[36] M. Schneider, G. P. Rajarathnam, M. E. Easton, A. F. Masters, T. Maschmeyer, A. M. Vassallo, *RSC Adv.* **2016**, *6*, 110548.
[37] M. Watanabe, M. L. Thomas, S. Zhang, K. Ueno, T. Yasuda, K. Dokko, *Chem. Rev.* **2017**, *117*, 7190.
[38] R. Kawano, M. Watanabe, *Chem. Commun.* **2005**, *16*, 2107.
[39] S. Park, D. H. Han, J. G. Lee, T. D. Chung, *Appl. Energy Mater.* **2020**, *3*, 5285.
[40] C. E. S. Côrtes, R. B. Faria, *Inorg. Chem.* **2004**, *43*, 1395.

[41] C. L. Bentley, A. M. Bond, A. F. Hollenkamp, P. J. Mahon, J. Zhang, *J. Phys. Chem. C* **2014**, *118*, 22439.
[42] I. Rubinstein, M. Bixon, E. Gileadi, *J. Phys. Chem.* **1980**, *84*, 715.
[43] I. Rubinstein, E. Gileadi, *J. Electroanal. Chem. Interfacial Electrochem.* **1980**, *108*, 191.
[44] A. Yao, F. Qu, Y. Liu, G. Qu, H. Lin, S. Hu, X. Wang, T. Chu, *Dalton Trans.* **2019**, *48*, 16249.
[45] K. Larsson, K. Binnemans, *Green Chem.* **2014**, *10*, 4595.
[46] X. Li, A. van den Bossche, T. Vander Hoogerstraete, K. Binnemans, *Chem. Commun.* **2018**, *54*, 475.
[47] A. van den Bossche, E. de Witte, W. Dehaen, K. Binnemans, *Green Chem.* **2018**, *20*, 3327.
[48] A. van den Bossche, W. Vereycken, T. Vander Hoogerstraete, W. Dehaen, K. Binnemans, *ACS Sustainable Chem. Eng.* **2019**, *7*, 14451.
[49] X. Li, Z. Li, M. Orefice, K. Binnemans, *ACS Sustainable Chem. Eng.* **2019**, *7*, 2578.
[50] A. I. Popov, D. H. Geske, *J. Am. Chem. Soc.* **1958**, *80*, 1340.
[51] A. I. Popov, D. H. Geske, *J. Am. Chem. Soc.* **1958**, *80*, 5346.
[52] A. Cerquetti, P. Longhi, T. Mussini, G. Natta, *J. Electroanal. Chem. Interfacial Electrochem.* **1969**, *20*, 411.
[53] I. G. Dioum, J. Vedel, B. Tremillon, *J. Electroanal. Chem. Interfacial Electrochem.* **1982**, *139*, 323.
[54] I. V. Nelson, R. T. Iwamoto, *J. Electroanal. Chem.* **1964**, *7*, 218.
[55] B. Bennett, J. Chang, A. J. Bard, *Electrochim. Acta* **2016**, *219*, 1.
[56] G. D. Allen, M. C. Buzzeo, C. Villagrán, C. Hardacre, R. G. Compton, *J. Electroanal. Chem.* **2005**, *575*, 311.
[57] G. D. Allen, M. C. Buzzeo, I. G. Davies, C. Villagrán, C. Hardacre, R. G. Compton, *J. Phys. Chem. B* **2004**, *108*, 16322.
[58] L. Yu, X. Jin, G. Z. Chen, *J. Electroanal. Chem.* **2013**, *688*, 371.
[59] A. P. Abbott, *ChemPhysChem* **2005**, *6*, 2502.
[60] F. A. Redeker, A. Kropman, C. Müller, S. E. Zewge, H. Beckers, B. Paulus, S. Riedel, *J. Fluorine Chem.* **2018**, *216*, 81.
[61] G. Chatel, J. F. B. Pereira, V. Debbeti, H. Wang, R. D. Rogers, *Green Chem.* **2014**, *16*, 2051.
[62] T. Iwasita, M. C. Giordano, *Electrochim. Acta* **1969**, *14*, 1045.
[63] J. G. Vos, A. Venugopal, W. A. Smith, M. T. M. Koper, *J. Electrochem. Soc.* **2020**, *167*, 46505.
[64] a) J. Cornog, E. E. Bauer, *J. Am. Chem. Soc.* **1942**, *64*, 2620; b) Y. Yagi, A. I. Popov, *Inorg. Nucl. Chem. Lett.* **1965**, *1*, 21; c) Y. Yagi, A. I. Popov, *J. Inorg. Nucl. Chem.* **1967**, *29*, 2223; d) A. Parlow, H. Hartl, *Z. Naturforsch. B* **1979**, *35*, 1930.
[65] N. G. Connelly, W. E. Geiger, *Chem. Rev.* **1996**, *96*, 877.
[66] S. M. Batterjee, M. I. Marzouk, M. E. Aazab, M. A. El-Hashash, *Appl. Organomet. Chem.* **2003**, *17*, 291.
[67] E. H. B. Anari, M. Romano, W. X. Teh, J. J. Black, E. Jiang, J. Chen, T. Q. To, J. Panchompoo, L. Aldous, *Chem. Commun.* **2016**, *52*, 745.
[68] J. C. Swarts, A. Nafady, J. H. Roudebush, S. Trupia, W. E. Geiger, *Inorg. Chem.* **2009**, *48*, 2156.
[69] R. J. Enemaerke, J. Larsen, T. Skrydstrup, K. Daasbjerg, *Organometallics* **2004**, *23*, 1866.
[70] K. S. Thanthiriwatte, M. Vasiliu, D. A. Dixon, K. O. Christe, *Inorg. Chem.* **2012**, *51*, 10966.
[71] a) S. Rozen, *Adv. Synth. Catal.* **2010**, *352*, 2691; b) V. I. Sobolev, V. B. Radchenko, R. V. Ostvald, V. D. Filimonov, I. I. Zherin, *Procedia Chem.* **2014**, *11*, 88.
[72] S. I. Ivlev, A. V. Malin, A. J. Karttunen, R. V. Ostvald, F. Kraus, *J. Fluorine Chem.* **2019**, *218*, 11.
[73] M. R. Ciumag, T. Tzedakis, C. A. Barrès, *Electrochim. Acta* **2012**, *70*, 142.
[74] H. Meinert, U. Groβ, *Z. Chem.* **1969**, *9*, 190.
[75] M. F. Wempe, *J. Mol. Struct.* **2001**, *562*, 63.
[76] a) G. Gritzner, J. Kuta, *Pure Appl. Chem.* **1984**, *56*, 461; b) C. G. Zoski, *Handbook of electrochemistry*, Elsevier, Amsterdam, Oxford, **2007**.
[77] S. Mattsson, G. Senges, S. Riedel, B. Paulus, *Chem. Eur. J.* **2020**, Accepted paper.

Manuscript received: September 4, 2020
Revised manuscript received: December 11, 2020

3.2. Synthesis, Crystallization, and Electrochemical Characterization of Room Temperature Ionic Liquid Bromidostannates(II/IV)

The pages 73–82 contain the printed article, which is available at

https://doi.org/10.1021/acs.inorgchem.1c00706.

The table of contents graphic and the pages 135–181 containing the supporting information of the article are available under the same URL.

Tyler A. Gully, Karsten Sonnenberg, Julia Bader, and Sebastian Riedel*
Inorg. Chem., **2021**, *60*, 8093-8102.

https://doi.org/10.1021/acs.inorgchem.1c00706

Author contributions

M.Sc. Tyler A. Gully designed the project, performed the experiments, synthesized and characterized the products, and analyzed the physicochemical, electrochemical, NMR, and spectroscopy data. Additionally, he wrote the original manuscript.

Dr. Karsten Sonnenberg helped design the project, performed the original synthesis of [OMIM][$SnBr_5$], and performed and analyzed all crystallography measurements. Additionally,

he corrected the original manuscript and was also responsible for the administration of the acquired funds leading to this publication.

Dr. Julia Bader provided scientific guidance and helped write the original manuscript.

Prof. Dr. Sebastian Riedel supervised the project and was responsible for conceptualization and the acquisition of the financial support for the project leading to this publication. He was also responsible for reviewing and editing the original draft of this publication.

3.3. Investigations Towards a Non-Aqueous Hybrid Redox-Flow Battery with a Manganese Based Anolyte and Catholyte

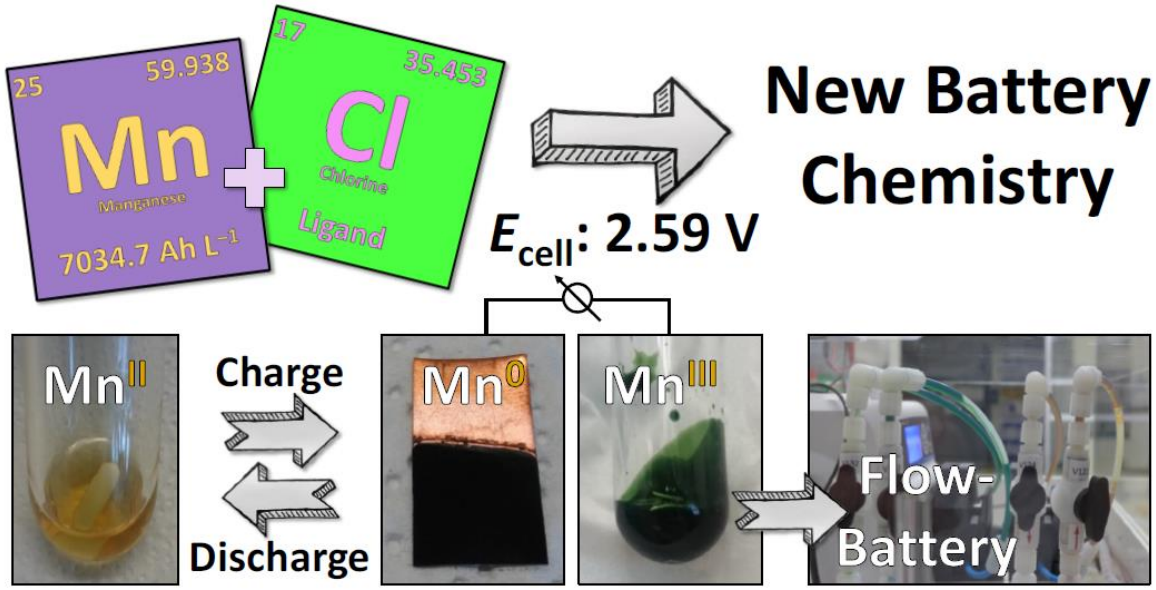

Maximilian Schmucker, **Tyler A. Gully**, Alexei Schmidt, Benjamin Schmidt, Kolja Bromberger, Joey Disch, Burkhard Butschke, Benedikt Burgenmeister, Karsten Sonnenberg, Sebastian Riedel and Ingo Krossing*.

Adv. Energy Mater., **2021**, *11*, 2101261.

https://doi.org/10.1002/aenm.202101261

Author Contributions

M.Sc. Tyler A. Gully designed, performed, and analyzed the spectroelectrochemical experiments as well as the conductivity, viscosity, and Walden plot measurements. He also synthesized, characterized, and performed CV measurements of the alternative cations and of the Mn(II) and Mn(III) species. He was also responsible for the visualization and writing the original draft of the respective data. Additionally, he was involved in electrolyte and cation characterization and optimization, reviewing and editing the original draft of this publication. As a final point, he was in charge of directing the research at FU Berlin.

M.Sc. Maximilian Schmucker designed, performed and analyzed the battery experiments (including the membrane testing and electrolyte optimization), cyclic voltammetric (CV) measurements, half-cell experiments, as well as the manganese deposition experiments. He was also involved in the mass spectrometric measurements and did the respective analysis. He was further involved in electrolyte preparation and characterization, including the electrolyte for the flow-cell measurements. Additionally, he was responsible for the visualization of the presented data and writing the original draft of this publication. Further, he was involved in reviewing and editing the original draft.

M.Sc. Alexei Schmidt was involved in electrolyte synthesis and characterization, battery experiments, CV measurements, half-cell experiments as well as the manganese deposition experiments. He was also involved in the electrolyte preparation for the flow-cell measurements.

Dr. Benjamin Schmidt was responsible for the synthesis and characterization of the alternative cations. He also supported the electrochemical analysis of the prepared cations. Furthermore, he participated in project administration.

M.Sc. Dipl.-Ing. (FH) Kolja Bromberger was responsible for the develoPHMent of the flow-cell setup, including the design of the flow-cell. He also supervised all measurements performed with the flow-cell and was involved in the visualization of the presented data and in reviewing and editing parts of the original draft of this publication.

M.Sc. Joey Disch performed the measurements with the flow-cell and was involved in the visualization of the presented data.

Dr. Burkhard Butschke performed the mass spectrometric experiments and was involved in the respective analysis. He was also involved in reviewing and editing parts of the original draft of this publication.

Dr. Benedikt Burgenmeister did project administration and conceptualization. Additionally, he was responsible for the acquisition of the financial support for the project leading to this publication.

Dr. Karsten Sonnenberg did project administration and was involved in the synthesis and characterization of the alternative cations. He was also responsible for the administration of the acquired funds leading to this publication.

Prof. Dr. Sebastian Riedel supervised the project and was responsible for conceptualization and the acquisition of the financial support for the project leading to this publication. He was also responsible for reviewing and editing the original draft of this publication.

Prof. Dr. Ingo Krossing supervised the project and was responsible for conceptualization and the acquisition of the financial support for the project leading to this publication. He was also involved in writing the original draft of this publication and responsible for reviewing and editing the original draft of this publication.

ADVANCED ENERGY MATERIALS
www.advenergymat.de

Investigations toward a Non-Aqueous Hybrid Redox-Flow Battery with a Manganese-Based Anolyte and Catholyte

*Maximilian Schmucker, Tyler A. Gully, Alexei Schmidt, Benjamin Schmidt, Kolja Bromberger, Joey Disch, Burkhard Butschke, Benedikt Burgenmeister, Karsten Sonnenberg, Sebastian Riedel, and Ingo Krossing**

A new all-Manganese flow battery (all-MFB) as a non-aqueous hybrid redox-flow battery is reported. The discharged active material $[Cat]_2[Mn^{II}Cl_4]$ (Cat = organic cation) utilized in both half-cells supports a long cycle life. The reversible oxidation of $[Mn^{II}Cl_4]^{2-}$ to $[Mn^{III}Cl_5]^{2-}$ at the positive electrode and manganese metal deposition from $[Mn^{II}Cl_4]^{2-}$ at the negative electrode give a cell voltage of 2.59 V. Suitable electrolytes are prepared and optimized, followed by a characterization in static battery cells and in a pumped flow-cell. Several electrode materials, solvents, and membranes are tested for their feasibility in the all-MFB. An electrolyte consisting of $[EMP]_2[MnCl_4]$ and some solvent γ-butyrolactone is cycled 500 times, both in a static as well as a flow-cell, over a period of two months, with coulombic efficiencies up to 83%. With the electrolytes prepared in this work, energy densities up to 74 Wh L^{-1} are possible, exceeding the VRFB benchmark system, using solely the cheap and abundant element manganese as the active material. Although further optimizations are necessary, this system represents a new and promising setup toward sustainable stationary energy storage.

1. Introduction

The importance of electrical energy-storage systems (EES), for a successful integration of intermittent renewable energy sources into the electrical grid is beyond dispute.[1–4] For mobile applications, lithium ion batteries (LIBs) with high energy density prevail.[2,5,6] Although many efforts focus on alternative chemical systems (e.g., multivalent Al, Mg, and Ca), it is hard to imagine that LIBs will disappear in the near future.[4,7] Yet, for large scale stationary EES, there is no such prevailing technology. Although other alternatives, like pumped hydro or fuel cells are available, batteries are amongst the most promising technologies for this purpose.[1,3,8] With the energy density being slightly less relevant, other redox active materials could be employed in large scale EES, i.e., redox-flow batteries (RFBs) with their very long cycle life and decoupled capacity, power and energy output.[2,9,10] Their benchmark is the all-vanadium redox-flow battery (VRFB) with V^{II}/V^{III} and V^{IV}/V^{V} redox couples,[2] as well as a 15 000–20 000 charge/discharge cycles lifetime and an acceptable energy density of 25–35 Wh L^{-1} installed in up to 60 MWh capacity EES.[2,6] However, probably due to the high cost, a commercial breakthrough still has to come.[2,6,9] Considering abundancy and cost, few elements are suitable as redox active material in sustainable batteries.[4,11] Manganese is one of them and, therefore, finds application in LIB-cathode active materials (e.g., $LiMn_2O_4$ or $Li[Ni_{0.8}Co_{0.1}Mn_{0.1}]O_2$) or in cathode materials of primary batteries (MnO_2).[5,12] However, to the best of our knowledge, only one battery system exclusively using manganese compounds at both electrodes is described,[13] i.e., $Mn(acac)_3$ acetonitrile (MeCN) solutions with the Mn^{II}/Mn^{III} couple at the negative and the Mn^{III}/Mn^{IV} couple at the positive electrode. Yet, with E_{cell} of 1.1 V the system does not exploit the large potential range advantage of a non-aqueous electrolyte. Already the aqueous standard potential difference ΔE^0 of Mn^0/Mn^{II} and Mn^{II}/Mn^{III} redox couples amounts to an impressive 2.69 V. In addition, the Mn volumetric specific capacity is 7034.7 Ah L^{-1} (two-electron-process). It clearly exceeds that of zinc (5853.8 Ah L^{-1}), which in the zinc

M. Schmucker, A. Schmidt, Dr. B. Butschke, Dr. B. Burgenmeister, Prof. I. Krossing
Institut für Anorganische und Analytische Chemie and Freiburger Materialforschungszentrum (FMF)
Albert-Ludwigs-Universität Freiburg
Albertstr. 21, 79104 Freiburg, Germany
E-mail: krossing@uni-freiburg.de

T. A. Gully, Dr. B. Schmidt, Dr. K. Sonnenberg, Prof. S. Riedel
Fachbereich Biologie
Chemie
Pharmazie
Institut für Chemie und Biochemie – Anorganische Chemie
Freie Universität Berlin
Fabeckstr. 34–36, 14195 Berlin, Germany

K. Bromberger, J. Disch
Bereich Wasserstofftechnologien
Fraunhofer-Institut für Solare Energiesysteme ISE
Heidenhofstr. 2, 79110 Freiburg, Germany

The ORCID identification number(s) for the author(s) of this article can be found under https://doi.org/10.1002/aenm.202101261.

DOI: 10.1002/aenm.202101261

bromine flow battery (ZBFB) represents the benchmark system for hybrid redox-flow batteries.[2] Therefore, the two-electron-deposition and stripping of Mn as possible negative electrode reactions may lead to an all-MFB with favorable energy density. Since hydrogen evolution is one of the major side reactions upon manganese deposition (E^0 = –1.18 V) and oxygen evolution may compete with the Mn^{II}/Mn^{III} redox couple (E^0 = +1.51 V), non-aqueous electrolytes are preferable.[14] To increase cycle-life, the same electrochemically active species has to be used in both half-cells. Therefore, a manganese ion allowing manganese deposition, but also forming stable Mn^{III}/Mn^{IV} compounds was needed. Chloromanganates were identified as an option for the active species. Of those, the Cambridge Structural Database includes 49 entries for the $[Mn^{II}Cl_4]^{2-}$ anion, but only three containing $[Mn^{III}Cl_5]^{2-}$.[15] Only three inorganic variants are known for the $[Mn^{IV}Cl_6]^{2-}$ anion (Inorganic Crystal Structure Database).[16–18] However, well characterized $[Mn^{III}Cl_5]^{2-}$ and $[Mn^{IV}Cl_6]^{2-}$ salts are known (vide infra = v.i.). Thus, starting from well-known $[Mn^{II}Cl_4]^{2-}$,[19–27] Equations (1) and (2) represent possible cell reactions of an all-Mn battery:

$$3[Mn^{II}Cl_4]^{2-} \underset{\text{charge}}{\overset{\text{discharge}}{\rightleftharpoons}} Mn^0 + 2[Mn^{III}Cl_5]^{2-} + 2Cl^- \quad (1)$$

$$2[Mn^{II}Cl_4]^{2-} \underset{\text{charge}}{\overset{\text{discharge}}{\rightleftharpoons}} Mn^0 + [Mn^{IV}Cl_6]^{2-} + 2Cl^- \quad (2)$$

At the positive electrode an oxidation of $[Mn^{II}Cl_4]^{2-}$ into known $[Mn^{III}Cl_5]^{2-}$ or $[Mn^{IV}Cl_6]^{2-}$ is conceivable.[16,17,28–34] Reaching the oxidation state +IV in a two-electron-process in $[Mn^{IV}Cl_6]^{2-}$ would favorably improve the energy density. Yet, the expected high redox potential of Mn^{IV} might lead to the formation of Cl_2 as main or side reaction. In addition, non-aqueous manganese deposition from $[Mn^{II}Cl_4]^{2-}$ is unknown.[35,36] Table S19 (Supporting Information) includes the expected energy densities for an all-Mn battery based on the conservative Equation (1) with 1–2 mol L^{-1} electrolyte concentration and a cell potential E_{cell} of 2.69 V (aqueous redox potentials). With a theoretical energy density around 44–87 Wh Kg^{-1}, the all-Mn battery would have the potential to exceed VRFB and ZBFB in energy density and use the cheap and abundant elements manganese and chlorine. Here we investigated, if such a battery can be realized.

2. Results and Discussion

This paper is organized by a synthesis and characterization section that demonstrates the feasibility of the proposed battery chemistry on classical chemical and electrochemical grounds before investigating the battery performance in static symmetric, half as well as full cells, and finally in pumped flow cells. A section on the performance of the all-MFB discussing all experimental data is placed at the end, after describing the flow operation.

2.1. Synthesis and Characterization of the $[Cat]_2[Mn^{II}Cl_4]$ Salts

$[Cat]_2[Mn^{II}Cl_4]$-syntheses with organic cations $[Cat]^+$ are reported since 1959[27] and available according to Equation (3) in yields >99%; we found the products to be stable under atmospheric conditions. Focus is placed on the $[Mn^{II}Cl_4]^{2-}$ salts with 1-butyl-1-methylpyrrolidinium ($[BMP]^+$) and 1-ethyl-1-methylpyrrolidinium ($[EMP]^+$) cation; other cations were tested (Supporting Information).

$$MnCl_2 + 2[Cat]Cl \xrightarrow[\text{e.g. MeCN}]{\text{organic solvent}} [Cat]_2[MnCl_4] \quad (3)$$

All syntheses were performed under inert conditions to prevent contamination with water and its electrochemical side reactions. The organic cation $[Cat]^+$ in the product can easily be varied by simply using the chloride salt [Cat]Cl of the desired cation, also salts with two different cations are possible ($[Cat_1][Cat_2][Mn^{II}Cl_4]$). This gives access to a broad variety of different $[Mn^{II}Cl_4]^{2-}$ salts with electrochemically inert cations that could be used to influence the morphology of the electrochemical metal deposition,[37] optimize solubility, conductivity, and viscosity of the electrolyte. $[Mn^{II}Cl_4]^{2-}$ salts have prior been extensively characterized by scXRD, UV/Vis-, IR-, and Raman spectroscopy.[19–26,38,39] **Figure 1**a,b shows the IR- and the Raman spectra of solid $[BMP]_2[Mn^{II}Cl_4]$ relevant to this work and Table S1 (Supporting Information) contains the corresponding stretching frequencies that agree with the literature.

Raman- and UV/Vis spectroscopy demonstrate that $[Mn^{II}Cl_4]^{2-}$ is not stable in the presence of water (see Figure S3, Supporting Information), since the ν_1-stretching frequency disappeared completely. In contrast, in MeCN- and GBL-solutions the relevant ν_1-stretching frequencies were observed (see Figure 1), showing that the $[Mn^{II}Cl_4]^{2-}$-anion is stable and the respective solvents are suitable for electrolyte preparation. This is further supported by the UV/Vis spectra (Figure 1c,d and Table S2: Supporting Information).

2.2. Electrochemical Investigations toward Battery Application

2.2.1. Spectroelectrochemistry

The charged active species in the all-MFB – the $[Mn^{III}Cl_5]^{2-}$ anion – was prior characterized with scXRD, UV/Vis- Raman- and IR-spectroscopy,[28–32,40] but all known preparation routes start with Mn^{III}- or Mn^{IV}-species. By contrast, in the all-MFB the $[Mn^{II}Cl_4]^{2-}$ is electrochemically oxidized to $[Mn^{III}Cl_5]^{2-}$. **Figure 2**a shows the CV of $EL_{GBL\text{-}BMP\text{-}50}$. The current response is assigned to a reversible oxidation of $[Mn^{II}Cl_4]^{2-}$ with a half-peak potential ($E_{p/2}$) at 1.17 V versus Fc/Fc^+ using a platinum working electrode (Pt-WE) and 1.28 V versus Fc/Fc^+ using a glassy carbon working electrode (GC-WE). These potentials are rather close to the Mn^{2+}/Mn^{3+} redox couple in aqueous media (1.11 V vs Fc/Fc^+).[41,42] The characteristic dark green coloration (see Figure 2b) suggested $[Mn^{III}Cl_5]^{2-}$ formation at the WE during the anodic scan.

Spectroelectrochemical Raman and UV/Vis-measurements, which easily distinguish $[Mn^{II}Cl_4]^{2-}$ and $[Mn^{III}Cl_5]^{2-}$, were conducted. In Figure 2c) the Raman spectra of tetrahedral $[Mn^{II}Cl_4]^{2-}$ as $[EMP]_2[Mn^{II}Cl_4]$ and $[BMP]_2[Mn^{II}Cl_4]$ display the characteristic ν_1-stretching frequency of the anion at 251 and 253 cm^{-1}, respectively. After applying a potential

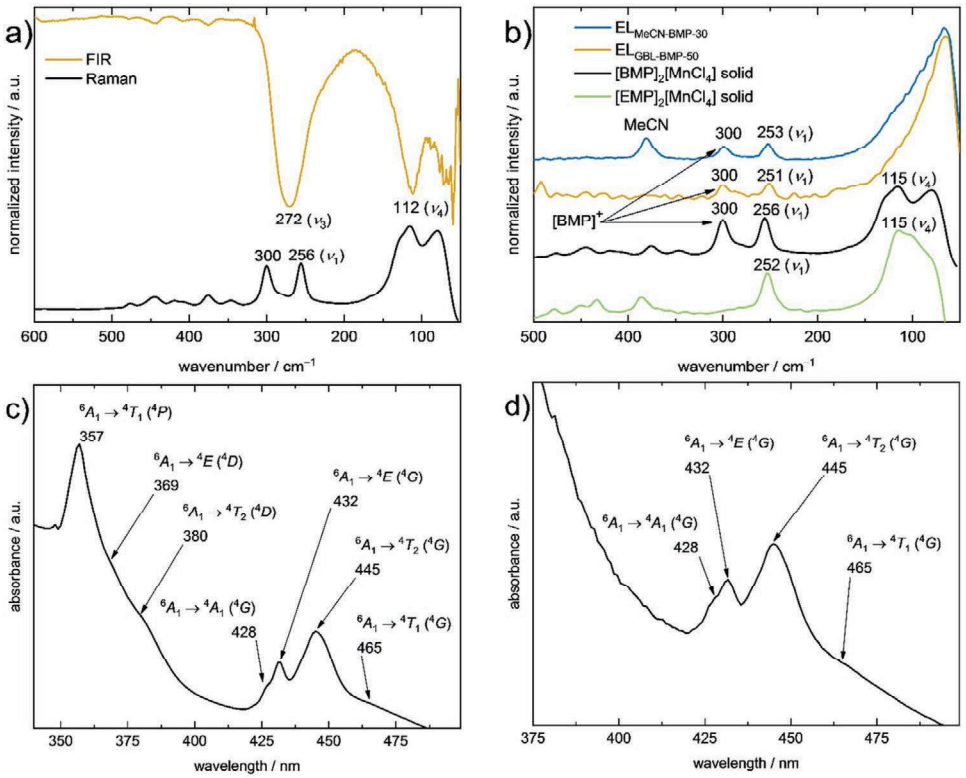

Figure 1. a) IR- and Raman spectra of solid $[BMP]_2[Mn^{II}Cl_4]$. b) Raman spectra of $[BMP]_2[Mn^{II}Cl_4]$ and $[EMP]_2[Mn^{II}Cl_4]$ as solids and $[BMP]_2[Mn^{II}Cl_4]$ dissolved in GBL (50 wt% GBL, $c = 1.2$ mol L^{-1}, $EL_{GBL\text{-}BMP\text{-}50}$) and MeCN (30 wt% MeCN, $c = 1.6$ mol L^{-1}, $EL_{MeCN\text{-}BMP\text{-}30}$). The stretching mode at 300 cm^{-1} can be assigned to $[BMP]^+$, since it is not observed in the spectrum of $[EMP]_2[Mn^{II}Cl_4]$. c) UV/Vis spectrum of $[BMP]_2[Mn^{II}Cl_4]$ in MeCN (90 wt% MeCN, $c = 3.2$ mmol L^{-1}). d) UV/Vis spectrum of $[BMP]_2[Mn^{II}Cl_4]$ in GBL (90 wt% GBL, $c = 0.22$ mol L^{-1}).

of 1.65 V versus q-Pt, a new band at 289 cm^{-1} appears. For the $[BMP]^+$ cation, a band at 300 cm^{-1} (cf. Figure 1b) slightly obscures this region, but it can be clearly observed in the spectrum starting from $[EMP]_2[Mn^{II}Cl_4]$. Comparison with known C_{4v}-symmetric $[Mn^{III}Cl_5]^{2-}$ compounds in Table S7 (Supporting Information) reveals strongest vibrational bands between 289 and 296 cm^{-1}, suggesting that $[Mn^{III}Cl_5]^{2-}$ can be formed electrochemically from $[Mn^{II}Cl_4]^{2-}$. Also, the Raman spectra of the chemically with dichlorine oxidized $[BMP]_2[Mn^{II}Cl_4]$ and $[NEt_4]_2[Mn^{II}Cl_4]$ include the characteristic $[Mn^{III}Cl_5]^{2-}$ stretch at 292 and 287 cm^{-1} (Figure S7, Supporting Information). As a final proof that $[Mn^{III}Cl_5]^{2-}$ forms electrochemically, a crystal structure was obtained from the electrochemical oxidation product of $[NEt_4]_2[Mn^{II}Cl_4]$ (see Figure 2). Since the electrooxidation of $[NEt_4]_2[Mn^{II}Cl_4]$ in MeCN was not quantitative, a cocrystal with $[Mn^{II}Cl_4]^{2-}$ was formed. In all of these experiments the dark green coloration of $[Mn^{III}Cl_5]^{2-}$ was characteristic and UV/Vis-spectroscopy further supports the electrochemical formation of $[Mn^{III}Cl_5]^{2-}$. In Figure 2d) the electronic transitions of $[Mn^{II}Cl_4]^{2-}$ at 431 and 446 nm are visible when no voltage is applied. After applying 1.74 V versus q-Pt or more, these transitions vanish and the intense transitions of $[Mn^{III}Cl_5]^{2-}$ become visible. Table S8 (Supporting Information) shows the assignments of the respective transitions, in accordance with the literature. The spectroelectrochemical analysis in MeCN with Raman and UV/Vis spectra is shown in Figure S6 (Supporting Information).

2.2.2. Mn Electrodeposition from $[Mn^{II}Cl_4]^{2-}$ Solutions

Manganese can be deposited from aqueous solutions[14] and, although hydrogen evolution is a major side reaction, only few reports on manganese-deposition from non-aqueous media are known.[35,36] Yet, depositions from non-aqueous $[Mn^{II}Cl_4]^{2-}$ solution are unknown but possible from the related, but water containing, deep eutectic solvent choline chloride + urea (1:2) upon addition of $Mn^{II}Cl_2 \cdot 4H_2O$.[43] To investigate, whether electrochemical deposition and striping of manganese from an anhydrous solution is possible, the CVs of three $[Cat]_2[Mn^{II}Cl_4]$ salts were measured in several solvents (**Figure 3**).[44] In MeCN a deposition and a stripping of manganese can be observed for every salt tested. With $[EMP]^+$ and $[BMP]^+$ the current profiles look very similar. Mn deposition and stripping are separated by 0.87 and 0.95 V respectively. Additionally, two current maxima can be observed for the stripping, whereas only one current maximum is present with the $[N_{2225}]^+$ salt. Cations can influence the morphology of metal deposition,[37] thus the cations may be an explanation for the differing stripping behavior. However, with $[N_{2225}]^+$ the two processes are 1.26 V apart, making the $[EMP]^+$ and $[BMP]^+$ salt with lower overpotential more interesting. $[Mn^{II}Cl_4]^{2-}$- solutions in propylene carbonate (PC) and GBL only deposit, but do not strip manganese. Further Mn was deposited on Pt-foils (current density 0.25 mA cm^{-2}; 11.2 mA h = 11.3 mg Mn; Figure 3b). The Pt-foil is completely blank after the electrolysis in GBL, whereas a black layer was observed after deposition from MeCN.

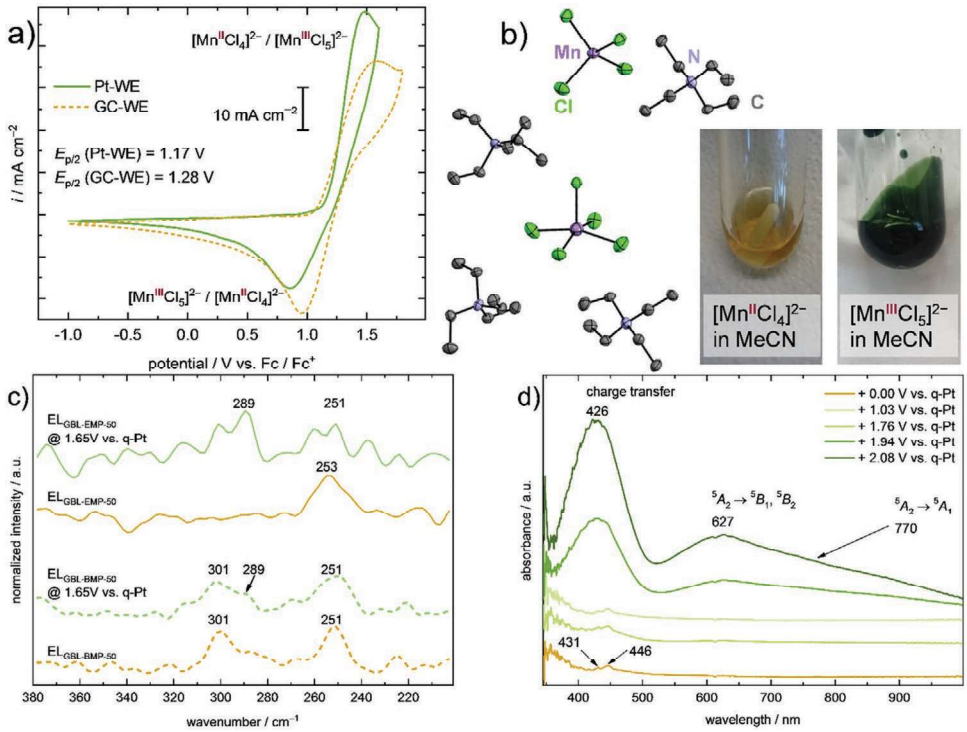

Figure 2. a) CV of $EL_{GBL\text{-}BMP\text{-}50}$ at a Pt-WE and a GC-WE with 100 mV s^{-1}. b) Molecular structure of the cocrystal $[NEt_4]_4[Mn^{II}Cl_4][Mn^{III}Cl_5]$, H-atoms and disorder of $[NEt_4]^+$ were omitted for clarity, thermal ellipsoids were drawn with 50% probability. Color of $[Mn^{II}Cl_4]^{2-}$ and $[Mn^{III}Cl_5]^{2-}$ dissolved in MeCN. c) Raman spectroelectrochemistry with $[EMP]_2[Mn^{II}Cl_4]$ in GBL (50 wt% GBL, c = 1.4 mol L^{-1}, $EL_{GBL\text{-}EMP\text{-}50}$) and $EL_{GBL\text{-}BMP\text{-}50}$. d) UV/Vis spectroelectrochemistry with $[BMP]_2[Mn^{II}Cl_4]$ in GBL (90 wt% GBL, c = 0.22 mol L^{-1}).

Apparently, $[Mn^{II}Cl_4]^{2-}$ is reduced at the electrode but the Mn metal formed does not stick to it. Figure 3b shows a typical photograph of an electrolyte after deposition in which the reduced Mn seems to end up as a black suspension. From MeCN, Mn deposition / stripping on a copper electrode was repeated 24 times with the respective voltage profiles / coulombic efficiency (CE) given in Figure 3c,d.

The CE slightly improves over the 24 cycles to still only 43%, probably due to the incomplete stripping of the mechanically unstable Mn layer that is formed. Thus, the photographs in Figure 3d demonstrate that the deposited Mn layer can easily be removed by washing the electrode with excess solvent. Note that manganese metal crystallizes in a unique elemental structure with 58 independent Mn atoms in the unit cell.[45] Apparently, Mn deposition on metal surfaces with closed-packed typical metal structures like Pt or Cu are a bad choice concerning the mechanical stability of the Mn film. To confirm that the black deposit is manganese, pXRD data of the black deposit powders on copper were recorded. **Figure 4**a shows the pXRD trace of a sample prepared under atmospheric conditions. The broad reflexes speak for an almost amorphous structure and fit very well to the pXRD of MnO instead of Mn, although the main reflex of α-manganese seems still to be present.[45,46] In the sample prepared under inert conditions (Figure 4b) MnO-reflexes are absent and the sample assigns as α-Mn. The oxidation of the deposited Mn to MnO under atmospheric conditions is expected and an indirect proof for the deposition of pure manganese under inert conditions (cf. Figure S9 (Supporting Information) for an EDX mapping). The SEM images of the deposited manganese films on different electrode materials always revealed a cauliflower like structure (see Figure 4), similar to the reported Mn deposits from non-aqueous media that delaminate very easily by washing the electrode.[35,36]

Before entering the huge field of Mn deposition, where temperature, deposition potential, additives and cations strongly influence the morphology of the deposited Mn films, we were satisfied with the fact that it is possible to deposit Mn from $[Mn^{II}Cl_4]^{2-}$ solutions and continued with first battery experiments, to check whether it is worth to return to Mn deposition later.

2.2.3. Linear Sweep Voltammetry (LSV)

LSV was used on a Mn-electrode to investigate, whether anodic dissolution is possible or hindered by passivation of the electrode surface, as often observed due to precipitation of insoluble species upon anodic dissolution in media with high chloride ion concentration.[47] Note that the chloride ion concentration in the Mn^0/Mn^{II}-half-cell will be high in the charged state. Since in GBL solutions of $[Cat]_2[Mn^{II}Cl_4]$ no stripping of Mn was observed (Mn^0-delamination? Figure 3b), the LSV of a solution of [EMP]Cl in GBL (1.9 mol L^{-1}) was recorded (Figure S12, Supporting Information). The anodic dissolution of Mn^0 starts at –0.65 V and does not show the typical current profile for a passivation, described in the literature.[47] Still at –0.45 and –0.2 V the current levels off for a short time, creating two plateaus. This is an

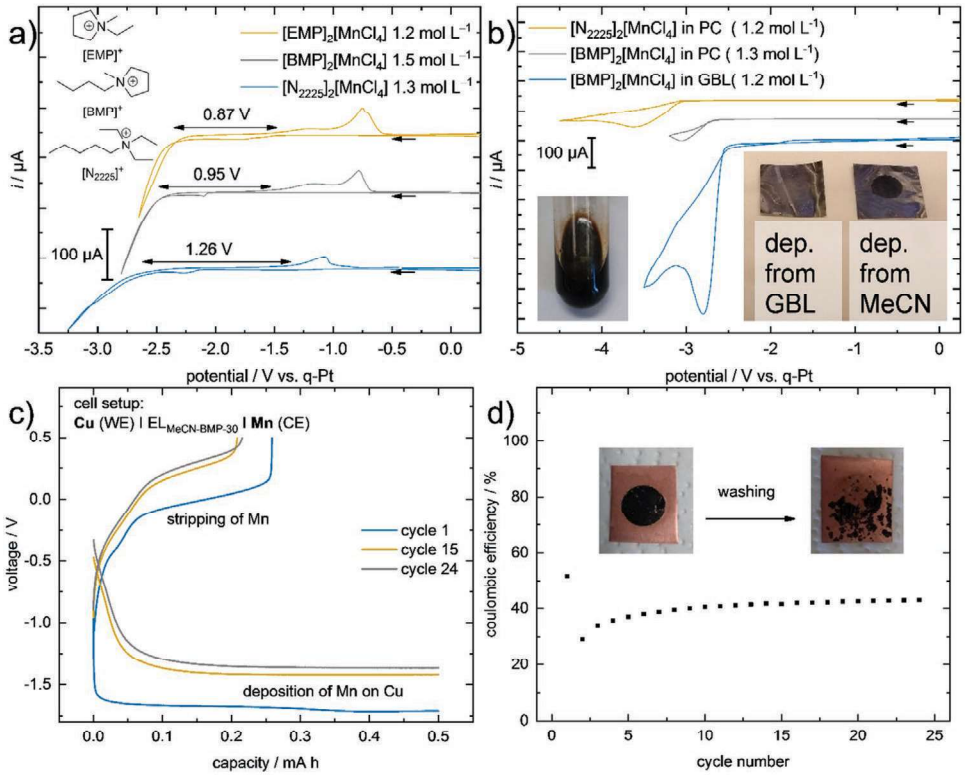

Figure 3. a) CVs of different $[Cat]_2[MnCl_4]$ salts in MeCN at a Pt-WE with a scan rate of 50 mV s^{-1}. b) CVs of different $[Cat]_2[MnCl_4]$ salts in PC and GBL at a Pt-WE with a scan rate of 50 mV s^{-1} plus photographs of Mn deposits from MeCN and GBL. c) Voltage profiles of the electrochemical deposition and stripping of Mn from a solution of $[BMP]_2[MnCl_4]$ in MeCN (1.6 mol L^{-1}, 30 wt% MeCN, $EL_{MeCN\text{-}BMP\text{-}30}$) using a Cu-electrode and a current density of 0.88 mA cm^{-2}. d) CE of the respective experiment plus photographs of the mechanically unstable Mn-layer (deposition of 2 mA h).

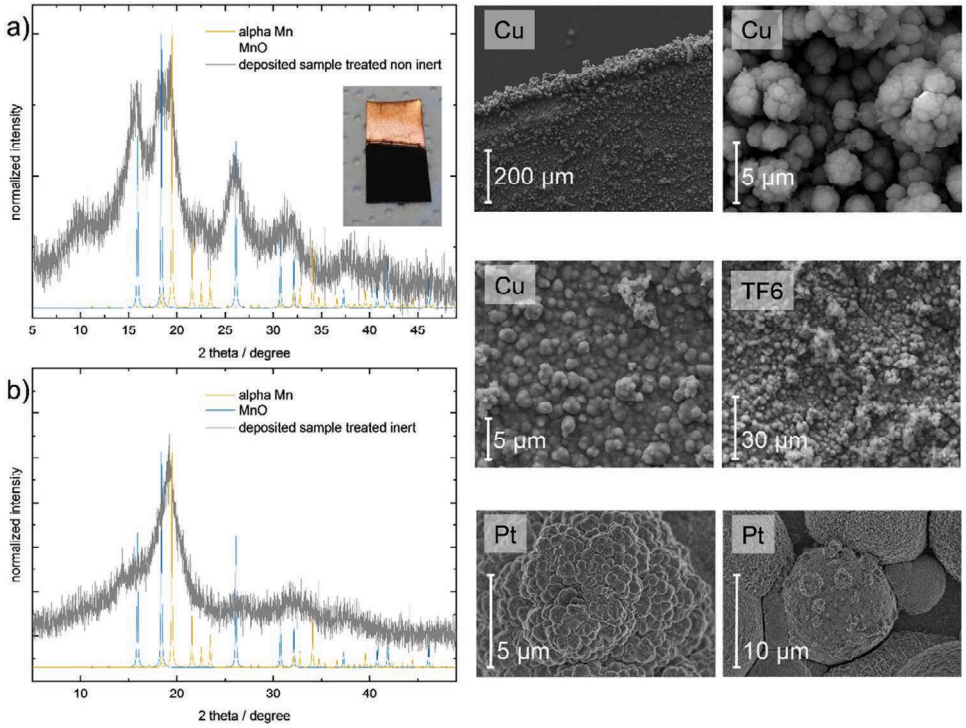

Figure 4. pXRD of manganese, deposited from $EL_{MeCN\text{-}BMP\text{-}30}$ on Cu a) handled under atmospheric conditions. b) Handled under inert conditions. SEM images of Mn deposits on Cu ($EL_{MeCN\text{-}BMP\text{-}30}$), TF6 ($EL_{MeCN\text{-}BMP\text{-}30}$) and Pt ($EL_{MeCN\text{-}BMP\text{-}Cl\text{-}30}$).

indication that the anodic dissolution slows down for a moment, i.e., that the layer is not blocking the surface but just somewhat restricting flow. Since we are significantly away from the oxidation potentials for Mn^{III}, this suggests the system is not changing the oxidation state, but rather that the speciation changes as the metal concentration close to the electrode surface changes, e.g., $[Mn^{II}Cl_4]^{2-}$ could have a different solubility to a hypothetically formed ion $[Mn^{II}{}_2Cl_x]^{(4-x)}$ (x = 5–7) at the plateaus. Thus, the anodic dissolution of Mn is similar to the anodic dissolution of Zn or Sn.[47] Afterward the current increases further and indicates an almost unhindered dissolution of Mn^0. The final formation of the stable $[Mn^{II}Cl_4]^{2-}$ ion appears to be a very strong driving force, limiting the detrimental passivation.

2.2.4. Electrolytes

Table 1 summarizes the key parameters of the different electrolytes used throughout this work. Electrolyte optimizations (see the Supporting Information) revealed that the addition of extra [Cat]Cl to a solution of $[Cat]_2[Mn^{II}Cl_4]$ reduces the charge voltage (U_{SoC5}) by up to 0.62 V. Therefore, only electrolytes with [Cat]Cl as an additive were used for cycling experiments. Upon characterization of the BMP-GBL-electrolyte with 50 wt% GBL we observed that $[Mn^{II}Cl_4]^{2-}$ salts can precipitate, if the temperature drops. Thus, we decided to use 55 wt% GBL in the battery measurements and successfully prevented any precipitation. Although it was necessary to add more GBL (58 wt%) to dissolve all of the $[EMP]_2[MnCl_4]$ and [EMP]Cl ($EL_{GBL\text{-}EMP\text{-}Cl\text{-}58}$), its $[Mn^{II}Cl_4]^{2-}$ concentration is still higher compared to the $[BMP]^+$ based electrolyte with only 50 wt% of GBL ($EL_{GBL\text{-}BMP\text{-}Cl\text{-}50}$) (1.0 mol L^{-1} vs 0.9 mol L^{-1}).

MeCN-based electrolytes never showed any sign of precipitation even at a low solvent content of only 30 wt%, so we used these electrolytes for the characterization and the battery measurements. The acronyms used for the electrolytes EL include the solvent, the cation and the amount of solvent added to the salt in wt% in the subscript. This means, $EL_{GBL\text{-}BMP\text{-}50}$ stands for an electrolyte using $[BMP]_2[Mn^{II}Cl_4]$ as conducting salt and 50 wt% GBL as auxiliary solvent. If nothing is mentioned always Mn(II), i.e., $[Mn^{II}Cl_4]^{2-}$ is used. If Mn(III) is included with the subscript, the electrolyte contains $[Mn^{III}Cl_5]^{2-}$, e.g., $EL_{MeCN\text{-}BMP\text{-}Mn(III)\text{-}30}$. If "Cl" is included with the subscript, a 1:1 molar ratio of the cation chloride was added as in $EL_{MeCN\text{-}BMP\text{-}Cl\text{-}30}$ (cf. Table 1). An electrolyte marked with a * refers to an electrolyte, diluted with pure solvent to one half of the concentration of the active species.

2.2.5. Conductivity, Viscosity, and Ionicity

We investigated conductivity and viscosity of the all-MFB electrolytes based on $[BMP]_2[Mn^{II}Cl_4]$ and $[EMP]_2[Mn^{II}Cl_4]$ in GBL and MeCN. Both solvents have almost the same polarity (ε_{GBL} = 39.0; ε_{MeCN} = 36.64 at 25 °C), but differ in their viscosity (η_{GBL} = 1.738 cP; η_{MeCN} = 0.369 cP at 25 °C).[48,49] With respect to the diffusing entities, the larger $[BMP]^+$ ($V_{VdW,cat}$ 158 Å^3) and the smaller $[EMP]^+$ ($V_{VdW,cat}$ 124 Å^3) differ only slightly (chemical structures Figure S15, Supporting Information).[50] Overall, electrolytes based on more fluid MeCN and the smaller $[EMP]^+$ cation would be expected to perform better. Indeed, MeCN-electrolytes with $[EMP]^+$ showed the best conductivity and lowest viscosity of electrolytes tested (cf. Table 1). Therefore, and because it was the only solvent that allowed Mn film

Table 1. Abbreviations for the electrolytes used in this work and their physicochemical characteristics.

Electrolyte abbreviation[a)]	$[Cat]_2[MnCl_{4/5}]$	[Cat]Cl	$[Cat]_2[MnCl_4]$: [Cat]Cl (molar ratio)	Solvent [wt%]	c ($[MnCl_4]^{2-}$)/mol L^{-1}	Conductivity/mS cm^{-1} [T/°C]	Viscosity at 30 °C/cP
$EL_{GBL\text{-}BMP\text{-}50}$	$[BMP]_2[MnCl_4]$	–	–	GBL (50)	1.2	6.2 (30 °C)	13.9
$EL_{GBL\text{-}BMP\text{-}Mn(III)\text{-}50}$	$[BMP]_2[MnCl_5]$	–	–	GBL (50)	1.2	5.96 (30 °C)	14.6
$EL_{GBL\text{-}BMP\text{-}Cl\text{-}50}$	$[BMP]_2[MnCl_4]$	[BMP]Cl	1 : 1	GBL (50)	0.9	6.1 (31 °C)	14.9
$EL_{GBL\text{-}BMP\text{-}55}$	$[BMP]_2[MnCl_4]$	–	–	GBL (55)	1.1	6.08 (32 °C)	–
$EL_{GBL\text{-}BMP\text{-}Cl\text{-}55}$	$[BMP]_2[MnCl_4]$	[BMP]Cl	1 : 1	GBL (55)	0.8	6.07 (32 °C)	–
$EL_{GBL\text{-}BMP\text{-}Cl\text{-}55}{}^{*b)}$	$[BMP]_2[MnCl_4]$	[BMP]Cl	1 : 1	GBL (84)	0.4	–	–
$EL_{GBL\text{-}EMP\text{-}50}$	$[EMP]_2[MnCl_4]$	–	–	GBL (50)	1.4	8.59 (30 °C)	15.0
$EL_{GBL\text{-}EMP\text{-}Mn(III)\text{-}50}$	$[EMP]_2[MnCl_5]$	–	–	GBL (50)	1.3	9.46 (30 °C)	17.4
$EL_{GBL\text{-}EMP\text{-}Cl\text{-}58}$	$[EMP]_2[MnCl_4]$	[EMP]Cl	1 : 1	GBL (58)	1.0	10.57 (29 °C)	5.2
$EL_{GBL\text{-}EMP\text{-}Cl\text{-}58}{}^{*b)}$	$[EMP]_2[MnCl_4]$	[EMP]Cl	1 : 1	GBL (82)	0.5	–	–
$EL_{MeCN\text{-}BMP\text{-}30}$	$[BMP]_2[MnCl_4]$	–	–	MeCN (30)	1.6	12.6 (30 °C)	13.3
$EL_{MeCN\text{-}BMP\text{-}Mn(III)\text{-}30}$	$[BMP]_2[MnCl_5]$	–	–	MeCN (30)	1.5	9.22 (30 °C)	13.7
$EL_{MeCN\text{-}BMP\text{-}Cl\text{-}30}$	$[BMP]_2[MnCl_4]$	[BMP]Cl	1 : 1	MeCN (30)	1.1	11.7 (32 °C)	–
$EL_{MeCN\text{-}BMP\text{-}Cl\text{-}30}{}^{*b)}$	$[BMP]_2[MnCl_4]$	[BMP]Cl	1 : 1	MeCN (74)	0.55	–	–
$EL_{MeCN\text{-}EMP\text{-}50}$	$[EMP]_2[MnCl_4]$	–	–	MeCN (50)	1.2	30.1 (32 °C)	2.3
$EL_{MeCN\text{-}EMP\text{-}Mn(III)\text{-}50}$	$[EMP]_2[MnCl_5]$	–	–	MeCN (50)	1.1	30.6 (30 °C)	2.2

[a)]The electrolytes with the highest concentrations in Table 2 are close to the maximal concentration of the respective combination of salt and solvent; [b)]Electrolyte, diluted with pure solvent to one half of the concentration of the active species.

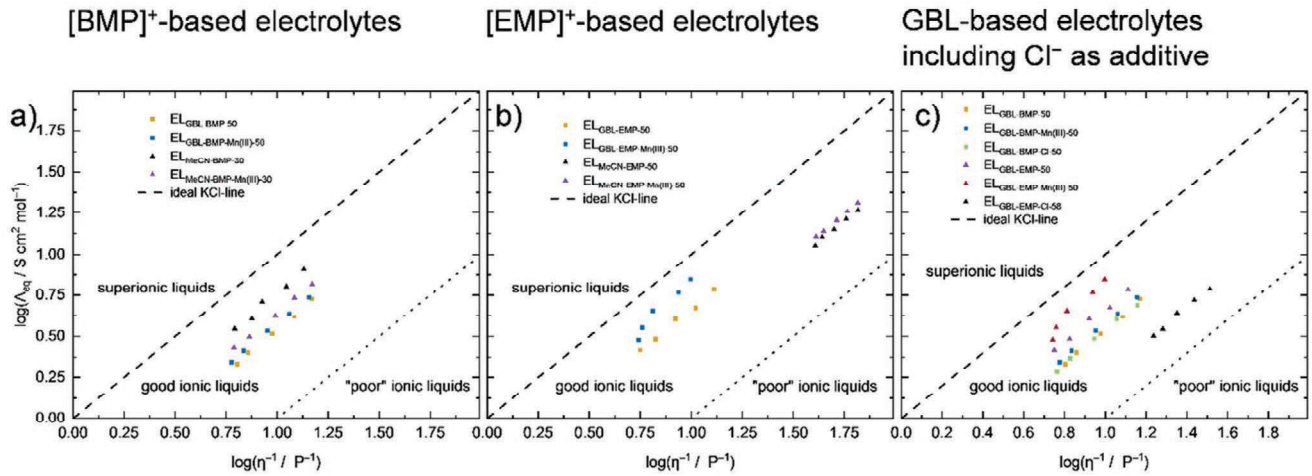

Figure 5. Walden plots for a) $EL_{GBL\text{-}BMP\text{-}50}$, $EL_{GBL\text{-}BMP\text{-}Mn(III)\text{-}50}$, $EL_{MeCN\text{-}BMP\text{-}30}$ and $EL_{MeCN\text{-}BMP\text{-}Mn(III)\text{-}30}$; b) $EL_{GBL\text{-}EMP\text{-}50}$, $EL_{GBL\text{-}EMP\text{-}Mn(III)\text{-}50}$, $EL_{MeCN\text{-}EMP\text{-}50}$ and $EL_{MeCN\text{-}EMP\text{-}Mn(III)\text{-}50}$, and c) $EL_{GBL\text{-}BMP\text{-}50}$, $EL_{GBL\text{-}BMP\text{-}Mn(III)\text{-}50}$, $EL_{GBL\text{-}BMP\text{-}Cl\text{-}50}$, $EL_{GBL\text{-}EMP\text{-}50}$, $EL_{GBL\text{-}EMP\text{-}Mn(III)\text{-}50}$, and $EL_{GBL\text{-}EMP\text{-}Cl\text{-}58}$.

formation during deposition, we decided to further use MeCN, despite not being desirable for a battery application. The alternative solvent GBL, was already used in Lithium ion batteries (LIBs) and is well-known for its low flammability and great electrochemical stability.[51–53] Figure S15 (Supporting Information) shows the Arrhenius plots of the ionic conductivity and viscosity of the $[BMP]^+$ and $[EMP]^+$ salts in GBL and MeCN. High ionic conductivity of the electrolyte is important at any state of charge (SoC). Thus, the corresponding $[Mn^{III}Cl_5]^{2-}$-salts, that dominate the ionic conductivity at higher SoCs, were also analyzed (Figure S15, Supporting Information). Comparing the for the battery cycling relevant electrolytes $EL_{MeCN\text{-}BMP\text{-}30}$ and $EL_{GBL\text{-}BMP\text{-}50}$ with similar viscosity (13.3 vs 13.9 cP), the doubled conductivity in MeCN (12.6 vs 6.2 mS cm^{-1} in GBL) in part originates from the higher concentration of $[BMP]_2[Mn^{II}Cl_4]$ accessible in MeCN (1.6 mol L^{-1} vs 1.2 mol L^{-1}). But apparently this does not reflect the entire change. Further insight is gained from a "Walden plot" (**Figure 5**), where $\ln(\Lambda_m)$ is plotted against $\ln(\eta)$. Because $[Cat]_2[Mn^{II}Cl_4]$ is a 2:1-salt we used the equivalent conductivity (Λ_{eq}) instead of the molar conductivity (Λ_m), otherwise a comparison to the ideal KCl-line would not be valid. In the Walden plot basing on Walden's rule Equation (4)

$$\Lambda_m \eta = \text{constant} \quad (4)$$

the location of the electrolyte compared to the ideal KCl-line is relevant. If an electrolyte lies on the ideal KCl-line, all ions are fully dissociated, move independently and contribute maximal to the ionic conductivity.[54] The further apart from the KCl-line the electrolyte, the more ion-pairing takes place. Comparing the $[BMP]^+$ salts in GBL and MeCN, the data points for $EL_{MeCN\text{-}BMP}$ are closer to the ideal KCl-line than $EL_{GBL\text{-}BMP}$. This higher ionicity of $EL_{MeCN\text{-}BMP}$ presumably contributes to their better conductivity in addition to their higher concentration. By contrast, the $[EMP]^+$ salts are more soluble in GBL than in MeCN, i.e., 1.4 mol L^{-1} versus 1.2 mol L^{-1}. Still the $EL_{MeCN\text{-}EMP}$ conductivity is much better than that of $EL_{GBL\text{-}EMP}$, apparently due to the much lower viscosity of the electrolytes with MeCN, e.g., $EL_{MeCN\text{-}EMP\text{-}50}$ at 2.3 versus 12.6 cP for $EL_{GBL\text{-}EMP\text{-}50}$ both containing 50 wt% solvent (cf. Table 1). Notably, the $EL_{MeCN\text{-}EMP\text{-}50}$ conductivity reaches more than 30 mS cm^{-1} for a 1.2 M solution. This is about three times higher than that of the optimized LP 30 LIB electrolyte (10.25 mS cm^{-1} @ 1.0 mol L^{-1} $Li[PF_6]$ in EC/DMC 1:1).[55] According to the Walden plots in Figure 5, the $[EMP]^+$ salts have a lower ionicity in MeCN than in GBL. Although $[BMP]^+$ and $[EMP]^+$ are structurally rather similar, the small volume difference of 34 $Å^3$ or 22% for $[EMP]^+$ results in huge changes toward the electrochemical properties of the electrolytes. Thus, tailor-made $[Mn^{II}Cl_4]^{2-}$ salts could further lift a great potential for optimized electrolyte properties. So far, $EL_{GBL\text{-}EMP\text{-}50}$ is the best candidate, just considering the ionicity. Referring to viscosity and conductivity $EL_{MeCN\text{-}EMP\text{-}50}$ exceeds the other electrolytes. Overall, $EL_{GBL\text{-}BMP\text{-}50}$ and $EL_{MeCN\text{-}BMP\text{-}30}$ are reasonable compromises concerning ionicity, conductivity, viscosity, and the availability of [Cat]Cl (where [BMP]Cl is quite a bit cheaper than [EMP]Cl).

Figure 5c also includes the electrolytes with additional [Cat]Cl in GBL. All electrolytes with $[EMP]_2[Mn^{II}Cl_4]$ in GBL show higher conductivity than the electrolytes with $[BMP]^+$. In the Walden plot, the $[EMP]^+$-based electrolyte with additional [EMP]Cl is further away from the ideal KCl-line as any of the $[BMP]^+$ based electrolytes. Therefore, we decided to analyze the $[BMP]^+$ salts more detailed because of the higher ionicity and the better comparability to the $EL_{MeCN\text{-}BMP\text{-}Cl\text{-}30}$. Besides, the conductivity of $EL_{GBL\text{-}BMP\text{-}Cl\text{-}50}$ (6.1 mS cm^{-1} at 31 °C) still lies at the bottom of the range of liquid electrolytes used in LIBs.[56] After the detailed electrochemical measurements with $EL_{GBL\text{-}BMP\text{-}Cl\text{-}50}$ we also performed a cycling experiment with more conducting $EL_{GBL\text{-}EMP\text{-}Cl\text{-}58}$ (10.57 mS cm^{-1} at 29 °C) to evaluate the differences.

2.3. Investigations in Static Battery Cells

For the identification of a suitable battery setup and first investigations of the different electrolytes, battery cycling experiments were performed in static cells with the FAPQ-375-PP AEM and the optimized electrolytes (Supporting Information). Additionally, the static cells need only 1.04 mL of electrolyte. In the flow cell, a minimum of 20 mL is needed just to fill the cell and the tubing, allowing to save material for orientation.

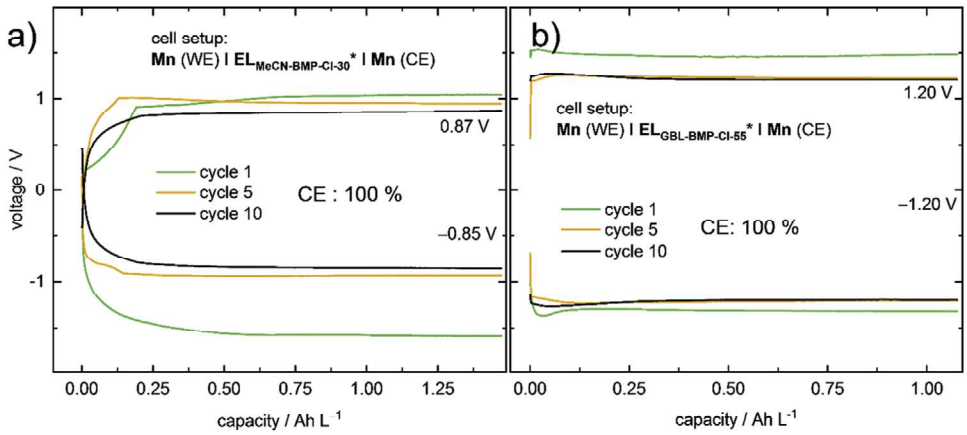

Figure 6. Half-cell experiments with a) $EL_{MeCN\text{-}BMP\text{-}Cl\text{-}30}$* using a Mn-WE and a Mn-CE d) $EL_{GBL\text{-}BMP\text{-}Cl\text{-}55}$* using a Mn-WE and a Mn-CE. All experiments were conducted with a current density of 0.25 mA cm^{-2}.

2.3.1. Half-Cell Experiments on Mn Deposition

To further investigate the deposition of manganese from $EL_{GBL\text{-}BMP\text{-}Cl\text{-}55}$* and $EL_{MeCN\text{-}BMP\text{-}Cl\text{-}30}$* half-cell experiments were conducted (**Figure 6**). Symmetrical cells with Mn^0 electrodes were built delivering an overpotential for the stripping and the deposition of Mn in $EL_{MeCN\text{-}BMP\text{-}Cl\text{-}30}$* that lies between 0.85 and 0.87 V. Since Mn is deposited on one electrode and stripped from the other, it is not possible to split the overpotential in a part for deposition and another part for stripping. Theoretically, both processes can be kinetically hindered. In the corresponding asymmetrical cell, where Mn was deposited on a Pt electrode, the potential for the Mn deposition on Pt and the simultaneous stripping of Mn is in the same region yielding +0.88 V (see Figure S22, Supporting Information). Since the Mn electrodes act as huge Mn reservoirs, the Mn|Mn-half-cell shows a CE of 100% over 10 cycles. Nevertheless, also this electrolyte does transform to a black suspension, due to "dead" manganese, showing that no stable Mn layer is formed during the deposition. At least, it clearly demonstrates that—favorably—the stripping of Mn takes place. $EL_{GBL\text{-}BMP\text{-}Cl\text{-}55}$* yields an even larger overpotential of 1.20 V for Mn deposition and stripping (Figure 6). The difference to $EL_{MeCN\text{-}BMP\text{-}Cl\text{-}30}$* is 0.33–0.35 V, which is also the difference between U_{SoC5} of respective full-cells measured with Pt electrodes (see Figure S16, Supporting Information). This could be a first hint that the measured overpotential is solely caused by the deposition of Mn, since anodic dissolution of Mn does not take place, while charging a full-cell. This is further supported by the LSV experiment (Figure S12, Supporting Information), which showed that the anodic dissolution of Mn is not hindered by any passivating effects. Although the conductivity of $EL_{MeCN\text{-}BMP\text{-}Cl\text{-}30}$ is almost twice as large as the conductivity of $EL_{GBL\text{-}BMP\text{-}Cl\text{-}55}$ at 32 °C (11.7 mS cm^{-1} vs 6.07 mS cm^{-1}), its influence on U_{SoC5} seems to be negligible.

2.3.2. Electrochemical Investigations of the $Mn^{II}|Mn^{III}$-Half-Cell

Unfortunately, we did not find a suitable half-cell experiment for the $Mn^{II}|Mn^{III}$-half-cell due to the lack of a suitable counter electrode. To learn more about the reversibility of the $[Mn^{II}Cl_4]^{2-}$/$[Mn^{III}Cl_5]^{2-}$ redox couple and the stability of $[Mn^{III}Cl_5]^{2-}$, **Figure 7** shows the CV of $EL_{GBL\text{-}BMP\text{-}50}$ with the current response of the $[Mn^{II}Cl_4]^{2-}$/$[Mn^{III}Cl_5]^{2-}$ couple at different scan rates (c = 1.2 mol L^{-1}; no supporting electrolyte).[57] Thus, the ratio of the cathodic and the anodic peak currents (i_{pc} and i_{pa}) was evaluated

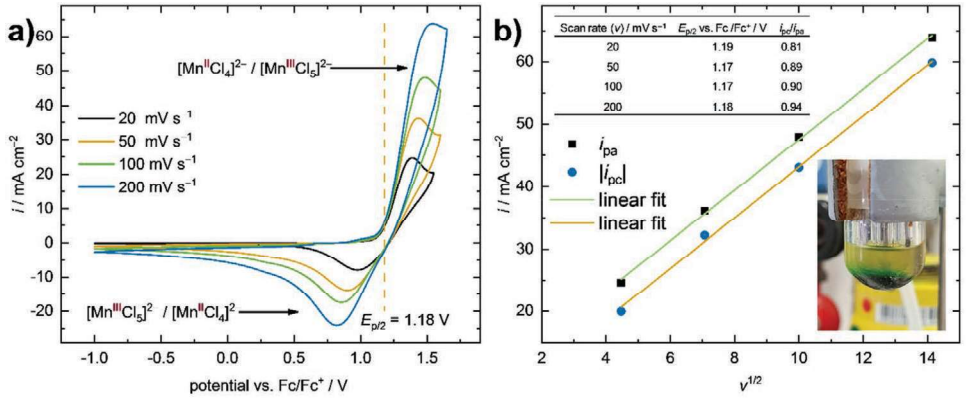

Figure 7. a) CV of $EL_{GBL\text{-}BMP\text{-}50}$ using a 1 mm Pt disc working electrode at different scan rates. b) Dependency of the peak currents (i_{pa} and i_{pc}) from the square root of the scan rate, independency of $E_{p/2}$ from the scan rate and a photograph of the CV cell after analyzing the $[Mn^{II}Cl_4]^{2-}$/$[Mn^{III}Cl_5]^{2-}$ redox couple, that shows the formation of a $[Mn^{III}Cl_5]^{2-}$ rich layer at the bottom of the cell due to its higher density.

for battery performance as it displays the possibility, if all of the electrochemically formed $[Mn^{III}Cl_5]^{2-}$ ions could be reduced. The ratio can be compared to the CE in a battery measurement, with a ratio of one being equivalent to a CE of 100% (Figure 7).

For the $[Mn^{II}Cl_4]^{2-}/[Mn^{III}Cl_5]^{2-}$ redox couple the i_{pa}/i_{pc} ratio increases from 0.81 to 0.94 with increasing scan rate. The i_{pa}/i_{pc} ratios were calculated according to Equation S8 (Supporting Information). This implies that 94% of the $[Mn^{III}Cl_5]^{2-}$ ions are again reduced to $[Mn^{II}Cl_4]^{2-}$ at a scan rate of 200 mV s^{-1}. At a scan rate of 20 mV s^{-1} this value is lower with 81%. This complies with the observation that the intense green coloration of the $[Mn^{III}Cl_5]^{2-}$ ion at the working electrode during the anodic scan moves away from the electrode through convection (Figure 7b) and suggests an increased density of the $[Mn^{III}Cl_5]^{2-}$ rich layer formed at the electrode. As a result, $[Mn^{III}Cl_5]^{2-}$ ions leave the diffusion layer in front of the electrode and are no longer available for the reduction to $[Mn^{II}Cl_4]^{2-}$ during the reverse scan. This behavior also explains why the i_{pa}/i_{pc} ratio is closer to one at faster scan rates, since the available time for the $[Mn^{III}Cl_5]^{2-}$ anion to leave the diffusion layer at the electrode is drastically lowered.[58] Yet, the $E_{p/2}$ versus Fc/Fc^+ of the $[Mn^{II}Cl_4]^{2-}/[Mn^{III}Cl_5]^{2-}$ couple at 1.18±0.01 V are independent from the scan rate and the peak currents (i_p) are proportional to the square root of the scan rate and indicate electrochemical reversibility (Figure 7). Since 94% of $[Mn^{III}Cl_5]^{2-}$ can be reduced at a scan rate of 200 mV s^{-1} and a clear trend toward an i_{pa}/i_{pc} ratio of one follows for increasing scan rates, the electrochemical reversibility of the $[Mn^{II}Cl_4]^{2-}/[Mn^{III}Cl_5]^{2-}$ redox couple is sufficient for the battery. In addition, the convection of the $[Mn^{III}Cl_5]^{2-}$ becomes irrelevant in a flow-cell, since a mixing of the electrolyte occurs in the storage tank and therefore, the availability of $[Mn^{III}Cl_5]^{2-}$ at the electrode during discharge of the battery is guaranteed at any time.

2.3.3. Electrode Material for the Positive Electrode

Due to its inertness and the possibility to combine it with felt electrodes, graphite is a very commonly used, economical inert electrode material used in the VRFB. But is it applicable as the positive electrode in the all-MFB? To keep the system during initial testing as simple as possible, planar plate electrodes were preferred over porous felt electrodes, given the caveat that higher current densities will not be achieved. **Figure 8** shows full cell cycling experiments to evaluate the hard-carbon TF6. Mn plates were used as counter electrodes, to ensure that enough Mn is available at any time to be oxidized during discharge.

For the $EL_{GBL\text{-}BMP\text{-}Cl\text{-}55}/EL_{GBL\text{-}BMP\text{-}Cl\text{-}55}{}^{*}$ cell U_{SoC5} is almost the same, regardless whether a TF6- or a Pt electrode is used. In both cases, a higher U_{SoC5} was observed during the first cycle compared to the 5th and 10th cycle. We attribute this to Mn deposition, since the same phenomenon was observed in the Mn|Mn-half-cells (Figure 6). However, a significant difference occurs in the voltage profiles of the discharge plateaus. Only one plateau was observed using TF6 as the positive electrode, which is exactly to be expected for a battery with one reversible electrochemical process at each electrode. With Pt used as the positive electrode, two clearly separated plateaus appeared, indicating that two different electrochemical processes took place

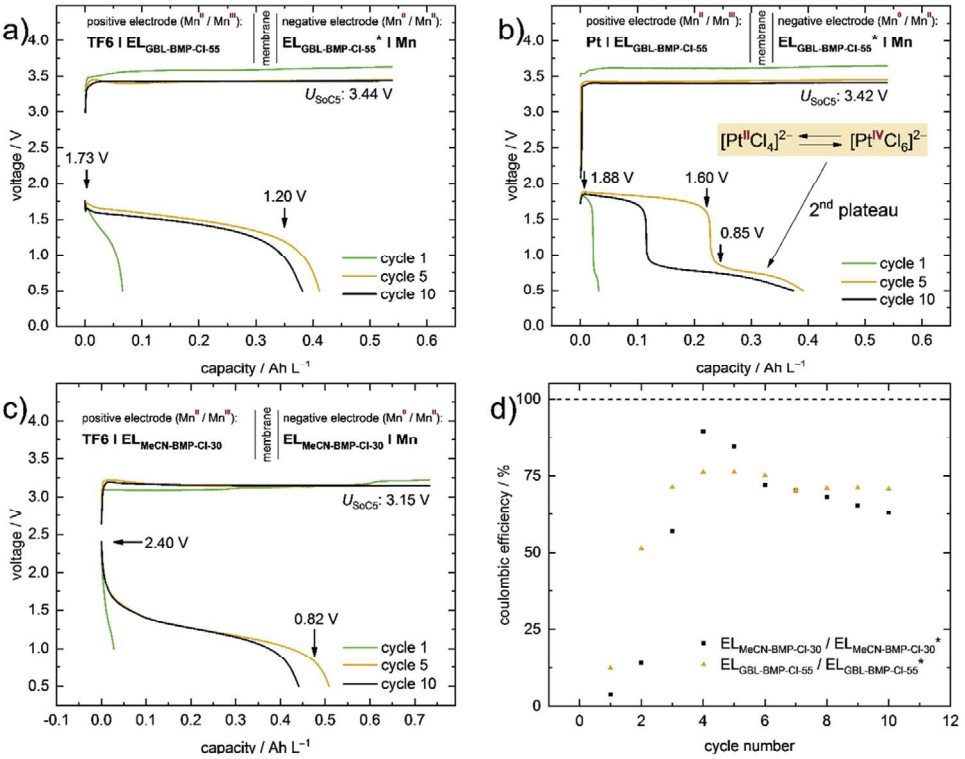

Figure 8. Cycling experiment with $EL_{GBL\text{-}BMP\text{-}Cl\text{-}55}/EL_{GBL\text{-}BMP\text{-}Cl\text{-}55}{}^{*}$ and a current density of 0.25 mA cm^{-2} a) using a graphite-WE (TF6) and a Mn-CE. b) Using a Pt-WE and a Mn-CE. c) Cycling experiment with $EL_{MeCN\text{-}BMP\text{-}Cl\text{-}30}/EL_{MeCN\text{-}BMP\text{-}Cl\text{-}30}$ and a current density of 0.5 mA cm^{-2} using a graphite-WE (TF6) and a Mn-CE. d) Coulombic efficiencies of the batteries described in (a) and (c).

during discharge. Since the negative electrode is exactly the same for both experiments these processes have to be located at the Pt electrode. We found that the Pt electrode is non-innocent under these conditions and reacts to give $[Pt^{II}Cl_4]^{2-}$ and $[Pt^{IV}Cl_6]^{2-}$. Thus, next to the reduction of $[Mn^{III}Cl_5]^{2-}$, $[Pt^{IV}Cl_6]^{2-}$ is reduced to $[Pt^{II}Cl_4]^{2-}$ during discharge, which is responsible for the 2nd plateau (see the Supporting Information for an extended section). However, with TF6 as electrode material, the intended cell reactions proceed, which means that it is suitable as electrode material and was therefore used in the following experiments. The CE of the TF6|Mn-full-cell reaches a plateau 70%, during the last four cycles. With Mn as negative electrode a CE of 100% should be expected, since the $[Mn^{II}Cl_4]^{2-}/[Mn^{I-II}Cl_5]^{2-}$ redox couple is completely reversible. This means that the reduced CE has to originate from elsewhere. $EL_{MeCN\text{-}BMP\text{-}Cl\text{-}30}$ shows a slightly reduced CE compared to the respective cell with $EL_{GBL\text{-}BMP\text{-}Cl\text{-}55}/EL_{GBL\text{-}BMP\text{-}Cl\text{-}55}$*. However, U_{SoC5} is advantageously reduced by 0.29 V in the cell with $EL_{MeCN\text{-}BMP\text{-}Cl\text{-}30}$.

2.3.4. Effect of EL-Concentration on Cycling

In the cell with $EL_{MeCN\text{-}BMP\text{-}Cl\text{-}30}$ (Figure 8), the same concentration of $[Mn^{II}Cl_4]^{2-}$ was used in both half cells. Since Mn deposition is a 2 e^- process and $[Mn^{II}Cl_4]^{2-}$ oxidation a 1 e^- process, $EL_{GBL\text{-}BMP\text{-}Cl\text{-}55}$* was used at the negative electrode, containing only half of the $[Mn^{II}Cl_4]^{2-}$ concentration compared to $EL_{GBL\text{-}BMP\text{-}Cl\text{-}55}$, used at the positive electrode.[59] Figure S26 (Supporting Information) shows a similar cycling experiment of a cell with $EL_{MeCN\text{-}BMP\text{-}Cl\text{-}30}$* at the negative electrode. Yet, using $EL_{MeCN\text{-}BMP\text{-}Cl\text{-}30}$* at the negative electrode resulted in a strong decrease of the CE. Over ten cycles the CE was between 12% and 22%, whereas in the cell with $EL_{MeCN\text{-}BMP\text{-}Cl\text{-}30}$ in both half cells the CE reached a plateau at 63%. This is a reduction of more than 40% compared to the cell presented in Figure 8. Apparently, $EL_{MeCN\text{-}BMP\text{-}Cl\text{-}30}$* has such a decreased viscosity compared to $EL_{MeCN\text{-}BMP\text{-}Cl\text{-}30}$, that the self-discharge through leaching is accelerated and leads to the observed decrease of the CE. Figure S27 (Supporting Information) shows the voltage profile and the CE of a cell with $EL_{GBL\text{-}BMP\text{-}Cl\text{-}55}$ in both half cells. Compared to the cell with $EL_{GBL\text{-}BMP\text{-}Cl\text{-}55}$ at the positive and $EL_{GBL\text{-}BMP\text{-}Cl\text{-}55}$* at the negative electrode (Figure 8) the CE is slightly higher. This further supports the assumption that a reduced viscosity of the electrolyte promotes leaching. But since the GBL based electrolytes are more viscous than the MeCN based electrolytes the effect is much weaker there, which might be an additional advantage of GBL with respect to MeCN.

2.3.5. Electrode Material for the Negative Electrode

Only the unfavorable deposition of Mn on various metal electrodes leading to either a mechanically unstable Mn film or no film at all were hitherto found. Therefore, we investigated graphite as a material for the negative electrode. From LIB work it is known that Mn deposition takes place on graphite, although it is not favored in this case.[60] In the next section only $EL_{GBL\text{-}BMP\text{-}Cl\text{-}55}/EL_{GBL\text{-}BMP\text{-}Cl\text{-}55}$* will be used to analyze the TF6|TF6 versus a TF6|Mn-full-cell cycling in **Figure 9**. U_{SoC5} decreases by 0.41 V compared to the full-cell with Mn as negative electrode, whereas the CE shows the same trend and reaches a plateau at 75% (Figure S28, Supporting Information). Unfortunately, the corresponding half-cell experiment for the deposition of Mn shows that unclear electrochemical reactions take place at the TF6 electrode during charging and discharging. Although a distinct voltage plateau is reached in the first cycle during the presumed deposition of Mn on TF6, an extreme drop in the charge voltage occurred at the beginning of the 5th and the 10th cycle. This was not observed in any other half-cell experiment so far and may be assigned to an alteration of the TF6 material during cycling. The photographs of the TF6 plate after cell-disassembly (Figure 9 and Figure S29: Supporting Information) prove this alteration. Upon charging the battery the electrolyte cations may intercalate into the TF6 material accompanied by electroreduction of the graphite. Upon battery discharge, the cations are removed leaving behind a strongly altered graphite surface. Possibly this facilitates intercalation in the next charge/discharge steps and may account for the drop in the charge voltage in the 5th and 10th cycle of the half-cell experiment.

Since Mn deposition is favored on graphite materials rather than the intercalation of Mn^{2+} ions, the intercalation of $[BMP]^+$ is suggested.[61,62,63] Intercalation into the TF6 material is

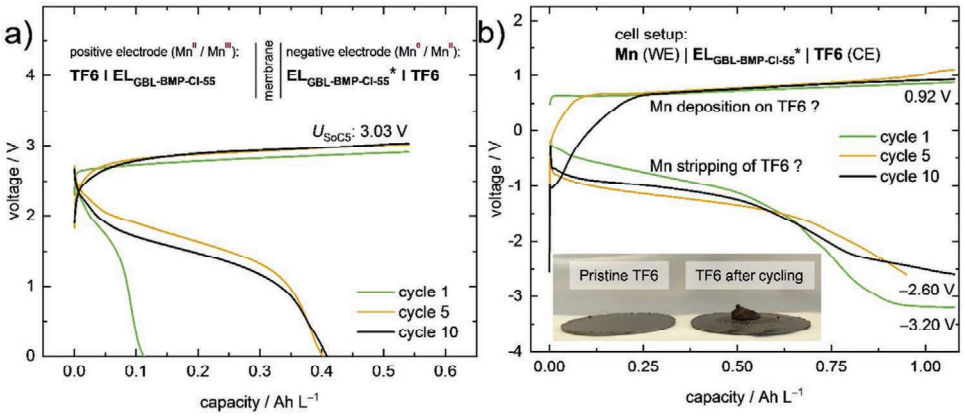

Figure 9. a) Full-cell cycling experiment with $EL_{GBL\text{-}BMP\text{-}Cl\text{-}55}/EL_{GBL\text{-}BMP\text{-}Cl\text{-}55}$* using a TF6 counter and working electrode. b) Half-cell experiment with $EL_{GBL\text{-}BMP\text{-}Cl\text{-}55}$* using a Mn working and a TF6 counter electrode. For both experiments a current density of 0.25 mA cm^{-2} was used.

further supported by the voltage profiles of the half-cell experiment that should belong to the stripping of manganese. No clear plateau is distinguishable. The voltage slowly decreases until it reaches −3.20 V in the first cycle. At this voltage the oxidation of $[Mn^{II}Cl_4]^{2-}$ should already take place and probably does. On the other hand, the SEM image of the Mn deposition on TF6 looks very similar to the images for the deposition on Cu and Pt. It is therefore also possible that Mn deposition takes place and the alteration of the TF6 surface is caused by another effect via an interaction of the TF6 material at negative potentials with the solvent. CV experiments with the electrochemically inert supporting electrolyte $[NBu_4][PF_6]$ (see Figure S30, Supporting Information) demonstrate that the TF6 surface is altered strongly at negative potentials, supporting the argument for intercalation of $[BMP]^+$ in a reduced TF6 electrode material.

2.3.6. SoC 80 Cycling

Previously, all cycling experiments to identify the most promising battery setup only aimed at a SoC of 5% to save time. With the large volume of the setup, the high energy content of the electrolytes and the low current density of 0.25 mA cm^{-2}, applicable with the planar electrodes, charging to SoC5 already took 2.4 h, while going to SoC100 (10.75 Ah L^{-1}) would take 47.1 h. After identifying our most promising static battery, the TF6|Mn-cell with $EL_{GBL\text{-}BMP\text{-}Cl\text{-}55}/EL_{GBL\text{-}BMP\text{-}Cl\text{-}55}$*, cycling between a SoC of 0 and 80% was performed. **Figure 10** shows the voltage profiles of the corresponding battery experiment.

When charging from SoC5 to SoC80, the voltage slowly rises by 0.25 V and reaches an U_{SoC80} of 3.69 V after the first cycle (Figure 10), apparently induced by overpotentials during Mn deposition. In the following cycles U_{SoC80} increased further from 3.69 to 3.98 V in the 7th cycle and later the cycling stopped by reaching the voltage limit of 4 V. In addition, Figure S25 (Supporting Information) shows that the cell resistance during the deposition of Mn increased from 77 to 143 Ω. Both may be attributed to the reduced Mn^0-particles that do not stick to the electrode surface and potentially block the pores of the membrane preventing the necessary charge transport. The CEs reduced to 16% and 35%, significantly lower compared to the SoC5 cycling experiment with CEs around 70% and probably due to serious self-discharge by $[Mn^{III}Cl_5]^{2-}$ leaching. More pronounced for SoC80, because one cycle takes 2.4 h for SoC5 but 37 h for SoC80. Apparently, through increased cell resistance and Mn^{III}-leaching the lower cut-off voltage is reached prior to full battery discharge. Secondary evidence stems from the intensely green-colored electrolyte (→ Mn^{III}) withdrawn from the Mn^{II}/Mn^{III}-half-cell, although the battery was disassembled presumably discharged with a cut-off voltage of 0.5 V reached.

2.3.7. Full Cell Battery Measurements with $[EMP]_2[Mn^{II}Cl_4]$ in GBL

Since the electrolyte with $[EMP]_2[Mn^{II}Cl_4]$ and [EMP]Cl in GBL ($EL_{GBL\text{-}EMP\text{-}Cl\text{-}58}/EL_{GBL\text{-}EMP\text{-}Cl\text{-}58}$*) has higher conductivity, lower viscosity, but also lower ionicity than $EL_{GBL\text{-}BMP\text{-}Cl\text{-}55}/EL_{GBL\text{-}BMP\text{-}Cl\text{-}55}$*, it appeared interesting to be used for a last static test series. Figure S31 (Supporting Information) shows the voltage profiles (SoC5) of the respective battery measurements and the corresponding CEs. Although U_{SoC5} is the same, the discharge plateau of the battery with $EL_{GBL\text{-}EMP\text{-}Cl\text{-}58}/EL_{GBL\text{-}EMP\text{-}Cl\text{-}58}$* is reduced by around 0.18 V. In addition, the OCV at SoC80 is reduced by 0.26 V compared to the cell with the $EL_{GBL\text{-}BMP\text{-}Cl\text{-}55}/EL_{GBL\text{-}BMP\text{-}Cl\text{-}55}$*. More drastic is the decrease of the CE, which is reduced around 40%. All these observations agree with the leaching of $[Mn^{III}Cl_5]^{2-}$ into the Mn^0/Mn^{II}-half-cell. Due to the much higher fluidity of $EL_{GBL\text{-}EMP\text{-}Cl\text{-}58}$ compared to $EL_{GBL\text{-}BMP\text{-}Cl\text{-}50}$ (5.8 vs 17.2 cP), this process is more dominant in $EL_{GBL\text{-}EMP\text{-}Cl\text{-}58}$ cells. Cycling between SoC0 and SoC80 with $EL_{GBL\text{-}EMP\text{-}Cl\text{-}58}/EL_{GBL\text{-}EMP\text{-}Cl\text{-}58}$* yielded a CE below 5%, which agrees with the further accelerated Mn^{III}-leaching in the more fluid electrolyte. Yet, the lower ionicity of $EL_{GBL\text{-}EMP\text{-}Cl\text{-}58}/EL_{GBL\text{-}EMP\text{-}Cl\text{-}58}$* does not influence the battery measurement.

2.4. Energy Density of All-MFB Electrolytes from Static Measurements

The practical energy densities realized for the all-MFB were investigated. For the theoretical specific capacities (C_s^{th}) of each half-cell (Equation (S2) Supporting Information) the only variable

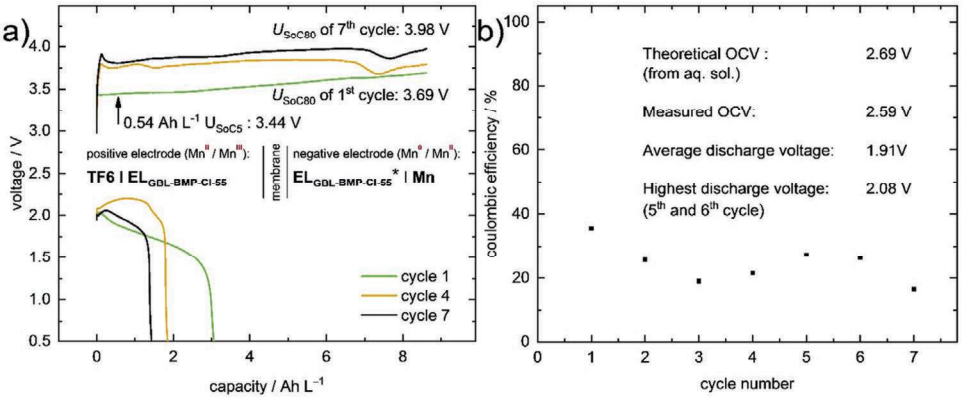

Figure 10. a) Voltage profiles of the TF6|Mn^0-full-cell with $EL_{GBL\text{-}BMP\text{-}Cl\text{-}55}/EL_{GBL\text{-}BMP\text{-}Cl\text{-}55}$* cycled between SoC0 and SoC80 with a current density of 0.25 mA cm^{-2}. The cycling between SoC0 and SoC80 was performed directly after the cycling between SoC0 and SoC5 with the same battery cell. b) Corresponding CEs and relevant parameters for the calculation of the energy density.

Table 2. Specific capacities (C_s) and energy densities (W_s) of different electrolytes tested throughout this work with a cell potential (E_{cell}) of 2.59 V.

Electrolyte		$c([Mn^{II}Cl_4]^{2-})$/mol L^{-1}		C_s/Ah L^{-1}		$C_{s,\,total}$/Ah L^{-1} [e]	$W_s(E_{cell} = 2.59\ V)$/[Wh L^{-1}]
Negative electrode[a]	Positive electrode[b]	Anolyte[c]	Catholyte[d]	Anol.	Cathol.	Anol. + Cathol.	Overall
$EL_{GBL\text{-}BMP\text{-}50}$	$EL_{GBL\text{-}BMP\text{-}50}$	1.2	1.2	64.3	32.2	21.4	55.5
$EL_{GBL\text{-}BMP\text{-}Cl\text{-}55}$	$EL_{GBL\text{-}BMP\text{-}Cl\text{-}55}$	0.8	0.8	42.9	21.4	14.3	37.0
$EL_{GBL\text{-}BMP\text{-}Cl\text{-}55}$	$EL_{GBL\text{-}BMP\text{-}Cl\text{-}55}$*	0.4	0.8	21.4	21.4	10.7	27.8
$EL_{MeCN\text{-}BMP\text{-}30}$	$EL_{MeCN\text{-}BMP\text{-}30}$	1.6	1.6	85.8	42.9	28.6	74.0
$EL_{MeCN\text{-}BMP\text{-}Cl\text{-}30}$	$EL_{MeCN\text{-}BMP\text{-}Cl\text{-}30}$	1.1	1.1	59.0	29.5	19.7	50.9
$EL_{GBL\text{-}EMP\text{-}50}$	$EL_{GBL\text{-}EMP\text{-}50}$	1.4	1.4	75.0	37.5	25.0	64.8
$EL_{GBL\text{-}EMP\text{-}Cl\text{-}58}$	$EL_{GBL\text{-}EMP\text{-}Cl\text{-}58}$	1.0	1.0	53.6	26.8	17.9	46.3

[a]Mn^0/Mn^{II}-half-cell; [b]Mn^{II}/Mn^{III}-half-cell; [c]anolyte = electrolyte at the negative electrode; [d]catholyte = electrolyte at the positive electrode; [e]Since a two-electron process takes place at the negative electrode, whereas a one-electron process is present at the positive electrode, the amount of anolyte is cut by half compared to the amount of catholyte. This has to be considered, when calculating the capacity ($C_{s,\,total}$) for the entire system. $C_{s,\,total}$ in Ah L^{-1} is one third of C_s for the anolyte, or two thirds of C_s for the catholyte.

is the active Mn^{II} concentration. **Table 2** shows their influence on C_s^{th}. For $[BMP]_2[Mn^{II}Cl_4]$ with MeCN ($EL_{MeCN\text{-}BMP\text{-}30}$) the largest, currently observed concentration of Mn^{II} (1.6 mol L^{-1}) was obtained. Yet, the addition of [Cat]Cl leads to a reduction of C_s^{th} from 21.4 to 14.3 Ah L^{-1} going from $EL_{GBL\text{-}BMP\text{-}50}$ to $EL_{GBL\text{-}BMP\text{-}Cl\text{-}55}$ and from 28.6 to 19.7 Ah L^{-1} going from $EL_{MeCN\text{-}BMP\text{-}30}$ to $EL_{MeCN\text{-}BMP\text{-}Cl\text{-}30}$. Nevertheless, addition of [Cat]Cl seems to be necessary to reduce overpotentials, but [EMP]Cl and [BMP]Cl might be replaced by other additives inducing smoother deposition and stripping at lower cost of active mass/concentration. Additionally, an optimized membrane would improve the charge transport of chloride ions and allow for a reduction of the [Cat]Cl additive. An alternative solvent may further improve concentration. A last point, the variation of the cation in $[Cat]_2[Mn^{II}Cl_4]$ offers an opportunity to increase concentrations.

A high cell voltage (E_{cell}) is also necessary for a good energy density (cf. Equation (S1) Supporting Information). Unfortunately, a theoretical cell potential, which is often used for the calculation of the energy densities, is not accessible from the CV in GBL due to the high overpotential of the deposition reaction and the absence of the manganese stripping. However, in MeCN a cell potential of 2.48 V was estimated from the CV in Figure S16 (Supporting Information), in which all relevant electrochemical processes were observed, albeit with the overpotentials such that the true cell potential could be even higher. In addition, the open circuit potential (OCV) of a charged cell with $EL_{MeCN\text{-}BMP\text{-}Cl\text{-}30}$ was measured fifteen minutes after the battery was charged to SoC80 (Figure S32, Supporting Information) displayed an OCV of 2.42 V – in pleasing agreement with the CV experiment. For the $EL_{GBL\text{-}BMP\text{-}Cl\text{-}55}/EL_{GBL\text{-}BMP\text{-}Cl\text{-}55}$* cell, the same measurement yielded an increased OCV of 2.59 V. Since the theoretical cell potential in aqueous solution with Mn^{II}/Mn^{III} and Mn^0/Mn^{II} redox couples is 2.69 V, we assume that 2.59 V as measured here is a very reasonable lower limit (SoC80[64]) for E_{cell}. So far, the best all-MFB battery with respect to the number of realized cycles used $EL_{GBL\text{-}BMP\text{-}Cl\text{-}55}/EL_{GBL\text{-}BMP\text{-}Cl\text{-}55}$*. The energy density of this electrolyte is 27.8 Wh L^{-1}, which is, compared to new, state of the art VRFBs that have up to 40 Wh L^{-1}, quite unspectacular.[65,66] Given the fact that the investigation of VRFBs has been going on for several decades now, the energy density we realized already is quite impressive. Moreover, the $[EMP]^+$ based electrolyte $EL_{GBL\text{-}EMP\text{-}Cl\text{-}58}$ (46.3 Wh L^{-1}) already exceeds the energy density of the VRFB, with the potential to reach 64.8 Wh L^{-1} by reducing the amount of the [Cat]Cl additive. The highest energy density of 74.0 Wh L^{-1} observed was found for $EL_{MeCN\text{-}BMP\text{-}30}$ with MeCN as a solvent (Table 2).

2.5. Investigations in a Pumped Flow-Cell

Figure 11 shows the single cell setup used for the investigations in a pumped flow-cell, despite the battery casing would allow a series connection of up to three cells. The short distance between the electrodes necessitates the utilization of graphite felt electrodes (GFA6, from SGL Carbon), otherwise the membrane and the TF6 bipolar plate come into contact due the deflection of the membrane caused by small differential pressure in both half-cells. TF6 was used as electrode material for the positive and the negative electrode, since a solid manganese plate in the required size would be too brittle and expensive. The temperature of the flow-cell can be kept at a constant level, using heating foil placed behind the current collectors. The atmosphere in the battery cell, as well as the tubing was kept inert with a vacuum pump and an argon port that can be used alternatingly. The electrolyte was transferred to the tanks in an argon filled glovebox, which was coupled to the rest of the system under inert conditions. All components – the battery cell, the pump, the electrolyte tanks and the entire tubing – were placed in a specially designed box, in which the temperature was kept constant during the measurements using a heat exchanger. Additionally, to keep the atmosphere inert, a constant flow of nitrogen was passed through the box. Since we observed that the filling level of the catholyte tank decreased during cycling, accompanied by an increased filling level of the anolyte tank, a third tank with pure solvent was introduced into the system that allowed to adjust the filling level of the catholyte tank under inert conditions. After using a concentrated electrolyte in the first experiment, we decided to use diluted electrolytes afterward, since the amount of $[Cat]_2[Mn^{II}Cl_4]$ needed, is very high. A more detailed description of the Flow-cell setup can be found in the Supporting Information (Figures S33, S34, and S35, Supporting Information). All electrolytes used in the flow-cell are summarized in **Table 3**.

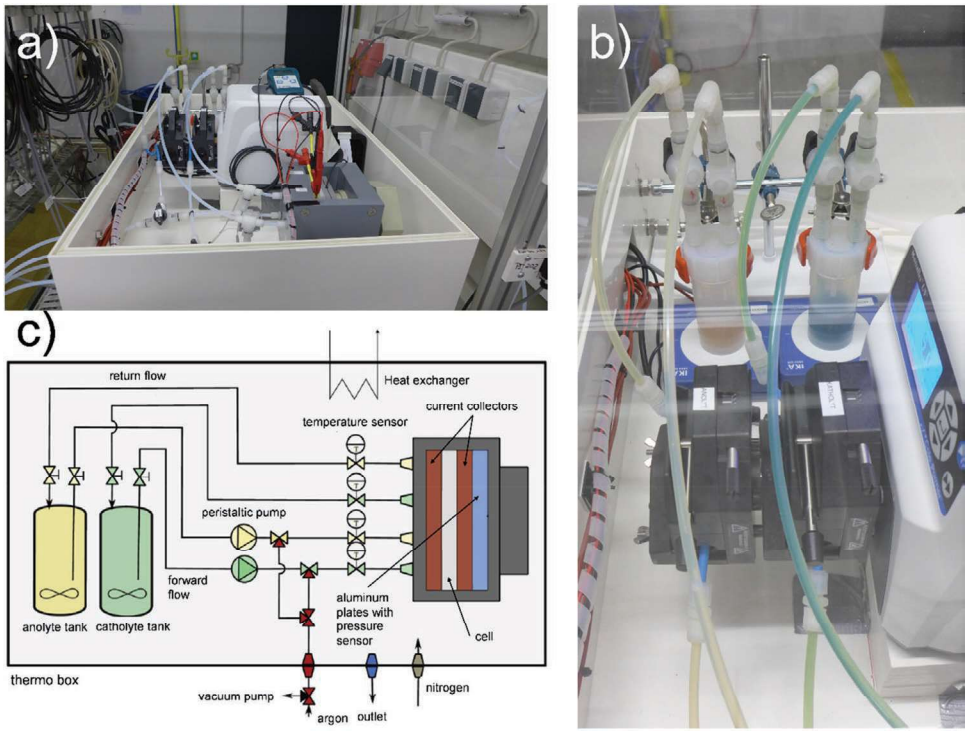

Figure 11. a) Setup for the measurements in a pumped flow-cell. b) Electrolyte tanks and tubing that display the characteristic colors of $[Mn^{II}Cl_4]^{2-}$ and $[Mn^{III}Cl_5]^{2-}$. c) Schematic view of the entire setup.

2.5.1. MeCN Based Electrolytes

MeCN had a series of negative effects on the materials, used for assembling the flow-cell, such as distorting PVDF frames and evaporating from the system during the experiment (see Figure S37, Supporting Information). Therefore, it was not possible to conduct a long-term cycling experiment with a MeCN based electrolyte. Nevertheless, we investigated the area specific resistance (ASR) and the cell potential (E_{cell}). The respective electrolytes, only differed in the Mn^{II} concentration (see Table 3). **Figure 12**a shows OCV measurements at SoC50 under various conditions. A stable voltage (U_{cell}) between 2.54 and 2.48 V was established for 69 h in the constantly pumped stack without felt electrodes with $EL_{MeCN\text{-}BMP\text{-}1.4}$ (blue line). This measurement, supports our estimations of E_{cell} of the all-MFB (CV: 2.48 V; OCV static cell: 2.42 V). After the measurement with a constant electrolyte flow, the pumps were stopped (orange line), showing that U_{cell} drops due to leaching immediately. A similar voltage drop appears, when the OCV of a static cell is measured in a charged state (see Figure S32, Supporting Information). In another experiment with low viscosity $EL_{MeCN\text{-}BMP\text{-}0.24}$ and felt electrodes a strong drop of U_{cell} was observed immediately after we stopped charging at SoC50, even though the electrolyte was pumped through the cell. Leaching seems to be enhanced through the felt electrodes, probably because $[Mn^{III}Cl_5]^{2-}$ is formed directly at the membrane. Although $EL_{MeCN\text{-}BMP\text{-}0.24}$ is diluted compared to $EL_{MeCN\text{-}BMP\text{-}1.4}$, we believe that the enhanced leaching can be assigned mainly to the utilization of the felt electrodes. This shows, that an optimized membrane is essential for the all-MFB because otherwise the round-trip efficiency suffers extremely. Figure 12b shows the ASR, determined at different temperatures, flow rates and with/without felt electrodes. The measurements with $EL_{MeCN\text{-}BMP\text{-}1.4}$ and different flow-rates showed a trend toward lower ASR-values at higher flow rates further reducing in going from 30°C to 40°C. A huge reduction of the ASR was observed with a diluted electrolyte and felt electrodes. Additionally, the ASR for charging and discharging the battery is at the same level if using felt electrodes. Without, the ASR for discharging was

Table 3. Abbreviations for the MeCN and GBL based electrolytes used in the flow-cell plus key parameters.

Electrolyte abbreviation	$[Cat]_2[Mn^{II}Cl_4]$	[Cat]Cl	$[Cat]_2[MnCl_4]$:[Cat]Cl (molar ratio)	Capacity[b]/Ah L^{-1}	c ($[Mn^{II}Cl_4]^{2-}$)/mol L^{-1}
$EL_{MeCN\text{-}BMP\text{-}1.4}$	$[BMP]_2[Mn^{II}Cl_4]$	–	–	18.76	1.40
$EL_{MeCN\text{-}BMP\text{-}0.24}$	$[BMP]_2[Mn^{II}Cl_4]$	–	–	3.22	0.24
$EL_{GBL\text{-}BMP\text{-}0.33\text{-}F}$[a]	$[BMP]_2[MnCl_4]$	–	–	4.39	0.33
$EL_{GBL\text{-}EMP\text{-}Cl\text{-}0.33\text{-}F/S}$[a]	$[EMP]_2[MnCl_4]$	[EMP]Cl	1:1	4.39	0.33

[a]The superscript -S or -F indicates, whether the measurements were performed in a static (-S) or a flow-cell (-F); [b]The volumetric capacity refers to the whole system (catholyte plus anolyte) and was calculated without the consideration of a two-electron process for the anolyte.

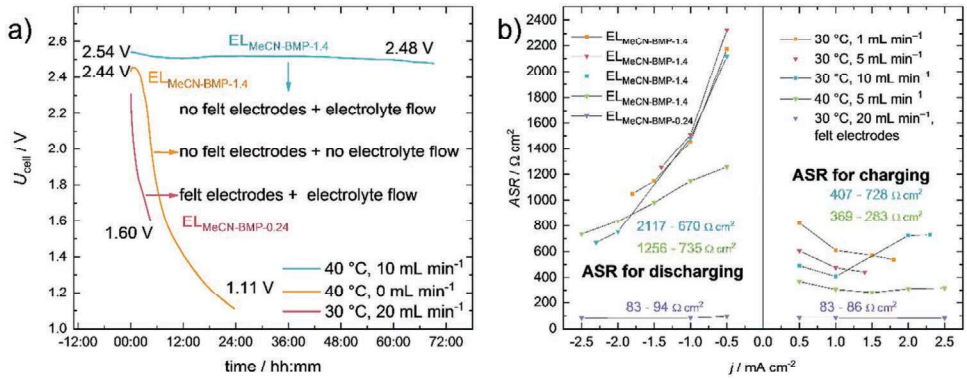

Figure 12. a) OCV measurements at SoC50. b) ASR measurements at SoC50.

significantly higher than for charging. Even with felt electrodes and a diluted electrolyte the ASR (82.6–94.4 Ω cm^2) is very high. Since it was established that an ASR < 5 Ω cm^2 is necessary for non-aqueous RFBs to be economically feasible,[67,68] the all-MFB is still far away from this requirement.

2.5.2. GBL Based Electrolytes

In contrast to the MeCN based electrolytes, two long-term cycling experiments with GBL based electrolytes were performed. Table 3 includes the key parameters of the two different electrolytes tested in the flow-cell. From $EL_{GBL\text{-}BMP\text{-}0.33}$ to $EL_{GBL\text{-}EMP\text{-}Cl\text{-}0.33}$ two essential modifications were made: The cation was changed from $[BMP]^+$ to $[EMP]^+$ in $[Cat]_2[MnCl_4]$ and additionally, [EMP]Cl was added as additive. With $EL_{GBL\text{-}EMP\text{-}Cl\text{-}0.33}$, 500 cycles over a period of two months were recorded. Table S20 (Supporting Information) shows the protocol used for the characterization of the electrolytes in a flow-cell. $EL_{GBL\text{-}EMP\text{-}Cl\text{-}0.33}$ was additionally tested in a static cell to evaluate the differences. **Figure 13** shows the corresponding results. Charging galvanostatically to SoC50 was not possible with $EL_{GBL\text{-}BMP\text{-}0.33\text{-}F}$, because the upper cutoff

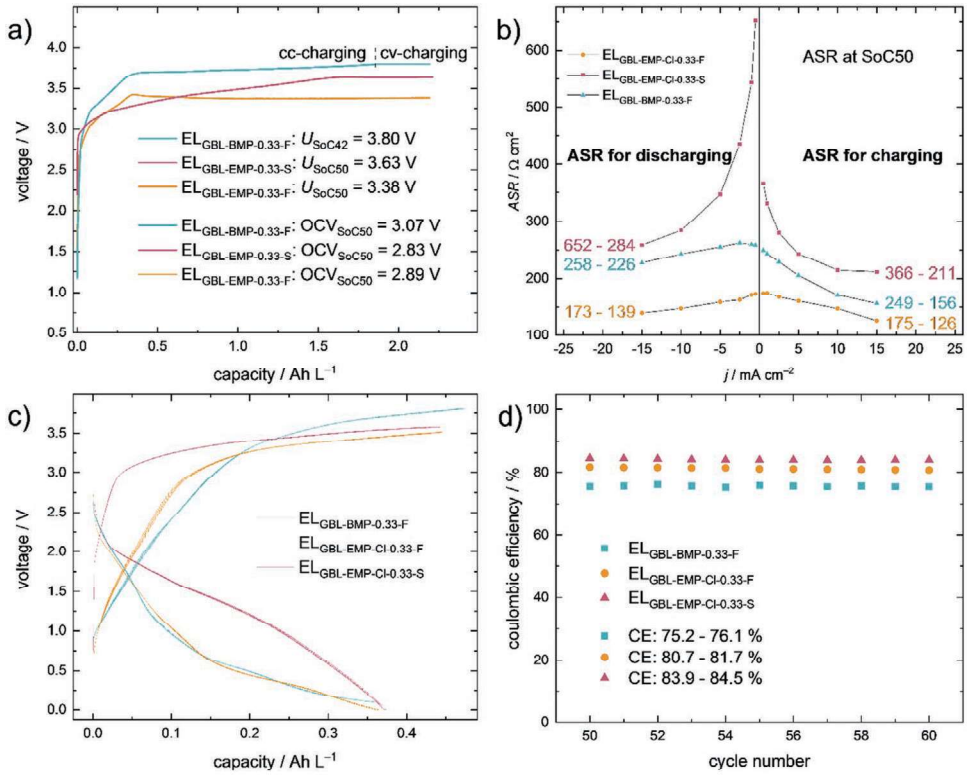

Figure 13. a) Voltage profiles of charging to SoC50 in a flow-cell with $EL_{GBL\text{-}BMP\text{-}0.33\text{-}F}$ and $EL_{GBL\text{-}EMP\text{-}Cl\text{-}0.33\text{-}F}$ and with $EL_{GBL\text{-}EMP\text{-}Cl\text{-}0.33\text{-}S}$ in a static cell. The current density was 1 mA cm^{-2} for each experiment. b) ASR at SoC50 for $EL_{GBL\text{-}BMP\text{-}0.33\text{-}F}$, $EL_{GBL\text{-}EMP\text{-}Cl\text{-}0.33\text{-}F}$ and $EL_{GBL\text{-}EMP\text{-}Cl\text{-}0.33\text{-}S}$. c) Voltage profiles of the cycles 50–60 of a cycling experiment, using 10%/11% of the capacity and a current density of 1.5 mA cm^{-2}. d) Corresponding coulombic efficiencies. For all experiments in the flow-cell a flow rate of 5 mL min^{-1} was used. The temperature for each experiment was 30 °C.

voltage (3.8 V) was reached at SoC42. To reach SoC50 the cell was further charged with a constant voltage of 3.8 V. The higher charging voltage, needed for $EL_{GBL\text{-}BMP\text{-}0.33\text{-}F}$ without extra [Cat]Cl compared to $EL_{GBL\text{-}EMP\text{-}Cl\text{-}0.33\text{-}F}$ is caused by the higher ASR at SoC50 for the applied current density (Figure 13b).

By contrast, using $EL_{GBL\text{-}EMP\text{-}Cl\text{-}0.33\text{-}F}$ with extra chloride resulted in a desired stable voltage plateau around 3.38 V (U_{SoC50}). This shows the improvements resulting from the utilization of $[EMP]^+$ instead of $[BMP]^+$ and the addition of [EMP]Cl, with $EL_{GBL\text{-}EMP\text{-}Cl\text{-}0.33\text{-}F}$ having a lower ASR at all current densities compared to $EL_{GBL\text{-}BMP\text{-}0.33\text{-}F}$. The ASR of $EL_{GBL\text{-}EMP\text{-}Cl\text{-}0.33\text{-}S}$ (static cell) at SoC50 is higher at all current densities, compared to both electrolytes tested in the pumped flow-cell, probably due to the utilization of felt electrodes in the flow-cell (v.i.) absent in the static cell. As a result, the stable voltage plateau using $EL_{GBL\text{-}EMP\text{-}Cl\text{-}0.33\text{-}S}$ is established later compared to $EL_{GBL\text{-}EMP\text{-}Cl\text{-}0.33\text{-}F}$ and also higher by 0.25 V, lying around 3.63 V (U_{Soc50}). Figure 13c shows the voltage profiles of the cycles 50–60 of the cycling experiments. The charge voltages (U_{SoC10}) follow the same order observed for U_{SoC50}. Favorably, while the voltages during discharge for $EL_{GBL\text{-}EMP\text{-}Cl\text{-}0.33\text{-}F}$ and $EL_{GBL\text{-}BMP\text{-}0.33\text{-}F}$ (flow-cell) are very similar, the voltage of $EL_{GBL\text{-}EMP\text{-}Cl\text{-}0.33\text{-}S}$ (static cell) is clearly higher. This is surprising, given the ASR for discharging is significantly higher for $EL_{GBL\text{-}EMP\text{-}Cl\text{-}0.33\text{-}S}$ compared to $EL_{GBL\text{-}BMP\text{-}0.33\text{-}F}$ and $EL_{GBL\text{-}EMP\text{-}Cl\text{-}0.33\text{-}F}$. Again, the utilization of felt electrodes in the pumped cell might be the reason for this. In the static cell, without the felt electrodes, the electrochemical reactions are spatially separated from the membrane. In the flow-cell, while charging, $[Mn^{III}Cl_5]^{2-}$ is formed directly at the membrane. This leads to a drastically decreased distance that has to be traveled by diffusion, for passing the membrane, which is probably accelerated further by the constant electrolyte flow in the flow-cell. Therefore, through leaching, $[Mn^{III}Cl_5]^{2-}$ enters the negative half-cell much faster in the flow-cell and can influence the voltage while discharging. This goes along very well with the observations made with $EL_{MeCN\text{-}BMP\text{-}0.24}$, where the introduction of felt electrodes also enhanced leaching. The assumption is further supported by the CE, which is 3% higher for $EL_{GBL\text{-}EMP\text{-}Cl\text{-}0.33\text{-}S}$ compared to $EL_{GBL\text{-}EMP\text{-}Cl\text{-}0.33\text{-}F}$. The higher CE in the static cell results from the reduced leaching. The 5% lower CE of $EL_{GBL\text{-}BMP\text{-}0.33\text{-}F}$ compared to $EL_{GBL\text{-}EMP\text{-}Cl\text{-}0.33\text{-}F}$ is probably caused by the higher ASR of $EL_{GBL\text{-}BMP\text{-}0.33\text{-}F}$. Thus, the lower cutoff voltage (0 V) is reached before the battery is discharged completely. During the experiments in the flow-cell, a decrease of the filling level in the catholyte tank (Mn^{II}/Mn^{III} half-cell) was observed, accompanied by an increase of the filling level in the anolyte tank (Mn^{II}/Mn^{0} half-cell), for both, $EL_{GBL\text{-}BMP\text{-}0.33\text{-}F}$ and $EL_{GBL\text{-}EMP\text{-}Cl\text{-}0.33\text{-}F}$. This phenomenon cannot be observed in a static cell, even if it takes place. The reason for the change in the filling levels is probably osmotic pressure, caused by an increasing number of ions in the anolyte while charging. For each manganese atom that is deposited, four chloride ions are released. On the other hand, the number of ions in the catholyte remains constant, since the chloride ions that pass the membrane for charge balancing react with $[Mn^{II}Cl_4]^{2-}$ to form $[Mn^{III}Cl_5]^{2-}$ upon oxidation. To continue cycling the battery, pure solvent was introduced to the system by a refill of the catholyte tank under inert conditions. For $EL_{GBL\text{-}BMP\text{-}0.33\text{-}F}$ this refill was necessary after 66 cycles, whereas for $EL_{GBL\text{-}EMP\text{-}Cl\text{-}0.33\text{-}F}$ the refill took place after cycle 207 (see **Figure 14**d), showing an improved cycling stability. Hence, the introduction of additional [Cat]Cl already improved this problem and gives hope that it can be overcome completely by adding optimized amounts of [Cat]Cl to the anolyte and the catholyte. Thus, $EL_{GBL\text{-}EMP\text{-}Cl\text{-}0.33}$ is superior to $EL_{GBL\text{-}BMP\text{-}0.33}$ concerning the ASR, the CE, and the cycling stability. Whether the different cation or the addition of [Cat]Cl has the larger impact cannot be distinguished, but we assume that both modifications have a significant participation.

2.5.3. Long Term Cycling

Figure 14 shows the results of the entire cycling experiment (500 cycles) with $EL_{GBL\text{-}EMP\text{-}Cl\text{-}0.33\text{-}F}$ with a refill of the catholyte tank with pure GBL after 207 cycles at 30°C. During these cycles the CE was between 61% and 83%, decreasing from 76% to 74% during the last 50 cycles before the GBL refill. During the following 13 cycles at 30 °C the CE was at 76% again. At 40 °C the CE dropped to 58%, probably caused by the increased mobility of $[Mn^{II}Cl_5]^{2-}$, resulting in an enhanced leaching. Back at 30 °C, the CE stabilized around 70% again. At 50 °C, the CE dropped even further to 21%, but started to increase after the temperature was set back to 30 °C after 18 cycles. When the capacity utilization (C_U) started to fade after 333 cycles from 10% to 2% over the next 170 cycles, the CE was again at 30%. At the end of the last 170 cycles the CE reached 75% again. Although the battery was cycled in a range of only 10% of the entire capacity, the number of cycles, before the capacity started to fade shows that the principle of using $[Mn^{II}Cl_4]^{2-}$ as active material in both half cells, to achieve a long lifetime of the battery, works. The ability to regenerate the CE after increased temperatures shows additionally that the system can tolerate harsh conditions. Figure 14e) shows the development of the ASR over the time of the whole experiment. During the first 207 cycles at 30 °C, the ASR increased, which is probably the reason for the slowly decreasing CE (83–74%). Refilling the catholyte tank with GBL did not influence the ASR. At 40 °C, the ASR is at its minimum during the entire experiment. However, the enhanced leaching prevents an improvement of the CE through the lower ASR. At 50 °C the ASR rises again, especially upon discharging. Afterwards at 30 °C the ASR is at its maximum. Figure 14c) shows a photograph of the membrane after the cycling experiment. A strong alteration of the originally white membrane surface to black/brown can be observed. It is therefore possible that the pores of the membrane became blocked by particles over the course of the experiment. This might explain the constantly rising ASR during the cycling and is probably also the reason for the decreasing capacity, starting after cycle 333. The TF6 material at the negative electrode showed the same type of alteration, observed during the measurements in the static cells, which might have an influence on the ASR as well.

Table 4 shows a comparison of the ASR with different electrolytes. Using $[EMP]^+$ and additional [Cat]Cl in $EL_{GBL\text{-}EMP\text{-}Cl\text{-}0.33\text{-}F}$ compared to $EL_{GBL\text{-}BMP\text{-}0.33\text{-}F}$ resulted in a significant decrease of the ASR. Still, the ASR with $EL_{GBL\text{-}EMP\text{-}Cl\text{-}0.33\text{-}F}$ is significantly higher compared to the ASR of $EL_{MeCN\text{-}BMP\text{-}0.24}$, although $[BMP]^+$ was used as a cation and no additional [Cat]Cl was added.

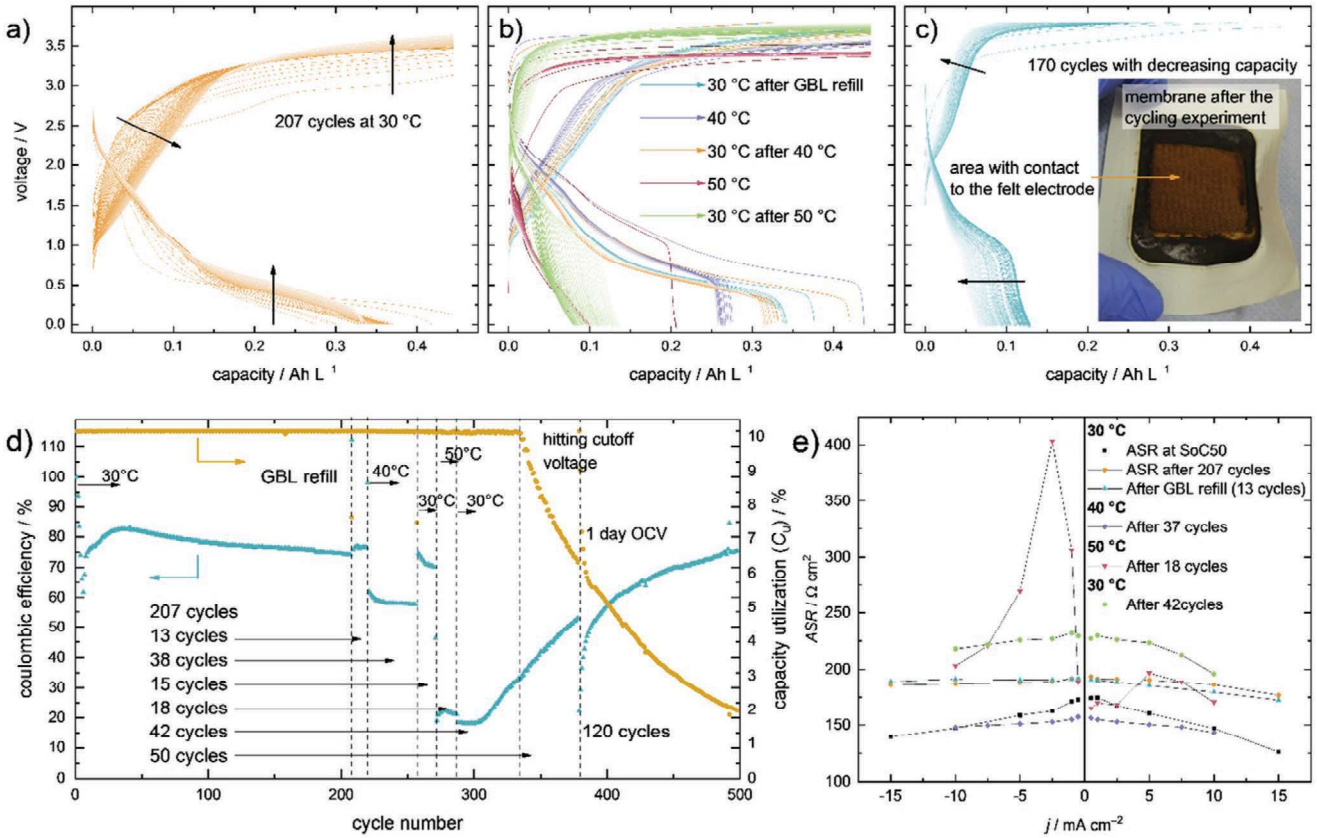

Figure 14. Voltage profiles with $EL_{GBL\text{-}EMP\text{-}Cl\text{-}0.33\text{-}F}$ using a current density of 1.5 mA cm^{-2}, a flow rate of 5 mL min^{-1} and a temperature of 30 °C. a) Cycles 1–207 b) cycles 208–333 c) cycles 331 to 500, while the capacity utilization (C_U) fades plus photograph of the membrane after the cycling experiment. d) Overview of the entire cycling experiment with $EL_{GBL\text{-}EMP\text{-}Cl\text{-}0.33\text{-}F}$ using a current density of 1.5 mA cm^{-2}, a flow rate of 5 mL min^{-1}. e) ASR measured at different moments during the cycling experiment.

2.6. Processes that Influence the Performance of the All-MFB

Figure 15 shows a comparison of the pumped flow-cell and a static battery cell using $EL_{GBL\text{-}EMP\text{-}Cl\text{-}0.33}$, TF6 as electrode material at the positive and the negative electrode and the FAPQ-375-PP membrane. Graphite felt electrodes were used additionally in the flow-cell (v.s.), whereas only the planar TF6 electrode material was used in the static battery cell. Figure 15a,b show the CE and the C_u of the two cells. Since a temperature control is not possible in the static cells, the measurement took place at ≈30 °C, whereas a temperature variation was conducted with the flow-cell (v.s.).

In both experiments the CE rises at the beginning, reaching a maximum after 14 cycles in the static cell and 41 cycles in the pumped flow-cell with CEs of 85.5% and 83.2%, respectively. After this maximum, the CE decreases slowly, reaching 79.0% (static) and 74.5% (pumped) after 200 cycles. In the flow-cell a GBL refill for the catholyte tank was necessary after cycle 207, and after cycle 220 the temperature variation started, which had a huge impact on the CE (see Figure 15b). Therefore, it is not possible to compare the CE any further after cycle 200. In the static cell however, the CE continues to decrease slowly ending at 74.2% at cycle 500. In the pumped flow-cell, the CE is slightly lower compared to the static cell (74.5–83.2% vs 79.0–85.5%). We explain this difference with the utilization of felt electrodes in the flow-cell. Due to the felt electrodes, the active species are generated directly next to the membrane, with the consequence that the distance that has to be travelled for leaching is drastically reduced. The enhanced leaching in the pumped flow-cell, caused by felt electrodes, is further supported by the observation of a strong drop in U_{cell} (Figure 12a, red line). Without felt electrodes, a stable U_{cell} can be observed for 69 h (Figure 12a, blue line). Apart from this difference, the behavior of the CE is in great accordance between the static cell and the

Table 4. Comparison of the ASR at SoC50 for different electrolytes in the flow-cell.

	ASR at SoC50 for charging/Ω cm^2	ASR at SoC50 for discharging/Ω cm^2	Solvent	$[Cat]^+$	Add. [Cat]Cl
$EL_{GBL\text{-}BMP\text{-}0.33\text{-}F}$	156–249	226–258	GBL	$[BMP]^+$	no
$EL_{GBL\text{-}EMP\text{-}Cl\text{-}0.33\text{-}F}$	126–175	139–173	GBL	$[EMP]^+$	yes
$EL_{MeCN\text{-}BMP\text{-}0.24}$	83–86	83–94	MeCN	$[BMP]^+$	no

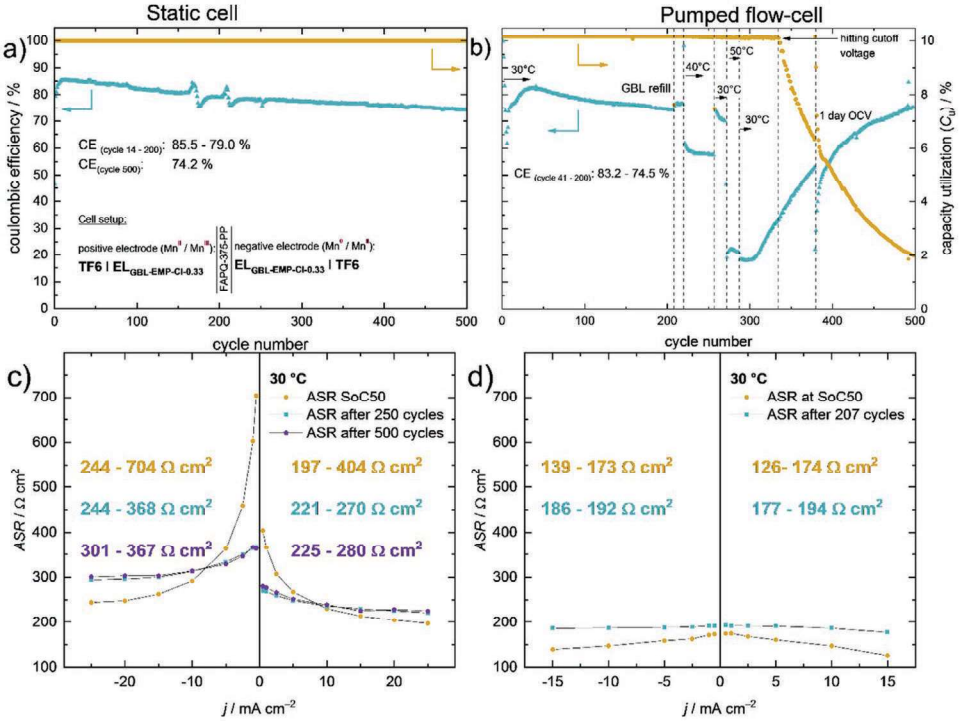

Figure 15. a) CE and C_u of a static battery cell with $EL_{GBL-EMP-Cl-0.33}$ over 500 cycles using a current density of 1.5 mA cm^{-2} at 30 °C. b) CE and C_u of a pumped flow-cell with $EL_{GBL-EMP-Cl-0.33}$ over 500 cycles using a current density of 1.5 mA cm^{-2} at different temperatures. c) ASR of a static battery cell with $EL_{GBL-EMP-Cl-0.33}$ at different moments during the cycling experiment. d) ASR of a pumped flow-cell with $EL_{GBL-EMP-Cl-0.33}$ at different moments during the cycling experiment.

pumped flow-cell. Nevertheless, CEs between 74.2% and 85.5% (static cell) are not satisfying, and have to be further improved. Although in a pumped setup, leaching is reduced to the electrolyte in the cell, when the pumps do not work (v.s.), it has to be reduced as much as possible to improve the overall efficiency.

2.7. Potential for Further CE-Optimization

During this work, the following parameters were identified having an impact on the CE: the membrane, the ASR and the Mn deposition.

2.7.1. Membrane

The impact, of different membranes on the CE is shown in Figure S13 (Supporting Information). A membrane that cannot prevent the leaching of $[Mn^{III}Cl_5]^{2-}$ into the negative half-cell contributes to a reduced CE, because the desired cell reactions occur chemically instead of electrochemically. Yet, the AEM FAPQ-375-PP is prone to leaching, but was the best alternative, we had at our disposal and with changing from FAPQ-310 (CE = 49.9%) to FAPQ-375-PP (CE = 88.4%) the CE already improved by 38.5%. Without any membrane, the CE was around 14.4%. The reduction of the CE between the SoC5 and the SoC80 cycling experiments (70% vs 35%) also shows the strong effect of leaching on the CE. With a membrane especially designed for the all-MFB, the CE could therefore be improved drastically.

2.7.2. ASR

Not only the CE, but also the C_u, can be improved with a reduction of the ASR. Figure 15c,d shows the ASR for the static, as well as the pumped flow-cell at different moments during the cycling experiment. In general, the ASR of the static cell is much higher compared to the ASR in the flow-cell, due to the utilization of felt electrodes and a constant electrolyte flow in the pumped flow-cell. Many parameters influence the ASR and we do not claim to cover all effects, but at least the ones we observed during this work. Table 4 shows, that the addition of [Cat]Cl, as well as the solvent have a huge impact on the ASR. With a MeCN based electrolyte ($EL_{MeCN-BMP-0.24}$), values between 83 and 94 Ω cm^2 were measured. Although the respective electrolyte did not contain extra [Cat]Cl, the ASR is already lower compared to a GBL based electrolyte with add. [Cat]Cl ($EL_{GBL-EMP-Cl-0.33}$; ASR = 126–175 Ω cm^2). The reason, appears to be the higher conductivity and lower viscosity of MeCN based electrolytes compared to GBL based electrolytes (cf. Table 1). Continuing the search for electrochemically stable solvents that show a good solubility of $[Cat]_2[Mn^{II}Cl_4]$, high conductivity and low viscosity, might be very rewarding. With a high ASR the CE is lower and the discharge of the battery is not complete, because the lower cut-off voltage is hit, before the battery is discharged completely. Often, a green catholyte ($[Mn^{III}Cl_5]^{2-}$) was withdrawn from the presumably discharged battery cells. Thus, a reduction of the ASR will improve the CE. The following parameters can also influence the ASR: the membrane, electrode materials, pre-treatment of the electrode materials, improved kinetics of the electrochemical reactions and the flow geometry.

2.7.3. Manganese Deposition

Experiments concerning the deposition of manganese (Figures 3, 4, and 6) showed that a mechanically unstable Mn layer is formed when the battery is charged. Manganese does not stick to the electrode ("dead" manganese). Therefore, it cannot be stripped during discharge, which leads to a reduction of the CE. However, the complexity of metal deposition is high and many parameters like temperature, current density, additives and more exist to influence these processes, maybe leading to a dense and stable Mn layer.[69] Yet, before that, a better suited electrode material has to be found. We already showed in this work, that TF6 is sub-optimal, since it is not electrochemically inert at the negative potential necessary for Mn deposition (Figure S30, Supporting Information). Still, many different types of graphite exist and a suitable variant for the deposition of Mn may become available. Since the LSV experiment (Figure S12, Supporting Information) suggests only limited passivation of the electrode surface during the anodic dissolution of Mn^0, we believe that the high overpotential of 0.85 to 0.87 V (see Figure 6), results mainly from the deposition of manganese, potentially due to its unusual elemental structure. The unfavorable electrochemical reduction of Mn^{II} as the dianion $[Mn^{II}Cl_4]^{2-}$, i.e., Coulomb repulsion at the negatively charged electrode, might be a reason for that. It could be overcome with the utilization of additives. Together with the other parameters, mentioned earlier, the high overpotential, which is much too high for technical application, could be reduced reaching acceptable energy efficiencies and higher CEs.

Despite a CE between 74.2% and 85.5% (static cell), we believe that the all-MFB is a very promising system. Approaching the key problems, discussed in this paragraph, we think that the performance of the all-MFB has the potential to be pushed to a level, where it becomes a serious competitor for EES.

3. Conclusion

In this work we investigated the feasibility of $[Cat]_2[Mn^{II}Cl_4]$ as an active material for the positive and the negative electrode of a hybrid-RFB, showing on a first principle level that the intended all-MFB works in a pumped flow-cell. **Figure 16** shows a schematic representation of the cell reactions, namely the oxidation of $[Mn^{II}Cl_4]^{2-}$ to $[Mn^{III}Cl_5]^{2-}$ at the positive electrode and Mn^0 deposition from $[Mn^{II}Cl_4]^{2-}$ at the negative electrode. Using different methods, including cyclic voltammetry, linear sweep voltammetry and symmetric half-cell experiments we showed that these reactions are electrochemically reversible in MeCN and GBL.

Using these solvents, electrolytes were developed for a systematic study in static battery cells, before testing the most promising electrolytes in an actual pumped flow-cell. Using temperature dependent viscosity and conductivity measurements, we showed that the performances of the electrolytes are comparable to electrolytes used in LIBs. According to Walden plots, derived from these measurements, an acceptable ionicity was observed, leaving room for further improvements. In the battery, the main problems, we identified are the formation of a mechanically unstable Mn film, a high overpotential (≈0.88 V) for the

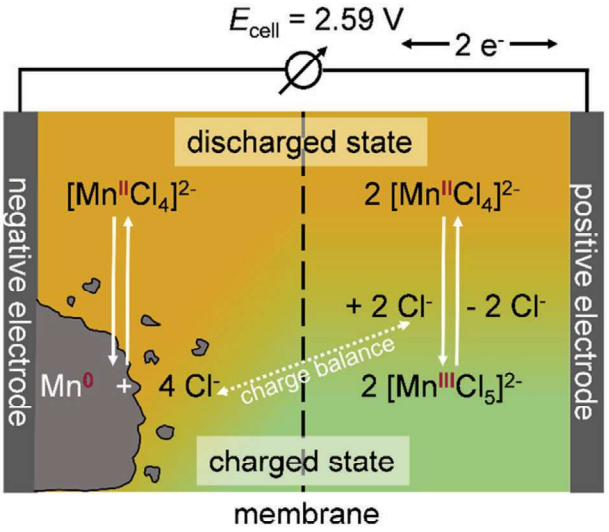

Figure 16. Schematic representation of the electrochemical processes taking place in the all-Mn battery, also showing the problems, namely leaching and Mn deposition.

deposition of manganese and the leaching of $[Mn^{II}Cl_5]^{2-}$ toward the negative electrode. Capacity fading, due to "dead" manganese, a low energy efficiency and a reduced CE (74.2–85.5% in a static cell) result. The mechanically unstable Mn film is caused by a cauliflower like deposition of manganese, shown with SEM measurements. However, for the formation of a mechanically stable Mn film and the reduction of the overpotential a broad variety of parameters can be optimized, such as the utilization of additives, alternative electrode materials, different pretreatments of the electrode materials, other solvents, conditioning cycles and so on. The leaching problem may be overcome with an optimized membrane, preventing $[Mn^{III}Cl_5]^{2-}$ from passing, but allowing chloride ions to do so. With an electrolyte based on $[EMP]_2[Mn^{II}Cl_4]$ energy densities up to 64.8 Wh L^{-1} are possible in GBL, whereas 74 Wh L^{-1} can be reached with a $[BMP]_2[Mn^{II}Cl_4]$ electrolyte in MeCN. A cell potential (E_{cell}) of 2.59 V and concentrations of up to 1.6 mol L^{-1} enable these energy densities. The straight forward synthesis of $[Cat]_2[Mn^{II}Cl_4]$, which was conducted on a 200 g scale, allows a variation of the cation and even the introduction of two different cations. This might lead to improved solubility and therefore to even higher energy densities. At the positive electrode, we identified graphite materials as suitable, whereas at the negative electrode the graphite is not electrochemically inert any more at the applied potentials, which was shown with CV measurements using an electrochemically inert supporting electrolyte. Apparently, intercalation of $[Cat]^+$ takes place, next to the deposition of manganese. In a pumped flow-cell, an electrolyte based on $[EMP]_2[Mn^{II}Cl_4]$ and [EMP]Cl in GBL (0.33 mol L^{-1}) was cycled over two months, with CEs up to 83%, which is comparable to the CE, observed in the static cells. 333 cycles were recorded with a capacity utilization (C_U) of 10% as designated, followed by 170 cycles with a fading C_U. This shows, that the principle of using $[Mn^{II}Cl_4]^{2-}$ as active material in both half-cells works, to achieve a long cycle life. The capacity fading, during the last 170 cycles probably resulted from the increasing area specific resistance (ASR) during the cycling. Therefore, the

upper cut-off voltage of 3.8 V was hit, before the battery could be charged to a C_U of 10%. It is possible that the electrolyte could be cycled further, but the ASR became too high for that. From this, and other experiments in the flow-cell, we learned that the ASR is too high in the all-MFB, already at the beginning of the cycling. With a MeCN based electrolyte an ASR between 83 and 94 Ω cm^2 was measured, which is still far away from 5 Ω cm^2, which has to be beaten for an economically feasible battery. However, a lot of parameters can be improved to further reduce the ASR. Since this is a first principle study, focusing on the question, whether an all-MFB is possible at all, we did not focus on the optimization of every parameter. The following parameters for reducing the ASR, starting with the most promising ones are: membrane/separator, electrode materials, pre-treatments of electrode materials, increased electrolyte conductivity and a mechanically stable manganese deposition. This lists the parameters, which are the most relevant ones in our opinion, but does not claim to be complete. Maybe other parameters like an optimized flow geometry might also have a huge impact. Compared to the benchmark VRFB system, the all-MFB has a higher energy density and is based on the cheap and abundant element manganese. Additionally, there is still a lot of room for improvements, making the all-MFB presented in this work an interesting field for further research.

Supporting Information

Supporting Information is available from the Wiley Online Library or from the author.

Acknowledgements

This work was supported by the Albert-Ludwigs-Universität of Freiburg, the FU Berlin and the BMBF in the project IL-RFB (FKZ 03SF0526A). A special thanks goes to Dr. Thilo Ludwig for measuring the pXRD and Anita Becherer for support in obtaining SEM-EDX measurements. The use of the SEM-EDX set up, acquired through the BMBF project EDELKAT (FKZ 03X5524), is gratefully acknowledged. The authors also thank Dr. Simon Steinhauer, Patrick Voßnacker and Thomas Keilhack from the FU Berlin as well as Dr. Valentin Radtke from Freiburg for helpful scientific discussions.

Open access funding enabled and organized by Projekt DEAL.

Conflict of Interest

The authors declare no conflict of interest.

Data Availability Statement

The data that support the findings of this study are available from the corresponding author upon reasonable request.

Keywords

anolytes, catholytes, manganese, non-aqueous, redox-flow batteries

Received: April 21, 2021
Published online: May 24, 2021

[1] P. Alotto, M. Guarnieri, F. Moro, *Renewable Sustainable Energy Rev.* **2014**, *29*, 325.
[2] E. Sánchez-Díez, E. Ventosa, M. Guarnieri, A. Trovò, C. Flox, R. Marcilla, F. Soavi, P. Mazur, E. Aranzabe, R. Ferret, *J. Power Sources* **2021**, *481*, 228804.
[3] Z. Yang, J. Zhang, M. C. W. Kintner-Meyer, X. Lu, D. Choi, J. P. Lemmon, J. Liu, *Chem. Rev.* **2011**, *111*, 3577.
[4] D. Larcher, J.-M. Tarascon, *Nat. Chem.* **2015**, *7*, 19.
[5] T. Kim, W. Song, D.-Y. Son, L. K. Ono, Y. Qi, *J. Mater. Chem. A* **2019**, *7*, 2942.
[6] X. Wei, W. Pan, W. Duan, A. Hollas, Z. Yang, B. Li, Z. Nie, J. Liu, D. Reed, W. Wang, V. Sprenkle, *ACS Energy Lett.* **2017**, *2*, 2187.
[7] Y. Liang, H. Dong, D. Aurbach, Y. Yao, *Nat. Energy* **2020**, *5*, 646.
[8] H. Chen, T. N. Cong, W. Yang, C. Tan, Y. Li, Y. Ding, *Prog. Nat. Sci.* **2009**, *19*, 291.
[9] Á. Cunha, J. Martins, N. Rodrigues, F. P. Brito, *Int. J. Energy Res.* **2015**, *39*, 889.
[10] Q. Huang, Q. Wang, *ChemPlusChem* **2015**, *80*, 312.
[11] R. Borah, F. R. Hughson, J. Johnston, T. Nann, *Mater. Today Chem.* **2020**, *6*, 100046.
[12] D. K. Walanda, G. A. Lawrance, S. W. Donne, *J. Power Sources* **2005**, *139*, 325.
[13] A. E. S. Sleightholme, A. A. Shinkle, Q. Liu, Y. Li, C. W. Monroe, L. T. Thompson, *J. Power Sources* **2011**, *196*, 5742.
[14] J. Lu, D. Dreisinger, T. Glück, *Hydrometallurgy* **2014**, *141*, 105.
[15] C. R. Groom, I. J. Bruno, M. P. Lightfoot, S. C. Ward, *Acta Crystallogr., Sect. B: Struct. Sci., Cryst. Eng. Mater.* **2016**, *72*, 171.
[16] P. C. Moews, *Inorg. Chem.* **1966**, *5*, 5.
[17] R. A. Lalancette, N. Elliott, I. Bernal, *J. Cryst. Mol. Struct.* **1972**, *2*, 143.
[18] G. Bergerhoff, I. D. Brown, *Crystallographic Databases*.
[19] R. J. H. Clark, T. M. Dunn, *J. Chem. Soc.* **1963**, 1198.
[20] H. G. M. Edwards, M. J. Ware, L. A. Woodward, *Chem. Commun.* **1968**, 540.
[21] H. G. M. Edwards, L. A. Woodward, M. J. Gall, M. J. Ware, *Spectrochim. Acta* **1970**, *26*, 287.
[22] S. Pitula, A.-V. Mudring, *Chem. – Eur. J.* **2010**, *16*, 3355.
[23] J.-C. Chang, W.-Y. Ho, I.-W. Sun, Y.-K. Chou, H.-H. Hsieh, T.-Y. Wu, *Polyhedron* **2011**, *30*, 497.
[24] F. A. Cotton, L. M. Daniels, P. Huang, *Inorg. Chem.* **2001**, *40*, 3576.
[25] H. Mashiyama, N. Koshiji, *Acta Crystallogr., Sect. B: Struct. Sci.* **1989**, *45*, 467.
[26] A. R. Parent, C. P. Landee, M. M. Turnbull, *Inorg. Chim. Acta* **2007**, *360*, 1943.
[27] N. S. Gill, R. S. Nyholm, *J. Chem. Soc.* **1959**, 3997.
[28] C. F. Bell, D. N. Waters, *J. Inorg. Nucl. Chem.* **1977**, *39*, 773.
[29] W. Levason, C. A. McAuliffe, *Dalton Trans.* **1973**.
[30] Y. Rojas, M. Tadrosse, C. Assaf, I. Bernal, R. A. Lalancette, *Struct. Chem.* **2020**, *31*, 1309.
[31] M. Matsui, S. Koda, S.'i. Ooi, H. Kuroya, I. Bernal, *Chem. Lett.* **1972**, *1*, 51.
[32] I. Bernal, N. Elliott, R. Lalancette, *J. Chem. Soc. D* **1971**, *0*, 803.
[33] S. Walha, H. Naili, S. Yahyaoui, B. F. Ali, M. M. Turnbull, T. Mhiri, T. Bataille, *Solid State Sci.* **2011**, *13*, 204.
[34] R. F. Weinland, P. Dinkelacker, *Z. Anorg. Chem.* **1908**, *60*, 173.
[35] J. Sniekers, J. C. Malaquias, L. van Meervelt, J. Fransaer, K. Binnemans, *Dalton Trans.* **2017**, *46*, 2497.
[36] J.-K. Chang, C.-H. Huang, W.-T. Tsai, M.-J. Deng, I.-W. Sun, P.-Y. Chen, *Electrochim. Acta* **2008**, *53*, 4447.
[37] S. Zein El Abedin, E. M. Moustafa, R. Hempelmann, H. Natter, F. Endres, *ChemPhysChem* **2006**, *7*, 1535.
[38] J. S. Avery, C. D. Burbridge, D. M. L. Goodgame, *Spectrochim. Acta* **1968**, *24*, 1721.
[39] F. A. Cotton, D. M. L. Goodgame, M. Goodgame, *J. Am. Chem. Soc.* **1962**, *84*, 167.

[40] T. S. Davis, J. P. Fackler, M. J. Weeks, *Inorg. Chem.* **1968**, *7*, 1994.
[41] A. F. Holleman, E. Wiberg, N. Wiberg, *Lehrbuch der anorganischen Chemie*, de Gruyter, Berlin **2007**.
[42] A. M. Bond, E. A. McLennan, R. S. Stojanovic, F. G. Thomas, *Anal. Chem.* **1987**, *59*, 2853.
[43] W. D. Sides, Q. Huang, *Electrochim. Acta* **2018**, *266*, 185.
[44] Since we were mainly interested whether a deposition is possible, we did not focus on the exact potential and used a Pt-wire as a quasi-reference electrode, which is sufficient for such experiments.
[45] J. A. Oberteuffer, J. A. Ibers, *Acta Crystallogr., Sect. B: Struct. Sci.* **1970**, *26*, 1499.
[46] S. SASAKI, K. FUJINO, Y. TAKÉUCHI, *Proc. Jpn. Acad., Ser. B* **1979**, *55*, 43.
[47] A. P. Abbott, G. Frisch, J. Hartley, W. O. Karim, K. S. Ryder, *Prog. Nat. Sci.* **2015**, *25*, 595.
[48] D. R. Lide, in *CRC Handbook of Chemistry and Physics*, CRC Press, Boca Raton, FL **2007**, p. 2006.
[49] D. H. S. Ramkumar, A. P. Kudchadker, *J. Chem. Eng. Data* **1989**, *34*, 463.
[50] W. Beichel, P. Eiden, I. Krossing, *ChemPhysChem* **2013**, *14*, 3221.
[51] J. Kasnatscheew, R. W. Schmitz, R. Wagner, M. Winter, R. Schmitz, *J. Electrochem. Soc.* **2013**, *160*, A1369.
[52] R. W. Schmitz, P. Murmann, R. Schmitz, R. Müller, L. Krämer, J. Kasnatscheew, P. Isken, P. Niehoff, S. Nowak, G.-V. Röschenthaler, N. Ignatiev, P. Sartori, S. Passerini, M. Kunze, A. Lex-Balducci, C. Schreiner, I. Cekic-Laskovic, M. Winter, *Prog. Solid. State Chem.* **2014**, *42*, 65.
[53] N. Takami, T. Ohsaki, H. Hasebe, M. Yamamoto, *J. Electrochem. Soc.* **2002**, *149*, A9.
[54] D. R. MacFarlane, M. Forsyth, E. I. Izgorodina, A. P. Abbott, G. Annat, K. Fraser, *Phys. Chem. Chem. Phys.* **2009**, *11*, 4962.
[55] M. Schleep, S. Reininger, P. Eiden, P. Klose, C. Schulz, H. Scherer, S. Laule, S. Bodendorfer, M. Schmidt, A. Garsuch, I. Krossing, *ChemElectroChem* **2016**, *3*, 774.
[56] J. B. Goodenough, Y. Kim, *Chem. Mater.* **2010**, *22*, 587.
[57] Therefore, it is possible that migration of the electrochemically active species is not eliminated during the measurement. Strictly, it is therefore not possible to apply the common diagnostic criteria to evaluate the reversibility of the $[Mn^{II}Cl_4]^{2-}/[Mn^{III}Cl_5]^{2-}$ redox couple. Nevertheless, in the absence of a theory that would describe such a system we decided to use the existing criteria. Measuring the CVs with the concentrated solution of the electrolyte is in our opinion more relevant considering that a very diluted solution with additional supporting electrolyte does not represent the actual situation in a battery.
[58] Additionally, a small amount of the formed $[Mn^{III}Cl_5]^{2-}$ will react with the platinum of the WE (see Supporting Information), and therefore not be available for a reduction towards $[Mn^{II}Cl_4]^{2-}$, further reducing the i_{pa}/i_{pc}-ratio.
[59] In an actual RFB the same $[Mn^{II}Cl_4]^{2-}$-concentrations would be used in both half-cells to prevent any problems due to osmotic pressure. Unfortunately, in our practical setup we had to use the same amount of electrolyte in each half-cell and therefore decided to use a reduced concentration at the negative electrode. By doing this we mimic the effect that the $[Mn^{II}Cl_4]^{2-}$-concentration decreased during the charge of the battery. Otherwise we would have an excess of $[Mn^{II}Cl_4]^{2-}$ at any time at the negative electrode.
[60] Y. K. Lee, J. Park, W. Lu, *J. Electrochem. Soc.* **2017**, *164*, A2812.
[61] S. Komaba, N. Kumagai, Y. Kataoka, *Electrochim. Acta* **2002**, *47*, 1229.
[62] Y. Maeda, P. Touzain, *Electrochim. Acta* **1988**, *33*, 1493.
[63] pXRD investigations of the affected TF6 material were not conclusive. If dismounted in the potentially charged state, the pXRD signatures were very broad and did at least give no clear evidence for any Mn-intercalation. If the $[BMP]^+$ cation was intercalated, the material is amorphous and not visible in pXRD.
[64] At SoC100 an even higher value of E_{cell} can be expected according to the Nernst equation.
[65] Y. Cheng, X. Wang, S. Huang, W. Samarakoon, S. Xi, Y. Ji, H. Zhang, F. Zhang, Y. Du, Z. Feng, S. Adams, Q. Wang, *ACS Energy Lett.* **2019**, *4*, 3028.
[66] L. Li, S. Kim, W. Wang, M. Vijayakumar, Z. Nie, B. Chen, J. Zhang, G. Xia, J. Hu, G. Graff, J. Liu, Z. Yang, *Adv. Energy Mater.* **2011**, *1*, 394.
[67] J. D. Milshtein, J. L. Barton, T. J. Carney, J. A. Kowalski, R. M. Darling, F. R. Brushett, *J. Electrochem. Soc.* **2017**, *164*, A2487.
[68] R. M. Darling, K. G. Gallagher, J. A. Kowalski, S. Ha, F. R. Brushett, *Energy Environ. Sci.* **2014**, *7*, 3459.
[69] A. P. Abbott, G. Frisch, K. S. Ryder, *Annu. Rev. Mater. Sci.* **2013**, *43*, 335.

4. Conclusion

The theory concerning the synthesis and electrochemical characteristics of ionic liquids, as low temperature salt melts, has been thoroughly discussed. The chemical and physicochemical characteristics of ionic liquids such as conductivity, viscosity, and diffusion, are heavily dependent upon the individual substituents in each cation and anion. The resulting diversity in chemical characteristics makes ionic liquids useful in a wide variety of applications, especially in metal recycling, Li-ion batteries and redox-flow batteries. Of particular interest were the polyhalogen monoanion ($[X_n]^-$; X = Cl, Br, I, n = odd) and halidometallate anion ($[MX_n]^-$; M = Sn, Mn, X = Cl, Br, n = 3 – 5) based ionic liquids as active species in metal recycling and the development of a non-aqueous redox-flow battery as an alternative to the current vanadium redox-flow battery.

Neat ionic liquids benefit from being liquid ionic media that do not need additional solvents for reactions. Due to the lack of solvent, the energy density and amount of active material per unit volume is relatively large compared to solvent based chemistry. This property was beneficial in metal recycling with the polyhalogen monoanion based ionic liquids because the amount of total electrolyte is comparatively smaller to aqueous methods. This is especially important given that useful metals such as Au, Cu, Sn, or Pt can be recycled in ionic liquids. Additionally, in regards to polyhalogen monoanion based ILs there diffusion properties are based on a Grotthuss style mechanism leading to greater conductivity, diffusion rates, and therefore faster reaction times with the relevant metal species.

Current redox-flow batteries are typically based on vanadium or zinc as the active species, but in ionic liquids two halidometallate based sources are available, $[Cat.][AlBr_4]$ and $[Cat.]_2[MnCl_4]$. The all manganese redox-flow battery based around $[Cat.]_2[MnCl_4]$ is very promising due again to the high energy density of ionic liquids, the cell voltage between Mn(0)/Mn(II) and Mn(II)/Mn(III), and the relative abundance of manganese. Given the current demand for higher voltage, more efficient energy storage devices, in regards to the changing world climate, using an ionic liquid active species as an electrolyte in future battery chemistries could provide promising results.

By furthering research in the field of ionic liquids, in particular, that of the strongly oxidizing polyhalogen monoanions and the energy dense halidometallate anion based ionic liquids, progress was made towards reducing waste through metal recycling, and storing alternatively generated energy more efficiently. The research in this dissertation demonstrates that halidometallate anion and polyhalogen monoanion based ionic liquids as electrolytes in

modern electrochemical applications is successful and provides a solid basis for future experiments in the field of metal recycling and emerging battery technologies.

Appendix

A. Publications and Conference Contributions

A.1 Publications

(1) **T. A. Gully**, P. Voßnacker, J. R. Schmid, H. Beckers, and S. Riedel, *ChemistryOpen* **2021**, *10*, 255-264.
https://doi.org/10.1002/open.202000263

(2) **T. A. Gully**, K. Sonnenberg, J. Bader, and S. Riedel, *Inorg. Chem.*, **2021**, *60*, 8093-8102.
https://doi.org/10.1021/acs.inorgchem.1c00706

(3) M. Schmucker, **T. A. Gully**, A. Schmidt, B. Schmidt, K. Bromberger, J. Disch, B. Butschke, B. Burgenmeister, K. Sonnenberg, S. Riedel, and I. Krossing, *Adv. Energy Mater.*, **2021**, *11*, 2101261 .
https://doi.org/10.1002/aenm.202101261

A.2 Conference Contributions

(1) **T. A. Gully**, K. Sonnenberg, S. Riedel: Room Temperature Ionic Liquid Bromostannates: Synthesis and Electrochemical Characterization, *69th Annual Meeting of the International Society of Electrochemistry*, Nuovo Polo Congressuale Bologna, Bologna, Italy, **2018**.

(2) **T. A. Gully**, K. Sonnenberg, S. Riedel: Room Temperature Ionic Liquid Bromostannates: Synthesis and Electrochemical Characterization, *19. Vortragstagung der Wöhler-Vereinigung,* Regensburg, Germany, **2018**.

(3) **T. A. Gully**, B. Schmidt, S. Riedel: Spectroelectrochemical Investigations of Chloridomanganates for Redox-Flow Battery Application, *7. Tag der Anorganischen Chemie*, Freie Universität Berlin, Berlin, Germany, **2019**.

B. Curriculum Vitae

Education:

11.2017 – Present	**Dr. rer. nat. Chemistry**, (desired title) Freie Universität Berlin
03.2015 – 08.2017	**M. Sc. Chemistry**, Freie Universität Berlin Master Thesis: Electrochemical analysis of halometallate ionic liquids in redox-flow batteries
09.2011 – 12.2014	**B. Sc. Chemistry**, University of California, Irvine
07.2012 – 07.2013	**Study Abroad**, Freie Universität Berlin
09.2009 – 06.2011	**Associate of Art**, College of the Canyons

Research Experience:

03.2014 – 12.2014	Advisor: Prof. Dr. A. J. Shaka (UC Irvine) Objective: Neutron profiling of a TRIGA Mk III nuclear reactor using gamma-ray spectroscopy

Honors:

UCI Dean's Honor List**:** Spring 2014, Fall 2014

Language Proficiency:

English: Mother tongue

German: C1 level,

Work Experience:

08.2016 – 06.2017	Repro-Kopier-Läden CSV GmbH

Volunteer Work:

06.2011 – 07.2012	VITAS Innovative Hospice Care; Home patient volunteer

C. Publications – Supporting Information

C.1 Supporting Information – Conductivity and Redox Potentials of Ionic Liquid Trihalogen Monoanions $[X_3]^-$, $[XY_2]^-$, and $[BrF_4]^-$ (X=Cl, Br, I and Y=Cl, Br)

Tyler A. Gully, Patrick Voßnacker, Jonas R. Schmid, Helmut Beckers, and Sebastian Riedel*

ChemistryOpen **2021**, *10*, 255-264.
DOI: https://doi.org/10.1002/open.202000263

This is an invited contribution to a Special Issue dedicated to Material Synthesis in Ionic Liquids.

ChemistryOpen

Supporting Information

Conductivity and Redox Potentials of Ionic Liquid Trihalogen Monoanions $[X_3]^-$, $[XY_2]^-$, and $[BrF_4]^-$ (X = Cl, Br, I and Y = Cl, Br)

Tyler A. Gully, Patrick Voßnacker, Jonas R. Schmid, Helmut Beckers, and Sebastian Riedel*

Supporting Information:

Synthesis

[NEt_3Me][Cl_3]

19.4 g (128.2 mmol, 1.0 equiv.) [NEt_3Me]Cl was dried *in vacuo* at 100 °C for one hour. 8.9 g (125.3 mmol, 1.0 equiv.) Cl_2 was condensed onto the solid at –196 °C. The reaction mixture was warmed to room temperature. To obtain homogeneous [NEt_3Me][Cl_3], the reaction mixture was liquefied at *r.t.*. A yellow liquid was obtained.

Raman (Neat, *r.t.*, 2 cm^{-1}): $\tilde{\nu}$ = 3029 (s), 2985 (vs), 2947 (vs), 2885 (s), 1453 (m), 1123 (w), 1071 (m), 684 (s), 455 (vs), 342 (vs), 277 (vs) cm^{-1};

Raman ([BMP][OTf] DSIL, *r.t.*, 2 cm^{-1}): $\tilde{\nu}$ = 3028 (m), 2989 (s), 2955 (s), 2880 (m), 1453 (m), 1223 (m), 1123 (w), 1068 (w), 1033 (vs), 904 (m), 757 (s), 686 (w), 573 (m), 349 (vs), 313 (vs), 297 (vw), 276 (s), 162 (s) cm^{-1}.

UV-*vis* ([BMP][OTf] DSIL, in MeCN, *r.t.*,): λ = 407 nm.

[NEt_3Me][Br_3]

9.6 g (49.1 mmol) [NEt_3Me]Br was dried *in vacuo* at 100 °C for one hour. 7.9 g (49.1 mmol, 1.0 equiv.) Br_2 was condensed onto the solid at –196 °C. The reaction mixture was warmed to room temperature. To obtain homogeneous [NEt_3Me][Br_3], the reaction mixture was liquefied at 50 °C and cooled back to room temperature. A red partial liquid-solid was obtained.

Raman (Neat, *r.t.*, 2 cm^{-1}): $\tilde{\nu}$ = 3036 (w), 2993 (m), 2944 (m), 2878 (m), 1454 (m),680 (m), 258 (vs), 201 (vs), 162 (vs) cm^{-1};

Raman ([BMP][OTf] DSIL, *r.t.*, 2 cm^{-1}): $\tilde{\nu}$ = 3027 (m), 2982 (s), 2944 (s), 2881 (m), 1454 (m), 1225 (w), 1033 (s), 756 (m), 680 (vw), 574 (w), 349 (m), 313 (m), 191 (w), 162 (s) cm^{-1}.

UV-*vis* ([BMP][OTf] DSIL, in MeCN, *r.t.*,): λ = 440 nm.

[NEt_3Me]I

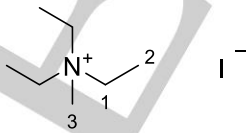

[NEt_3Me]I was prepared according to literature procedure. [1]

^{1}H NMR (400 MHz, chloroform-D_1, 295.0 K) = 3.55 (q, δ = 7.68 Hz, 2H, H-1), 3.20 (s, 3H, H-3), 1.38 (t, δ = 7.55 Hz, 3H, H-2) ppm;

^{13}C NMR (100 MHz, chloroform-D_1, 295.0 K) = 56.54 (C-1), 47.84 (C-3), 8.59 (C-2) ppm.

[NEt_3Me][I_3]

3.0 g (12.5 mmol, 1.0 equiv.) [NEt_3Me]I was dried *in vacuo* at 100 °C for one hour. 3.2 g (49.1 mmol, 1.0 equiv.) I_2 was added to the salt at *r.t.*. To obtain homogeneous [NEt_3Me][I_3], the reaction mixture was liquefied at 80 °C and cooled back to room temperature. A dark purple-brown solid was obtained.

Raman (Neat, *r.t.*, 2 cm^{-1}): $\tilde{\nu}$ = 3023 (w), 2977 (m), 2943 (m), 2881 (vw), 1440 (vw), 680 (w), 155 (m), 138 (s), 110 (vs) cm^{-1};

Raman ([BMP][OTf] DSIL, *r.t.*, 2 cm^{-1}): $\tilde{\nu}$ = 2995 (s), 2971 (s), 2943 (s), 2878 (s), 1460 (m), 1226 (w), 1063 (vw), 1033 (vs), 903 (m), 756 (s), 571 (w), 348 (s), 312 (s), 297 (vw), 276 (s), 146 (s), 136 (m), 113 (s) cm^{-1}.

UV-*vis* ([BMP][OTf] DSIL, in MeCN, *r.t.*,): λ = 492 and 558 nm.

[HMIM][I_3]

7.2 g (24.3 mmol, 1.0 equiv.) [HMIM]I was dried *in vacuo* at 100 °C for one hour. 6.8 g (26.8 mmol, 1.1 equiv.) I_2 was added to the salt at *r.t.*. To obtain homogeneous [HMIM][I_3], the reaction mixture was liquefied at 35 °C and cooled back to room temperature. A dark purple-brown liquid was obtained.

Raman (Neat, *r.t.*, 2 cm^{-1}): $\tilde{\nu}$ = 2948 (vs), 2930 (s), 2909 (m), 2893 (s), 2867 (s), 2853 (s), 1412 (w), 1024 (w), 168 (vs), 147 (vs), 111 (vs) cm^{-1};

[NEt_3Me][$BrCl_2$]

7.5 g (49.2 mmol, 1.0 equiv.) [NEt_3Me]Cl was dried *in vacuo* at 100 °C for one hour. 3.9 g (24.6 mmol, 0.5 equiv.) Br_2 and 1.8 g (25.8 mmol, 0.5 equiv.) Cl_2 were condensed onto the solid at –196 °C. The reaction mixture was warmed to room temperature. To obtain homogeneous [NEt_3Me][$BrCl_2$], the reaction mixture was liquefied at 80 °C and cooled back to room temperature. A yellow glass-similar semi-solid was obtained.

Raman (Neat, *r.t.*, 2 cm^{-1}): $\tilde{\nu}$ = 3025 (w), 2985 (m), 2947 (m), 2888 (m), 1458 (m), 1120 (m), 1071 (m), 684 (s), 275 (vs), 217 (s), 194 (m) cm^{-1};

Raman ([BMP][OTf] DSIL, *r.t.*, 2 cm^{-1}): $\tilde{\nu}$ = 3027 (m), 2992 (s), 2946 (s), 2881 (m), 1455 (m), 1123 (w), 1063 (w), 1035 (s), 904 (m), 758 (s), 681 (w), 575 (w), 348 (m), 313 (m), 298 (w), 195 (m), 162 (s) cm^{-1}.

UV-*vis* ([BMP][OTf] DSIL, in MeCN, *r.t.*,): λ = 396 nm.

[NEt_3Me][IBr_2]

9.6 g (49.1 mmol, 1 equiv.) [NEt_3Me]Br was dried *in vacuo* at 100 °C for one hour. 6.4 g (25.3 mmol, 0.5 equiv.) I_2 was added and 3.9 g (24.6 mmol, 0.5 equiv.) Br_2 was condensed onto the solids at –196 °C. The reaction mixture was warmed to room temperature. To obtain homogeneous [NEt_3Me][IBr_2], the reaction mixture was liquefied at 120 °C and cooled back to room temperature. A bright red solid was obtained.

Raman (Neat, *r.t.*, 2 cm^{-1}): $\tilde{\nu}$ = 3023 (s), 2987 (vs), 2945 (vs), 1459 (m), 1122 (w), 1071 (m), 1003 (w), 961 (w), 684 (s), 322 (w), 160 (vs), 134 (m) cm^{-1};

Raman ([BMP][OTf] DSIL, *r.t.*, 2 cm^{-1}): $\tilde{\nu}$ = 3032 (m,sh), 2996 (s), 2943 (vs), 2877 (vs), 1456 (m), 1223 (w), 1066 (w), 1032 (vs), 904 (m), 757 (s), 686 (vw), 348 (s), 314 (s), 160 (s), 134 (w) cm^{-1}.

UV-*vis* ([BMP][OTf] DSIL, in MeCN, *r.t.*,): λ = 416 nm.

[NEt_3Me][ICl_2]

7.5 g (49.2 mmol, 1.0 equiv.) [NEt_3Me]Cl was dried *in vacuo* at 100 °C for one hour. 6.3 g (24.6 mmol, 0.5 equiv.) I_2 were added and 1.8 g (25.8 mmol, 0.5 equiv.) Cl_2 was condensed onto the solids at –196 °C. The reaction mixture was warmed to room temperature. To obtain homogeneous [NEt_3Me][ICl_2], the reaction mixture was liquefied at 100 °C and cooled back to room temperature. A red-brown solid was obtained.

Raman (Neat, *r.t.*, 2 cm^{-1}): $\tilde{\nu}$ = 3028 (s), 2989 (vs), 2947 (vs), 2880 (w), 1486 (w), 1462 (m), 1126 (w), 1072 (vw), 997 (w), 965 (w), 685 (s), 260 (vs), 191 (m), 151 (m) cm^{-1};

Raman ([BMP][OTf] DSIL, *r.t.*, 2 cm^{-1}): $\tilde{\nu}$ = 3031 (m), 2989 (s), 2945 (vs), 2880 (s), 1495 (w), 1454 (m), 1224 (m), 1121 (w), 1065 (w), 1032 (vs), 906 (m), 758 (s), 681 (w), 574 (m), 351 (s), 315 (s), 267 (w), 151 (s) cm^{-1}.

UV-*vis* ([BMP][OTf] DSIL, in MeCN, *r.t.*,): λ = 408 nm.

[NEt_3Me][BrF_4]

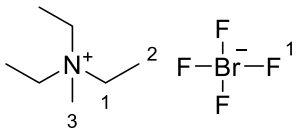

0.3 g (1.5 mmol, 1.0 equiv.) [NEt_3Me]Br was added into a dry Schlenk tube and dissolved in acetonitrile (4.5 mL). Under inert conditions a PFA capillary was put in the solution, hold in position by a quickfit. An Ar stream (20 mL/min) was passed through the PFA tube. The excess gases were past though the Schlenk adapter, connected to a PFA tube and released in the back of the fume hood. Under cooling (–40 °C), the argon gas was exchanged for a gas mixture consisting of 10% fluorine in Ar (20 mL/min) and passed through the liquid for 45 min (2.4 equiv.). Argon was passed through the liquid after full conversion to get rid of any excess fluorine gas. A colorless liquid was obtained.

Raman (In MeCN, 233 K, 2 cm^{-1}): $\tilde{\nu}$ = 3000 (s), 2989 (w), 2937 (vs), 2249 (s), 522 (w), 446 (w) cm^{-1};

^{1}H NMR (400 MHz, MeCN, ext. aceton-D6, 295.0 K) = 3.91 (q, δ = 6.86 Hz, 2H, H-1), 3.52 (s, 3H, H-3), 1.93 (t, δ = 7.20 Hz, 3H, H-2) ppm;

^{19}F NMR (376 MHz, MeCN, ext. aceton-D6, 295.0 K) = –35.54 (F-1) ppm.

Raman Spectroscopy

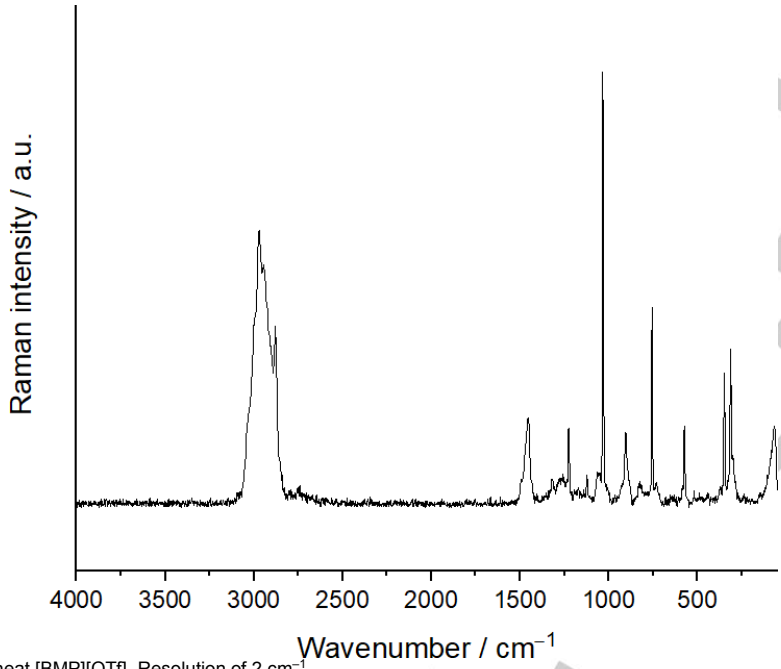

Figure S 1. Raman spectrum of neat [BMP][OTf]. Resolution of 2 cm^{-1}.

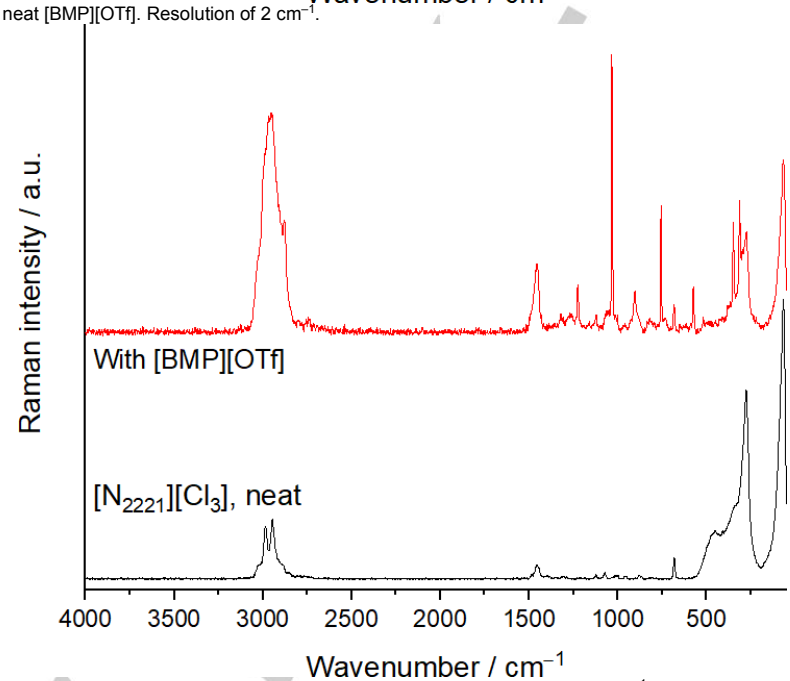

Figure S 2. Raman spectrum of neat [N_{2221}][Cl_3] and mixed with [BMP][OTf] ([Cl_3]$^-$ 0.5 M). Resolution of 2 cm^{-1}.

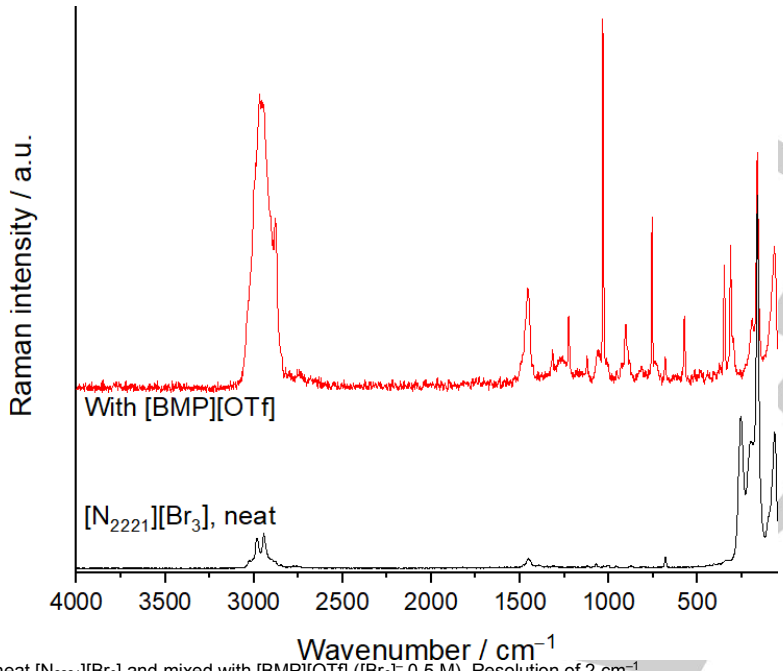

Figure S 3. Raman spectrum of neat $[N_{2221}][Br_3]$ and mixed with [BMP][OTf] ($[Br_3]^-$ 0.5 M). Resolution of 2 cm^{-1}.

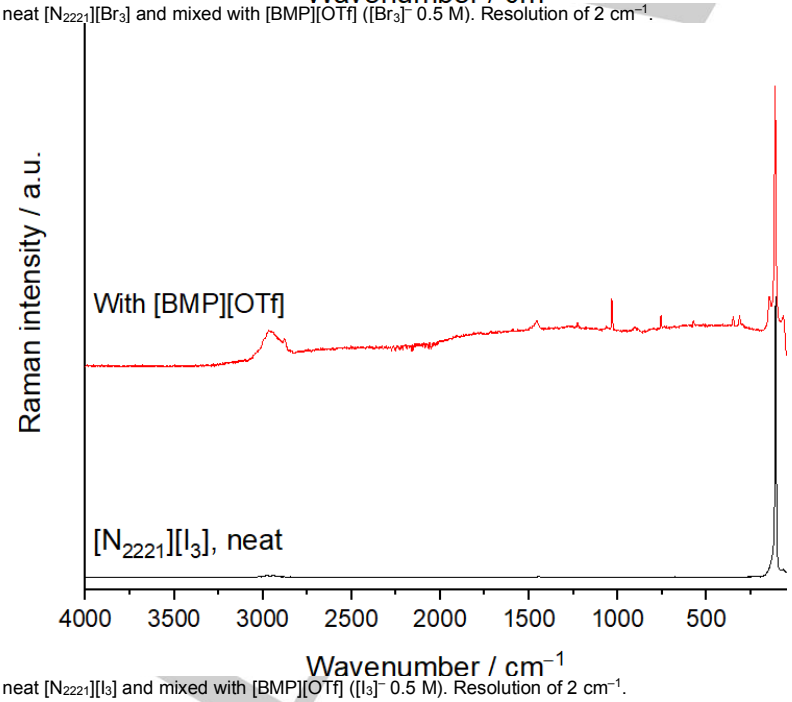

Figure S 4. Raman spectrum of neat $[N_{2221}][I_3]$ and mixed with [BMP][OTf] ($[I_3]^-$ 0.5 M). Resolution of 2 cm^{-1}.

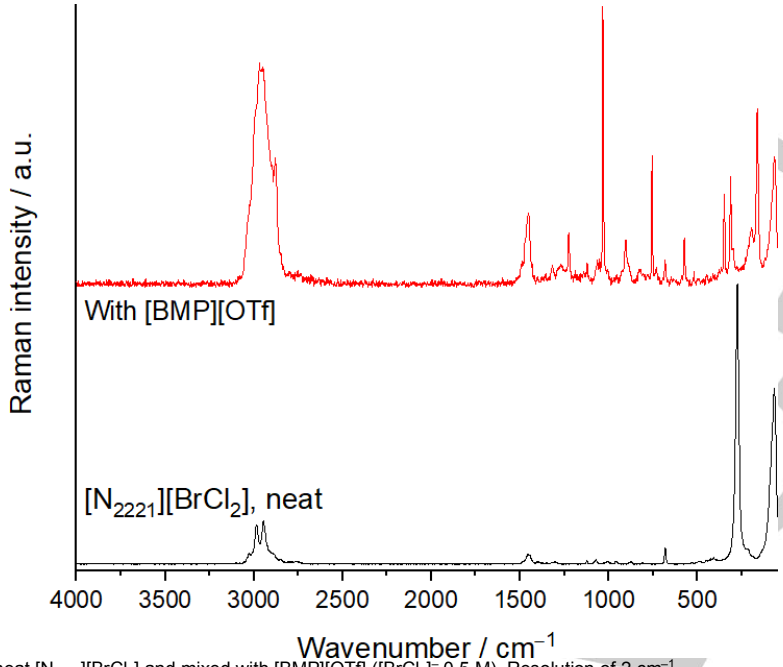

Figure S 5. Raman spectrum of neat $[N_{2221}][BrCl_2]$ and mixed with [BMP][OTf] ($[BrCl_2]^-$ 0.5 M). Resolution of 2 cm^{-1}.

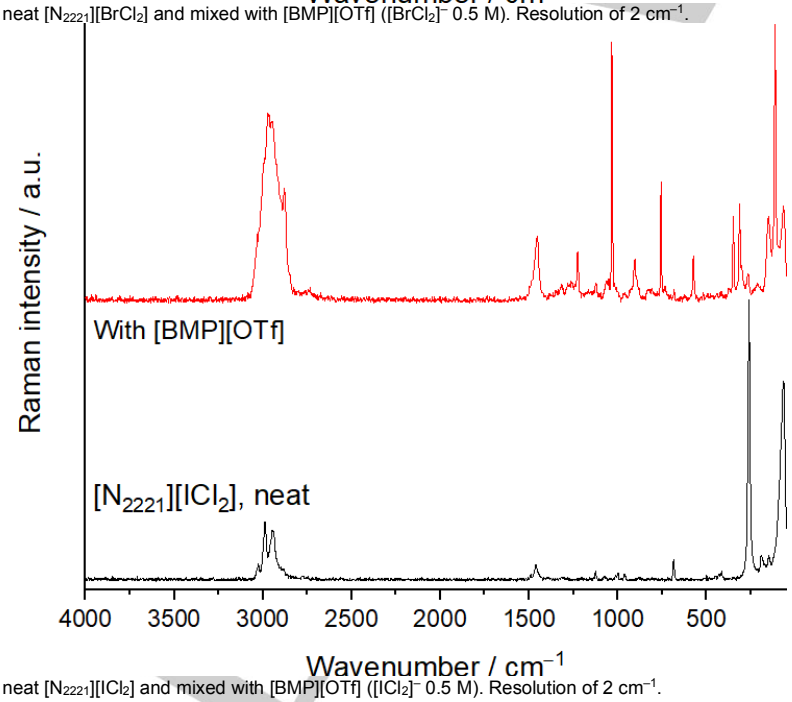

Figure S 6. Raman spectrum of neat $[N_{2221}][ICl_2]$ and mixed with [BMP][OTf] ($[ICl_2]^-$ 0.5 M). Resolution of 2 cm^{-1}.

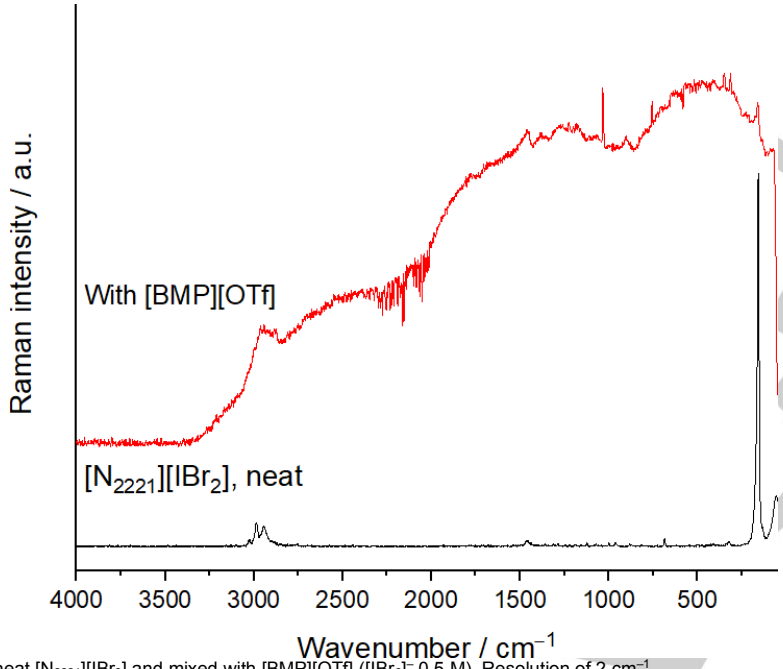

Figure S 7. Raman spectrum of neat $[N_{2221}][IBr_2]$ and mixed with [BMP][OTf] ($[IBr_2]^-$ 0.5 M). Resolution of 2 cm^{-1}.

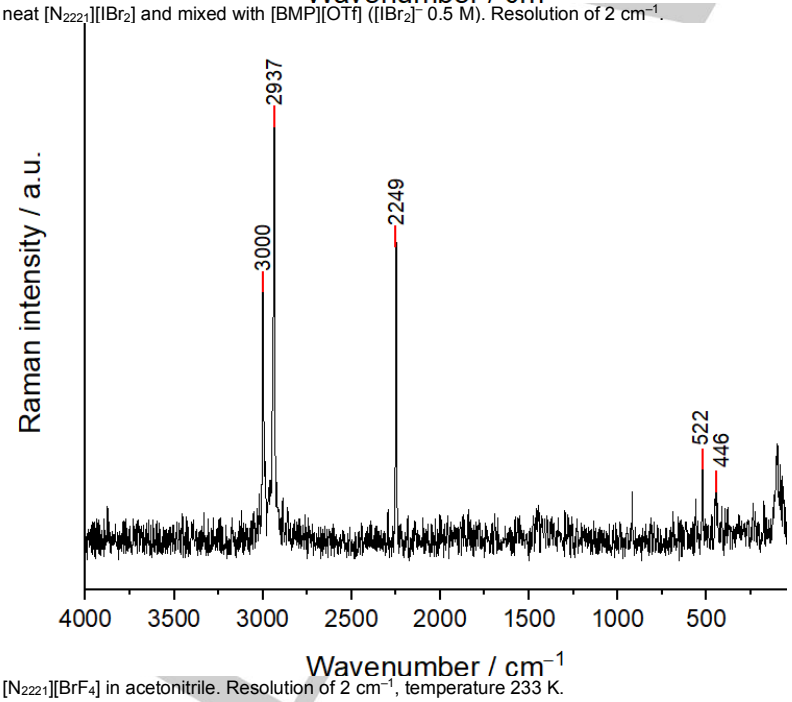

Figure S 8. Raman spectrum of $[N_{2221}][BrF_4]$ in acetonitrile. Resolution of 2 cm^{-1}, temperature 233 K.

UV-*vis* Spectroscopy

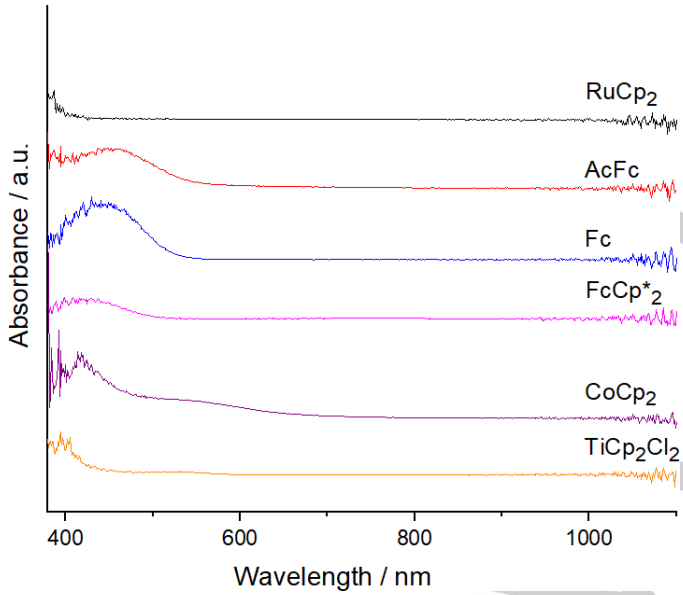

Figure S 9. The UV-*vis* spectra of various metallocenes in acetonitrile.

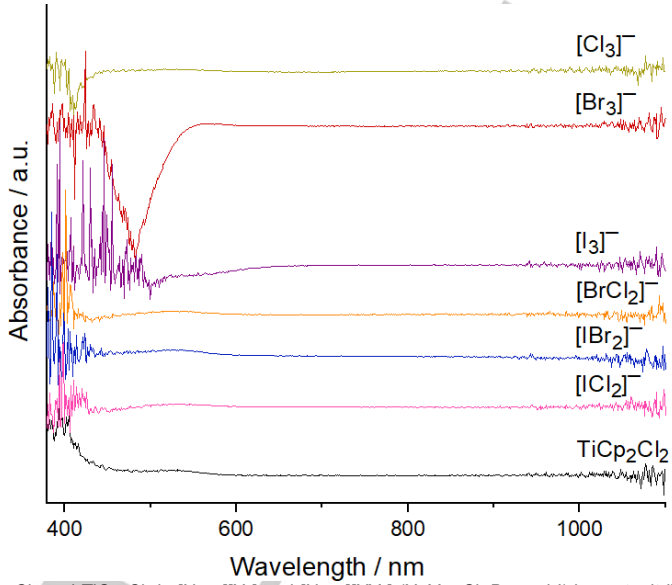

Figure S 10. The UV-*vis* spectra of $TiCp_2Cl_2$ and $TiCp_2Cl_2$ in $[N_{2221}][X_3]$ and $[N_{2221}][XY_2]$ (X, Y = Cl, Br, and I) in acetonitrile. The polyhalogen-metallocene spectra are background subtracted against their respective the polyhalogen in acetonitrile solution.

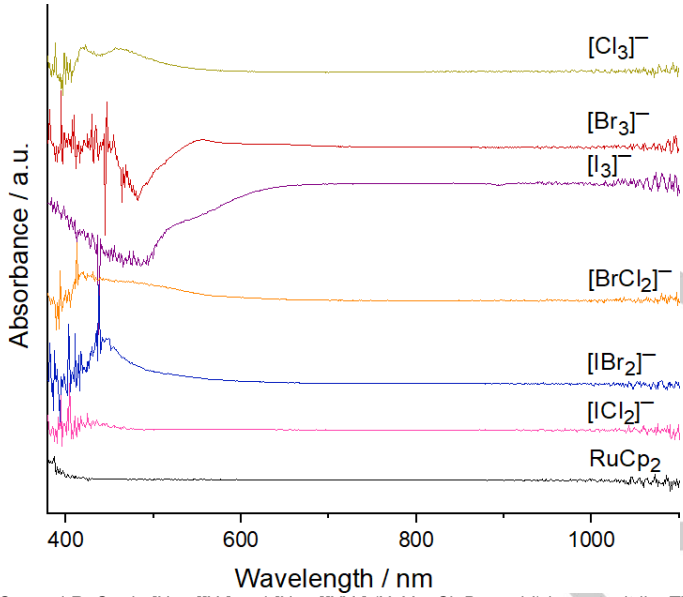

Figure S 11. The UV-*vis* spectra of $RuCp_2$ and $RuCp_2$ in $[N_{2221}][X_3]$ and $[N_{2221}][XY_2]$ (X, Y = Cl, Br, and I) in acetonitrile. The polyhalogen-metallocene spectra are background subtracted against their respective the polyhalogen in acetonitrile solution. $RuCp_2$ is not soluble enough in acetonitrile to produce the related absorption wavelength (λ = 458 nm).[2]

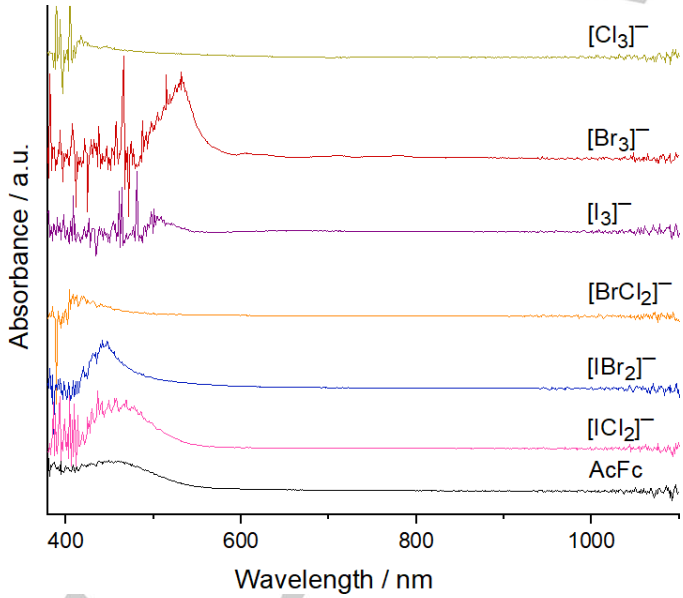

Figure S 12. The UV-*vis* spectra of AcFc and AcFc in $[N_{2221}][X_3]$ and $[N_{2221}][XY_2]$ (X, Y = Cl, Br, and I) in acetonitrile. The polyhalogen-metallocene spectra are background subtracted against their respective the polyhalogen in acetonitrile solution.

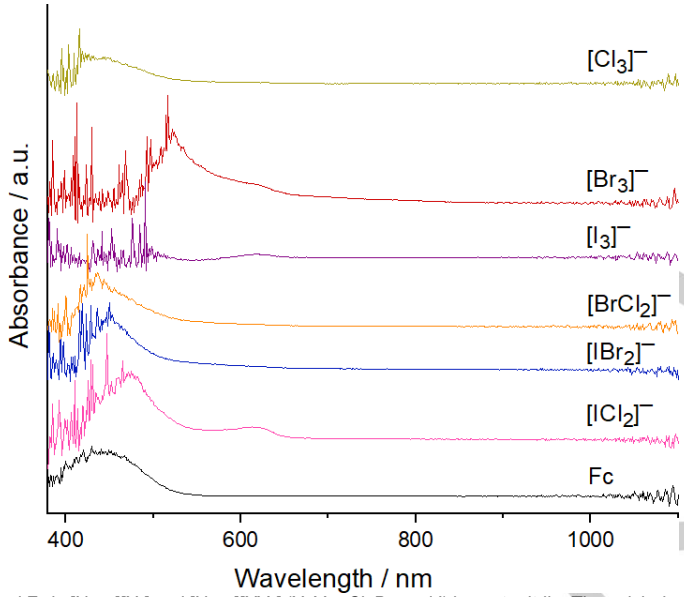

Figure S 13. The UV-*vis* spectra of Fc and Fc in $[N_{2221}][X_3]$ and $[N_{2221}][XY_2]$ (X, Y = Cl, Br, and I) in acetonitrile. The polyhalogen-metallocene spectra are background subtracted against their respective the polyhalogen in acetonitrile solution.

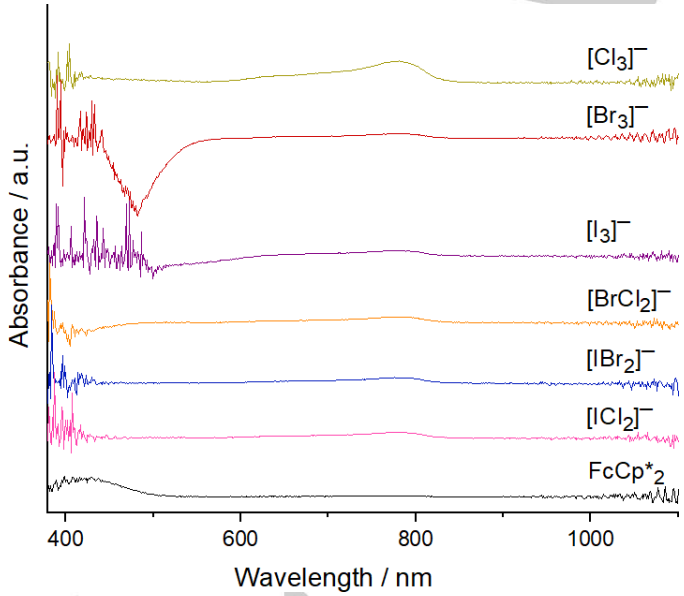

Figure S 14. The UV-*vis* spectra of $FcCp^*_2$ and $FcCp^*_2$ in $[N_{2221}][X_3]$ and $[N_{2221}][XY_2]$ (X, Y = Cl, Br, and I) in acetonitrile. The polyhalogen-metallocene spectra are background subtracted against their respective the polyhalogen in acetonitrile solution.

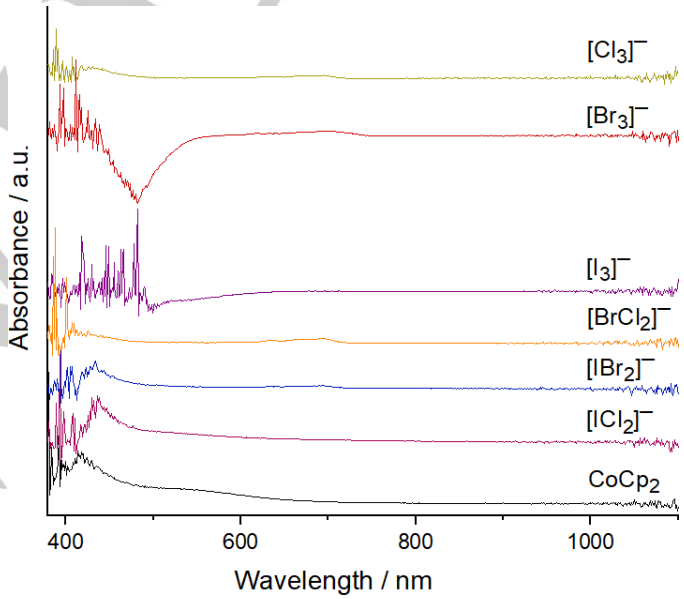

Figure S 15. The UV-*vis* spectra of $CoCp_2$ and $CoCp_2$ in $[N_{2221}][X_3]$ and $[N_{2221}][XY_2]$ (X, Y = Cl, Br, and I) in acetonitrile. The polyhalogen-metallocene spectra are background subtracted against their respective the polyhalogen in acetonitrile solution.

Table S 1. Absorption wavelengths of various metallocenes and the DSILs $[N_{2221}][X_3]$ and $[N_{2221}][XY_2]$ (X,Y = Cl, Br, and I) in [BMP][OTf] ($[X_3]^-/[XY_2]^-$ 0.5 M) diluted in acetonitrile. For the polyhalogen-metallocene solutions, only the absorption wavelengths of the resulting metallocene solution will be described. Wavelengths in nm.

Compound	Metallocene	λ_1	λ_2	λ_3	λ_4
$RuCp_2$		458 [a,2]			
AcFc		459			
Fc		444			
$FcCp^*_2$		431			
$CoCp_2$		420	550		
$TiCp_2Cl_2$		533			
$[N_{2221}][Cl_3]$		407			
	$TiCp_2Cl_2$	535			
	$RuCp_2$	462	739		
	AcFc		447	673	
	Fc	449	625		
	$FcCp^*_2$		632	784	
	$CoCp_2$		635	667	695
$[N_{2221}][Br_3]$		440			
	$TiCp_2Cl_2$	533			
	$RuCp_2$	454			
	AcFc	466			
	Fc		624		
	$FcCp^*_2$		647	779	
	$CoCp_2$		619	670	699
$[N_{2221}][I_3]$		492	558		
	$TiCp_2Cl_2$	536			
	$RuCp_2$	454			
	AcFc	464			
	Fc		622		
	$FcCp^*_2$		643	785	
	$CoCp_2$		630	663	
$[N_{2221}][BrCl_2]$		396			
	$TiCp_2Cl_2$	530			
	$RuCp_2$	446	498		
	AcFc	440			
	Fc	439	623		
	$FcCp^*_2$		640	783	
	$CoCp_2$		634	667	694
$[N_{2221}][ICl_2]$		416			
	$TiCp_2Cl_2$	531			
	$RuCp_2$	450			
	AcFc	447			
	Fc	451	638		
	$FcCp^*_2$		638	779	
	$CoCp_2$		633	662	694
$[N_{2221}][IBr_2]$		408			
	$TiCp_2Cl_2$	533			
	$RuCp_2$	455			
	AcFc	458			
	Fc	447	620		
	$FcCp^*_2$		632	779	
	$CoCp_2$		628	661	

[a] $RuCp_2$ diffuse reflectance spectra in the solid state. $RuCp_2$ is not sufficiently soluble in MeCN to register an absorbance wavelength.

Conductivity

Table S 2. Temperature dependent specific conductivity of neat $[N_{2221}][X_3]$ and $[N_{2221}][XY_2]$ salts (X,Y = Cl, Br, and I).

Temperature [°C]	Specific conductivity [mS·cm^{-1}]					
	$[N_{2221}][Cl_3]$	$[N_{2221}][Br_3]$	$[N_{2221}][I_3]$	$[N_{2221}][BrCl_2]$	$[N_{2221}][ICl_2]$	$[N_{2221}][IBr_2]$
25.0	12.52[f]					
30.0	17.23	15.24[a,f]		8.42[c]		
35.0	22.2	21.6		17.93[f]		
40.0	27.5	26.7		23.4		
45.0	32.9	28.8	2.22[b]	27.5		
50.0	38.7	34.1	4.43	31.8	20.9[d,f]	
55.0	44.8	39.5	11.98[f]	36.6	21.7	
60.0	51.7	45.3	14.39	41.9	24.7	
65.0	57.6	52.4	17.04	46.5	28.5	32.4[e,f]
70.0	63.4	58.2	19.76	51.8	32.7	33.4
75.0	70.0	64.1	22.7	56.8	36.5	35.9
80.0	77.9	69.7	25.7	61.7	40.3	40.1
85.0	83.1	75.4	28.5	66.2	44.2	43.8
90.0	89.2	80.3	31.5	71.8	48.8	47.6
95.0	93.9	86.0	34.6	78.7	52.8	51.0
100.0	97.5	91.0	38.9	84.6	56.9	54.6

[a] T_m = 32.7 °C, [b] T_m = 46.2 °C, [c] T_m = 33.0 °C, [d] T_m = 54.1 °C, [e] T_m = 68.4 °C, [f] homogeneous melt of salt.

Table S 3. Temperature dependent specific conductivity of $[N_{2221}][X_3]$ and $[N_{2221}][XY_2]$ salts (X,Y = Cl, Br, and I) mixed in [BMP][OTf] ($[X_3]^-/[XY_2]^-$ 0.5

Temperature [°C]	Specific conductivity [$mS \cdot cm^{-1}$]						
	[BMP][OTf] neat	$[N_{2221}][Cl_3]$	$[N_{2221}][Br_3]$	$[N_{2221}][I_3]$	$[N_{2221}][BrCl_2]$	$[N_{2221}][ICl_2]$	$[N_{2221}][IBr_2]$
10.0	0.500	0.714	0.556	0.394	0.565	0.733	0.691
15.0	0.751	1.240	0.969	0.684	1.032	1.201	1.098
20.0	1.141	1.862	1.556	1.051	1.501	1.719	1.672
25.0	1.638	2.53	2.24	1.492	2.10	2.36	2.25
30.0	2.20	3.40	3.04	1.92	2.84	3.12	3.01
35.0	3.38	4.47	3.68	2.43	4.03	3.86	3.81
40.0	4.49	5.82	4.74	3.13	5.16	4.94	4.90
45.0	5.59	7.21	5.93	3.89	7.00	6.20	6.32
50.0	6.91	8.79	7.45	4.75	8.80	7.50	8.01
55.0	8.57	10.87	8.99	5.78	10.22	9.04	9.69
60.0	10.36	12.95	10.69	6.94	11.52	10.64	11.45
65.0	12.21	15.45	12.48	8.19	13.11	12.39	13.20
70.0	14.45	18.10	14.59	9.45	15.25	14.28	15.23
75.0	16.55	21.03	16.86	10.86	17.38	16.32	17.20
80.0	18.62	24.1	19.13	12.38	19.9	18.34	19.25
85.0	20.8	27	21.3	13.94	22.5	20.5	21.4
90.0	23.2	29.8	23.8	15.69	25.2	22.6	23.7
95.0	25.7	32.6	26.4	17.40	27.7	24.9	25.8
100.0	28.1	34.5	29.4	19.08	30.2	27.4	28.1

Vogel-Fulcher-Tamman Parameters

Table S 4. VFT conductivity equation parameters of neat $[N_{2221}][X_3]$ and $[N_{2221}][XY_2]$ salts (X,Y = Cl, Br, and I). Calculated via OriginPro.[3]

Compound	$[N_{2221}][Cl_3]$	$[N_{2221}][Br_3]$	$[N_{2221}][I_3]$	$[N_{2221}][BrCl_2]$	$[N_{2221}][ICl_2]$	$[N_{2221}][IBr_2]$
s_0	394.3 ± 30.1	491.2 ± 85.4	509.2 ± 182.2	599.8 ± 102.6	462.1 ± 70.9	425.9 ± 322.9
B	171.3 ± 13.7	231.3 ± 37.4	376.3 ± 90.2	298.4 ± 41.8	296.5 ± 37.1	311.8 ± 209.1
T_g	248.9 ± 3.4	235.3 ± 8.4	227.5 ± 14.8	221.7 ± 8.3	231.5 ± 7.4	221.2 ± 45.6
Reduced Chi-Sqr	0.7683	1.0770	0.0900	0.5160	0.0501	0.1543
R-Square (COD)	0.9992	0.9983	0.9991	0.9990	0.9997	0.9983
Adj. R-Square	0.9990	0.9980	0.9989	0.9988	0.9997	0.9975

Table S 5. VFT conductivity equation parameters of DSILs $[N_{2221}][X_3]$ and $[N_{2221}][XY_2]$ salts (X,Y = Cl, Br, and I) mixed in [BMP][OTf] ($[X_3]^-$/$[XY_2]^-$ 0.5 M). Calculated via OriginPro.[3]

Compound	[BMP][OTf] neat	$[N_{2221}][Cl_3]$	$[N_{2221}][Br_3]$	$[N_{2221}][I_3]$	$[N_{2221}][BrCl_2]$	$[N_{2221}][ICl_2]$	$[N_{2221}][IBr_2]$
s_0	352.4 ± 24.7	451.1 ± 90.2	660.8 ± 58.9	490.2 ± 35.4	495.8 ± 96.6	474.8 ± 25.8	295.7 ± 22.6
B	357.7 ± 15.7	367.0 ± 45.8	510.5 ± 24.0	543.0 ± 20.0	437.1 ± 49.2	459.4 ± 14.2	337.3 ± 17.1
T_g	231.6 ± 2.4	228.8 ± 6.9	209.3 ± 3.1	205.6 ± 2.5	216.9 ± 6.9	212.1 ± 2.0	229.7 ± 2.8
Reduced Chi-Sqr	0.0139	0.1773	0.0129	0.0032	0.0923	0.0055	0.0208
R-Square (COD)	0.9999	0.9988	0.9999	0.9999	0.9991	0.9999	0.9998
Adj. R-Square	0.9998	0.9986	0.9999	0.9999	0.9990	0.9999	0.9997

Cyclic Voltammograms

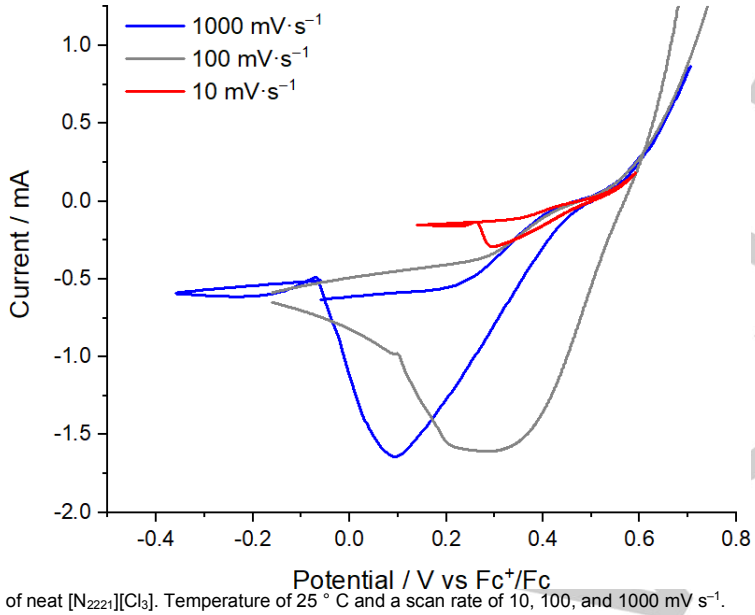

Figure S 16. Cyclic voltammogram of neat $[N_{2221}][Cl_3]$. Temperature of 25 ° C and a scan rate of 10, 100, and 1000 mV s^{-1}.

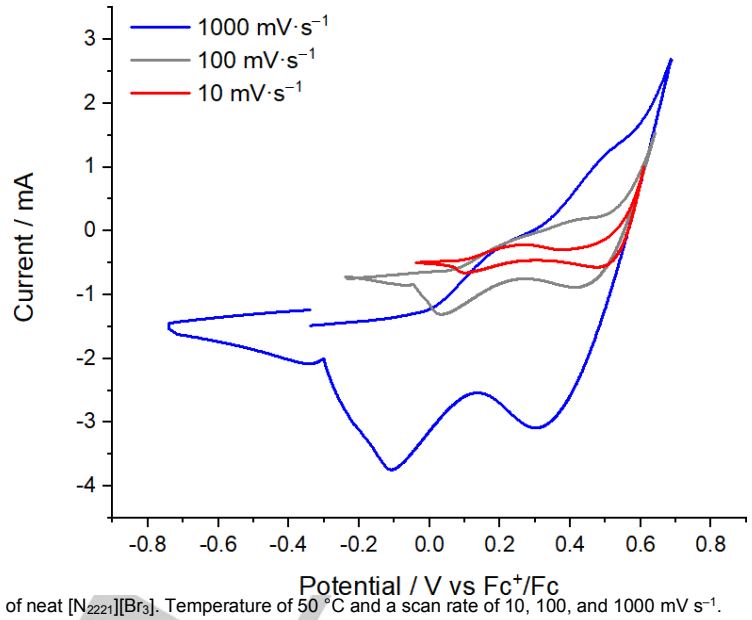

Figure S 17. Cyclic voltammogram of neat $[N_{2221}][Br_3]$. Temperature of 50 °C and a scan rate of 10, 100, and 1000 mV s^{-1}.

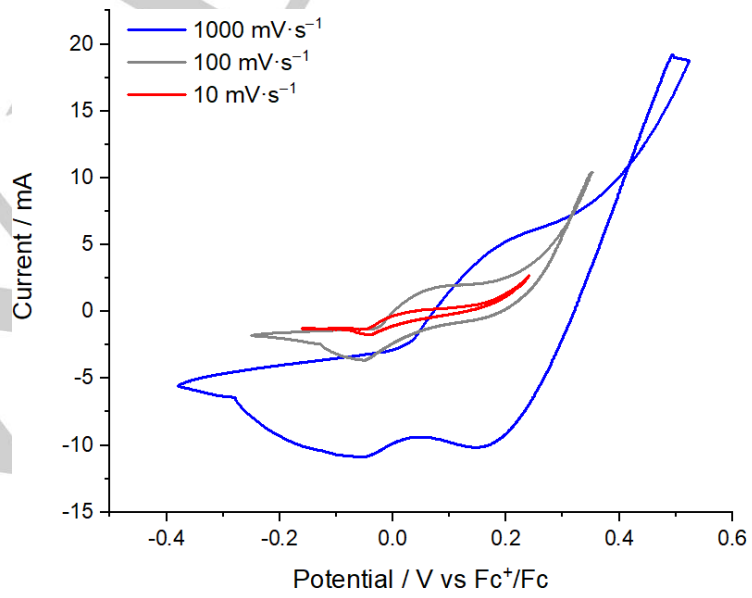

Figure S 18. Cyclic voltammogram of neat $[N_{2221}][I_3]$. Temperature of 80 °C and a scan rate of 10, 100, and 1000 mV s^{-1}.

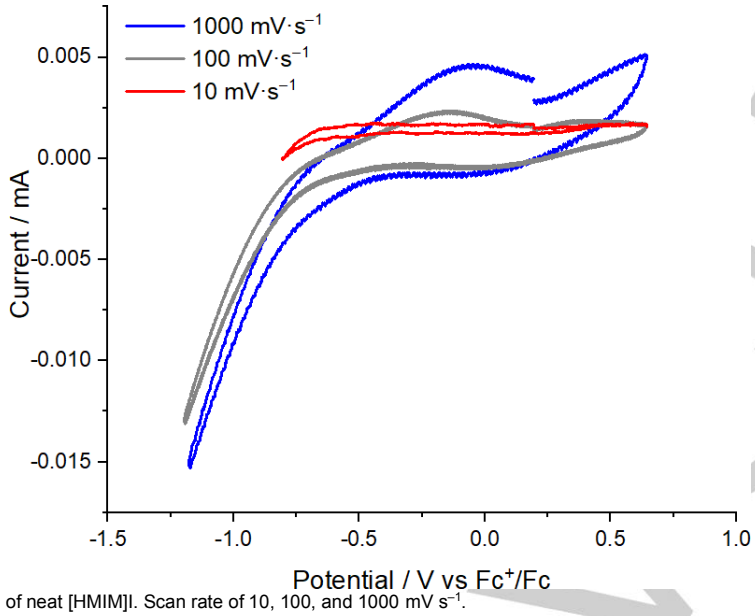

Figure S 19. Cyclic voltammogram of neat [HMIM]I. Scan rate of 10, 100, and 1000 mV s^{-1}.

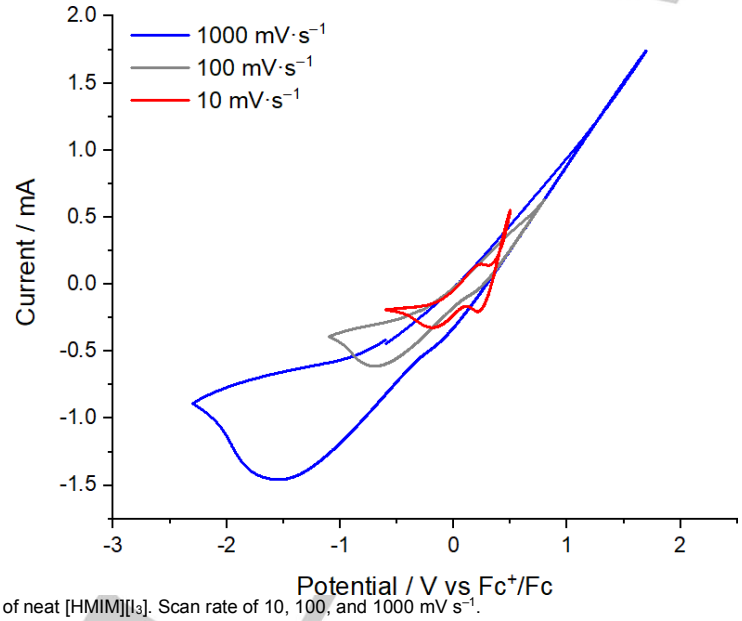

Figure S 20. Cyclic voltammogram of neat $[HMIM][I_3]$. Scan rate of 10, 100, and 1000 mV s^{-1}.

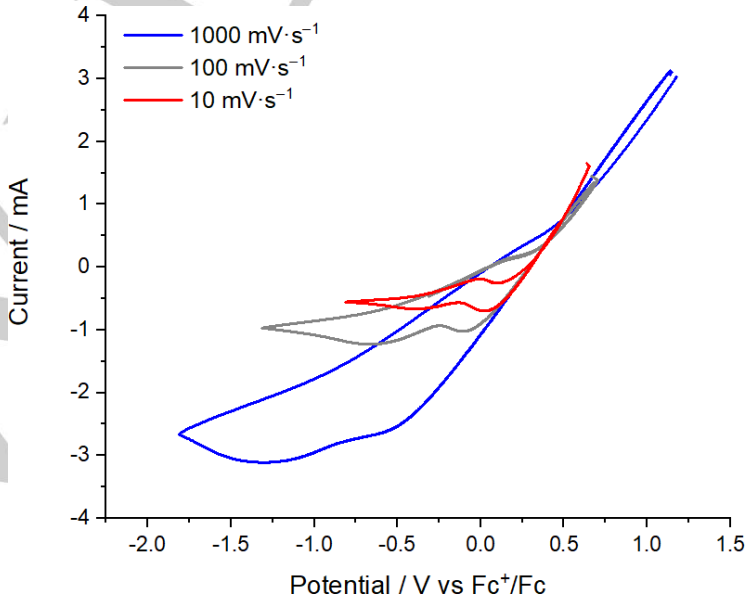

Figure S 21. Cyclic voltammogram of neat [HMIM]I + 1.5 eq. I_2. Scan rate of 10, 100, and 1000 mV s^{-1}.

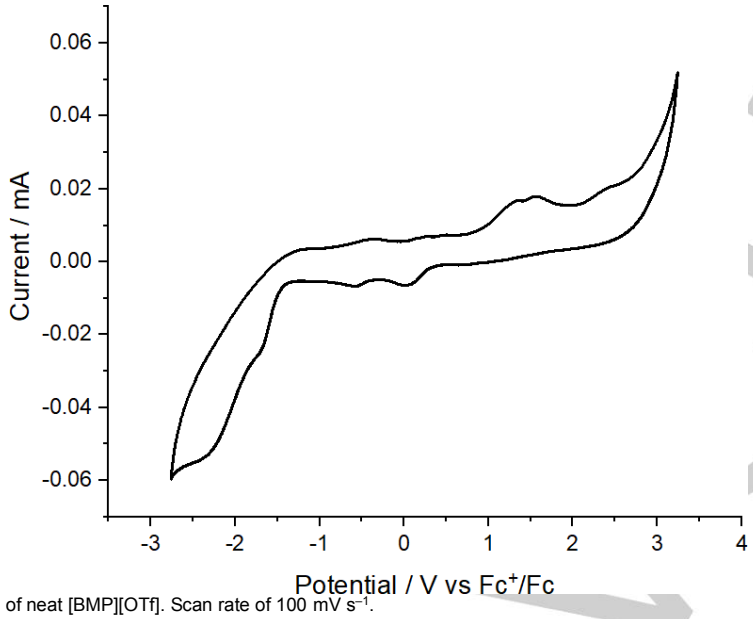

Figure S 22. Cyclic voltammogram of neat [BMP][OTf]. Scan rate of 100 mV s^{-1}.

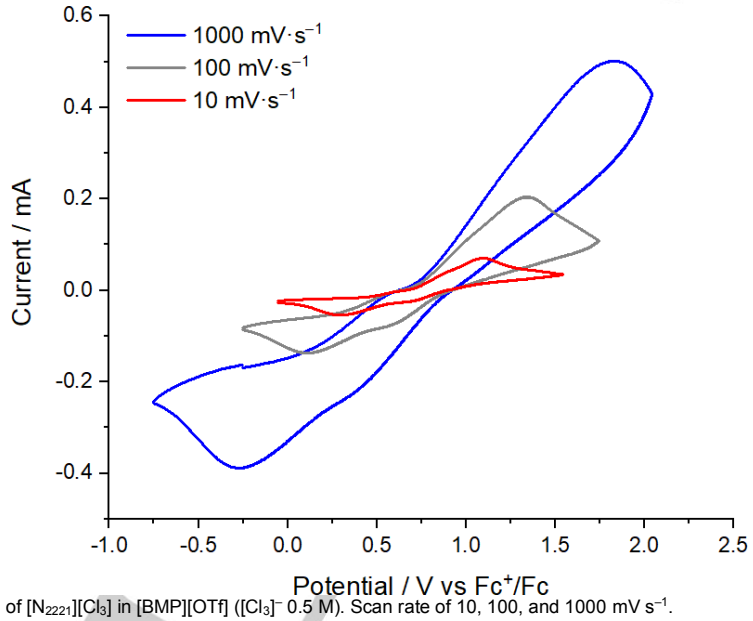

Figure S 23. Cyclic voltammogram of $[N_{2221}][Cl_3]$ in [BMP][OTf] ($[Cl_3]^-$ 0.5 M). Scan rate of 10, 100, and 1000 mV s^{-1}.

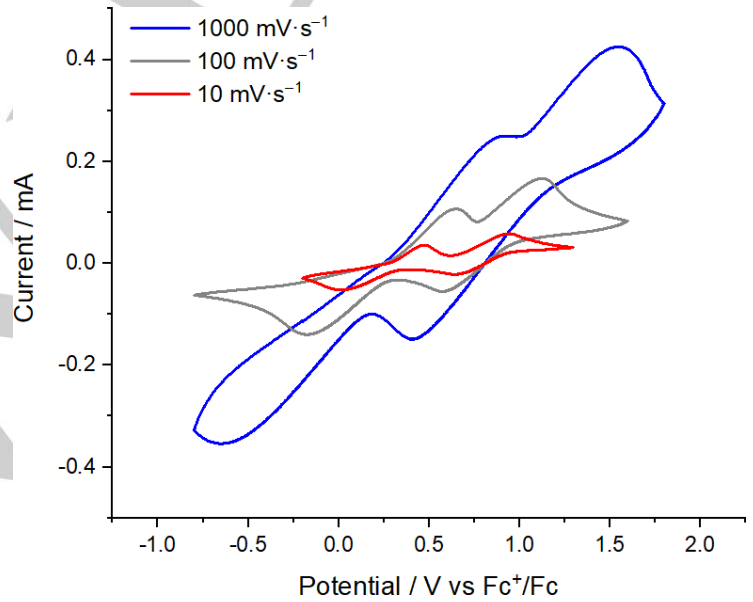

Figure S 24. Cyclic voltammogram of $[N_{2221}][Br_3]$ in [BMP][OTf] ($[Br_3]^-$ 0.5 M). Scan rate of 10, 100, and 1000 mV s^{-1}.

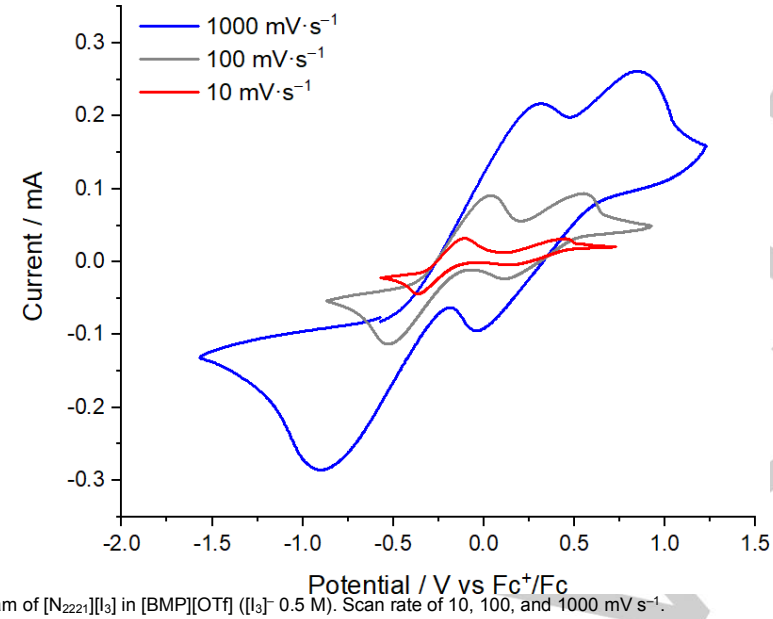

Figure S 25. Cyclic voltammogram of $[N_{2221}][I_3]$ in [BMP][OTf] ($[I_3]^-$ 0.5 M). Scan rate of 10, 100, and 1000 mV s^{-1}.

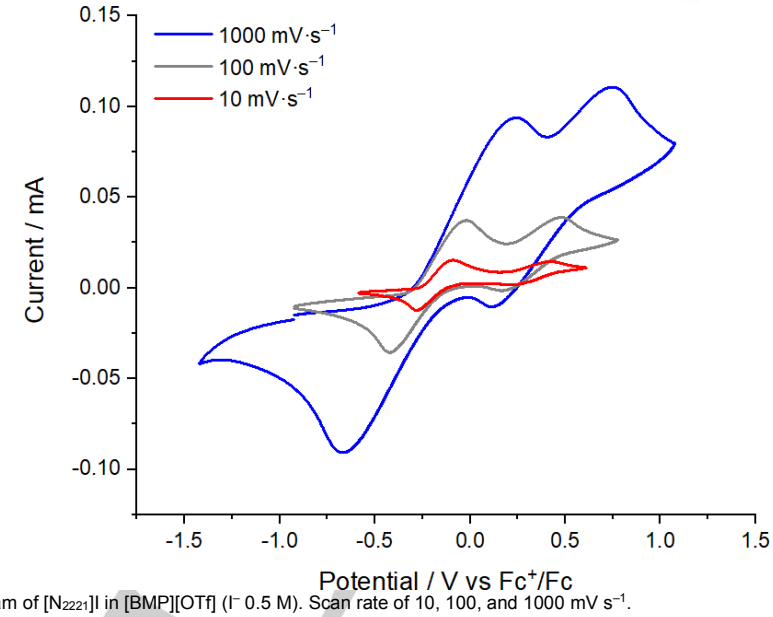

Figure S 26. Cyclic voltammogram of $[N_{2221}]I$ in [BMP][OTf] (I^- 0.5 M). Scan rate of 10, 100, and 1000 mV s^{-1}.

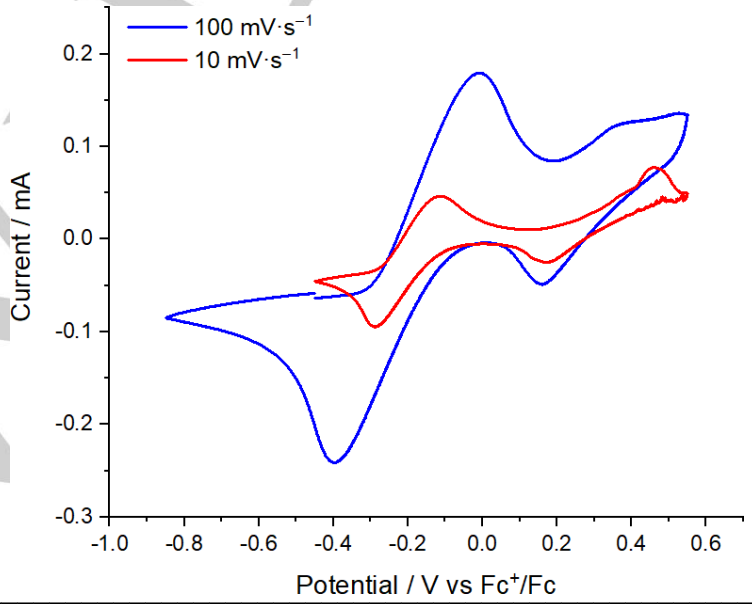

Figure S 27. Cyclic voltammogram of [HMIM][I_3] in [EMIM][OTf] ($[I_3]^-$ 0.3 M). Scan rate of 10 and 100 mV s^{-1}.

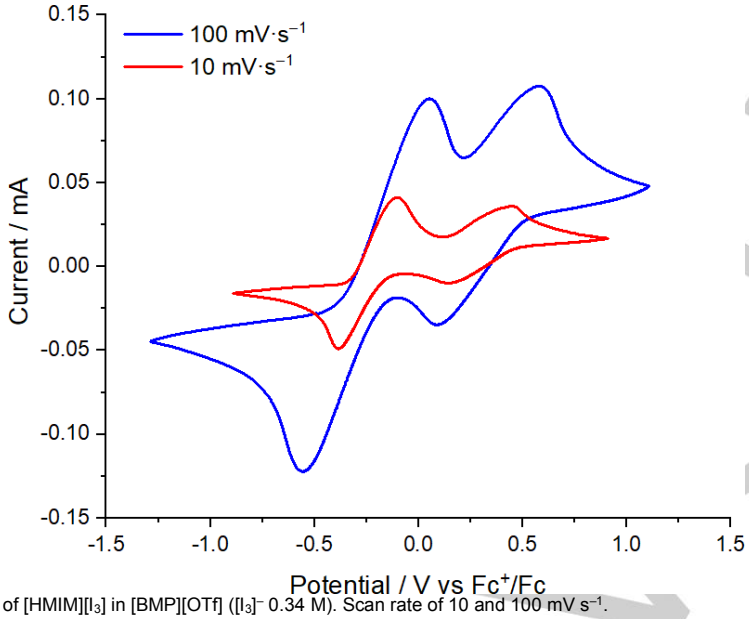

Figure S 28. Cyclic voltammogram of [HMIM][I_3] in [BMP][OTf] ($[I_3]^-$ 0.34 M). Scan rate of 10 and 100 mV s^{-1}.

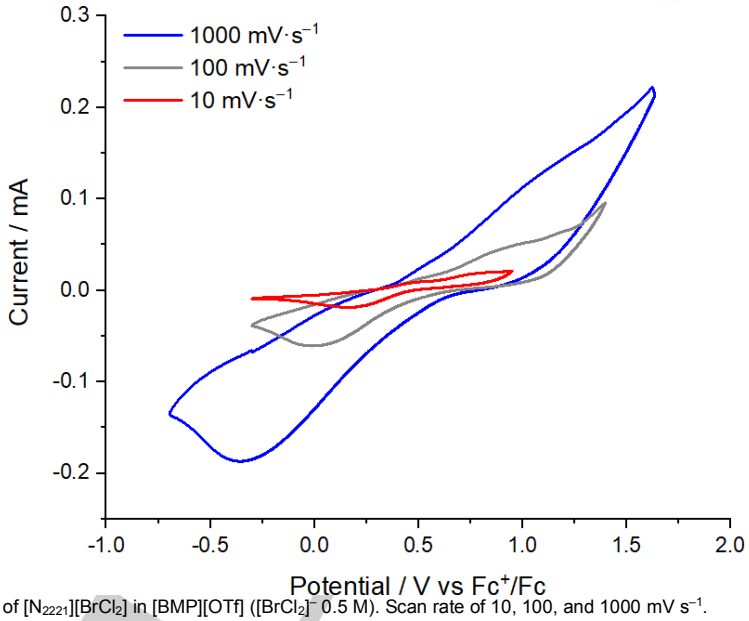

Figure S 29. Cyclic voltammogram of [N_{2221}][$BrCl_2$] in [BMP][OTf] ($[BrCl_2]^-$ 0.5 M). Scan rate of 10, 100, and 1000 mV s^{-1}.

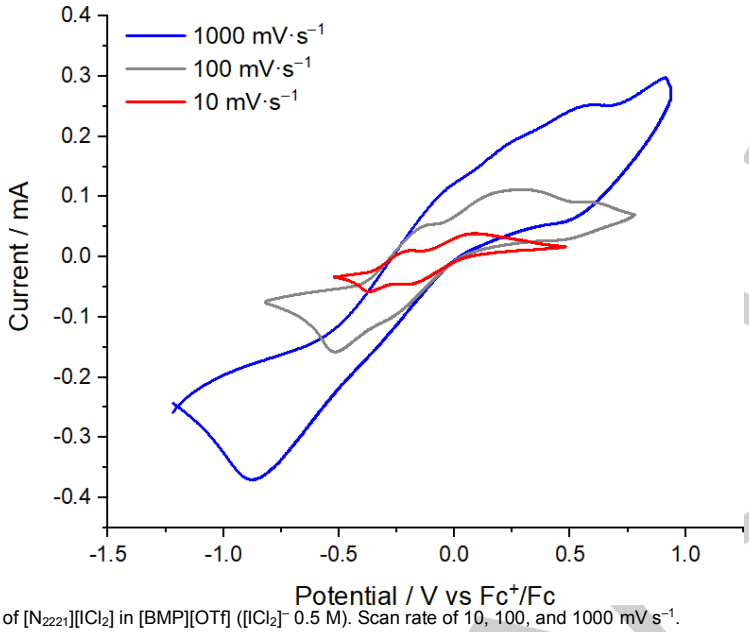

Figure S 30. Cyclic voltammogram of $[N_{2221}][ICl_2]$ in [BMP][OTf] ($[ICl_2]^-$ 0.5 M). Scan rate of 10, 100, and 1000 mV s^{-1}.

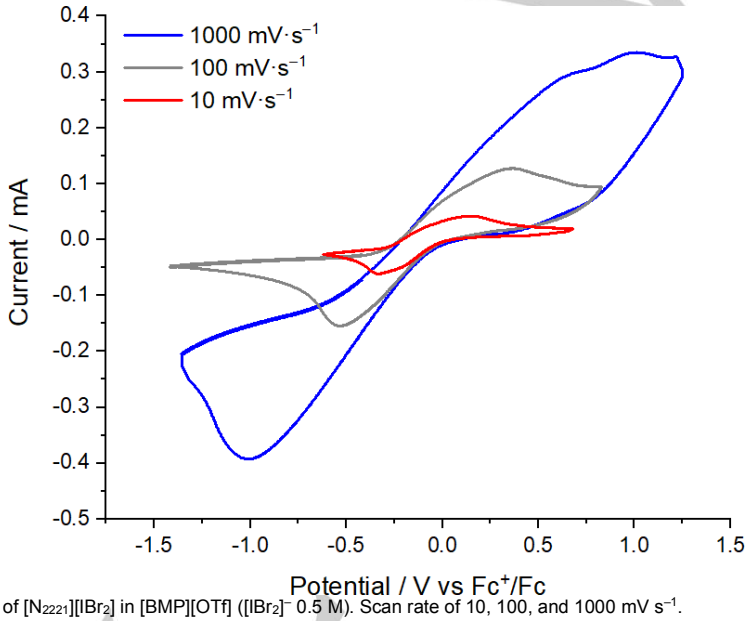

Figure S 31. Cyclic voltammogram of $[N_{2221}][IBr_2]$ in [BMP][OTf] ($[IBr_2]^-$ 0.5 M). Scan rate of 10, 100, and 1000 mV s^{-1}.

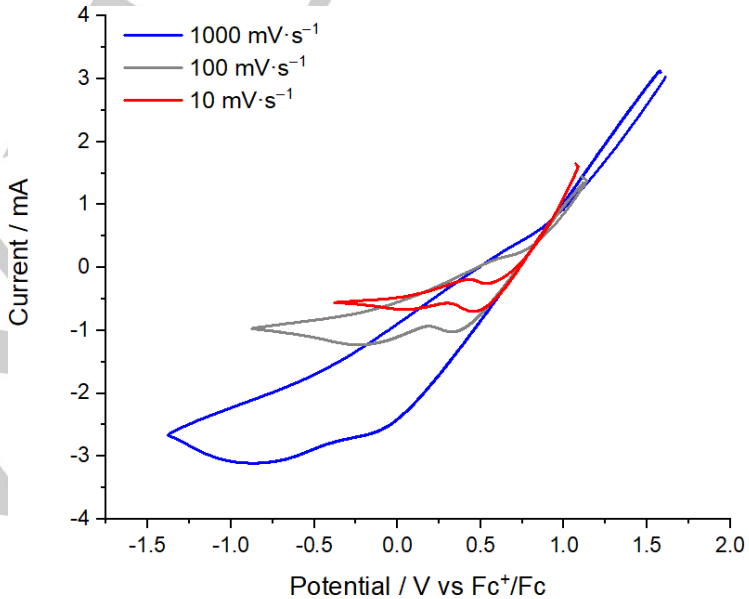

Figure S 32. Cyclic voltammogram of $[N_{2221}]Br$ in MeCN (Br^- 0.33 M). Measured at a temperature of 0 °C and a scan rate of 10, 100, and 1000 mV s^{-1}.

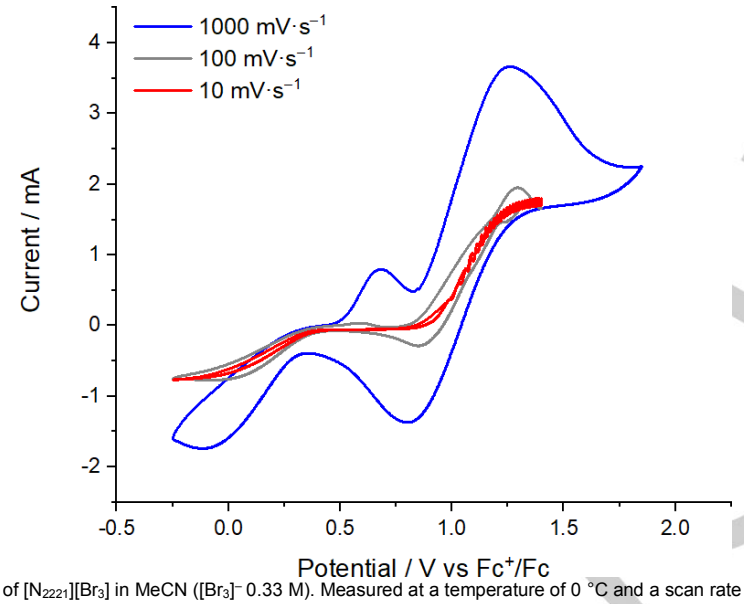

Figure S 33. Cyclic voltammogram of $[N_{2221}][Br_3]$ in MeCN ($[Br_3]^-$ 0.33 M). Measured at a temperature of 0 °C and a scan rate of 10, 100, and 1000 mV s^{-1}.

References

[1] M.F. Wempe, *J. Mol. Struct.* **2001**, *562*, 63.

[2] S. Furugori, A. Kobayashi, A. Watanabe, M. Yoshida, M. Kato, *ACS omega* **2017**, *2*, 3901.

[3] OriginLab Corporation, *Origin(Pro), Version 2020*, Northhampton, MA, USA.

C.2 Supporting Information – Synthesis, Crystallization, and Electrochemical Characterization of Room Temperature Ionic Liquid Bromidostannates(II/IV)

Tyler A. Gully, Karsten Sonnenberg, Julia Bader, and Sebastian Riedel*

Inorg. Chem., **2021**, *60*, 8093-8102.

https://doi.org/10.1021/acs.inorgchem.1c00706

The pages 72–82 contain the printed article, which is available at

https://doi.org/10.1021/acs.inorgchem.1c00706.

The pages 135–181 contain the supporting information of the article,

which is available under the same URL.

C.3 Supporting Information – Investigations Towards a Non-Aqueous Hybrid Redox-Flow Battery with a Manganese Based Anolyte and Catholyte

Maximilian Schmucker, **Tyler A. Gully**, Alexei Schmidt, Benjamin Schmidt, Kolja Bromberger, Joey Disch, Burkhard Butschke, Benedikt Burgenmeister, Karsten Sonnenberg, Sebastian Riedel and Ingo Krossing*.

Adv. Energy Mater., **2021**, 11, 2101261.

https://doi.org/10.1002/aenm.202101261

ADVANCED ENERGY MATERIALS

Supporting Information

for *Adv. Energy Mater.,* DOI: 10.1002/aenm.202101261

Investigations toward a Non-Aqueous Hybrid Redox-Flow Battery with a Manganese-Based Anolyte and Catholyte

*Maximilian Schmucker, Tyler A. Gully, Alexei Schmidt, Benjamin Schmidt, Kolja Bromberger, Joey Disch, Burkhard Butschke, Benedikt Burgenmeister, Karsten Sonnenberg, Sebastian Riedel, and Ingo Krossing**

Supporting Information

Methods and Experimental Section

Syntheses: All reactions and manipulations were carried out under an inert argon atmosphere using standard Schlenk-line and glovebox techniques.

$MnCl_2$

$MnCl_2$ (*Acros*, 99+%, anhydrous, 80 mesh) was dried by first refluxing over thionylchloride for approx. 6 h. After the removal of thionylchloride by distillation, the solid $MnCl_2$ was subsequently dried under reduced pressure at 80 °C before being placed into a glove box under argon atmosphere (H_2O and O_2 < 0.1 ppm).

[Cat]Cl

All [Cat]Cl (99%) salts were provided by *Io-li-tec*. Before use, the salts were dried under reduced pressure (10^{-3} mbar) at 80 °C for approx. 24 h. For storage and further use the salts were placed into a glove box under argon atmosphere (H_2O and O_2 < 0.1 ppm).

MeCN

MeCN (VWR) was refluxed over CaH_2 for 3 h and then distilled on activated 3 Å molecular sieves. The solvent was used once the water content, checked by Karl-Fischer titration, was below 10 ppm.

GBL

GBL (Acros Organics, Aldrich) was distilled onto activated 3 Å molecular sieves. The solvent was used once the water content, checked by Karl-Fischer titration, was below 5 ppm.

Synthesis of $[Cat]_2[MnCl_4]$ (Cat = suitable organic cation): $[Cat]_2[MnCl_4]$ salts were prepared on a 200 g scale. $MnCl_2$ was added to [Cat]Cl with a molar ratio of 1:2. MeCN was added and the reaction mixture was stirred at room temperature until all components dissolved completely. This needs approx. 3 mL MeCN per 1 g $MnCl_2$. The solution was then filtered over Celite® to remove a small amount of an insoluble impurity (presumably manganese oxides). Afterwards, all MeCN was removed under low pressure and the $[Cat]_2[MnCl_4]$ salt was obtained in typically >99% yield as an off-white solid in case of $[BMP]_2[MnCl_4]$ (BMP = N,N-butyl-methyl-pyrrolidinium) and $[N_{2225}]_2[MnCl_4]$ (N_{2225} = Triethyl-pentyl-ammonium) and a slightly brown solid in case of $[EMP]_2[MnCl_4]$ (EMP = N,N-Ethyl-methyl-pyrrolidinium). The synthesis and characterization of further salts with different $[Cat]^+$ is described in the next paragraph.

$[BMP]_2[MnCl_4]$: **FT-Raman** (RT, powder, 4cm^{-1}): 3030 (w), 3008 (m), 2963 (vs), 2941 (vs), 2875 (m), 2807 (vw), 2754 (vw), 1449 (m), 1378 (vw), 1348 (vw), 1315 (vw), 1283 (vw), 1239 (vw), 1189 (vw), 1122 (vw), 1065 (vw), 1051 (w), 1022 (vw), 967 (vw), 930 (vw), 903 (w), 823 (vw), 733 (vw), 632 (vw), 476 (vw), 445 (vw), 420 (vw), 376 (vw), 346 (vw), 300 (w), 256 (w), 116 (m). **UV-Vis** (RT, in GBL, 90 wt % GBL): 358(vs), 386(s), 428 (m), 432(m), 445(s),

465(w) nm. **Yield**: >99 %. **EA**: calcd. (%): C 44.92, H 8.38, N 5.82; found (%): C 44.78, H 8.39, N 5.74.

$[EMP]_2[MnCl_4]$: **FT-Raman** (RT, powder, 4cm^{-1}): 2985 (vs), 2954 (vs), 2900 (m), 2846 (vw), 2795 (vw), 2758 (vw), 1453 (m), 1403 (vw), 1367 (vw), 1320 (vw), 1299 (vw), 1238 (vw), 1197 (vw), 1114 (vw), 1085 (vw), 1053 (w), 999 (w), 1036 (vw), 937 (vw), 903 (w), 881 (vw), 825 (vw), 715 (vw), 587 (vw), 646 (vw), 563 (vw), 478 (vw), 451 (vw), 386 (vw), 434 (vw), 253 (w), 115 (m). **UV-Vis** (RT, in GBL, 90 wt % GBL): 427 (m) 432(m), 446(m), 470(w) nm. **Yield**: >99 %. **EA**: calcd. (%): C 39.55, H 7.59, N 6.59; found (%): C 39.12, H 7.42, N 6.48.

$[N_{2225}]_2[MnCl_4]$: **FT-Raman** (RT, powder, 4cm^{-1}): 2988 (vw), 2942 (vw), 2900 (vw), 2872 (vw), 2757 (vw), 2733 (vw), 1462 (vw), 1443 (vw), 1387 (vw), 1359 (vw), 1309 (vw), 1296 (vw), 1167 (vw), 1127 (vw), 1073 (vw), 1015 (vw), 1048 (vw), 1101 (vw), 945 (vw), 895 (vw), 799 (vw), 696 (vw), 423 (vw), 408 (vw), 391 (vw), 269 (vw), 253 (vw), 167 (vw) cm^{-1}. **Yield**: >99 %.

Synthesis of $[Cat]_2[MnCl_5]$: $[Cat]_2[MnCl_5]$ salts were prepared on a scale up to 90 g. $[Cat]_2[MnCl_4]$ was dissolved in MeCN (approx. 1.5 mL MeCN per 1 g $[BMP]_2[MnCl_4]$), giving a slightly yellow solution. Dichlorine was condensed onto the reaction mixture using a bath of dry ice in isopropanol with around –40 °C, and subsequently thawed. The reaction of Cl_2 with the $[Cat]_2[MnCl_4]$ produced a dark green solution. The MeCN was then removed under reduced pressure at 45 °C. The product was a green solid. An alternative method for bulk synthesis is to take the $[Cat]_2[MnCl_4]$ solution in MeCN and continually stir at room temperature while adding Cl_2 gas through an evacuated Schlenk-line. The $[BMP]_2[MnCl_4]$ reacts quickly, and because the product has a no vapor pressure, the reaction prevented pressure build-up of Cl_2 in the line.

$[BMP]_2[MnCl_5]$: **FT-Raman** (RT, powder, 4cm^{-1}): 2960 (vs), 2939 (vs), 2877 (vs), 1451 (w), 903 (vw), 292 (w), 254 (vw), 114 (w). **FT-Raman** (RT, in MeCN, c = 1.6 mol L^{-1}, 4cm^{-1}): 2993 (w), 2942 (vs), 2879 (vw), 2733 (vw), 2293 (vw), 2252 (s), 1451 (vw), 1375 (vw), 920 (vw), 380 (vw), 289 (vw), 252 (vw), 230 (vw). **UV-Vis** (*r.t.,* 90 wt. % GBL): 426(s), 627(m), 770(w) nm. **Yield**: >99 %.

$[EMP]_2[MnCl_5]$: **FT-Raman** (RT, in MeCN, 4cm^{-1}): 2994(s), 2939(vs), 2899(s), 2849(m), 2729(w), 2304(m), 2249(vs), 1448(m), 1373(w_, 1048(vw), 998(vw), 918(m), 716(vw) 585(vw), 381(m), 362(vw), 298(vw,sh), 287(m), 252(w), 231 (vw) cm^{-1}. **FT-Raman** (RT, in GBL, SEC, 4cm^{-1}): 2995(s), 2969(s), 2953(s), 2919(s), 2895(m), 1770(m), 1486(w), 1456(m), 1425(w), 1245(w), 1051(vw), 1035(vw), 998(w), 931(m), 901(w), 872(m), 803(m), 681(vw), 300(w), 289(m), 251(w), 237(vw) cm^{-1}. **UV-Vis** (*r.t.,* 90 wt. % GBL): 425(s), 627(m), 768(w) nm. **Yield**: >99 %.

Raman Spectroelectrochemical Analysis: Raman spectra were recorded on a Bruker MultiRam spectrometer equipped with a 5 mm aperture microscope and a low-temperature Ge detector (1064 nm, 30 – 100 mW, resolution 4 cm^{-1}). The electrochemical cell is an optically transparent thin layer electrochemical Ottle cell, normally used in a three-electrode configuration, with the WE between CE and RE. The CE and RE are a Pt-mesh with a mesh size of 52 (0.5×0.4 cm and wire diameter of 0.1 mm), and the WE is a Pt-mirror

(1.0×0.4×0.1 cm), treated with HNO_3 for 5 min before being rinsed with distilled water, acetone, and ethyl acetate. The Pt-mirror was polished using 1200 grit aluminum oxide in isopropanol, before being placed in an ultrasonic bath (isopropanol) for 5 min. The linear sweep voltage, LSV, was measured at a rate of 50 mV s^{-1} to determine the oxidation potential of Mn^{II}/Mn^{III} vs. *q-Pt* RE. Subsequently, controlled chronoamperometric electrolysis measurements at the oxidation potential were measured, while simultaneously Raman spectra were recorded.

UV / Vis Spectroelectrochemical Analysis: The UV-Vis spectra were recorded using a Perkin Elmer Lambda 465 photometer with deuterium and tungsten lamps. The spectroelectrochemical measurements were performed with a cell similar to the Raman spectroelectrochemical cell, where the working electrode is a Pt-mesh (52 mesh, 1.0×1.0 cm and wire diameter of 0.1 mm). UV-Vis measurements were recorded during the LSV, v = 10 mV s^{-1}.

pXRD: pXRD data were collected in capillaries with a STOE Stadi P powder diffractometer equipped with a Ge-(111)-monochromator, using Mo-Kα_1 radiation and a position sensitive detector (PSD). The data was processed with the WinXPow package (Stoe) and analyzed with the Diffrac.EVA package (Bruker AXS).

scXRD: The data were collected from a shock-cooled single crystal on a Bruker APEX2 QUAZAR three-circle diffractometer with a microfocus sealed X-ray tube using mirror optics as monochromator and a Bruker APEXII detector. The diffractometer was equipped with an Oxford Cryostream 800 low temperature device and used Mo-Kα radiation (λ = 0.71073 Å). All data were integrated with SAINT and a multi-scan absorption correction using SADABS was applied.[1,2] The structure was solved by direct methods using SHELXT and refined by full-matrix least-squares methods against F^2 by SHELXL-2018/3.[3,4] All non-hydrogen atoms were refined with anisotropic displacement parameters. The hydrogen atoms were refined isotropically on calculated positions using a riding model with their U_{iso} values constrained to 1.5 times the U_{eq} of their pivot atoms for terminal sp^3 carbon atoms and 1.2 times for all other carbon atoms. Disordered moieties were refined using bond lengths restraints and displacement parameter restraints. Some parts of the disorder model were introduced by the program DSR.[5,6] The graphical representation of the crystal structure was prepared with mercury (version 4.0).[7] CCDC 2031457 contains the supplementary crystallographic data for this paper. These data can be obtained free of charge from *The Cambridge Crystallographic Data Centre* via www.ccdc.cam.ac.uk/structures.

SEM and EDX Measurements: High-resolution scanning electron microscopy (SEM) was performed using a FEG-HRSEM SU8220 (HITACHI) equipped with a TE, a BSE and a SE detector. The same device was used for the EDX measurements using a X-Flash 6/30 detector

(Bruker) for a working distance of 15 mm and a QUANTAX FlatQUAD detector for a working distance of 10 mm.

Conductivity and Viscosity Measurements: The temperature dependent conductivity was measured using the *Mettler Toledo AG* SevenCompact S230 Conductivity Meter and INLAB® 710 sensor. The conductivity cell had an argon counter flow, while temperature was adjusted via a cryostat. The kinematic viscosity was measured using an Ubbelohde viscometer from *SI Analytics GmbH, Mainz* using Schlenk techniques under argon. Temperature regulation was controlled by submerging the viscometer into a heat bath of polyethylene glycol 400.

Cyclic Voltammetry: All cyclic voltammograms were recorded in an argon filled glovebox. A three-electrode arrangement was used with a 1 mm Pt disc working electrode, a Pt wire reference electrode and a Pt net as counter electrode. For the measurements the potentiostat VMP3 (Bio-Logic Science Instruments) was used, controlled via PC using the software EC-Lab (V11.21). Since the active species are salts and their concentrations are at least 1 M, no further supporting electrolyte was used.

Elemental analyses: Elemental analyses were performed using a vario MICRO cube (*Elementar Analysensysteme GmbH*).

Measurement of Cell Resistances: Cell resistances were measured with an existing method from EC-Lab.[8] The method is an impedance measurement with a high frequency (100000 kHz) to determine only the resistance of the solution.

Calculation of Energy Densities: Theoretical energy densities (W_s^{th}) were calculated according to [S 1],

$$W_s^{th} = C_s^{th} \times E_{cell} \qquad \text{[S 1]}$$

whereas C_s^{th} and E_{cell} are the theoretical specific capacity and the cell voltage, respectively. C_s^{th} was calculated for each half cell according to [S 2],

$$C_s^{th} = z \times c \times F \qquad \text{[S 2]}$$

with *z* being the number of transferred electrons, *c* the concentration of the active species and *F* the Faraday constant.

Mass Spectrometry: The mass-spectrometric experiments were performed with a Thermo-Fischer LTQ XL linear ion-trap mass-spectrometer equipped with an electrospray-ionization (ESI) source. Millimolar solutions of the samples were prepared in methanol. The sample solutions were injected through a fused-silica capillary to the ESI source at a flow rate of 10 µL min^{-1}. Nitrogen was used as a sheath, sweep, and auxiliary gas at flow rates adjusted to 5, 0, and 0, respectively (given in arbitrary units). The source voltage was set to 3.5 kV. The

tube lens voltage was adjusted to –100 V and the capillary voltage to –49 V. The capillary temperature was set to 150 °C. The identity of the ions was confirmed by comparison with the expected isotope patterns complemented by collision-induced dissociation (CID) experiments. In the CID experiments, helium served as the collision gas. The collision energy was adjusted by varying the normalized collision energy (NCE) between 0 and 30. Note that this value is given in arbitrary units, and a conversion to an E_{lab} scale is difficult. Simulation of the isotopic patterns was performed with the software package Xcalibur 3.0.63.

Battery Measurements in Static Cells: Battery measurements were conducted in homemade cells (Figure S 1 and Figure S 2). While the battery casing was made of polyvinylidene fluoride, the casing for the half-cells consist of Teflon. Through the modular design it is possible to have different Teflon insets that vary in thickness or the size of the opening. Therefore, the amount of electrolyte as well as the size of the electrode area can be adjusted for the respective experiment. The geometry of the electrodes was planar with the option to use a surface area of 0.95 cm^2 or 3.14 cm^2. The distance between the electrodes was 1.1 cm for full-cells and 0.55 cm for half-cells. The respective electrolyte volumes are therefore 0.52 mL (A = 0.95 cm^2) or 1.7 mL (A = 3.14 cm^2) for one half-cell. Even with just 0.52 mL in each half-cell the amount of active species is still very high (SoC100 = 11.2 mAh for $EL_{GBL\text{-}BMP\text{-}Cl\text{-}55}$, cf. Table 1). For a first screening, therefore, ten cycles between SoC0 and SoC5 were conducted to save time. If a battery measurement looked promising after this cycling to SoC5, we performed cycling between SoC0 and SoC80 directly afterwards, until the battery stopped working. Cycling experiments were conducted either with a current density of 0.5 mA cm^{-2} or with 0.25 mA cm^{-2}. For constant current charging an upper voltage limit was set at 4 V, whereas for discharging the limit was set to 0 V or 0.5 V. Each battery experiment was conducted in duplicate and for the coulomb efficiencies (CEs) the average of two experiments are shown in this work. TF6 bipolar plates from SGL carbon were used as graphite electrodes. Before use, the TF6 plates were cleaned with acetone and EA, dried at 60 °C for at least 12 h and brought into the glovebox, where they were used without any further pretreatment. The introduction of carbon felt electrodes is also possible and with the pressure sensor one can assure that the contact pressure is sufficient, for the felt electrodes to be contacted properly. With a good set of stamping tools, the right size of the sealing material can be produced. “Ice Cube” sealing from Freudenberg with a thickness of 0.8 mm was used for the battery setup. The sealing material was treated just like the TF6 plates before use. Since the single components are simply stacked on each other, different electrode materials can be used, whereas the thickness of the latter is irrelevant. The fixation of the whole cell is guaranteed by the big screw, that allows to apply more than 1kN of contact pressure. Through the small opening in the Teflon insets the electrolyte can be placed in the cell (see Figure S 2 b), and additionally they allow the withdrawal of samples during a measurement.

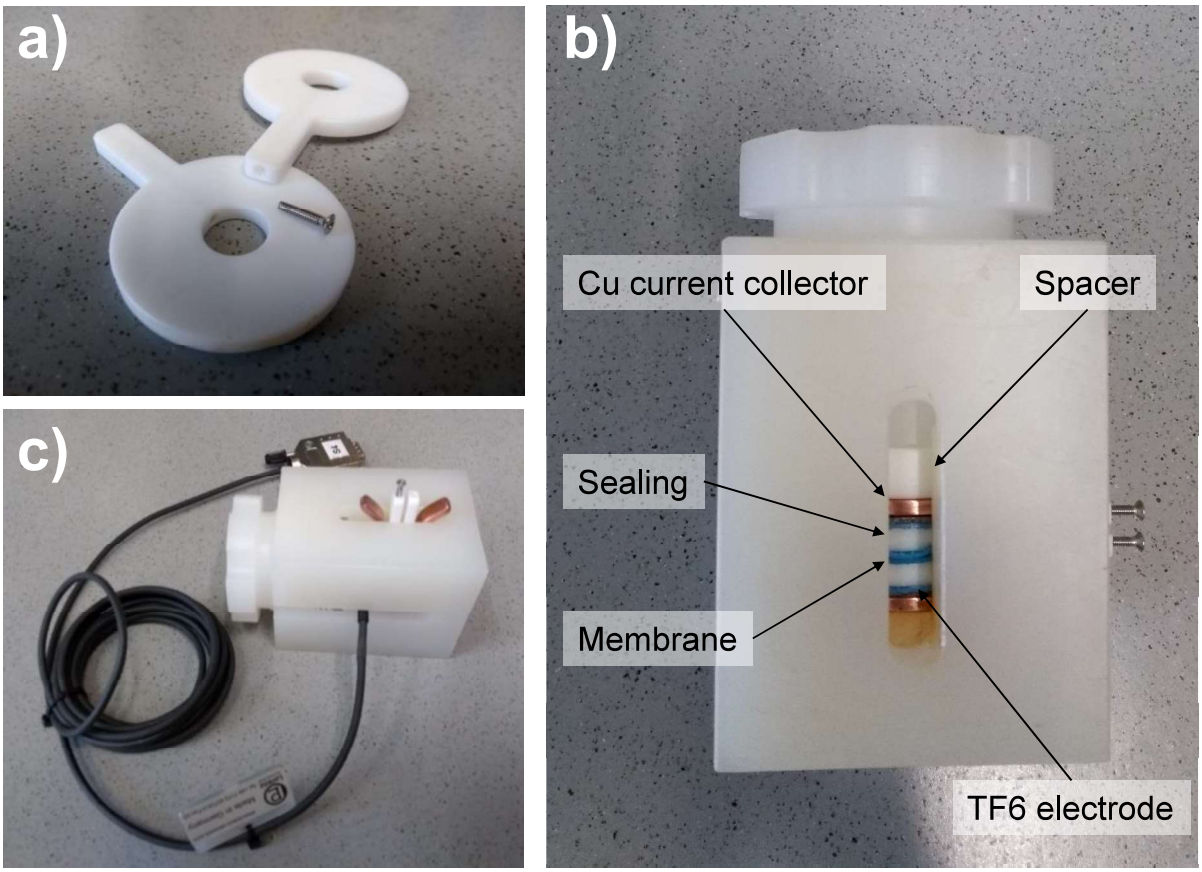

Figure S 1: a) Teflon insets that were used in the battery setup. Different insets are available with inner diameters of 5 mm, 11 mm and 20 mm, allowing to adapt the amount of electrolyte, depending on the experiment. Due to the design it is possible to take samples of the electrolyte during a measurement. b) Assembled battery with sealing between the Teflon insets and the electrodes as well as between the Teflon insets and the membrane. c) Battery equipped with a pressure sensor. More detailed photographs of the single components are shown in Figure S 2.

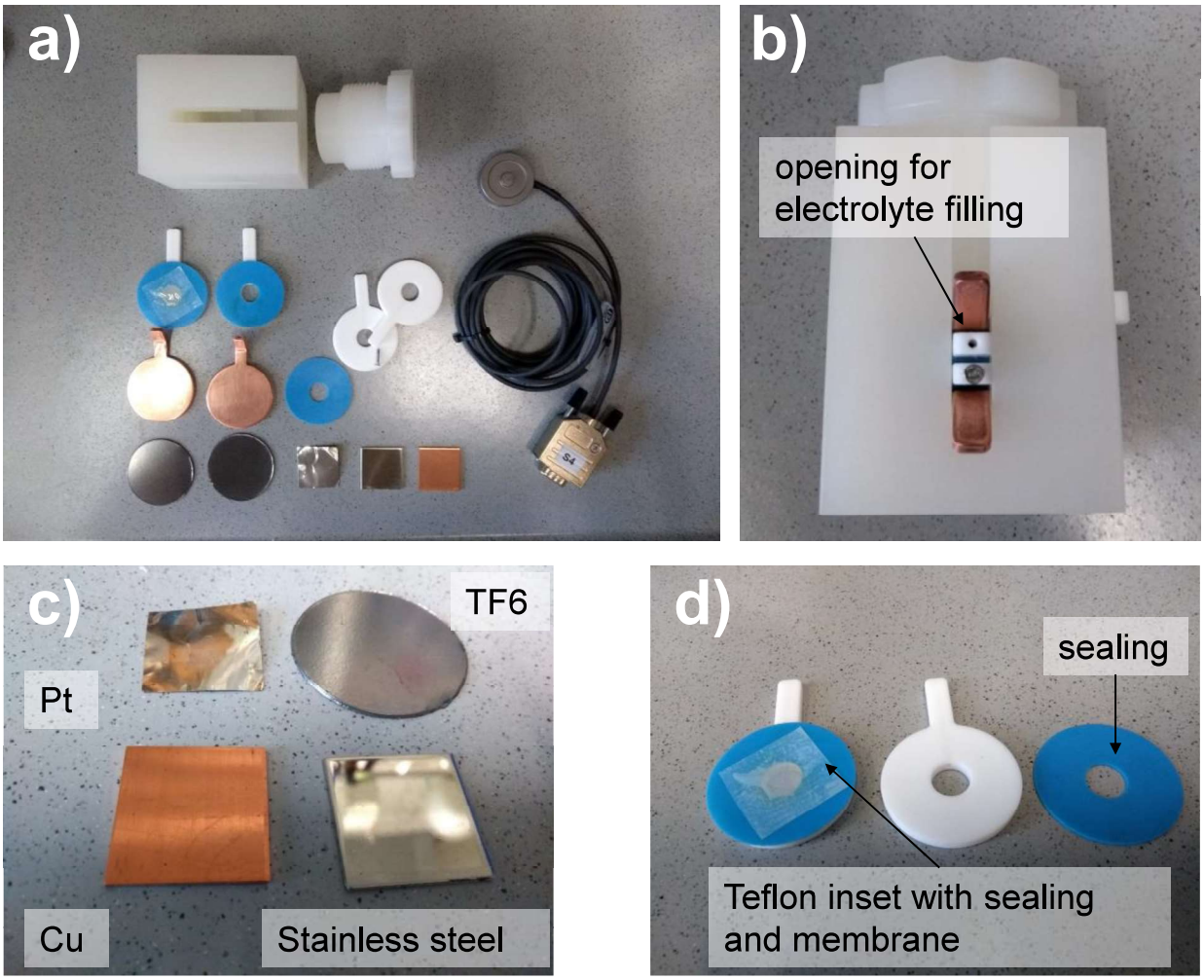

Figure S 2: All single components that are necessary for the assembly of a battery (a). Opening in the Teflon insets for placing the electrolyte in the cell and the withdrawal of samples during measurements (b). Different types of electrodes that can be used in the homemade cell setup (c). Demonstration, how the sealing material is used to incorporate the membrane in the cell (d).

Membranes: The ion-selective membranes used in this work were provided by Fumatech GmbH. For the requirements of our chemical systems we identified the anion exchange membranes (AEM) FAPQ-375-PP, FAPQ-310 and VM-FAPQ-230 as the most suited. The number in the membrane acronym equals the thickness of the membrane in µm, the ending PP in FAPQ-375-PP indicates that the membrane is supported by a polypropylene backbone.

Membrane Pretreatment: After cutting the membranes into pieces that fit into our homemade battery cells, these pieces were dried at 60 °C for 24 h. Then the warm membrane pieces were placed in the antechamber of the glovebox and evacuated for 12 h. Afterwards the membranes were stored in the glovebox and used without any further pretreatment for the assembly of the cells. After adding the electrolyte to a battery cell and prior to cycling, the cell resistance was controlled regularly until a constant value was reached. The time needed for the membrane

soaking process varied strongly, depending on the electrolyte between 0.5 h and 12 h. Only after the cell resistance was constant, cycling of the battery was started.*

Synthesis and characterization of the $[Cat]_2[MnCl_4]$ salts

Table S 1 shows IR and Raman (R) Mn-Cl stretching frequencies from different $[Cat]_2[Mn^{II}Cl_4]$ compounds prepared in this work and compares them to literature known compounds. Table S 2 show the electronic transitions assigned for the UV / Vis data of $[Mn^{II}Cl_4]^{2-}$ solutions in MeCN and GBL and comparison with available literature data in MeCN.

Table S 1: IR and Raman (R) Mn-Cl stretching frequencies from different $[Cat]_2[Mn^{II}Cl_4]$ compounds. Comparison between salts from this work and selected examples from the literature.

substance	ref.	phase	ν_1	ν_2	ν_3	ν_4
$[BMP]_2[MnCl_4]$	this work	solid	256 R	-	272 IR	115 R 112 IR
$[BMP]_2[MnCl_4]$	this work	in GBL	251 R	-	-	-
$[BMP]_2[MnCl_4]$	this work	in MeCN	253 R	-	-	-
$[EMP]_2[MnCl_4]$	this work	solid	252 R	-	-	115 R
$[NEt_4]_2[MnCl_4]$	[9]	solid	258 R	-	284 IR	116 R 118 IR
$[NEt_3H]_2[MnCl_4]$	[10]	solid	256 R	-	278, 301 IR	120 IR
$[NEt_3H]_2[MnCl_4]$	[10]	in MeCN	249 R	-	-	-

Table S 2: Electronic transitions assigned for the UV / Vis data of $[Mn^{II}Cl_4]^{2-}$ solutions in MeCN and GBL and comparison with available literature data in MeCN.

Subst.	electronic transitions / nm						
	$^6A_1 \rightarrow {}^4T_1$ (^4P)	$^6A_1 \rightarrow {}^4E$ (^4D)	$^6A_1 \rightarrow {}^4T_2$ (^4D)	$^6A_1 \rightarrow {}^4A_1$ (^4G)	$^6A_1 \rightarrow {}^4E_1$ (^4G)	$^6A_1 \rightarrow {}^4T_2$ (^4G)	$^6A_1 \rightarrow {}^4T_1$ (^4G)
$[BMP]_2[MnCl_4]$ in MeCN[a]	357	369 (sh)	380 (sh)	428 (sh)	432	445	465 (br, sh)
$[MePh_3P]_2[MnCl_4]$ in MeCN[11]	357	369 (sh)	379 (sh)	428 (sh)	432	446	465 (br, sh)
$[BMP]_2[MnCl_4]$ in GBL[a]	-	-	-	428	432	445	465

[a] this work. br = broad, sh = shoulder

* Soaking the membranes with the respective electrolyte before assembling a battery was not practical, because the membranes curled up extremely after contact with the electrolyte. In this condition it was not possible to place the membrane correctly in the battery cell.

Since $[MnCl_4]^{2-}$ is supposed to be the active species in the all-Mn-battery, it is important to exclude decomposition, when the solvent is added for electrolyte preparation. For this purpose, Raman spectroscopy is a very useful method. Figure S 3 shows for example that the $[MnCl_4]^{2-}$ anion is not stable in water, since the ν_1-stretching frequency disappears completely after the addition of water. This does not happen, when MeCN or GBL is added. Solvent molecules that coordinate stronger to Mn^{2+} than chloride can replace the latter, leading to a completely different species. In case of H_2O we assume that the hexa aquo complex $[Mn(H_2O)_6]^{2+}$ is formed, but did not further investigate that issue, since we were only interested, whether the $[MnCl_4]^{2-}$ anion is stable.

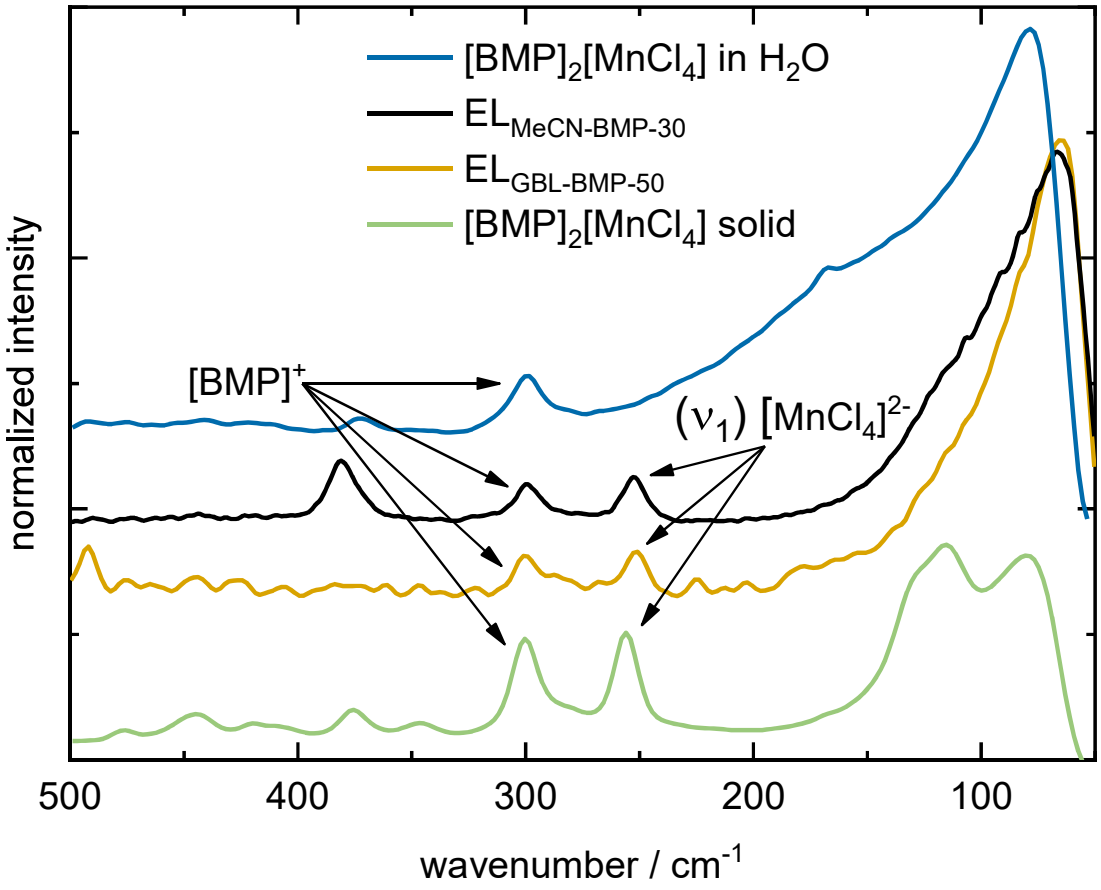

Figure S 3: Raman spectra of solid $[BMP]_2[MnCl_4]$, $EL_{GBL\text{-}BMP\text{-}50}$, $EL_{MeCN\text{-}BMP\text{-}30}$ and $[BMP]_2[MnCl_4]$ in H_2O (H_2O was added until $[BMP]_2[MnCl_4]$was dissolved completely). The stretching mode at 300 cm^{-1} can be assigned to the $[BMP]^+$, as discussed earlier.

Alternative Cations

Next to $[BMP]^+$ and $[EMP]^+$ we also synthesized and analyzed $[MnCl_4]^{2-}$-salts with other asymmetric cations. Figure S 4 shows the structures of the cations, whose chloride salts we used. [OMIM]Cl and [PMP]Cl were obtained from *Io-li-tec*. $[N_{221\text{-}3O1}]Cl$, [Me.3O1-pyrr]Cl and $[P_{4441}]Cl$ were synthesized.

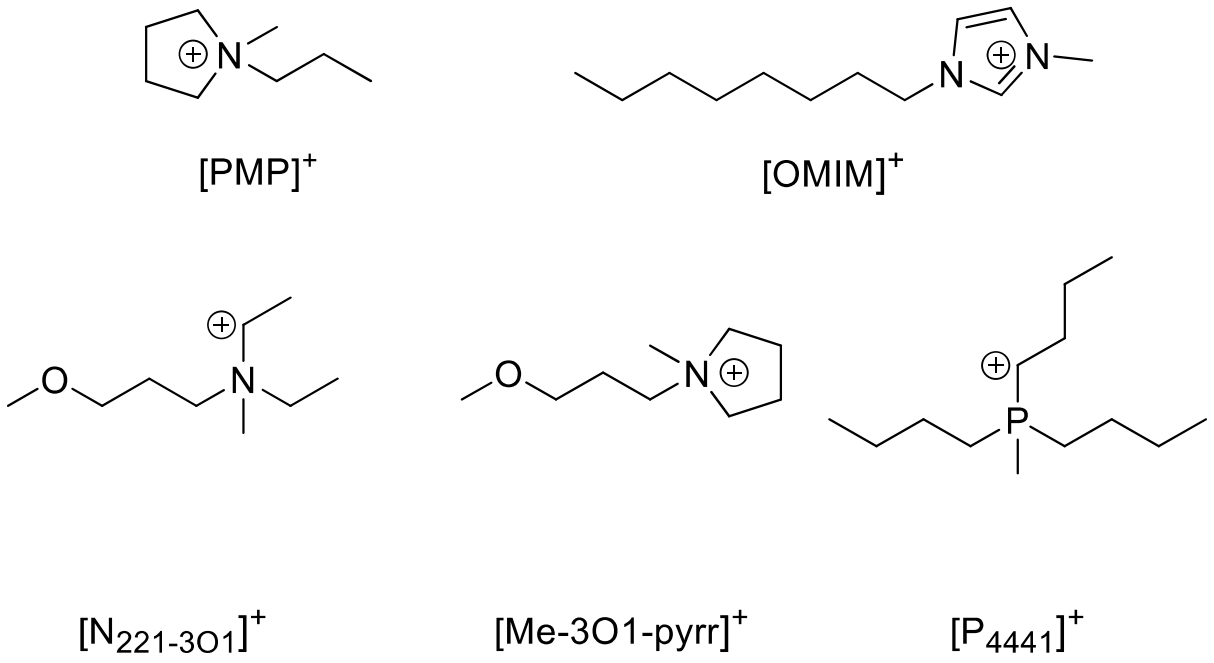

Figure S 4: Different asymmetric cations, whose chloride salts were used for the synthesis of $[MnCl_4]^{2-}$-salts.

3-methoxypropylpyrrolidin

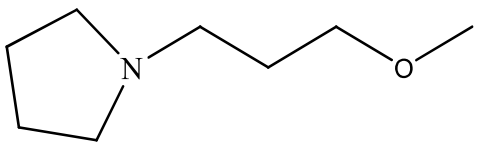

BrPrOMe (42.5 g, 278 mmol, 1 eq.) in 30 mL MeCN was added dropwise over an hour to a mixture of excess pyrrolidin, (59.2 g, 1.07 mol, 3 eq.) with K_2CO_3 (115 g, 833 mmol, 3 eq.) in 300 mL MeCN. During addition of BrPrOMe the solution was stirred at RT. Subsequently the reaction proceeded at 70 °C for 1.5 h. The product was fractionally distilled at 50 mbar and 90 °C. The product was isolated as a colorless liquid (81 % yield, 32.7 g, 225 mmol).

^{1}H NMR (400 MHz, $CDCl_3$, 22 °C): δ = 3.41 (t, *J* = 6.1 Hz, 2H), 2.50-2.46 (m, 11H), 1.81-1.73 (m, 4H) ppm;

$^{13}C\{^1H\}$ NMR (100 MHz, $CDCl_3$, 22 °C): δ = 71.4 (s), 58.5 (s), 54.3 (s), 53.5 (s), 52.9 (s), 29.2 (s), 23.7 (s) ppm;

ESI+ = [M^++H] 144.1322 m/z;

3-methoxypropyl-1-methylpyrrolidiniumchloride [Me-3O1-pyrr]Cl

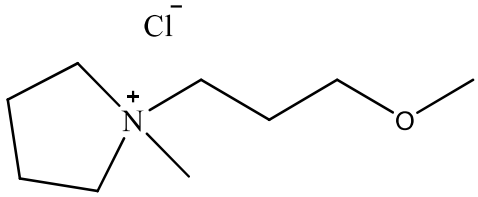

Methyl chloroformate, MeOCOCl, (29.2 g, 309 mmol, 3 eq.) in 15 mL DCM was added dropwise to 3-methoxypropylpyrrolidin (14.8 g, 103 mmol, 1 eq.) in 20 mL DCM over the course of an hour. The reaction was stirred for an hour at 0 °C and the temperature was slowly raised to 50 °C and stirred for another 7 h. The DCM was removed under low pressure resulting in a violet solid. The product was washed three times with pentane followed by diethyl ether. The product was dried under vacuum at 80 °C for 8 h, resulting in a white solid. Yield: 17.5 g, 90.6 mmol, 88%.

^{1}H NMR (400 MHz, $CDCl_3$, 22 °C): δ = 3.93 (t, *J* = 6.1 Hz, 2H), 3.80-3.76 (m, 4H), 3.68 (s, 3H), 3.51 (t, *J* = 5.2 Hz, 2H), 3.34 (s, 3H), 2.30 (m, 2H), 2.08 (m, 4H) ppm.

^{13}C{^{1}H} NMR (100 MHz, $CDCl_3$, 22 °C): δ = 69.1 (s), 65.6 (s), 64.5 (s), 62.0 (s), 59.0 (s), 58.8 (s), 48.8 (s), 26.6 (s), 21.8 (s) ppm.

ESI+ = [M^+] 158.1523 m/z;

***N,N*-diethyl-3-methoxypropylamine**

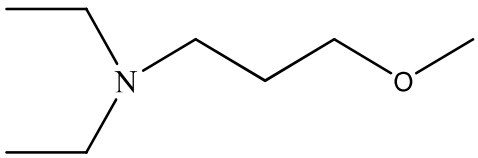

BrPrOMe (54.8 g, 360 mmol, 1 eq.) in 40 mL was added dropwise over an hour to a mixture of excess diethyl amine (78.6 g, 1.07 mol, 3 eq.) and K_2CO_3 (149 g, 1.07 mol, 3 eq.) in 260 mL MeCN. During addition of BrPrOMe the solution was stirred at RT. Subsequently the reaction proceeded at 70 °C for 1.5 h. The product was fractionally distilled at 90 mbar and 90 °C. The product was isolated as a colorless liquid. Yield: 30.1 g, 211 mmol, 58%.

^{1}H NMR (400 MHz, $CDCl_3$, 22 °C): δ = 3.36 (t, *J* = 6.2 Hz, 2H), 3.28 (s, 3H), 2.46 (m, 6H), 1.67 (m, 2H), 0.97 (t, *J* = 7.1 Hz, 6H) ppm.

$^{13}C\{^{1}H\}$ NMR (100 MHz, $CDCl_3$, 22 °C): δ = 116.6 (s), 71.7 (s), 46.9 (s), 46.7 (s), 15.6 (s), 15.3 (s), 14.9 (s), 1.93 (s) ppm.

ESI+ = $[M^+ + H]$ 146.1617 m/z

_N_,_N_-diethyl-_N_-methyl-3-methoxypropylammoniumchloride, $[N_{221\text{-}3O1}]Cl$

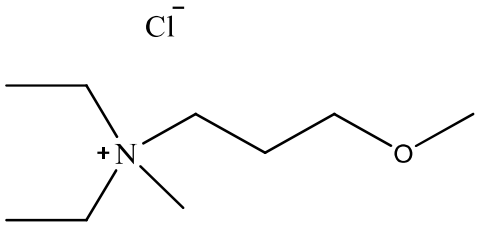

Methyl chloroformate, MeOCOCl, (46.4 g, 491 mmol, 3 eq.) in 25 mL DCM was added dropwise to *N*,*N*-dimethyl-3-methoxypropylamine (23.8 g, 164 mmol, 1 eq.) over the course of an hour. The reaction was stirred for an hour at 0 °C and the temperature was slowly raised to 50 °C and stirred for another 7 h. The DCM was removed under vacuum resulting in a violet solid. The product was washed three times with pentane followed by diethyl ether. The product was dried under vacuum at 80 °C for 8 h, resulting in a white solid. Yield: 11.6 g, 59.6 mmol, 36.4%.

^{1}H NMR (400 MHz, $CDCl_3$, 22 °C): δ = 3.60 (m, 4H), 3.40 (t, *J* = 6.6 Hz, 4H), 3.32 (s, 6H), 1.71 (m, 2H), 1.31 (m, 6H) ppm.

$^{13}C\{^{1}H\}$ NMR (100 MHz, $CDCl_3$, 22 °C): δ = 95.2 (s), 75.1 (s), 69.4 (s), 59.0 (s), 58.9 (s), 46.7 (s), 46.6 (s), 24.1 (s), 8.7 (s) ppm.

Synthesis of $[OMIM][BMP][MnCl_4]$

$[BMP]_2[MnCl_4]$ (10.1 g, 22.1 mmol, 1 eq.) was added to $[OMIM]_2[MnCl_4]$ (14.5 g, 24.7 mmol, 1.1 eq.) in 30 mL of MeCN. The mixture was stirred at 50 °C for 8 h. The MeCN was removed under low pressure at 100 °C, resulting in a dark yellow liquid. Yield: 24.6 g, 100 %.

FT-Raman (*r.t.*, in MeCN, res. = 4 cm^{-1}): 2997(s), 2966(s,sh), 2963(s), 2941(vs), 2907(m,sh), 2735(w), 2293(w), 2254(vs), 1457(m), 1430(m), 1420(m), 1378(m), 1024(vw), 920(s), 382(s), 297(vw), 254(w) cm^{-1}.

Tributylmethylphosphoniumchloride, $[P_{4441}]Cl$

$[P_{4441}]Cl$ was prepared according to literature.[12]

Synthesis of [OMIM][PMP][$MnCl_4$]

$[PMP]_2[MnCl_4]$ (7.6 g, 17.6 mmol, 1 eq.) was added to $[OMIM]_2[MnCl_4]$ (10.2 g, 17.4 mmol, 1 eq.) in 30 mL of MeCN. The mixture was stirred at 50 °C for 8 h. The MeCN was removed under low pressure at 100 °C, resulting in a light brown solid. Yield: 17.8 g, 100 %.

FT-Raman (*r.t.*, in MeCN, res. = 4 cm^{-1}): 2293(s), 2251(cs), 2223(w), 2202(w), 1449(m), 1421(m), 1375(m), 919(vs), 382(vs), 255(vw), 118(w,sh) cm^{-1}.

Synthesis of [BMP][PMP][$MnCl_4$]

$[BMP]_2[MnCl_4]$ (4.0 g, 8.3 mmol, 1 eq.) was added to $[PMP]_2[MnCl_4]$ (3.8 g, 8.3 mmol, 1 eq.) in 10 mL of MeCN. The mixture was stirred at 50 °C for 8 h. The MeCN was removed under low pressure at 100 °C, resulting in a light brown solid. Yield: 7.8 g, 100 %.

FT-Raman (*r.t.*, in MeCN, res. = 4 cm^{-1}): 2996(s), 2974(s,sh), 2950(vs), 2885(s), 2844(w), 2731(w), 2297(w), 2251(vs), 1454(m), 1377(m), 1050(vw), 925(s), 902(w), 381(s), 301(vw), 253(w) cm^{-1}.

Synthesis of $[PMP]_2[MnCl_4]$

[PMP]Cl (98%, 5.9 g, 38.9 mmol, 2 eq.) was added to $MnCl_2$ (2.5 g, 19.5 mmol, 1 eq.) in 20 mL of MeCN. The mixture was stirred at 50 °C for 8 h resulting in a green solution. The MeCN was removed under low pressure at 100 °C, resulting in a light brown solid. Yield: 8.4 g, 18.5 mmol, 95 %.

FT-Raman (*r.t.*, in MeCN, res. = 4 cm^{-1}): 3000(s), 2970(m), 2942(vs), 2888(m), 2840(m), 2733(m), 2293(s), 2251(vs), 1448(m), 1421(w), 1376(m), 1045(vw), 920(vs), 381(s), 254 cm^{-1}.

Synthesis of $[OMIM]_2[MnCl_4]$

[OMIM]Cl (98%, 29.9 g, 130 mmol, 2 eq.) was added to $MnCl_2$ (8.1 g, 64.5 mmol, 1 eq.). The mixture was stirred at 70 °C for 8 h. The product was a dark yellow liquid. Yield: 38.0 g, 64.5 mmol, 100 %.

FT-Raman (*r.t.*, in MeCN, res. = 4 cm^{-1}): 2998(s), 2987(m), 2963(s), 2941(vs), 2907(m,sh), 2874(s), 2861(s), 2733(w), 2292(w), 2253(vs), 1453(m), 1445(m), 1416(m), 1377(m), 1023(w), 921(s), 380(s), 253(vw) cm^{-1}.

Synthesis of $[N_{221\text{-}3O1}]_2[MnCl_4]$

$[N_{221\text{-}3O1}]Cl$ (11.6 g, 59.6 mmol, 2 eq.) was added to $MnCl_2$ (3.7 g, 29.4 mmol, 1 eq.) in 25 mL of MeCN. The mixture was stirred at 50 °C for 8 h. The MeCN was removed under low pressure at 100 °C, resulting in a light brown solid. Yield: 14.7 g, 97 %.

FT-Raman (*r.t.*, in MeCN, res. = 4 cm^{-1}): 3030(m,sh), 2988(vs), 2938(vs), 2894(s,sh), 2836(m), 2757(m), 2293(w), 2279(vw), 2251(s), 1487(m,sh), 1453(m), 1374(m), 1334(w), 1321(w),1307(w), 1116(w), 1079(w), 1071(w), 1023(vw), 971(w), 921(m), 886(w), 710(m), 480(w), 381(m), 301(vw), 250(m) cm^{-1}.

Synthesis of $[Me\text{-}3O1\text{-}pyrr]_2[MnCl_4]$

[Me-3O1-pyrr]Cl (17.5 g, 90.6 mmol, 2 eq.) was added to $MnCl_2$ (5.6 g, 45.3 mmol, 1 eq.) in 25 mL of MeCN. The mixture was stirred at 50 °C for 8 h. The MeCN was removed under low pressure at 100 °C, resulting in a light brown solid. Yield: 23.1 g, 99.4 %.

FT-Raman (*r.t.*, in MeCN, res. = 4 cm^{-1}): 2988(s), 2967(vs), 2936(s), 2839(m), 2814(m), 2734(w), 2293(vw), 2267(vw), 2251(s), 1492(w,sh), 1478(w), 1452(m), 1409(vw), 1378(m), 1323(w), 1280(w), 1246(vw), 1052(w), 923(m), 901(m), 818(w), 728(w), 639(w), 380(m), 300*(vw), 269(m), 256(m), 189(vw) cm^{-1}.

Synthesis of $[P_{4441}]_2[MnCl_4]$

$[P_{4441}]Cl$ (99%, 7.9 g, 31.5 mmol, 2.1 eq.) was added to $MnCl_2$ (1.9 g, 15.01 mmol, 1 eq.) in 20 mL of MeCN. The mixture was stirred at 50 °C for 8 h. The MeCN was removed under low pressure at 100 °C for 4°h, resulting in a light brown solid. Yield: 9.6 g, 101 %. A yield of 101 % results from the amount of $[P_{4441}]Cl$, which was slightly too high, but cannot be separated from the product.

FT-Raman (*r.t.*, in PC, res. = 4 cm^{-1}): 2993(vs), 2967(vs,sh), 2939(vs), 2917(vs), 2877(vs), 2757(m), 2737(m),1788(m), 1482(m), 1454(s), 1410(w), (1351(w), 1305(w), 1223(w), 1184(vw),1149(w), 118(w), 1098(w), 1068(w,sh), 1052(m), 960(m), 914(m,sh), 892(m), 867(m,sh),850(s),714(s), 642(w), 453(m), 301(vw), 256(w) cm^{-1}.

$[OMIM]_2[MnCl_4]$ and $[BMP][OMIM][MnCl_4]$ were already liquid at room temperature, probably due to the long alkyl chain of the $[OMIM]^+$. It is possible that other $[MnCl_4]^{2-}$-salts also are ionic liquids (IL), but we did not further investigate that. Although, ionic liquids are an interesting class of compounds, the conductivity of pure ILs is usually too low for an application in batteries. Figure S 5 c) shows the temperature dependent conductivity of the room temperature ionic liquids (RTIL) $[OMIM]_2[MnCl_4]$ and $[BMP][OMIM][MnCl_4]$. Even at 60°C, they have a conductivity of just 0.43 and 0.37 mS cm^{-1}, respectively, which is at least one order of magnitude too low for a battery application. To compare the conductivity of the salts, they were dissolved in MeCN (50 wt%). Table S 3 shows the results of the measurements, revealing that $[BMP]_2[MnCl_4]$, $[EMP]_2[MnCl_4]$ and $[BMP][PMP][MnCl_4]$ have the highest conductivity. $[PMP]_2[MnCl_4]$ however crystallizes from the solution in MeCN, which is the reason why no conductivity was measured. All the other salts have a comparable conductivity and are well

suited as electrolytes. Since $[N_{221\text{-}3O1}]^+$ and [Me-3O1-pyrr]$^+$ have ether functionalized side chains, which distinguishes them from all the cations, we decided to analyzed them further.

Table S 3: Conductivity of different $[Cat]_2[MnCl_4]$ salts dissolved in MeCN (50 wt %) at 45 °C.

$[Cat]_2[MnCl_4]$	Conductivity / mS cm^{-1}
$[BMP]_2[MnCl_4]$	21.4
$[PMP]_2[MnCl_4]$	Crystalizes
$[EMP]_2[MnCl_4]$	26.8
$[OMIM]_2[MnCl_4]$	13.1
$[Me\text{-}3O1\text{-}pyrr]_2[MnCl_4]$	14.8
$[N_{221\text{-}3O1}]_2[MnCl_4]$	19.6
$[BMP][PMP][MnCl_4]$	22.2
$[BMP][OMIM][MnCl_4]$	16.3
$[P_{4441}][MnCl_4]$	13.3
$[PMP][OMIM][MnCl_4]$	19.7

Figure S 5 (a) and b)) shows the temperature dependent conductivity of $[N_{221\text{-}3O1}]_2[MnCl_4]$ and $[Me\text{-}3O1\text{-}pyrr]_2[MnCl_4]$ in GBL (50 wt %) and MeCN (30 wt % for $[Me\text{-}3O1\text{-}pyrr]_2[MnCl_4]$, 50 wt % for $[N_{221\text{-}3O1}]_2[MnCl_4]$) and compares them directly to the conductivity of the [EMP]$^+$ and [BMP]$^+$ based electrolytes. The conductivity in MeCN and GBL is comparable to the conductivity of the [BMP]$^+$ based electrolytes, whereas $[Me\text{-}3O1\text{-}pyrr]_2[MnCl_4]$ has a higher conductivity in GBL than $[N_{221\text{-}3O1}]_2[MnCl_4]$. In MeCN however, it is the other way around. For $[Me\text{-}3O1\text{-}pyrr]_2[MnCl_4]$ the viscosity was measured in MeCN and GBL, allowing to compare the electrolytes to $EL_{GBL\text{-}BMP\text{-}50}$ and $EL_{MeCN\text{-}BMP\text{-}30}$ in a Walden plot (Figure S 5 d)). In GBL, as well as in MeCN, $[Me\text{-}3O1\text{-}pyrr]_2[MnCl_4]$ behaves very similar to $[BMP]_2[MnCl_4]$. Therefore, since [BMP]Cl and [EMP]Cl can be purchased and $[N_{221\text{-}3O1}]$Cl as well as [Me-3O1-pyrr]Cl have to be synthesized, we decided to conduct all of our battery experiments with the former salts. Table S 4, Table S 5 and Table S 6 show the data of the temperature dependent conductivity and viscosity of the discussed salts.

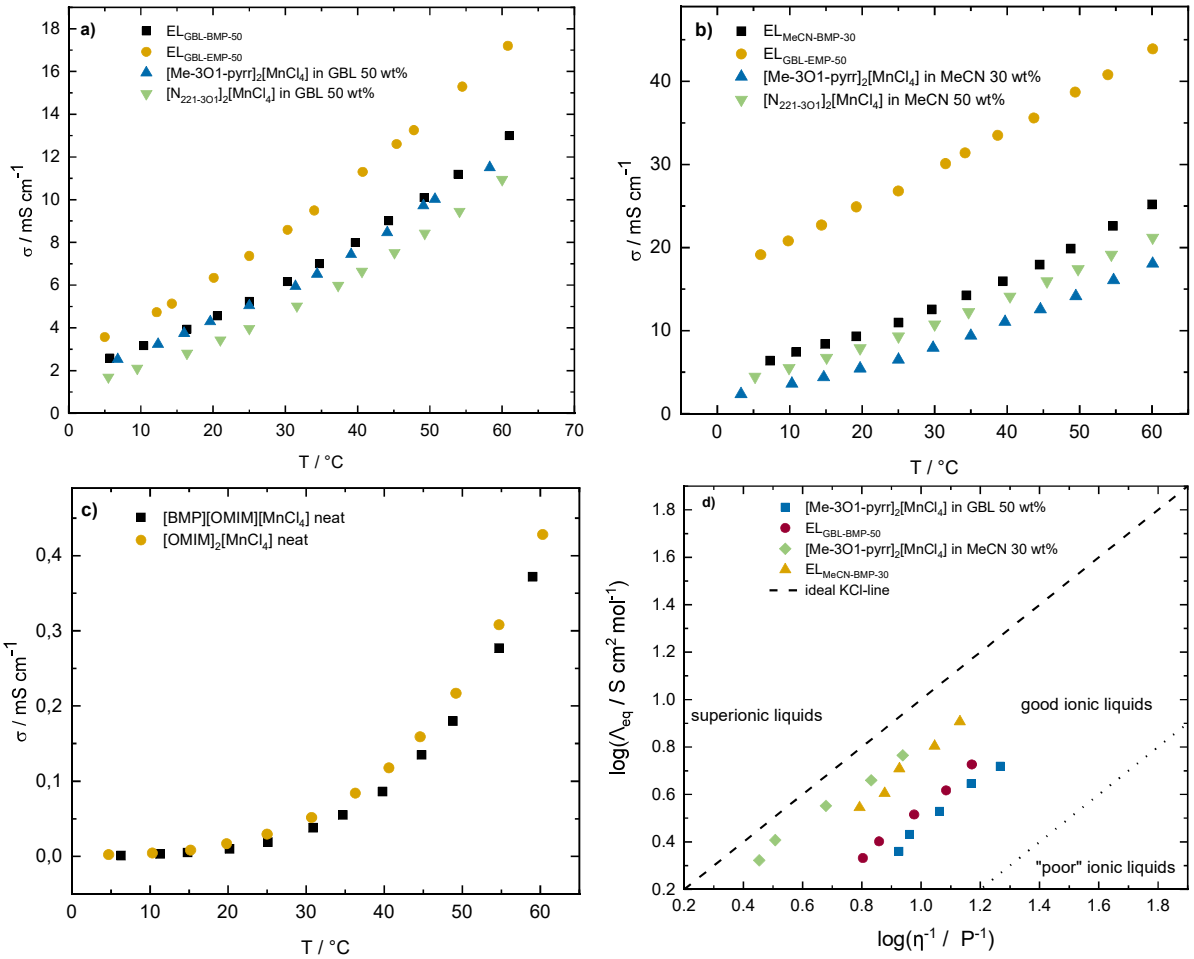

Figure S 5: Temperature dependent conductivity of EL$_{GBL-BMP-50}$, EL$_{GBL-EMP-50}$, [Me-3O1-pyrr]$_2$[MnCl$_4$] in GBL (50 wt % GBL, c = 1.1 mol L^{-1}) and [N$_{221-3O1}$]$_2$[MnCl$_4$] in GBL (50 wt % GBL, c = 1.10 mol L^{-1}) (a). Temperature dependent conductivity of EL$_{MeCN-BMP-50}$, EL$_{MeCN-EMP-50}$, [Me-3O1-pyrr]$_2$[MnCl$_4$] in MeCN (30 wt % MeCN, c = 1.55 mol L^{-1}) and [N$_{221-3O1}$]$_2$[MnCl$_4$] in MeCN (50 wt % MeCN, c = 0.96 mol L^{-1}) (b). Temperature dependent conductivity of [BMP][OMIM][MnCl$_4$] and [OMIM]$_2$[MnCl$_4$], which are room temperature ionic liquids (c). Walden plot with EL$_{GBL-BMP-50}$, EL$_{MeCN-BMP-30}$, [Me-3O1-pyrr]$_2$[MnCl$_4$] in GBL (50 wt % GBL, c = 1.1 mol L^{-1}) and [Me-3O1-pyrr]$_2$[MnCl$_4$] in MeCN (30 wt % MeCN, c = 1.55 mol L^{-1}) (d).

Table S 4: Temperature dependent conductivity of [Me-3O1-pyrr]$_2$[MnCl$_4$] and [N$_{221-3O1}$]$_2$[MnCl$_4$] in MeCN and GBL.

[Me-3O1-pyrr]$_2$[MnCl$_4$] in MeCN (30 wt %)		[N$_{221-3O1}$]$_2$[MnCl$_4$] in MeCN (50 wt %)		[Me-3O1-pyrr]$_2$[MnCl$_4$] in GBL (50 wt %)		[N$_{221-3O1}$]$_2$[MnCl$_4$] in GBL (50 wt %)	
T / °C	σ / mS cm^{-1}	T / °C	σ / mS cm^{-1}	T / °C	σ / mS cm^{-1}	T / °C	σ / mS cm^{-1}
3.3	2.4	5.2	4.5	6.8	2.5	5.5	1.7
10.3	3.6	9.9	5.5	12.4	3.2	9.5	2.1
14.7	4.4	15.1	6.7	16.0	3.8	16.4	2.8
19.7	5.4	19.7	7.9	19.6	4.3	21.0	3.4
25.0	6.5	25.0	9.3	25.0	5.0	25.0	4.0

29.8	7.9	30.0	10.8	31.4	5.9	31.6	5.0
35.0	9.4	34.7	12.3	34.4	6.5	37.3	6.0
39.7	11.1	40.4	14.1	39.1	7.4	40.6	6.6
44.6	12.6	45.5	15.9	44.1	8.5	45.1	7.5
49.5	14.2	49.8	17.4	49.1	9.7	49.3	8.4
54.7	16.1	54.4	19.2	50.7	10.0	54.1	9.5
60.1	18.1	60.1	21.2	58.3	11.5	60.0	10.9

Table S 5: Temperature dependent conductivity of the ILs $[OMIM]_2[MnCl_4]$ and [BMP]OMIM][$MnCl_4$].

$[OMIM]_2[MnCl_4]$		[BMP][OMIN][$MnCl_4$]	
T / °C	σ / µS cm^{-1}	T / °C	σ / µS cm^{-1}
4.7	2.1	6.3	1.0
10.3	4.3	11.3	3.0
15.2	8.1	14.8	5.0
19.8	17.0	20.2	10.0
25.0	29.5	25.0	19.0
30.7	51.6	30.9	38.0
36.3	84.1	34.7	55.0
40.6	117.6	39.8	86.0
44.6	159.1	44.8	135.0
49.2	217.0	48.8	180.0
54.7	308.0	54.7	277.0
60.3	428.0	59.0	372.0

Table S 6: Temperature dependent viscosity of $[Me\text{-}3O1\text{-}pyrr]_2[MnCl_4]$ in GBL and MeCN that were used for the Walden plot.

$[Me\text{-}3O1\text{-}pyrr]_2[MnCl_4]$ in MeCN (30 wt %)		$[Me\text{-}3O1\text{-}pyrr]_2[MnCl_4]$ in GBL (50 wt %)	
T / °C	η / cP	T / °C	η / cP
25	35.2	25	11.9
30	31.1	30	10.9
40	21.0	40	8.7
50	14.7	50	6.8
60	11.5	60	5.4

Spectroelectrochemistry

Spectroelectrochemical Raman and UV / Vis-measurements were conducted to investigate the electrochemical oxidation of $[MnCl_4]^{2-}$ to $[MnCl_5]^{2-}$, since these species can easily be distinguished with these methods. Table S 7 shows characteristic stretching frequencies of $[Mn^{III}Cl_5]^{2-}$ observed with Raman spectroscopy using spectroelectrochemistry (SEC) and compares them to literature known examples.

Table S 7: Characteristic stretching frequencies of $[Mn^{III}Cl_5]^{2-}$ observed with Raman spectroscopy using spectroelectrochemistry (SEC).

substance	ref.	phase	observed frequencies / cm^{-1}		
$[BMP]_2[Mn^{III}Cl_5]$	this work	GBL	-	289	-
$[EMP]_2[Mn^{III}Cl_5]$	this work	GBL	-	289	-
$[bipyH_2][Mn^{III}Cl_5]$	[13]	Solid	-	296 m	218 vw
$[phenH_2][Mn^{III}Cl_5]$	[13]	Solid	365 vw	296 s	235 w
$[NEt_4]_2[Mn^{III}Cl_5]$	[13]	Solid	-	289 s	233 vw
$[NMe_4]_2[Mn^{III}Cl_5]$	[13]	solid	360 vw	291 s	232 w
$[BMP]_2[Mn^{III}Cl_5]$	this work	solid	-	292	-

s = strong, m = medium, w = weak, vw = very weak

Table S 8 shows electronic transitions of $[Mn^{III}Cl_5]^{2-}$ obtained from UV / Vis spectra (from SEC) and comparison to the literature.

Table S 8: Electronic transitions of $[Mn^{III}Cl_5]^{2-}$ obtained from UV / Vis spectra (from SEC) and comparison to the literature.

substance	ref.	phase	electronic transitions / nm		
			charge transfer	$^5A_2 \rightarrow {}^5B_1, {}^5B_2$	$^5A_2 \rightarrow {}^5A_1$
$[BMP]_2[Mn^{III}Cl_5]$	this work	GBL	426	627	770
$[BMP]_2[Mn^{III}Cl_5]$	this work	MeCN	423	596	717
$[EMP]_2[Mn^{III}Cl_5]$	this work	GBL	425	627	768
$[bipyH_2][Mn^{III}Cl_5]$	[14]	acetone	417	575	758
$[phenH_2][Mn^{III}Cl_5]$	[14]	acetone	405	575	763
$[NEt_4]_2[Mn^{III}Cl_5]$	[14]	acetone	420	575	752
$[NMe_4]_2[Mn^{III}Cl_5]$	[14]	acetone	424	568	775

In Figure S 6 the Raman spectra of $EL_{MeCN\text{-}EMP\text{-}50}$ and $EL_{MeCN\text{-}BMP\text{-}30}$ show the characteristic ν_1-stretching frequency of $[MnCl_4]^{2-}$ at 253 and 255 cm^{-1}, respectively. After applying a potential of 1.65 V vs. q-Pt, a new frequency at 289 cm^{-1} appears in case of $EL_{MeCN\text{-}EMP\text{-}50}$ and 290 cm^{-1} in case of $EL_{MeCN\text{-}BMP\text{-}30}$. Since $[BMP]^+$ includes a band at 300 cm^{-1}, as discussed earlier, the appearance of the new vibration of $[MnCl_5]^{2-}$ can be observed much better in the spectra of $EL_{MeCN\text{-}EMP\text{-}50}$. The measurements suggest that $[MnCl_5]^{2-}$ can be formed electrochemically from $[MnCl_4]^{2-}$ in MeCN, as well as in GBL, which was discussed earlier. In Figure S 7 the Raman spectra of $[BMP]_2[MnCl_4]$ and $[NEt_4]_2[MnCl_4]$ chemically oxidized with dichlorine, also show the characteristic $[MnCl_5]^{2-}$ vibration at 292 and 287 cm^{-1}, respectively.

From the electrochemical oxidation of $[NEt_4]_2[MnCl_4]$ a crystal structure was obtained (see Figure 2), finally proving that it is possible to form $[MnCl_5]^{2-}$ electrochemically.

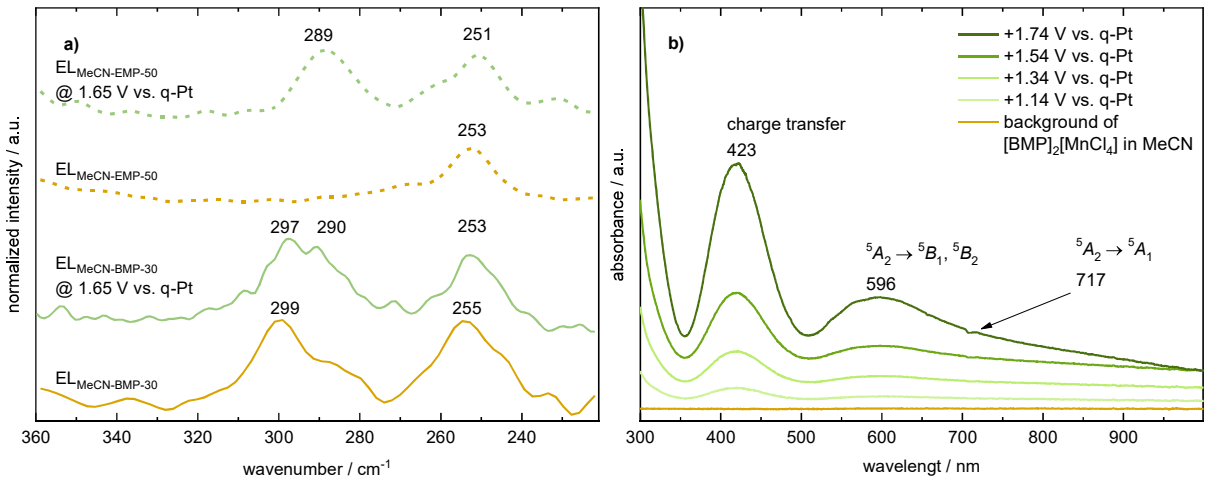

Figure S 6: Raman spectroelectrochemistry with $EL_{MeCN\text{-}EMP\text{-}50}$ and $EL_{MeCN\text{-}BMP\text{-}30}$ (a). UV / vis spectroelectrochemistry with $[BMP]_2[MnCl_4]$ in MeCN (90 wt % GBL, c = 1.69 mmol L^{-1}) (b).

After the addition of 0.5 eq of Cl_2 to $EL_{MeCN\text{-}BMP\text{-}30}$ the characteristic ν_1-stretching frequency of $[MnCl_4]^{2-}$ disappears completely, showing a complete oxidation towards $[MnCl_5]^{2-}$. In the Raman spectra of the samples with more equivalents of Cl_2, added to $EL_{MeCN\text{-}BMP\text{-}30}$ the ν_1-stretching frequency of $[MnCl_4]^{2-}$ can be observed again. The reason for this is probably, that the samples were dried under reduced pressure, which can cause decomposition of the $[MnCl_5]^{2-}$ anion. In the battery this kind of decomposition cannot be expected.

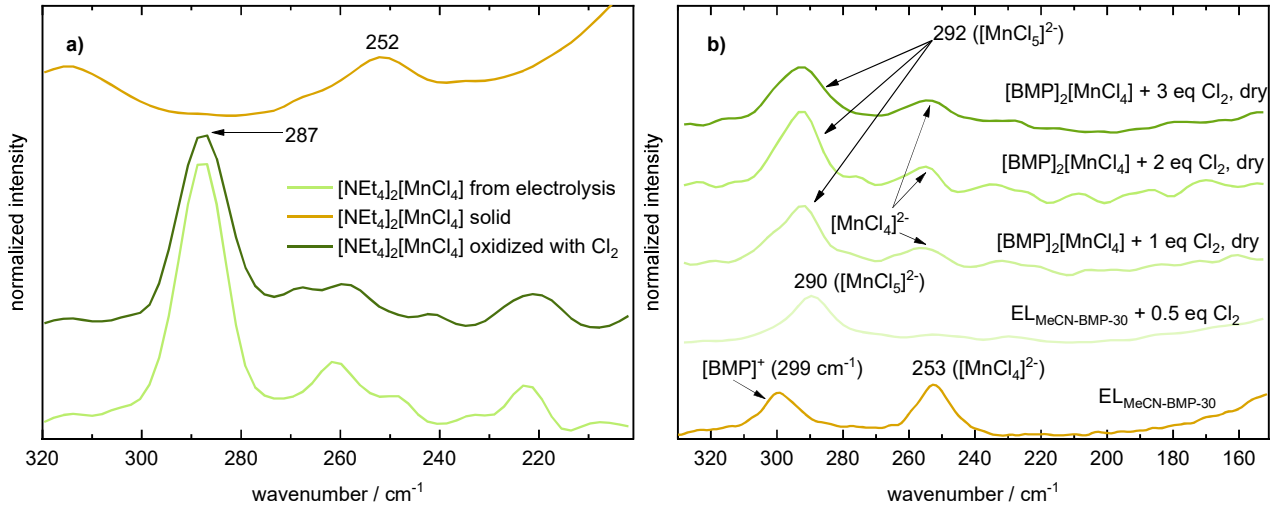

Figure S 7: Raman spectra of $[NEt_4]_2[MnCl_4]$ and the products of its chemical oxidation with chlorine and the electrochemical oxidation at graphite (TF6) (a). Chemical oxidation of $EL_{MeCN\text{-}BMP\text{-}30}$ with different stoichiometries for chlorine (b).

Mn deposition from solutions with $[MnCl_4]^{2-}$

Manganese deposition experiments were conducted in modified H-type glass cells (see Figure S 8). The copper plates were polished with sandpaper, cleaned with acetone and ethyl acetate (EA) and directly brought into the glovebox. The electrode, where Mn deposition was supposed to take place, was used as the working electrode (WE), whereas a Mn plate was used as counter electrode (CE) to assure that no contamination with other species takes place while Mn is deposited. As a reference electrode (RE) a Pt-wire was used, which was polished with sandpaper, cleaned in HNO_3 (concentrated), washed with H_2O (distilled), acetone and EA before the Pt-wire was brought into the glovebox.

Figure S 8 shows the setup, that was used for the deposition of manganese from various electrolytes. The first setup (Figure S 8 a. and b.) had the disadvantages of an undefined electrode surface and the possible contamination of the $Mn^0|Mn^{II}$ half-cell with $[MnCl_5]^{2-}$, since the two half cells were only separated by a porous frit. After the purchase of Mn foil, we changed the setup (Figure S 8 c.). Now we were able to deposit manganese on a defined electrode surface area and instead of $[MnCl_5]^{2-}$ formation at the counter electrode, elemental manganese was oxidized replacing the manganese that was deposited at the WE. The same principle was used for cycling of the half-cell experiments, described earlier. The advantage of the glass cell, compared to the screw cells, that were used for the cycling experiments, is that one can visibly observe that no $[MnCl_5]^{2-}$ is formed in this setup, which is a competing reaction to the stripping of manganese. We also assured that no $[MnCl_5]^{2-}$ is formed at the Mn-CE using Raman spectroscopy. Figure S 8 c. shows that the deposition of manganese starts at a distinct potential, here –1.3 V vs. q-Pt, and that the current increases strongly just going to –1.4 V and –1.5 V vs- q-Pt. This shows that the current density might be very important for the deposition of manganese and has to be investigated in detail.

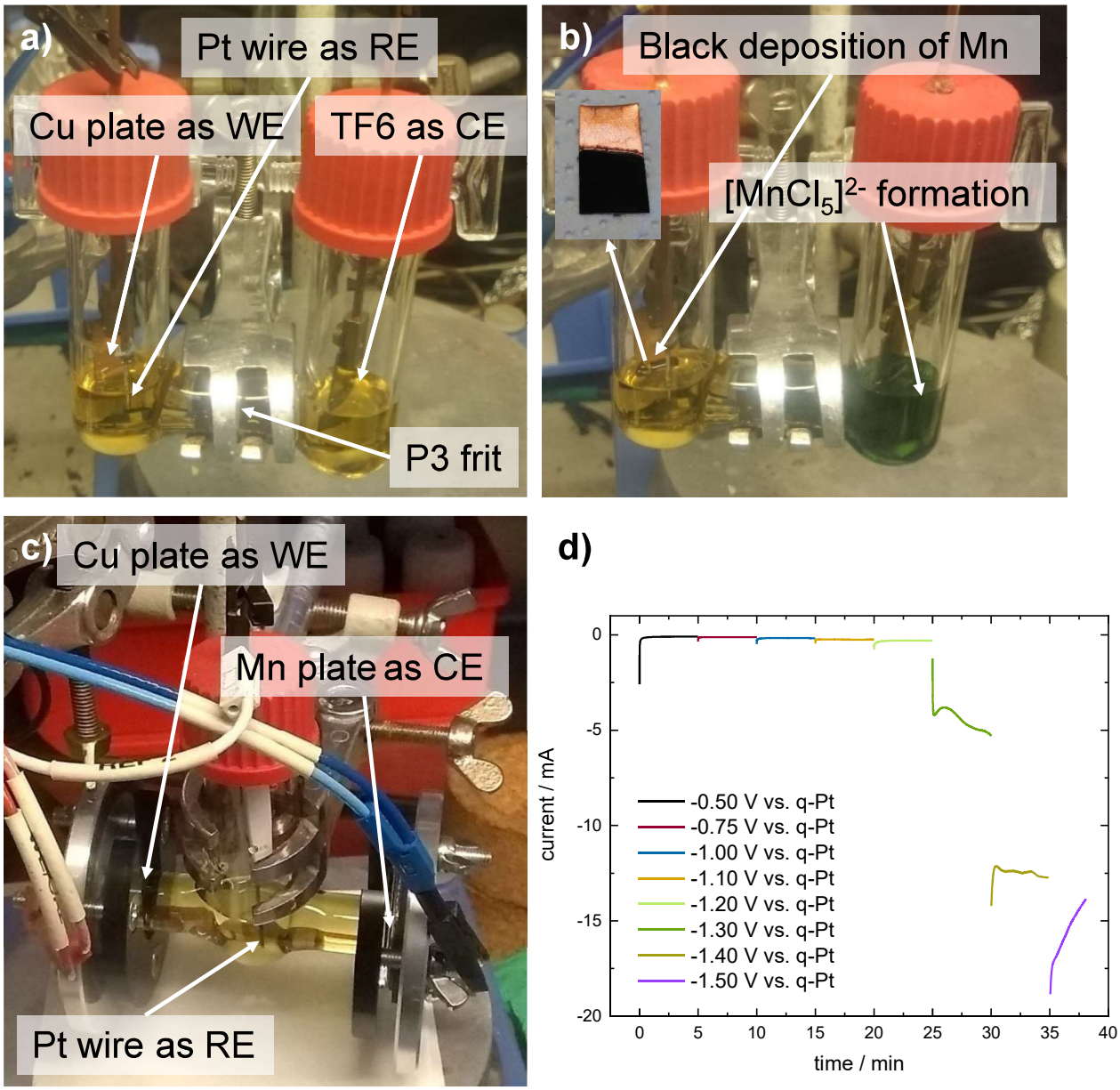

Figure S 8: Setup that was used for the deposition of Mn on different substrates (a and b). Improved setup for the deposition of Mn on different substrates (c). Advantages are a clearly defined electrode surface and no possible contamination with $[MnCl_5]^{2-}$. Current response for different negative potentials at the Cu electrode (d).

Figure S 9 shows the SEM image and the EDX mapping of manganese that was electrochemically deposited from $EL_{MeCN\text{-}BMP\text{-}Cl\text{-}30}$. The EDX mapping shows that manganese can only be found at the electrochemically active area of the Pt foil. This is also true for oxygen, which can be found, since it was not possible to conduct the measurement under inert conditions. Therefore, the manganese was oxidized to MnO, as described earlier. On the SEM image as well as on the image of the EDX mapping showing Pt and Mn a very uneven deposition of Mn on Pt can be observed, since there are areas with just manganese but also areas where Pt can still be seen at the electrochemically active area of the Pt foil. Chloride and

carbon can be found evenly distributed over the whole surface of the Pt foil. The reason for this is probably that the Mn film was washed very carefully to prevent delamination. As a consequence, residual [BMP]Cl was distributed evenly over the whole Pt foil.

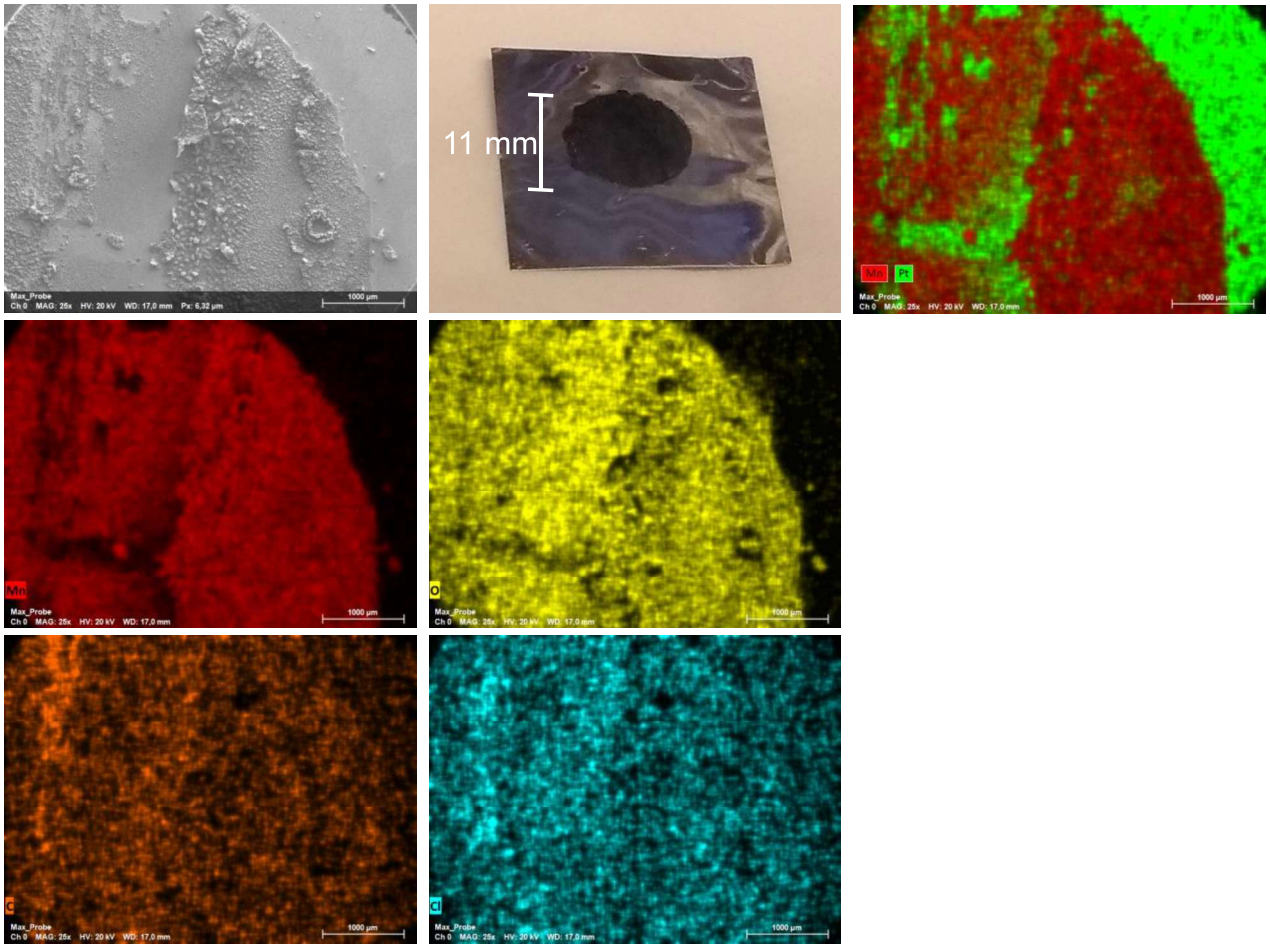

Figure S 9: SEM image of manganese electrochemically deposited on Pt from $EL_{MeCN\text{-}BMP\text{-}Cl\text{-}30}$. Photograph of the respective sample. EDX-Mapping of the area, seen on the SEM image. The sample was not kept under inert conditions.

Figure S 10 shows a SEM image of the same sample shown in Figure S 9. The structure of the deposited manganese varies strongly. In area 4 the surface still looks smooth, whereas in the areas 2 and 3 the surface seems to be more rough. Area 1 however looks completely different revealing the cauliflower like structure that is in our opinion the reason for the mechanically unstable Mn layers formed electrochemically. Figure S 11 shows the respective EDX spectra. As expected manganese and oxygen have the highest count number. Table S 9 shows the atom % of the relevant elements from the EDX spectra shown in Figure S 11.

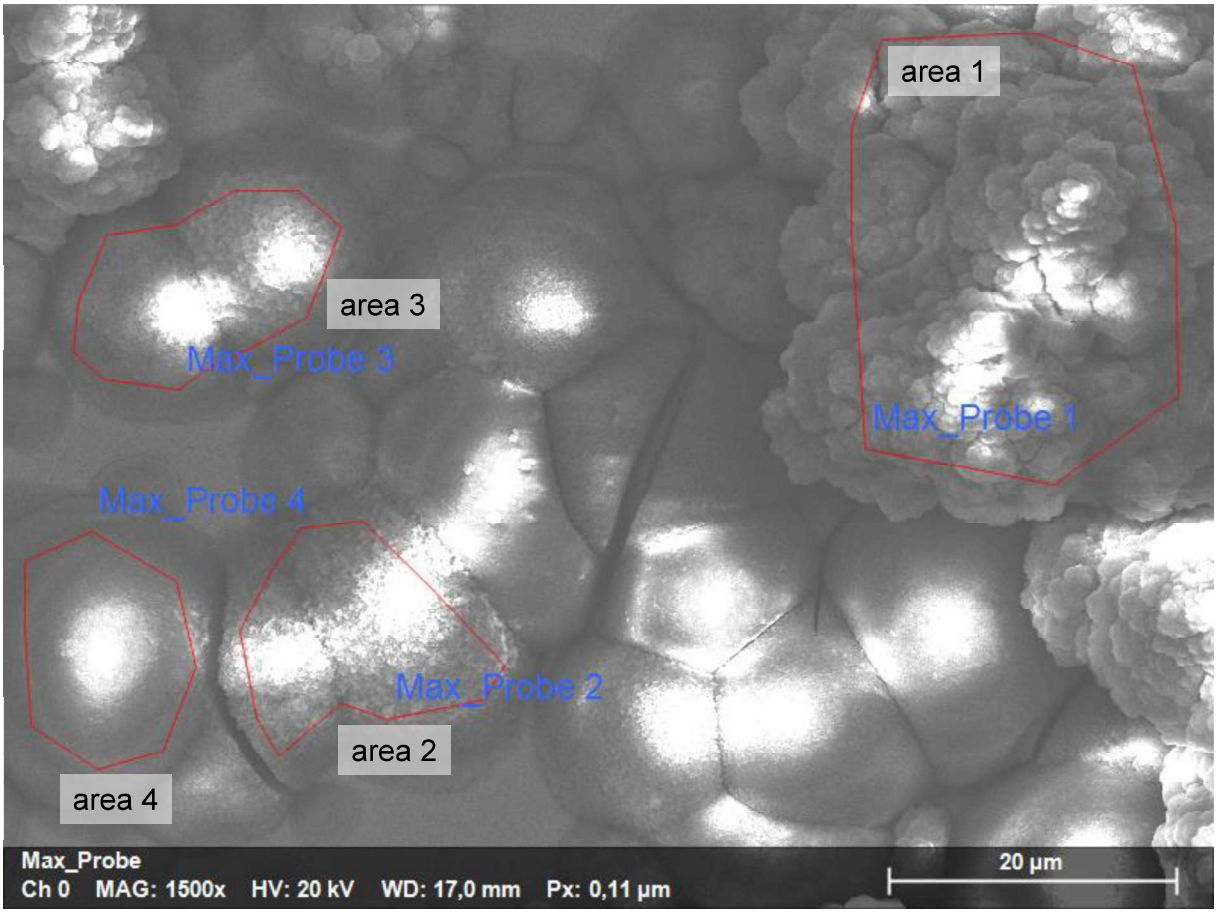

Figure S 10: SEM image of manganese electrochemically deposited on Pt from $EL_{MeCN\text{-}BMP\text{-}Cl\text{-}30}$ with the marked areas that were analyzed by EDX measurements. The sample was not handled under inert conditions after the deposition of manganese.

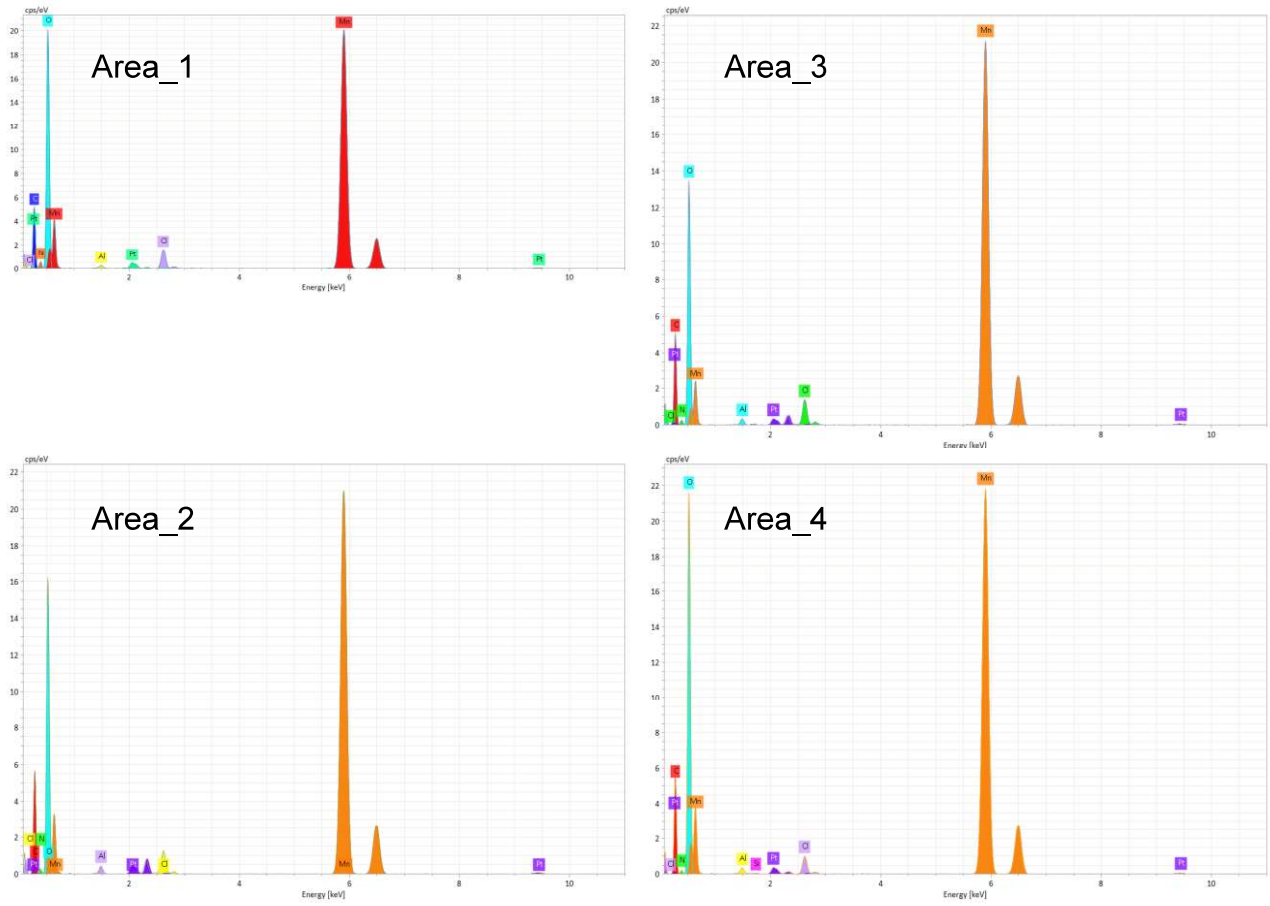

Figure S 11: EDX spectra of the areas marked in Figure S 10.

Table S 9: Atom % of the elements detected with EDX. The sample was not handled under inert conditions after the deposition of manganese.

	Mn / atom %	O / atom %	O / Mn-ratio	Cl / atom %	C / atom %
Area 1	19 ± 4	47 ± 10	1.6 - 3.8	0.8 ± 0.2	29 ± 5
Area 2	21 ± 4	42 ± 9	1.3 – 3.0	0.7 ± 0.2	34 ± 6
Area 3	23 ± 4	38 ± 7	1.1 – 2.4	0.9 ± 0.2	35 ± 5
Area 4	20 ± 4	47 ± 10	1.5 – 3.6	0.5 ± 0.2	30 ± 6

Figure S 12 shows the LSV experiment investigating the anodic dissolution of Mn metal in a solution of [EMP]Cl in GBL (1.9 mol L^{-1}).

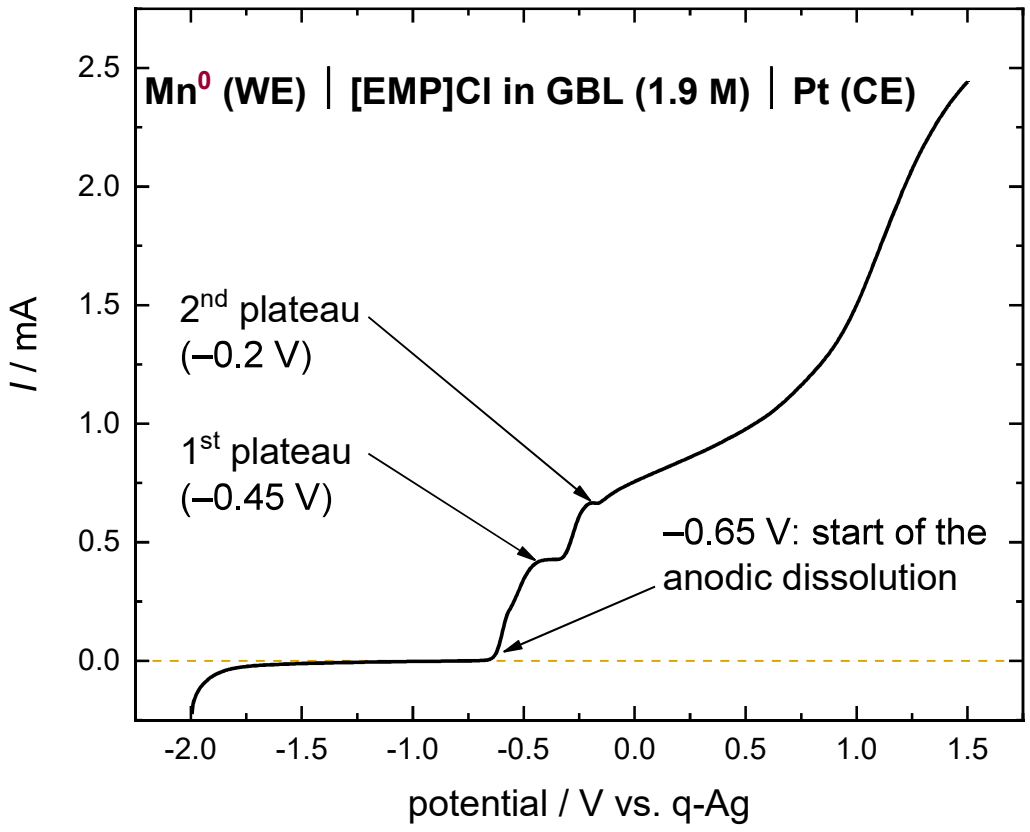

Figure S 12: LSV at 30 °C, using a 5 mm Mn disc electrode (WE), a Pt-CE and an Ag-RE. The electrolyte was a solution of [EMP]Cl in GBL (1.9 mol L^{-1}). The potential was scanned from –2 V to +1.5 V vs. q-Ag, with a scan rate of 5 mV s^{-1}.

Membrane Testing

The impact on the cell resistance and the cycling performance of the different available membranes were tested to find the best candidate for further investigations. Since GBL proved more relevant as a solvent compared to MeCN due to safety issues, the membranes were tested solely with GBL based electrolytes. In the all-MFB the membrane has to ensure that free chloride ions can pass for charge balancing, which is the reason, why only anion exchange membranes (AEM) were tested. Next to the free passage for chloride ions the AEM has to ensure that the $[Mn^{III}Cl_5]^{2-}$ that is formed during charge at the positive electrode remains in the Mn^{II}/Mn^{III}-half-cell (Figure S 13).† To figure out, which of the membranes is best suited for the all-MFB, four identical cells were assembled, following the protocol described in the experimental section. Each cell was equipped with a different membrane, except for one

† A leaching of $[Mn^{III}Cl_5]^{2-}$ towards the Mn^0/Mn^{II}-half-cell would result in a comproportionation reaction with the deposited Mn. In other redox-flow-batteries, for instance, the Fe-Cr-battery with two different electrolytes at the positive and the negative electrode leaching leads to capacity fading.[15,16] In the all-MFB a capacity loss is preventable, given the product of the comproportionation reaction is $[Mn^{II}Cl_4]^{2-}$ and is the active species in both half-cells in the discharged state, potentially increasing lifetime of the all-MFB, cf. all-Vanadium-RFB or other batteries that use the same redox-active element at both electrodes.[17,18] Nevertheless, the coulombic and energy efficiency still decreases due to leaching.

control cell without membrane to record the difference between the resistance that originates from the electrolyte and the resistance that is contributed by the membrane.

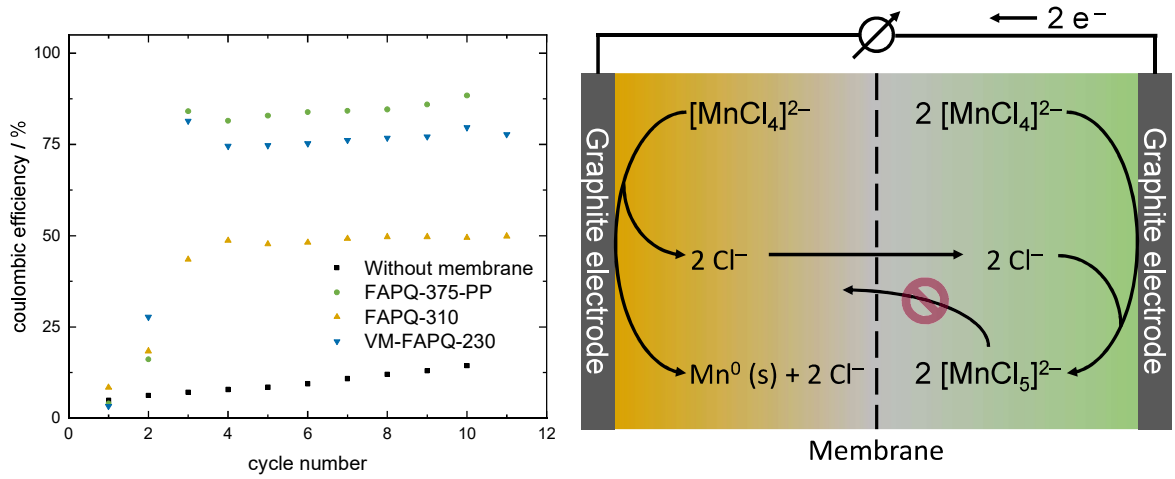

Figure S 13: Coulombic efficiencies with different membranes, using a solution of $[BMP]_2[MnCl_4]$ in GBL (1.1 mol L^{-1}, 55 wt % GBL, $EL_{GBL\text{-}BMP\text{-}55}$) as an electrolyte (left) and the suggested mechanism for the charging and charge balancing in the all-MFB (right).

Table S 10 shows the charge voltages (U_{SoC5}) at the end of the first cycle and the respective cell resistances.‡ The cell resistance with the membrane FAPQ-310 was for measurement reasons slightly lower than the resistance of the battery without a membrane. However, the values are rather close and looking at the cell resistances for the other AEMs the trend is clear: The cell with the FAPQ-375-PP membrane shows the highest cell resistance, which is 225 Ω larger than in the cell without a membrane. Next follows VM-FAPQ-230 (186 Ω lower compared to the FAPQ-375-PP) and then FAPQ-310.§

Table S 10: Cell resistances and U_{SoC5} of the battery cells with different membranes using $EL_{GBL\text{-}BMP\text{-}55}$. The cells were cycled between SoC0 and SoC5 with a current density of 0.5 mA cm^{-2}. The values marked green are considered as good, the yellow ones as neutral and the red ones as bad.

Membrane	Cell resistance / Ω	U_{SoC5} / V	CE of prior cycle / %
Without	**64**	3.42	14.4
FAPQ-375-PP	**289**	3.62	88.4
FAPQ-310	**57**	3.47	49.9
VM-FAPQ-230	**103**	3.93	77.7

‡ U_{SoC5} refers to the charge voltage at the end of a cycle, where the battery was charged to a SoC of 5 %. Analog U_{SoC80} is the charge voltage that was measured at the end of a cycle, where the battery was charged to a SoC of 80 %.

§ This trend almost follows the thickness of the membranes, which is represented by the number in the name of the membrane (in µm). The lower cell resistance of the thicker FAPQ-310 compared to VM-FAPQ-230 might be caused by the lack of a polymer backbone, since the FAPQ-375-PP membrane is grafted on a polypropylene backbone (PP).

Although the FAPQ-375-PP cell shows a higher cell resistance than the VM-FAPQ-230 cell, astonishingly U_{SoC5} of the latter is by 0.31 V higher than that of the FAPQ-375-PP cell. U_{SoC5} of the FAPQ-310 cell is almost identical to U_{SoC5} of the battery without any membrane (cf. also low cell resistances). Comparing U_{SoC5} of the FAPQ-375-PP and the FAPQ-310 cell, the latter is lower by 0.2 V, being favorable for energy efficiency. However, looking at the coulombic efficiencies (Figure S 13), the FAPQ-375-PP cell exceeds the FAPQ-310 cell by almost 40 %. In addition, the AEMs VM-FAPQ-230 and FAPQ-310 showed an extreme mechanical deformation after cycling, possibly due to the lack of a supporting PP polymer backbone. Thus, the swelling of FAPQ-310 could lead to an enlargement of the pores practically transforming the membrane into a porous separator, which induces leaching of $[Mn^{III}Cl_5]^{2-}$ that comproportionates with Mn^0 and reduces the CE. Indeed, the CE with the AEM FAPQ-375-PP was 88.4 % in the last cycle, whereas VM-FAPQ-230 showed a CE of 77.7 % in the last cycle. With a higher CE and a lower U_{SoC5}, FAPQ-375-PP was in favor to VM-FAPQ-230. And although FAPQ-310 showed the lowest U_{SoC5} among the cells with membranes, its low CE was the reason to stop using it. Yet, also the 88.4 % CE of FAPQ-375-PP is far from ideal. However, all of these membranes were optimized for aqueous electrolytes. Thus, a membrane, especially designed for the all-MFB could improve the CE drastically.** To investigate the all-MFB on a first principles basis the FAPQ-375-PP appeared reasonable.

Electrolyte Optimization

Charging the all-MFB starting with a solution of $[Cat]_2[Mn^{II}Cl_4]$ in both half cells is possible. Figure S 13 includes the suggested charging mechanism with charge transport over the membrane by chloride ions. Chloride is released upon deposition of Mn^0 from $[Mn^{II}Cl_4]^{2-}$ and is supposed to participate in the formation of $[Mn^{III}Cl_5]^{2-}$ during the oxidation of $[Mn^{II}Cl_4]^{2-}$. Due to the spatial separation of the electrodes it is impossible for chloride ions – released at the negative electrode upon charging – to be immediately available at the positive electrode for the formation of $[Mn^{III}Cl_5]^{2-}$. Therefore, we decided to add [Cat]Cl to the electrolyte to ensure that enough free chloride ions are available at any time for the reactions at the electrodes. The addition of extra [BMP]Cl has minimal impact on the conductivity of the resulting GBL based electrolytes, whereas the cell resistances are significantly improved (Table S 11). With increasing chloride concentration, the addition of [BMP]Cl led to lower cell resistances. Since the conductivity is almost not affected, we assume that Cl^- does not have an increased mobility in the electrolyte, if compared to $[Mn^{II}Cl_4]^{2-}$. This could be expected, because Cl^- is much smaller and carries a single negative charge. Thus, the reason for the lower cell resistance

** The decrease in the CE was also caused by a mechanical deformation of the FAPQ-375-PP membrane and could be improved given another membrane.

has to lie somewhere else. It appears that chloride ions can pass the FAPQ-375-PP membrane much easier than the dianion $[Mn^{II}Cl_4]^{2-}$ or $[BMP]^+$. The latter should anyway not be able to pass the membrane, since FAPQ-375-PP is an AEM.

Table S 11: Conductivity and cell resistances of electrolytes based on GBL and $[BMP]_2[Mn^{II}Cl_4]$ with different ratios of added [BMP]Cl. The AEM FAPQ-375-PP was used in each experiment.

Electrolyte[a]	Conductivity at 32 °C / mS cm^{-1}	Cell resistance / Ω	$[Mn^{II}Cl_4]^{2-}$ Concentration / mol L^{-1}
$[Mn^{II}Cl_4]^{2-}$	6.08	262[c]	1.1
$[Mn^{II}Cl_4]^{2-}$ + Cl^- (4:1) [b]	5.87	219[c]	1.0
$[Mn^{II}Cl_4]^{2-}$ + Cl^- (2:1) [b]	6.04	153[c]	0.9
$[Mn^{II}Cl_4]^{2-}$ + Cl^- (1:1) [b]	6.07	84[c]	0.8

[a] The amount of GBL in each electrolyte was 55 wt % compared to the weight of $[BMP]_2[Mn^{II}Cl_4]$ and [BMP]Cl. [b] Molar ratio. [c] The cell resistance shown here is the mean value originating from two different cells that were assembled identically.

This selectivity and permeability for chloride ions as charge carriers further supports the use of the AEM FAPQ-375-PP. Since the addition of extra [BMP]Cl diminishes the concentration of the electroactive species, solutions below the 1:1 ratio were not tested. Yet, this concentration improved the cell resistance considerably to a value that is only by 20 Ω larger (Table S 11) than in the cell without membrane (Table S 10). Figure S 14 shows that the addition of [BMP]Cl slightly improves the CE. Yet, more important is the strong positive influence on U_{SoC5}. Both effects agree with the reduced cell resistance. Comparing the cell with the electrolyte that does not contain [BMP]Cl and the electrolyte with a 1:1 molar ratio of $[BMP]_2[Mn^{II}Cl_4]$ and [BMP]Cl, U_{SoC5} is reduced by 0.62 V. This further reduction of U_{SoC5} led to the preferential use of electrolyte with additional [Cat]Cl.

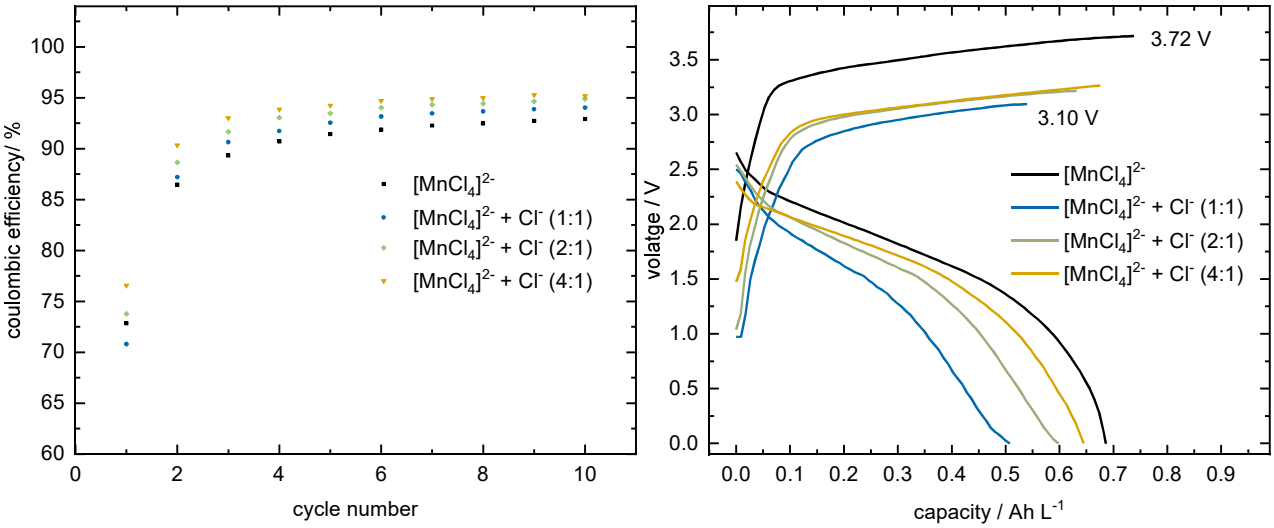

Figure S 14: CE (left) and voltage profiles of the 10th cycle (right) of GBL based electrolytes with different contents of additional [BMP]Cl. In each electrolyte the amount of GBL was 55 wt % compared to the weight of $[BMP]_2[Mn^{II}Cl_4]$ and [BMP]Cl. The FAPQ-375-PP membrane was used in each experiment and the cells were cycled between SoC0 and SoC5 with a current density of 0.5 mA cm^{-2}.

Conductivity and Viscosity

Figure S 15 shows the Arrhenius plots of the ionic conductivity and viscosity of the $[BMP]^+$ and $[EMP]^+$ salts in GBL and MeCN. The dotted lines represent the best fits according to the Vogel-Fulcher-Tammann (VFT) equation (Eq.[S 3] and Eq.[S 4]) and the respective fitting parameters can be found in Table S 16 and Table S 17. High ionic conductivity of the electrolyte is important at any state of charge (SoC). Thus, the corresponding $[Mn^{III}Cl_5]^{2-}$-salts, that dominate the ionic conductivity at higher SoCs, were also analyzed (Figure S 15). Comparing the for the battery cycling relevant electrolytes $EL_{MeCN\text{-}BMP\text{-}30}$ and $EL_{GBL\text{-}BMP\text{-}50}$ with similar viscosity (13.3 vs. 13.9 cP), the doubled conductivity in MeCN (12.6 vs. 6.2 mS cm^{-1} in GBL) in part originates from the higher concentration of $[BMP]_2[Mn^{II}Cl_4]$ accessible in MeCN (1.6 mol L^{-1} vs. 1.2 mol L^{-1}). But apparently this does not reflect the entire change.

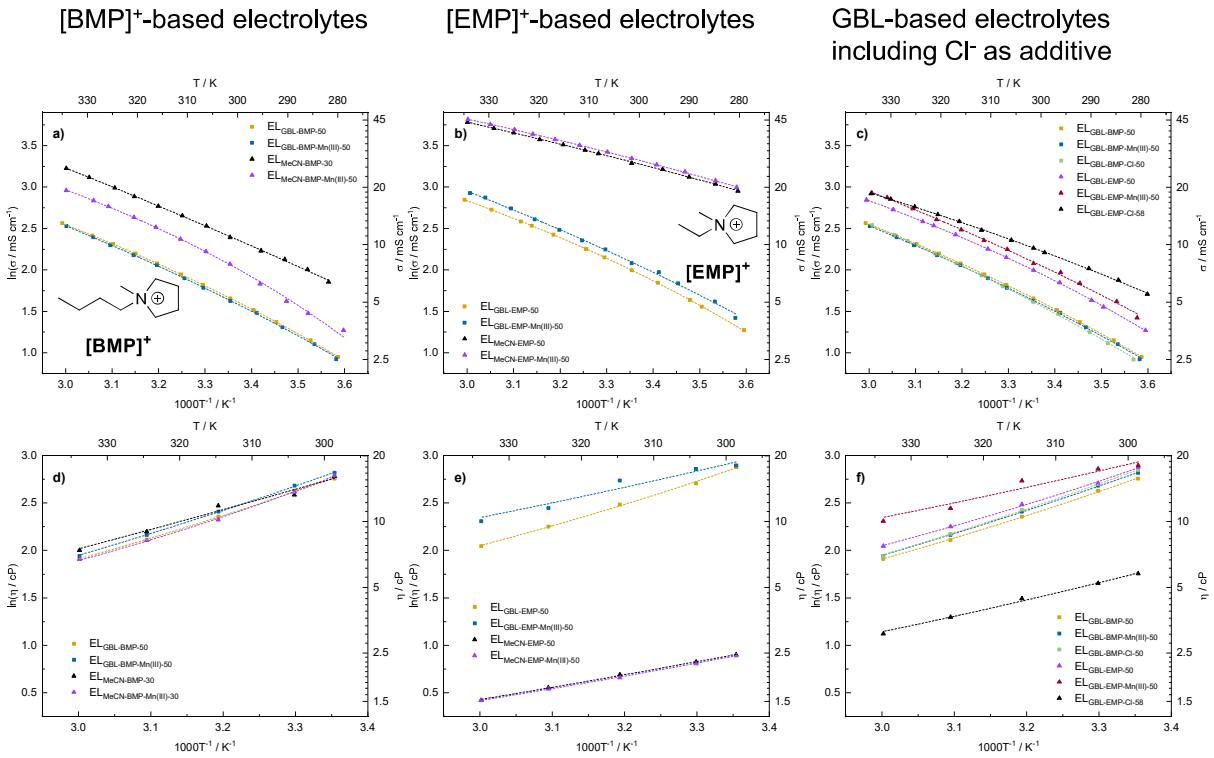

Figure S 15: Arrhenius plots of the ionic conductivity (a – c) and viscosity (d – f) for $[Cat]_2[Mn^{II}Cl_4]$, $[Cat][Mn^{III}Cl_5]$ and $[Cat]_2[Mn^{II}Cl_4]$ plus [Cat]Cl in MeCN and GBL ($[Cat]^+$ = $[BMP]^+$ and $[EMP]^+$). The dotted lines represent the best fit according to the VFT equation.

The Vogel-Fulcher-Tammann (VFT) parameters for the temperature dependent viscosity and conductivity were semi-empirically obtained using the following equations for viscosity and conductivity, respectively:

$$\sigma(T) = \sigma_0 exp\left(\frac{B}{T - T_g}\right) \quad [S\ 3]$$

$$\eta(T) = \eta_0 exp\left(\frac{B'}{T - T_{g'}}\right) \quad [S\ 4]$$

The η and σ are the viscosity and conductivity measured at a given temperature, respectively, η_0 and σ_0 are the viscosity and conductivity at infinite temperature, respectively, B and B' are related to the thermodynamic probability of particles to interact with each other, and T_g and T_g' are the glass transition temperatures. The semi-empirical VFT values were generated using the program Origin(Pro).[19] Λ_{eq} and Λ_m were calculated according to the equations [S 5] and [S 6],

$$\Lambda_m = \frac{\sigma}{c} \quad [S\ 5]$$

$$\Lambda_{eq} = \frac{\Lambda_m}{z} = \frac{\sigma}{c \times z} \qquad [S\ 6]$$

where *c* is the concentration of the salt, σ is the specific conductivity and *z* is the number of negative or positive charge that is released when one electrolyte molecule is dissolved (z = 2 for $[Cat]_2[MnCl_4]$). The equivalent conductivity of the electrolyte with additional [Cat]Cl was calculated according to Eq [S 7],

$$\Lambda_{\mathrm{eq}} = \frac{\sigma}{(c_1 \times z_1) + (c_2 \times z_2)} \qquad [S\ 7]$$

with c_1 and c_2 being the concentration of $[Cat]_2[MnCl_4]$ and [Cat]Cl respectively and z_1 and z_2 being the respective charge numbers (z_1 = 2 and z_2 = 1). Table S 12, Table S 13, Table S 14 and Table S 15 show the temperature dependent data for the conductivity and the viscosity of the different GBL- and MeCN based electrolytes that are discussed using the Walden plot.

Table S 12: Temperature dependent conductivity of the GBL based electrolytes that were used for the Walden plots.

$EL_{GBL\text{-}BMP\text{-}50}$		$EL_{GBL\text{-}BMP\text{-}Mn(III)\text{-}50}$		$EL_{GBL\text{-}BMP\text{-}Cl\text{-}50}$		$EL_{GBL\text{-}EMP\text{-}50}$		$EL_{GBL\text{-}EMP\text{-}Mn(III)\text{-}50}$		$EL_{GBL\text{-}EMP\text{-}Cl\text{-}58}$	
T / °C	σ / mS cm^{-1}	T / °C	σ / mS cm^{-1}	T / °C	σ / mS cm^{-1}	T / °C	σ / mS cm^{-1}	T / °C	σ / mS cm^{-1}	T / °C	σ / mS cm^{-1}
5.7	2.58	6	2.52	7	2.51	5	3.57	6.4	4.14	4.7	5.51
10.4	3.16	9.7	3.01	11.4	3.05	12.2	4.73	9.9	5.05	9.6	6.53
16.4	3.94	15.3	3.7	14.6	3.48	14.3	5.13	16.4	6.28	14.8	7.52
20.6	4.56	20	4.4	20.3	4.33	20.1	6.34	19.9	7.18	22.9	9.13
25.0	5.24	25	5.09	25	5.02	25	7.36	25	8	25	9.61
30.3	6.16	30.2	5.96	31	6.07	30.3	8.59	30.1	9.46	29.3	10.57
34.7	7.00	34	6.69	35.3	6.91	34	9.49	34.8	10.55	35.3	11.94
39.7	7.99	39.7	7.83	40.5	7.98	40.7	11.3	39.5	11.98	39.9	13.26
44.3	9.01	44.7	8.84	45.1	8.99	45.4	12.6	44.8	13.58	44.5	14.44
49.2	10.1	49.8	9.94	51.2	10.47	47.8	13.25	50	15.5	49.6	15.84
53.9	11.19	53.7	10.96	54.3	11.25	54.5	15.29	55.9	17.71	55.1	17.35
61	12.99	60	12.55	59.5	12.71	60.8	17.2	59.5	18.7	59.7	18.56

Table S 13: Temperature dependent conductivity of the MeCN based electrolytes that were used for the Walden plots.

$EL_{MeCN\text{-}BMP\text{-}30}$		$EL_{MeCN\text{-}BMP\text{-}Mn(III)\text{-}30}$		$EL_{MeCN\text{-}EMP\text{-}50}$		$EL_{MeCN\text{-}EMP\text{-}Mn(III)\text{-}50}$	
T / °C	σ / mS cm^{-1}	T / °C	σ / mS cm^{-1}	T / °C	σ / mS cm^{-1}	T / °C	σ / mS cm^{-1}
7.3	6.38	4.8	3.57	6	19.13	6.2	20
10.9	7.42	10.8	4.38	9.8	20.8	9.8	21.7
14.9	8.39	14.6	5.06	14.4	22.7	15.2	24.1
19.2	9.31	19.4	6.24	19.2	24.9	20.3	26.3

25	10.95	25	7.93	25	26.8	25	28.4
29.6	12.55	29.7	9.22	31.5	30.1	29.7	30.6
34.4	14.23	34.8	10.72	34.2	31.4	35.3	33.2
39.4	15.95	39.9	12.36	38.7	33.5	40.4	35.6
44.5	17.95	44.6	13.93	43.7	35.6	45.2	38
48.8	19.86	50.2	15.89	49.4	38.7	49.2	40.2
54.6	22.6	53.6	17.06	53.9	40.8	54.7	42.8
60	25.2	60	19.29	60.1	43.9	60	45.5

Table S 14: Temperature dependent viscosity of the GBL based electrolytes that were used for the Walden plots.

$EL_{GBL-BMP-50}$		$EL_{GBL-BMP-Mn(III)-50}$		$EL_{GBL-BMP-Cl-50}$		$EL_{GBL-EMP-50}$		$EL_{GBL-EMP-Mn(III)-50}$		$EL_{GBL-EMP-Cl-58}$	
T / °C	η / cP	T / °C	η / cP	T / °C	η / cP	T / °C	η / cP	T / °C	η / cP	T / °C	η / cP
25	15.7	25	16.7	25	17.2	25	17.8	25	18.1	25	5.7
30	13.9	30	14.6	30	14.9	30	15.0	30	17.4	30	5.2
40	10.5	40	11.1	40	11.3	40	12.0	40	15.4	40	4.4
50	8.2	50	8.7	50	8.8	50	9.5	50	11.5	50	3.7
60	6.7	60	7.0	60	7.0	60	7.7	60	10.1	60	3.1

Table S 15: Temperature dependent viscosity of the MeCN based electrolytes that were used for the Walden plots.

$EL_{MeCN-BMP-30}$		$EL_{MeCN-BMP-Mn(III)-30}$		$EL_{MeCN-EMP-50}$		$EL_{MeCN-EMP-Mn(III)-50}$	
T / °C	η / cP	T / °C	η / cP	T / °C	η / cP	T / °C	η / cP
25	16.1	25	16.3	25	2.5	25	2.4
30	13.3	30	13.7	30	2.3	30	2.2
40	11.8	40	10.2	40	2.0	40	1.9
50	9.0	50	8.2	50	1.7	50	1.7
60	7.4	60	6.7	60	1.5	60	1.5

Table S 16 and Table S 17 show the fit parameters of the fit results shown in Figure S 15. It was not possible to find a fit for each set of the five data points of the measured viscosity. Therefore, T_0 was used from the VFT fit of the conductivity, since it is the same temperature in theory.

Table S 16: VFT fit parameters obtained from ionic conductivity.

Electrolyte	B / K	T_0 / K	σ_0 / mS cm^{-1}
$EL_{GBL-BMP-50}$	–621.44294	157.89446	441.46604
$EL_{GBL-BMP-Mn(III)-50}$	–734.4231	145.48682	627.4908
$EL_{GBL-BMP-Cl-50}$	–741.6378	148.33391	708.61234
$EL_{GBL-EMP-50}$	–467.28978	174.57359	323.10528
$EL_{GBL-EMP-Mn(III)-50}$	–771.74128	136.74731	968.28474

$EL_{GBL\text{-}EMP\text{-}Cl\text{-}58}$	–550.92205	144.48815	347.00376
$EL_{MeCN\text{-}BMP\text{-}30}$	–1295.7446	80.61707	4261.21477
$EL_{MeCN\text{-}BMP\text{-}Mn(III)\text{-}30}$	–359.03608	196.32198	267.22503
$EL_{MeCN\text{-}EMP\text{-}50}$	–568.60816	111.1536	568.14444
$EL_{MeCN\text{-}EMP\text{-}Mn(III)\text{-}50}$	–467.0838	128.5929	446.28714

Table S 17: VFT fit parameters obtained from viscosity. Finding a fit to the five data points for each electrolyte was not possible. Therefore, T_0 from the VFT fit of the conductivity was used.

Electrolyte	B' / K	η_0 / cP
$EL_{GBL\text{-}BMP\text{-}50}$	597.94018	0.22311
$EL_{GBL\text{-}BMP\text{-}Mn(III)\text{-}50}$	713.00584	0.15753
$EL_{GBL\text{-}BMP\text{-}Cl\text{-}50}$	709.287	0.15191
$EL_{GBL\text{-}EMP\text{-}50}$	457.13636	0.43618
$EL_{GBL\text{-}EMP\text{-}Mn(III)\text{-}50}$	528.865	0.70849
$EL_{GBL\text{-}EMP\text{-}Cl\text{-}58}$	510.48347	0.2101
$EL_{MeCN\text{-}BMP\text{-}30}$	1164.3067	0.0749
$EL_{MeCN\text{-}BMP\text{-}Mn(III)\text{-}30}$	353.45472	0.50265
$EL_{MeCN\text{-}EMP\text{-}50}$	562.00087	0.12238
$EL_{MeCN\text{-}EMP\text{-}Mn(III)\text{-}50}$	466.21089	0.15597

Battery Measurements with Platinum Electrodes

Cycling experiments using platinum electrodes were conducted, allowing for a direct comparison between cyclic voltammograms (CV) that were also carried out using Pt-WEs. Figure S 16 shows the CVs of $EL_{MeCN\text{-}BMP\text{-}30}$ and $EL_{GBL\text{-}BMP\text{-}50}$, and the voltage profiles of the corresponding cycling experiments with $EL_{GBL\text{-}BMP\text{-}Cl\text{-}55}$ and $EL_{MeCN\text{-}BMP\text{-}Cl\text{-}30}$ at the positive electrode, and $EL_{GBL\text{-}BMP\text{-}Cl\text{-}55}$* and $EL_{MeCN\text{-}BMP\text{-}Cl\text{-}30}$* at the negative electrode, respectively. A direct comparison of the measured potentials is not possible, since the electrolytes in the battery contain additional [BMP]Cl, which was not present in the CV measurements. Nevertheless, strong similarities between the CVs and the cycling experiments were observed: For $EL_{MeCN\text{-}BMP\text{-}30}$ the potential was scanned from 0.1 V vs. q-Pt towards positive potentials. The half-peak potential ($E_{p/2}$) of the $[Mn^{II}Cl_4]^{2-}/[Mn^{III}Cl_5]^{2-}$ redox couple lies at +1.78 V, whereas the deposition of manganese starts around –1.5 V. Considering the current densities from the cycling experiment, the two processes that take place while charging the battery, lie 3.02 V

apart (CV).†† That goes along very well with U_{SoC5} of 3.03 V in the battery measurement. Stripping of the deposited Mn-layer can be observed in the CV over a range of 0.78 V with two current maxima at –0.60 V and –0.24 V. Therefore, the discharge voltage should occur in a region between 2.48 V and 1.70 V (Figure S 16). In the corresponding cycling experiment, the discharge plateau starts at 2.51 V and ends at 1.82 V and agrees with the respective CV data. For $EL_{GBL\text{-}BMP\text{-}50}$ the CV shows that $E_{p/2}$ of the $[Mn^{II}Cl_4]^{2-}/[Mn^{III}Cl_5]^{2-}$ redox couple, and the beginning of the Mn deposition lie 3.97 V apart.‡‡

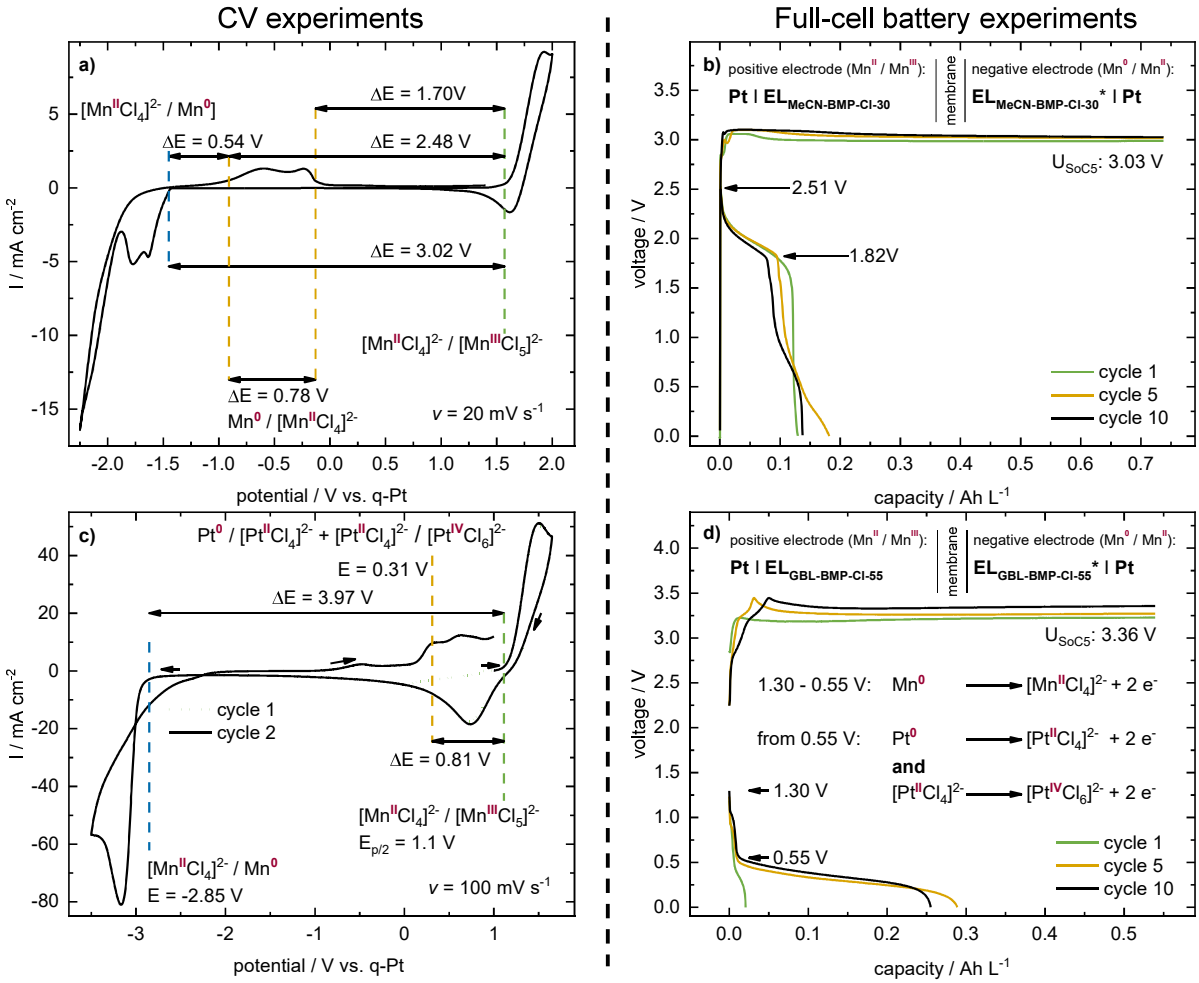

Figure S 16: a) Cyclic voltammogram of $EL_{MeCN\text{-}BMP\text{-}30}$ using a 1 mm Pt disc working electrode. b) Voltage profiles of the battery measurement with $EL_{MeCN\text{-}BMP\text{-}Cl\text{-}30}$ / $EL_{MeCN\text{-}BMP\text{-}Cl\text{-}30}$* using Pt electrodes. c) Cyclic voltammogram of $EL_{GBL\text{-}BMP\text{-}50}$ using a 1 mm Pt disc working electrode. d) Voltage profiles of the battery measurement with $EL_{GBL\text{-}BMP\text{-}Cl\text{-}55}$ / $EL_{GBL\text{-}BMP\text{-}Cl\text{-}55}$* with Pt electrodes. * means that the concentration of $[Mn^{II}Cl_4]^{2-}$ is cut in half with respect to the same electrolyte without *. The reason for

†† For a better comparison between the cycling experiments and the CVs the potentials of the oxidation and the reduction of manganese were used, measured at the same current density that was applied in the battery (0.25 mA cm^{-2}).

‡‡ Unfortunately, for the comparison with the battery measurement, it was not possible to use the potentials at the same current density that was applied in the battery. During the cathodic scan the current density in the CV exceeded the current density during cycling by more than 1 mA cm^{-2}. The reason might be strong capacitive currents. Therefore, for the comparison of the CV and the cycling experiments the voltages that seemed the most reasonable were used as shown in Figure S 15.

this is that the volume of the half-cells is the same, but at the negative electrode a two-electron process takes place, whereas at the positive electrode it is just a one electron process.

Compared to the CV in MeCN the separation of the charging processes is by 0.94 V higher. This trend can also be observed in the cycling experiment, but to a lesser extent. U_{SoC5} with $EL_{GBL\text{-}BMP\text{-}Cl\text{-}55}$ is 0.33 V higher than U_{SoC5} with $EL_{MeCN\text{-}BMP\text{-}Cl\text{-}30}$. Since it is not possible to deposit a stable Mn film on Pt from a GBL based electrolyte, it is no surprise that the discharge plateau of the cell with $EL_{GBL\text{-}BMP\text{-}Cl\text{-}55}$ is more than 1.27 V lower than for $EL_{MeCN\text{-}BMP\text{-}Cl\text{-}30}$. Since Mn cannot be stripped from the negative electrode during discharge another electrochemical reaction has to take place, otherwise no discharge plateau could be observed at all. We found that the Pt electrode is oxidized forming $[Pt^{II}Cl_4]^{2-}$ followed immediately by a subsequent oxidation to $[Pt^{IV}Cl_6]^{2-}$ (Figure S 17). The formation of $[Pt^{IV}Cl_6]^{2-}$ was verified by mass spectrometry of a sample of an electrolyte after cycling with Pt-electrodes (v.i.).

Mn^{II} / Mn^{III} half-cell (positive electrode)

$$2\ [Mn^{II}Cl_4]^{2-} + 2\ Cl^- \underset{\text{discharge}}{\overset{\text{charge}}{\rightleftharpoons}} 2\ [Mn^{III}Cl_5]^{2-} + 2\ e^-\ (E_{p/2} = 1.11\ \text{V vs. q-Pt})$$

and

$$Pt^0 + 2\ Cl^- + 2\ [Mn^{III}Cl_5]^{2-} \xrightarrow{\text{chemically}} [Pt^{II}Cl_4]^{2-} + 2\ [Mn^{II}Cl_4]^{2-}$$

$$[Pt^{II}Cl_4]^{2-} + 2\ [Mn^{III}Cl_5]^{2-} \xrightarrow{\text{chemically}} [Pt^{IV}Cl_6]^{2-} + 2\ [Mn^{II}Cl_4]^{2-}$$

Mn^{II} / Mn^0 half-cell (negative electrode)

$$[Mn^{II}Cl_4]^{2-} + 2\ e^- \xrightarrow{\text{charge}} Mn^0 + 4\ Cl^- \quad (E = -2.85\ \text{V vs. q-Pt})$$

$$[Pt^{II}Cl_4]^{2-} + 2\ e^- \xleftarrow{\text{discharge}} Pt^0 + 4\ Cl^- \quad (E = 0.31\ \text{V vs. q-Pt})$$

and

$$[Pt^{IV}Cl_6]^{2-} + 2\ e^- \xleftarrow{\text{discharge}} [Pt^{II}Cl_4]^{2-} \quad (E = 0.31\ \text{V vs. q-Pt})$$

Figure S 17: Proposed electrochemical processes that take place in the battery, set up with platinum electrodes using $EL_{GBL\text{-}BMP\text{-}Cl\text{-}55}$. The potentials of the respective processes originate from the CV measurement of $EL_{GBL\text{-}BMP\text{-}50}$.

From Table S 18 that includes the aqueous E^0 values of the underlying electrochemical processes, one realizes that it is plausible for $[Mn^{III}Cl_5]^{2-}$ to oxidize Pt^0 electrochemically and form $[Pt^{IV}Cl_6]^{2-}$, since the aqueous Mn^{II} / Mn^{III} redox potential lies 0.75 V above the potential of $Pt^0/[Pt^{II}Cl_4]^{2-}$ and 0.78 V above the potential of $[Pt^{II}Cl_4]^{2-}/[Pt^{IV}Cl_6]^{2-}$.

Table S 18: Standard electrode potentials (E_0) that are relevant for the battery. These standard electrode potentials can only be used in aqueous solutions. Nevertheless, we have no reason to believe that the order differs strongly in the solvents used for this study.

Redox system (aq, pH = 0)	E_0 / V
Mn^{2+} / Mn^{3+}	+1.51
Mn^{2+} / Mn^{3+}	+1.11[a]
Cl^- / Cl_2	+1.36
Pt / Pt^{2+}	+1.19
Pt / $[Pt^{II}Cl_4]^{2-}$	+0.76
$[Pt^{II}Cl_4]^{2-}$ / $[Pt^{IV}Cl_6]^{2-}$	+0.73
Mn^0/ Mn^{2+}	–1.18

[a] E_0 vs. Fc / Fc^+

Furthermore, the high chloride concentration in the battery is an additional driving force for $[Pt^{II}Cl_4]^{2-}$ and $[Pt^{IV}Cl_6]^{2-}$ formation. In the CV, the assumed anodic dissolution of Pt around 0.31 V cannot be observed during the first cycle, which started at 0.0 V, was scanned towards positive potentials and agrees with the lack of available chloride ions at this point. In the second cycle $[Mn^{II}Cl_4]^{2-}$ was already reduced, releasing chloride ions and therefore allowing the formation of $[Pt^{II}Cl_4]^{2-}$ and $[Pt^{IV}Cl_6]^{2-}$ at 0.31 V in the second cycle. Overall, Pt is not suited as a material for the positive electrode and other electrode materials had to be considered.

Mass Spectrometric Investigations into the Oxidation of Platinum by $[MnCl_5]^{2-}$: To investigate whether $[Mn^{III}Cl_5]^{2-}$ oxidizes the platinum electrodes to generate $[Pt^{II}Cl_4]^{2-}$ or $[Pt^{IV}Cl_6]^{2-}$, a battery with $EL_{GBL\text{-}BMP\text{-}Cl\text{-}55}$ was assembled using a Pt foil as the electrode material for the positive half-cell. The material for the negative electrode was a Mn foil, and the FAPQ-375-PP membrane was used to separate the two half-cells. After charging to a SoC of 70 %, the battery was disconnected. After 45 h, a sample (EL_{Pt}) was taken from the positive half-cell and analyzed using mass spectrometry (MS). This time was assumed to be long enough to ensure the chemical reaction of $[Mn^{III}Cl_5]^{2-}$ with the Pt^0 electrode. Figure S 18 shows the mass spectrum of EL_{Pt} together with the mass spectrum of fresh $EL_{GBL\text{-}BMP\text{-}Cl\text{-}55}$ (not having been used in a battery experiment before). In the mass spectrum of EL_{Pt}, a series of ions containing $[Pt^{IV}Cl_5]^-$ can be observed, which constitute aggregates with different numbers of [BMP]Cl ($[Pt^{IV}Cl_5]^-$ + $([BMP]Cl)_x$, x = 1 - 4). Additionally, $[Pt^{IV}Cl_6]^{2-}$ itself is present in the mass spectrum of EL_{Pt}. These signals are not observed in the mass spectrum of $EL_{GBL\text{-}BMP\text{-}Cl\text{-}55}$, thus clearly indicating that electrochemically generated $[Mn^{III}Cl_5]^{2-}$oxidized Pt^0 to $[Pt^{IV}Cl_6]^{2-}$. All signals in the mass spectrum (m/z = 100 – 1250) have been assigned to discreet species, thus revealing three different series containing the anions Cl^-, $[Mn^{II}Cl_3]^-$, and $[Mn^{II}_2Cl_5]^-$ each forming aggregates with [BMP]Cl. This behavior is well known for ionic liquids.[20,21] To validate the assignment of the various species (as listed in Figure S 18), the respective isotopic patterns were simulated and compared with the measured spectra (CID experiments were performed as well, mainly resulting in [BMP]Cl losses). Figure S 19 - Figure S 21 summarize these comparisons for a selected example of each series. Note that each signal was recorded both

in the normal scan mode and in the SIM mode (SIM = selected ion monitoring) employing both the Zoom and the Ultra-Zoom mode. When compared with the normal mode, the isotopic patterns are usually much more clearly resolved in the SIM mode. However, in the SIM mode, the relative intensities of the measured isotope patterns do not always match the simulated spectra very nicely. Yet, in the normal mode, the relative intensities match very well. In the case of $[Pt^{IV}Cl_6]^{2-}$, a CID spectrum (CID = collision-induced dissociation) is shown (Figure S 19), which indicates the fragmentation into $[Pt^{IV}Cl_5]^-$ and a chloride ion (not observed directly).

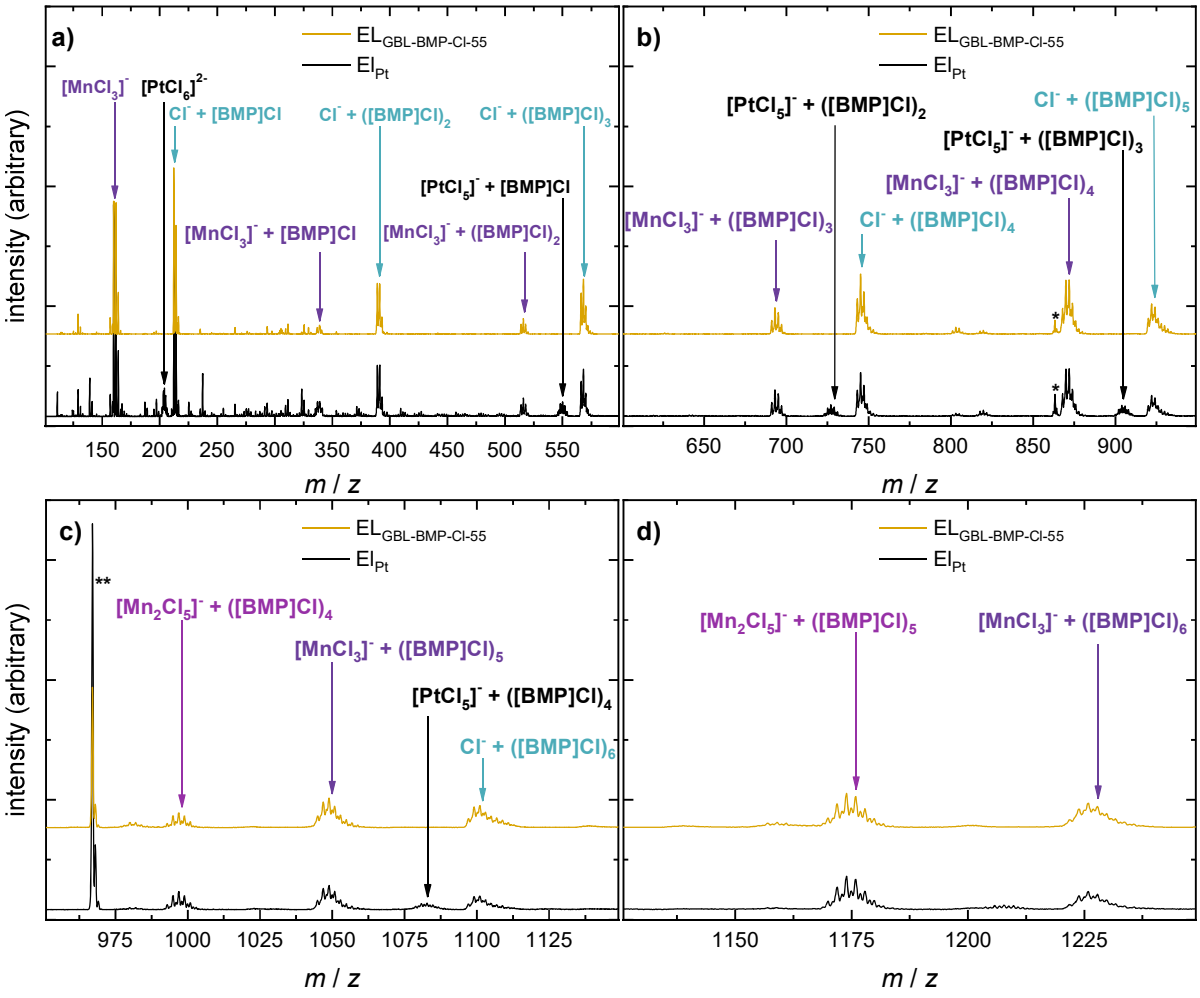

Figure S 18: Mass spectra (anion mode) of $EL_{GBL\text{-}BMP\text{-}Cl\text{-}55}$ and EL_{Pt} a) for *m*/*z* = 100 – 600, b) for *m*/*z* = 600 – 950 (the signals marked with an asterisk correspond to $[B(C_6H_3(CF_3)_2)_4]^-$ ($C_{32}H_{12}BF_{24}$), which is present in the spectrometer as a permanent contamination), c) for *m*/*z* = 950 – 1150 (the signal marked with two asterisks belongs to the $[Al(OC(CF_3)_3)_4)]^-$ ($C_{16}AlF_{36}O_4$), which is present in the spectrometer as a permanent contamination), and d) for *m*/*z* = 1125 – 1250. The different series containing the anions Cl^-, $[Mn^{II}Cl_3]^-$, $[Mn^{II}_2Cl_5]^-$, and $[Pt^{IV}Cl_5]^-$ are indicated by the color code.

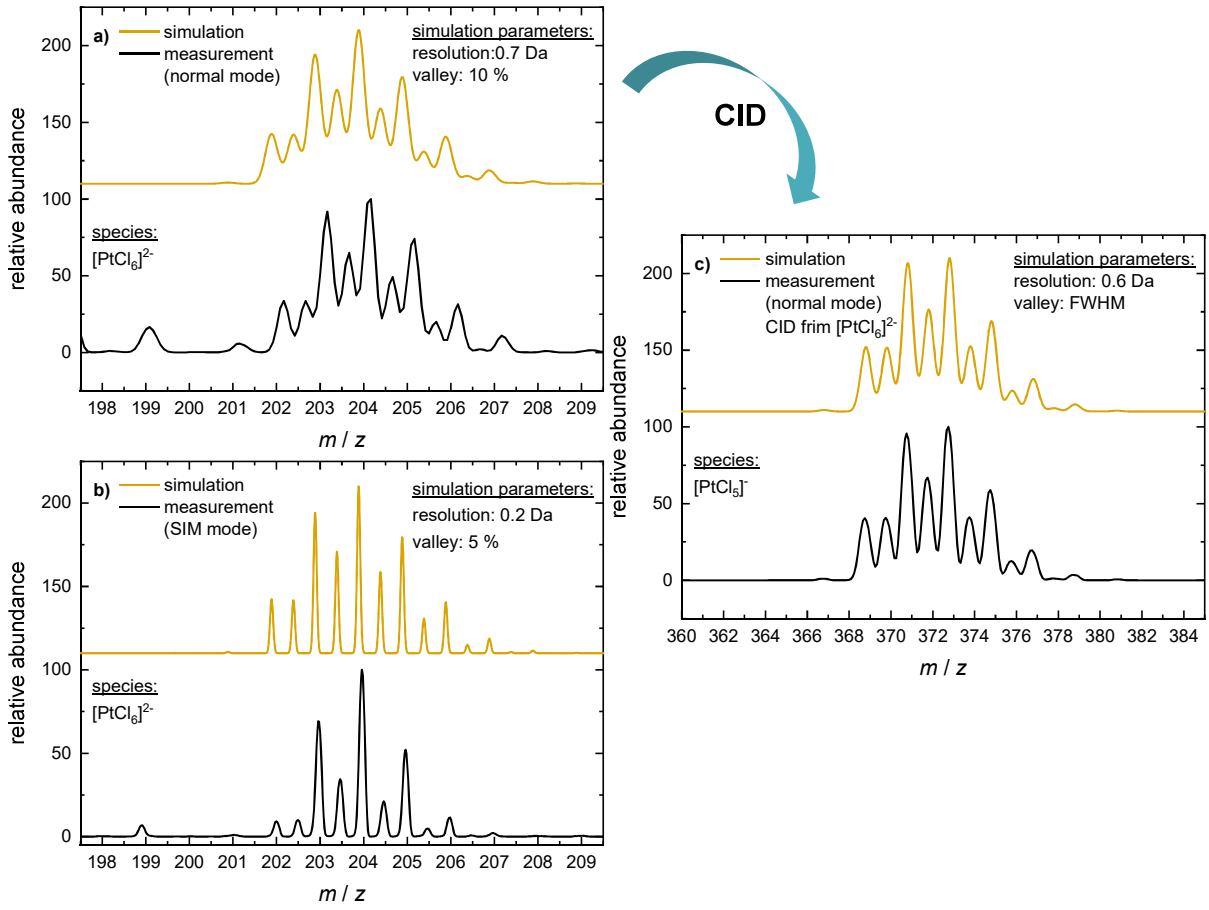

Figure S 19: Mass spectrum of $[Pt^{IV}Cl_6]^{2-}$ (together with the simulated spectrum) a) detected in the normal scan mode and b) detected in the SIM mode using the Zoom mode. c) Mass spectrum of $[Pt^{IV}Cl_5]^{-}$ (together with the simulated spectrum) generated by CID of $[Pt^{IV}Cl_6]^{2-}$ as detected in the normal scan mode.

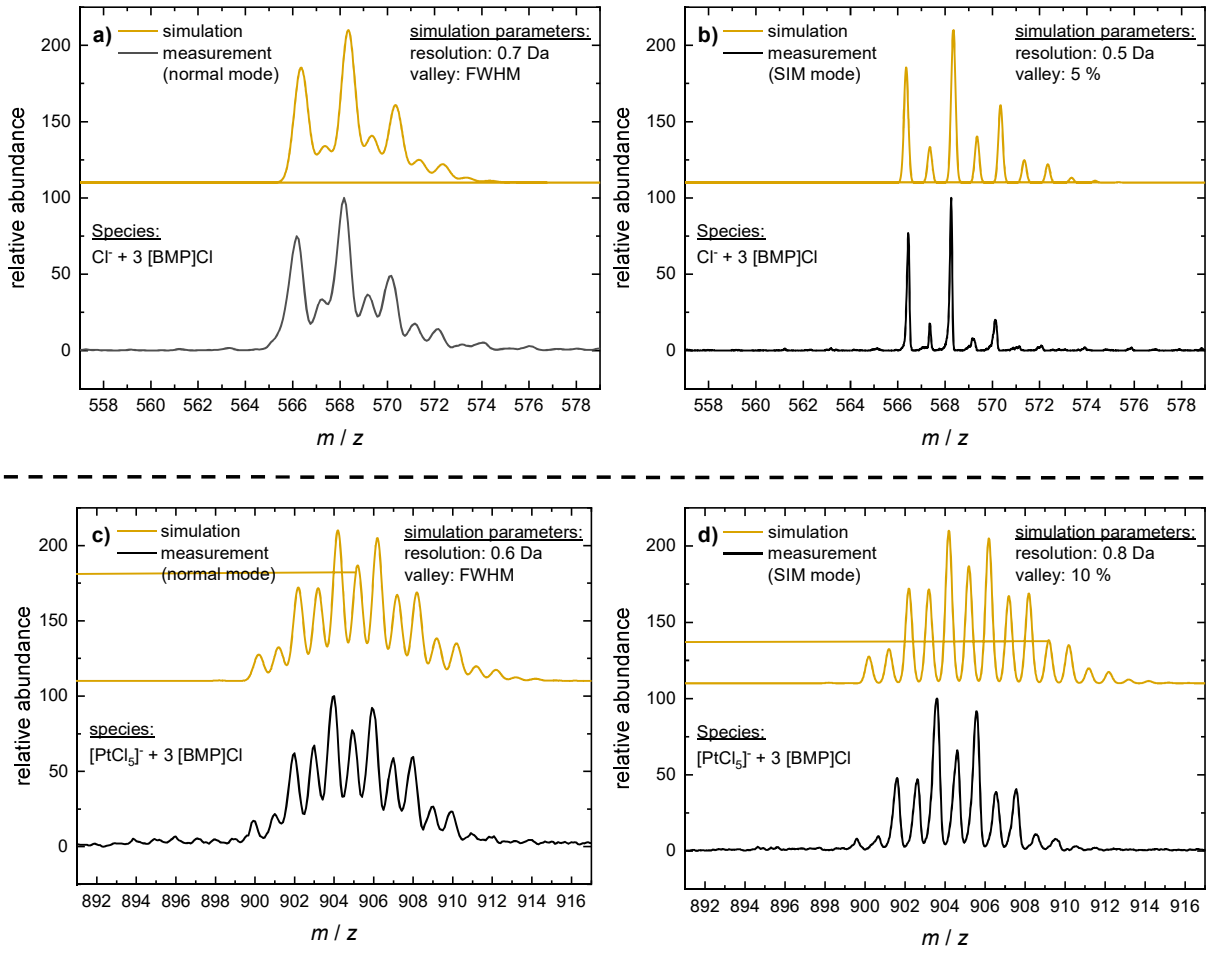

Figure S 20: Mass spectrum of Cl^- + 3 [BMP]Cl (together with the simulated spectrum) a) detected in the normal scan mode and b) detected in the SIM mode using the Ultra-Zoom scan-mode. Mass spectrum of $[Pt^{IV}Cl_5]^-$ + 3 [BMP]Cl (together with the simulated spectrum) c) detected in the normal scan mode and d) in the SIM mode using the Zoom scan-mode.

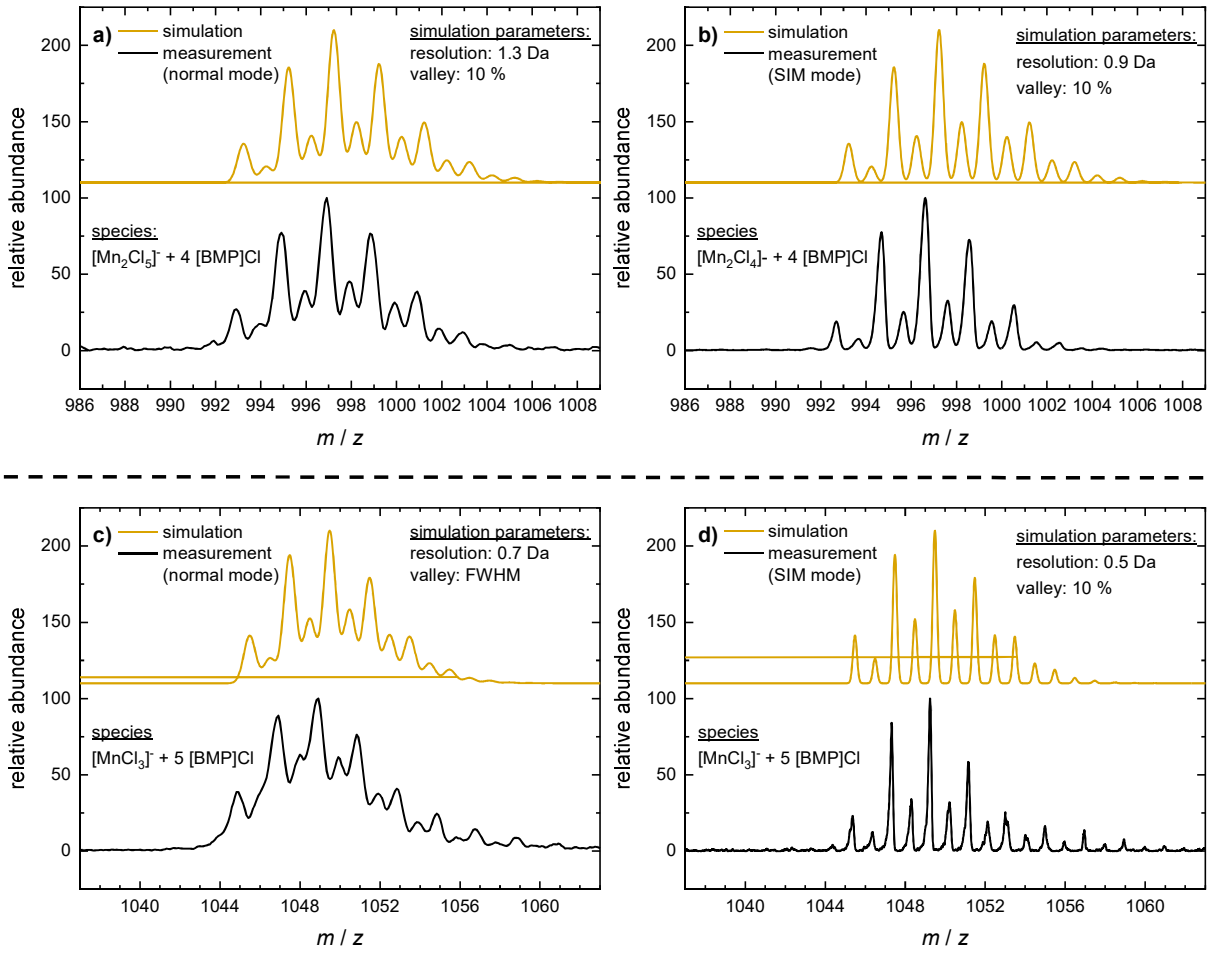

Figure S 21: Mass spectrum plus simulation of a) $[Mn_2Cl_5]^-$ plus 4 [BMP]Cl detected with the normal scan mode. b) $[Mn_2Cl_5]^-$ plus 4 [BMP]Cl detected with the selected ion mode using the Zoom scan-mode. c) $[MnCl_3]^-$ plus 5 [BMP]Cl detected with the normal scan mode. d) $[MnCl_3]^-$ plus 5 [BMP]Cl detected with the selected ion mode using the Ultra-Zoom scan-mode.

Half-cell experiments for the analysis of the Mn deposition: Asymmetrical half-cell experiments were conducted with $EL_{MeCN\text{-}BMP\text{-}Cl\text{-}30}$* and $EL_{GBL\text{-}BMP\text{-}Cl\text{-}55}$* investigating the Mn^0 deposition on Pt. With $EL_{MeCN\text{-}BMP\text{-}Cl\text{-}30}$* a stripping of Mn from Pt can be observed with a voltage plateau that starts around −0.60 V and ends at –0.94 V (Figure S 22 a). This plateau is in accordance with the stripping of manganese in the Mn|Mn-half-cell (Figure 6). The CE of the Mn|Pt-half-cell increases from 17 to 25 % and fits very well to the CE of the respective full cell described earlier (Figure S 16). Since the CEs of the Mn|Pt-half-cell and the Pt|Pt-full-cell are so close together, the deposition of Mn and the incomplete stripping is presumably the dominant reason for the reduced CE. In the Pt|Pt-full-cell the CE will also be partially reduced by the reaction of $[Mn^{III}Cl_5]^{2-}$ with the Pt electrode (cf. Figure S 17). So far, the data of the full-cell experiments and the half-cell experiments with $EL_{MeCN\text{-}BMP\text{-}Cl\text{-}30}$ fit closely to each other. The Mn deposition from $EL_{GBL\text{-}BMP\text{-}Cl\text{-}50}$* on a Pt electrode shows an overpotential of 1.24 V (Figure S 22 b). For the stripping of the deposited Mn layer a voltage plateau in a similar region should be expected as it was observed for $EL_{MeCN\text{-}BMP\text{-}Cl\text{-}30}$*. However, a very short plateau that

starts at –1.27 V and ends at –2.7 V can be observed, which we assign to the true stripping of Mn. Afterwards a stable plateau at –2.7 V is established, which we assign to the oxidation of Pt and the formation of $[Pt^{II}Cl_4]^{2-}$ and $[Pt^{IV}Cl_6]^{2-}$ (v.s.). In Figure S 16 (Pt|Pt-full-cell) a very short plateau between 1.3 V and 0.55 V can be observed that could be assigned to the oxidation of elemental Mn. Then the plateau at 0.55 V follows, which is assigned to the oxidation of Pt^0 and $[Pt^{II}Cl_4]^{2-}$. In comparison to the Pt|Pt-full-cell and the Pt|Mn-half-cell with $EL_{MeCN\text{-}BMP\text{-}Cl\text{-}30}$, the CEs of the respective battery cells with $EL_{GBL\text{-}BMP\text{-}Cl\text{-}55}$ cannot be brought into accordance. A CE of 100 % for the Mn|Pt-half-cell can only be explained with the oxidation of Pt. However, for the Pt|Pt-full-cell, an oxidation of Pt^0 towards $[Pt^{II}Cl_4]^{2-}$ and $[Pt^{IV}Cl_6]^{2-}$ occurs in the positive and the negative half-cell, reducing the CE. As a result, the CE rises up to 56 % (Figure S 22) and decreases afterwards.

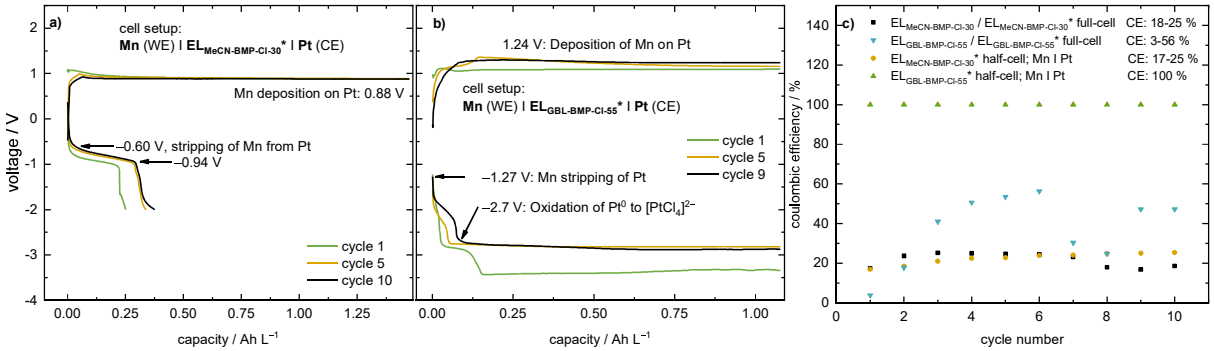

Figure S 22: Half-cell experiments with a) $EL_{MeCN\text{-}BMP\text{-}Cl\text{-}30}$* using a Mn-WE and a Pt-CE and b) $EL_{GBL\text{-}BMP\text{-}Cl\text{-}55}$* using a Mn-WE and a Pt-CE, c) coulombic efficiencies of the $EL_{MeCN\text{-}BMP\text{-}Cl\text{-}30}$ / $EL_{MeCN\text{-}BMP\text{-}Cl\text{-}30}$* full-cell, $EL_{MeCN\text{-}BMP\text{-}Cl\text{-}30}$* half-cell, $EL_{GBL\text{-}BMP\text{-}Cl\text{-}55}$ / $EL_{GBL\text{-}BMP\text{-}Cl\text{-}55}$* full-cell and $EL_{GBL\text{-}BMP\text{-}Cl\text{-}55}$* half-cell. All experiments were conducted with a current density of 0.25 mA cm^{-2}. As described above the * means that the concentration of $[MnCl_4]^{2-}$ is cut in half with respect to the same electrolyte without a *.

Electrode Material for the Positive Electrode: As already described, $[Mn^{III}Cl_5]^{2-}$ oxidizes Pt into $[Pt^{II}Cl_4]^{2-}$ and $[Pt^{IV}Cl_6]^{2-}$. This process accounts for the second discharge plateau in Figure 8, where $[Pt^{IV}Cl_6]^{2-}$ is reduced to $[Pt^{II}Cl_4]^{2-}$, while elemental Mn is further oxidized at the negative electrode. Figure S 23 shows all the relevant chemical and electrochemical reactions for this scenario. The difference between the aqueous standard electrode potentials of Mn^{II} / Mn^{III} and $[Pt^{II}Cl_4]^{2-}$ / $[Pt^{IV}Cl_6]^{2-}$ is 0.78 V (see Table S 18). Note that the difference between the two plateaus in Figure 8 is also around 0.78 V, supporting the suggested Pt-oxidation. In addition, Figure S 24 shows a photograph of the Pt foil that was used as positive electrode. The platinum surface changed drastically, presumably caused by $[Mn^{III}Cl_5]^{2-}$ corrosion.

Mn^{II} / Mn^{III}-half-cell (positive electrode)

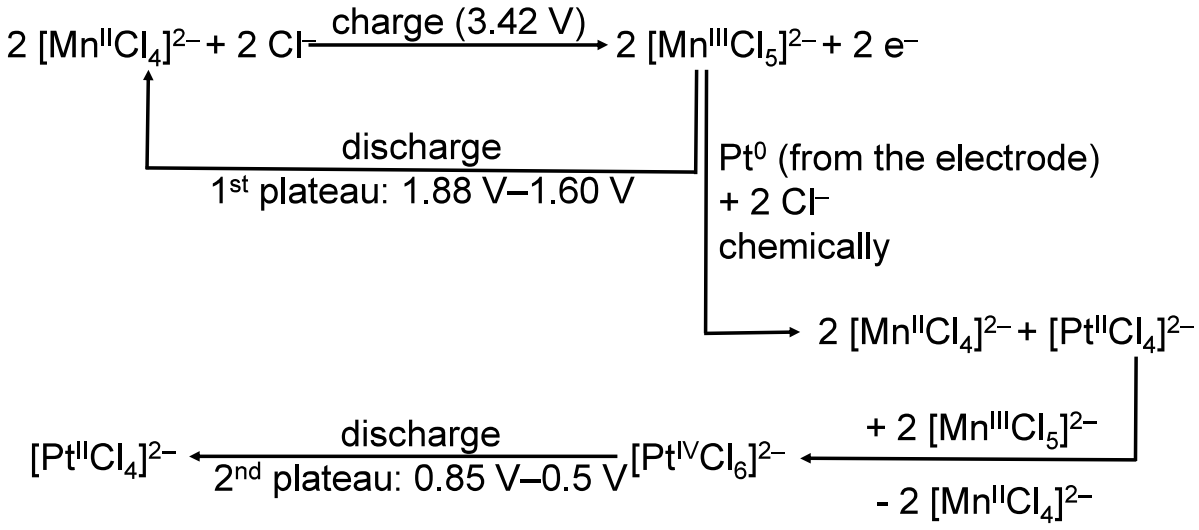

Mn^{0} / Mn^{II}-half-cell (negative electrode)

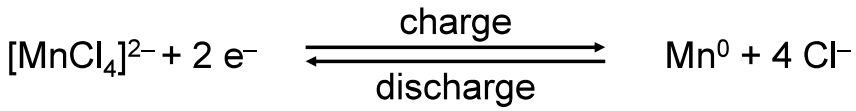

Figure S 23: Proposed chemical and electrochemical reactions that take place in the $EL_{GBL\text{-}BMP\text{-}Cl\text{-}55}$ / $EL_{GBL\text{-}BMP\text{-}Cl\text{-}55}$* Pt|Mn-full-cell.

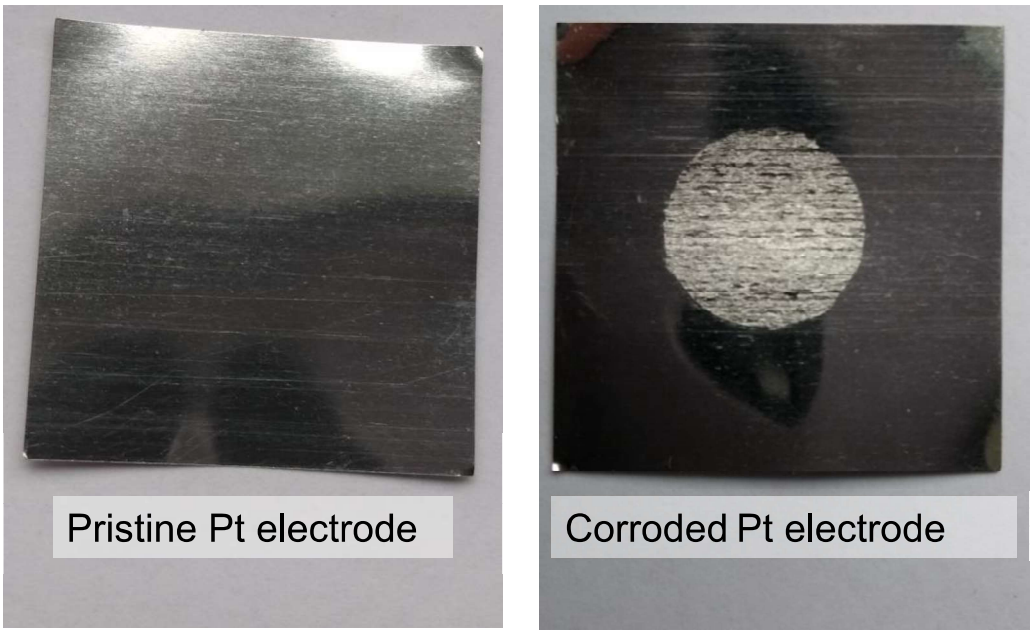

Figure S 24: Photograph of the pristine Pt electrode before it was used in the battery (left). Pt electrode that was used as positive electrode in the full cell with $EL_{GBL\text{-}BMP\text{-}Cl\text{-}55}$ and $EL_{GBL\text{-}BMP\text{-}Cl\text{-}55}$* (right). The Pt got clearly corroded while it was used as positive electrode in the battery, presumably by $[MnCl_5]^{2-}$.

Electrochemical Investigations of the Mn^{II} / Mn^{III}-half cell

Eq.[S 8] shows the empirical equation that was used to calculate i_{pc} and i_{pa}.[22]

$$\frac{i_{pc}}{i_{pa}} = \frac{i_{c0}}{i_{pa}} + \frac{0.485}{i_{pa}} \times i_{\lambda} + 0.086 \qquad \text{[S 8]}$$

Table S 18 shows standard electrode potentials (E_0) that are relevant for the all-MFB.[23] According to these potentials an aqueous all-MFB, using the Mn^{2+}/Mn^{3+} and the Mn^{0}/Mn^{2+} redox pairs would have a cell potential of 2.69 V. It is also noteworthy that the redox potential of $Pt/[Pt^{II}Cl_4]^{2-}$ compare to Pt/Pt^{2+} is 0.43 V lower, showing that the possibility to form $[PtCl_4]^{2-}$ is a strong driving force for the oxidation of Pt towards the oxidation state +2. This is probably the reason why the Pt electrodes can be oxidized by $[MnCl_5]^{2-}$.

Half-cell experiments for the analysis of the Mn-deposition

Figure S 25 shows among other things the voltage profiles of the deposition of Mn from $EL_{GBL\text{-}BMP\text{-}Cl\text{-}55}$* and $EL_{MeCN\text{-}BMP\text{-}30}$*. In the case of $EL_{GBL\text{-}BMP\text{-}Cl\text{-}55}$* the potential needed for the deposition of manganese at a current density of 0.25 mA cm^{-2} is higher at SoC80 compared to SoC5 (Δ =0.25 V). Charging a battery with $EL_{GBL\text{-}BMP\text{-}Cl\text{-}55}$ at the positive electrode and $EL_{GBL\text{-}BMP\text{-}Cl\text{-}55}$* at the negative electrode to SoC 80 shows the same increase in the voltage, needed for charging the battery. Therefore, we assign, as discussed earlier, that the increase in the voltage needed for charging the battery can be attributed to the deposition of

manganese. In the following cycles the charge voltage of the battery increases even further. Figure S 25 shows that the cell resistance is increased drastically after the deposition of manganese. As already discussed we believe that the cell resistance is increased because of the reduced manganese that does not stick to the electrode and ends up in the electrolyte. When using $EL_{MeCN\text{-}BMP\text{-}30}$* the same trends can be observed, however to a lower extend.

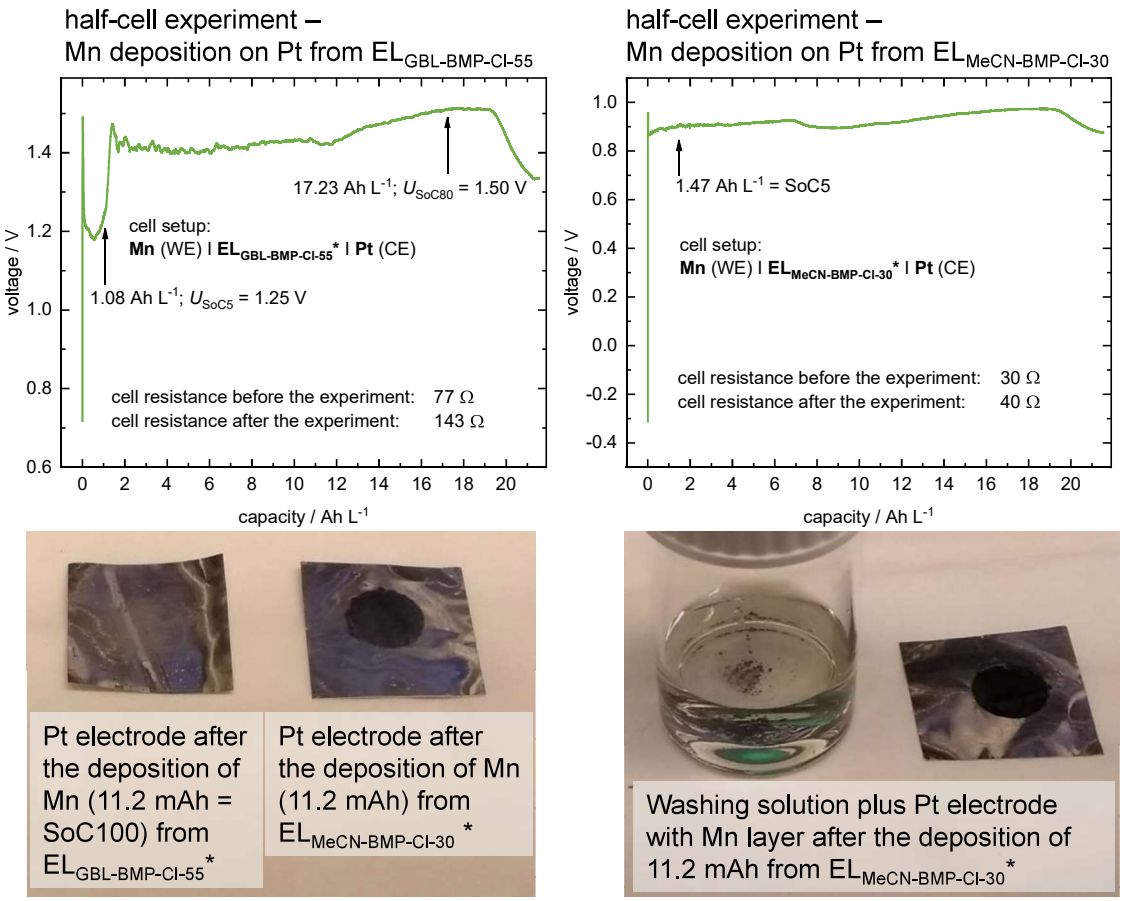

Figure S 25: Photographs of the Pt electrodes after the deposition of Mn on Pt from $EL_{GBL\text{-}BMP\text{-}Cl\text{-}55}$* and $EL_{MeCN\text{-}BMP\text{-}30}$* with the respective voltage profiles. The current density in these half-cell measurements was 0.25 mA cm^{-2} in both experiments.

Figure S 24 shows photographs of a pristine Pt foil and the Pt foil that was used for the positive electrode using $EL_{GBL\text{-}BMP\text{-}Cl\text{-}55}$ and $EL_{GBL\text{-}BMP\text{-}Cl\text{-}55}$* as electrolytes. The area of the Pt foil, which is electrochemically active during the cycling shows a strong alteration. As already discussed, we believe that the reason for this is the electrochemical oxidation of Pt towards $[Pt^{IV}Cl_6]^{2-}$ through $[MnCl_5]^{2-}$. Additionally, we believe that $[Pt^{IV}Cl_6]^{2-}$ is re reduced to $[Pt^{II}Cl_4]^{2-}$ again because otherwise we cannot explain the second discharge plateau seen in Figure 8 b).

Graphite as Electrode material for the positive Electrode

Figure S 26 (left) shows the voltage profiles of the cycling experiment with $EL_{MeCN\text{-}BMP\text{-}30}$ at the positive electrode an $EL_{MeCN\text{-}BMP\text{-}30}$* at the negative electrode. Compared to the cycling experiment using $EL_{MeCN\text{-}BMP\text{-}30}$ in both half cells, which is described above, U_{SoC5} and the

discharge plateau do not differ very much from each other except that the discharge plateau of the cell with $EL_{MeCN\text{-}BMP\text{-}30}$* at the negative electrode is much shorter. This is represented best, when looking at the CEs Figure S 26(right). The cycling experiment with $EL_{MeCN\text{-}BMP\text{-}30}$ in both half cells has a CE of 63 % in the last cycle, whereas the cell with $EL_{MeCN\text{-}BMP\text{-}30}$* at the negative electrode has only 10 %. We believe that the lower viscosity of $EL_{MeCN\text{-}BMP\text{-}30}$* is one reason for the dramatic decrease in the CE. Due to the lower viscosity the leaching of $[MnCl_5]^{2-}$ towards the Mn^0/Mn^{II} half-cell should be accelerated. Additionally, it has to be mentioned that in case of the cell with $EL_{MeCN\text{-}BMP\text{-}30}$ in both half cells a current density of 0.5 mA cm^{-2} was used, whereas a current density of 0.25 mA cm^{-2} was used in the cell with $EL_{MeCN\text{-}BMP\text{-}30}$* at the negative electrode. Therefore, charging the battery took twice as long for that cell, giving the $[MnCl_5]^{2-}$ more time for leaching. In the same scenario, with the GBL based electrolytes $EL_{GBL\text{-}BMP\text{-}Cl\text{-}55}$ and $EL_{GBL\text{-}BMP\text{-}Cl\text{-}55}$* a difference in the CE can be observed as well (Figure S 27, right). Here a current density of 0.25 mA cm^{-2} was used in both cycling experiments. The cell with $EL_{GBL\text{-}BMP\text{-}Cl\text{-}55}$ in both half cells has a CE of 80 % in the last cycle, whereas the cell with $EL_{GBL\text{-}BMP\text{-}Cl\text{-}55}$* at the negative electrode has a CE of 71 % in the last cycle. The same trend can be observed for the MeCN based electrolytes as well as for the GBL based electrolytes: The cells with the diluted Electrolytes ($EL_{GBL\text{-}BMP\text{-}Cl\text{-}55}$* and $EL_{MeCN\text{-}BMP\text{-}30}$*) show lower CE, which in our opinion can only be explained with the lower viscosity that enhances cross contamination. This assumption is further supported by the fact, that the effect is much stronger for the MeCN based electrolytes, which have generally a much lower viscosity compared to the GBL based electrolytes.

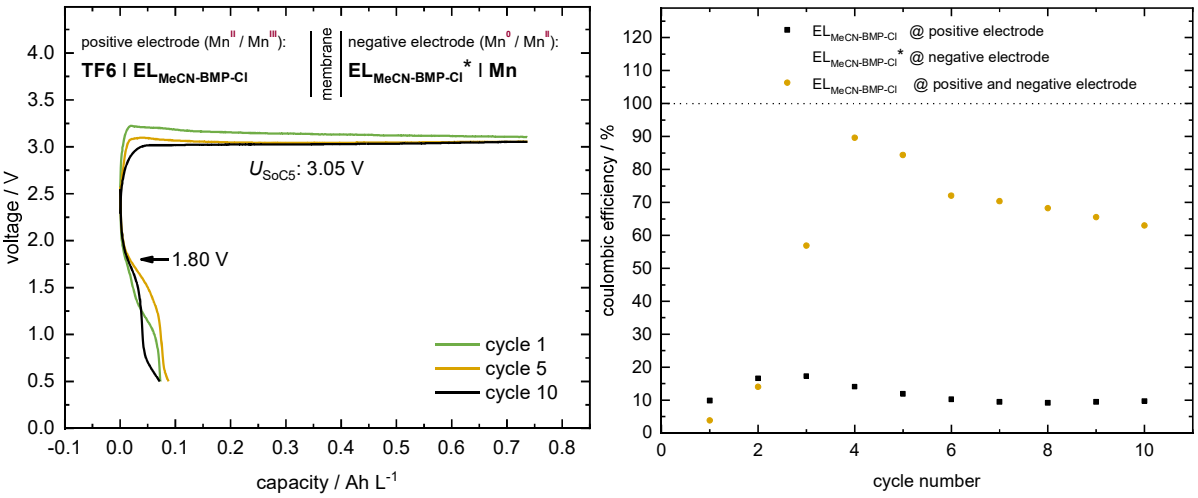

Figure S 26: Voltage profiles of the SoC5 cycling using $EL_{MeCN\text{-}BMP\text{-}30}$ at the positive electrode an $EL_{MeCN\text{-}BMP\text{-}30}$* at the negative electrode using a current density of 0.25 mA cm^{-2} (left) and the corresponding coulombic efficiencies compared to the cell with $EL_{MeCN\text{-}BMP\text{-}30}$ in both half-cells (right).

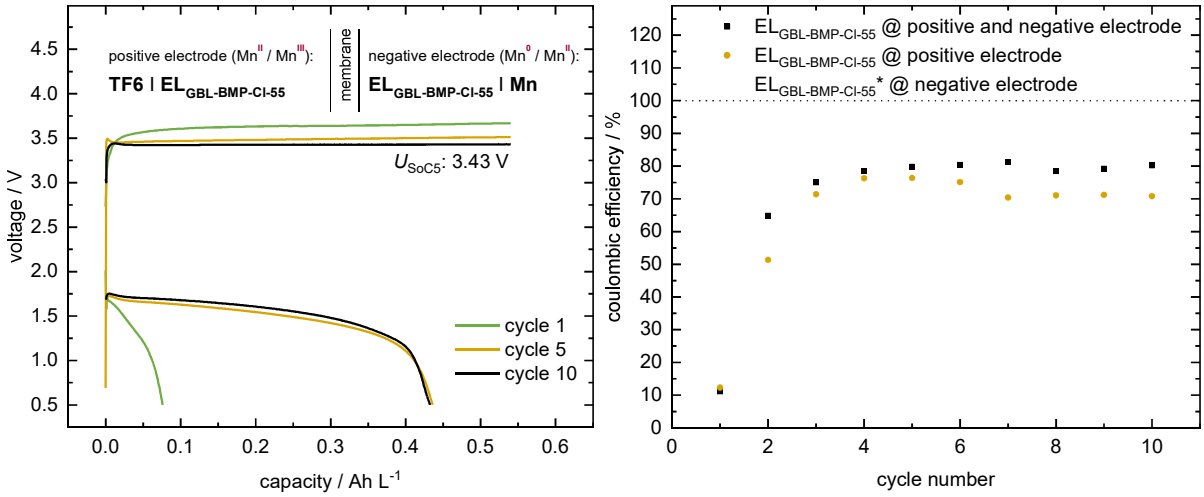

Figure S 27: Voltage profiles of the SoC5 cycling with EL$_{GBL-BMP-Cl-55}$ in both half cells using a current density of 0.25 mA cm^{-2} (left) and the corresponding coulombic efficiencies compared to the cell with EL$_{GBL-BMP-Cl-55}$ at the positive electrode an EL$_{GBL-BMP-Cl-55}$* at the negative electrode (right).

Graphite as Electrode Material for the negative Electrode

Figure S 28 shows the CE of the cell with EL$_{GBL-BMP-Cl-55}$ at the positive electrode an EL$_{GBL-BMP-Cl-55}$* at the negative electrode using TF6 as electrode material for both electrodes. With a CE of 75 % this cell is slightly better compared to the same cell with Mn as material for the negative electrode (71 %). Unfortunately, as discussed earlier TF6 is no alternative as electrode material for the negative electrode since the material is altered strongly during the measurement and we cannot be sure that manganese deposition is the only reaction that takes place at the TF6 (see Figure S 29).

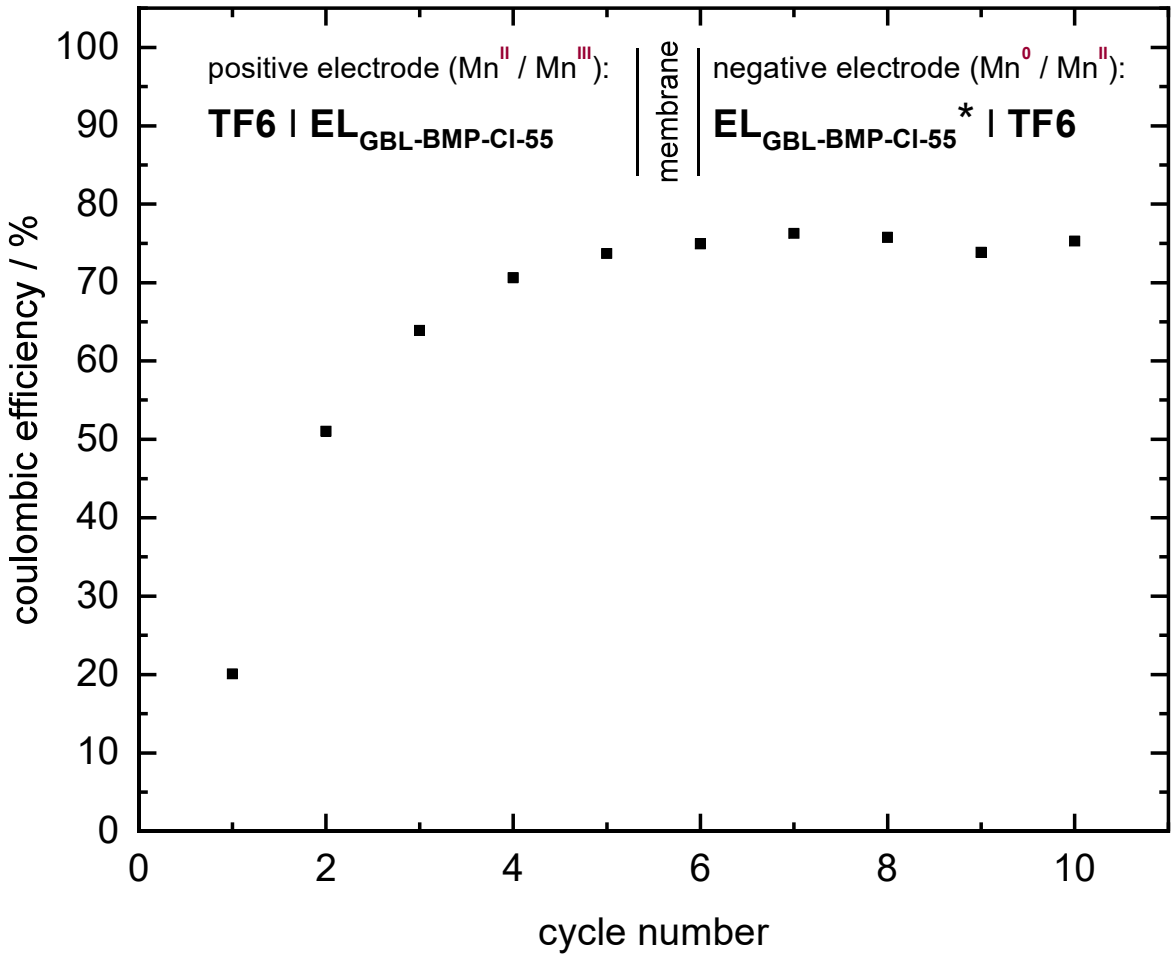

Figure S 28: Coulombic efficiency of the TF6|TF6-full-cell with $EL_{GBL-BMP-Cl-55}$ at the positive electrode an $EL_{GBL-BMP-Cl-55}$* at the negative electrode. A current density of 0.25 mA cm^{-2} was used in the experiment.

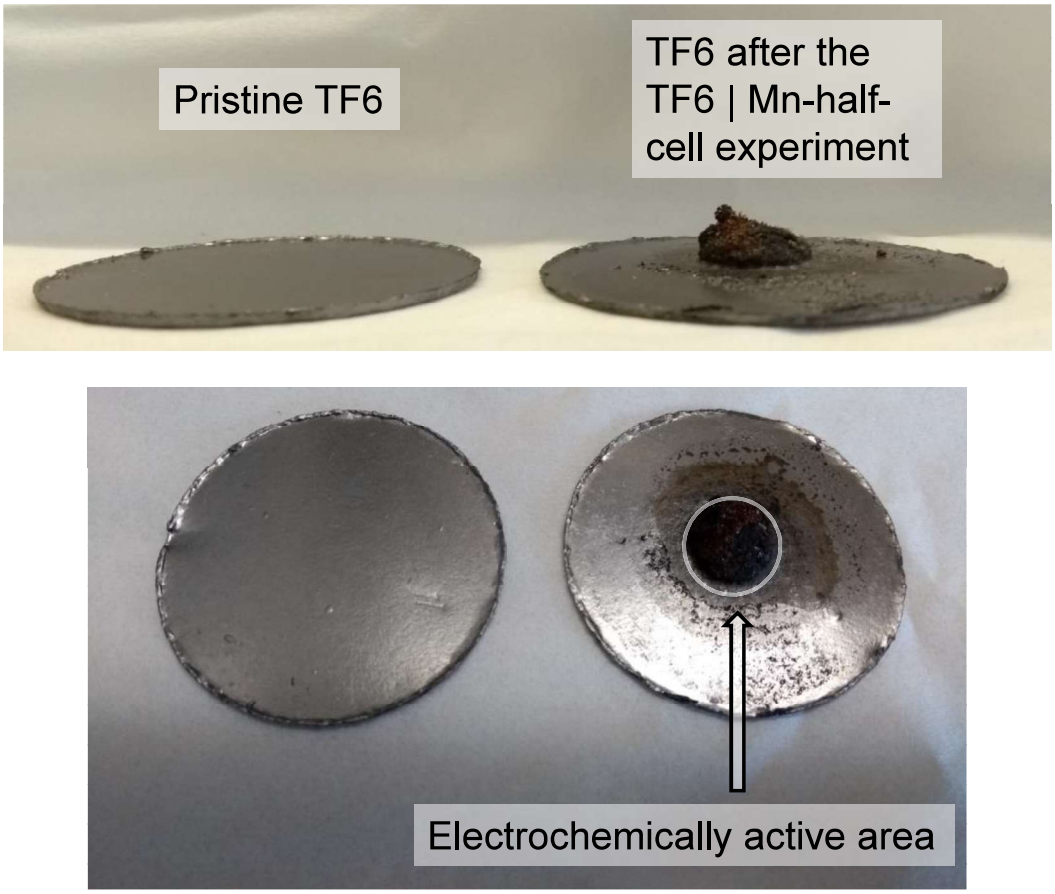

Figure S 29: Pristine TF6 electrode material (left) and TF6 electrode after the TF6|Mn^0-half-cell experiment (see Figure 10).

To investigate, whether TF6 is still an inert electrode material at the negative potential, necessary for the deposition of manganese, CV experiments with a solution of $[NBu_4][PF_6]$ in GBL were conducted with TF6 as WE. Since $[NBu_4][PF_6]$ and GBL are stable at these negative potentials any signal in the CV can be attributed to a reaction of the TF6. In Figure S 30 the CV shows that a reduction of TF6 appears at –1.8 V. For a better comparison the same measurement was also performed with a Pt WE, showing that the deposition of GBL does not start before –2.7 V. In addition, an oxidation of the reduced TF6 can be observed in the reverse scan, whereas no oxidation appears in the CV with Pt as WE. The photographs in Figure S 30 show that the initially smooth surface of the TF6 was altered towards a rough surface during the CV experiment. We did not further investigate what happened to the TF6 surface but besides a reduction of the graphite accompanied by an intercalation of $[NBu_4]^+$ there are not many alternatives that can be considered. This process hampers the deposition of manganese and shows that TF6 is no option as electrode material for the negative electrode of the all-MFB. However, using this kind of CV experiment is a good approach for identifying the right material.

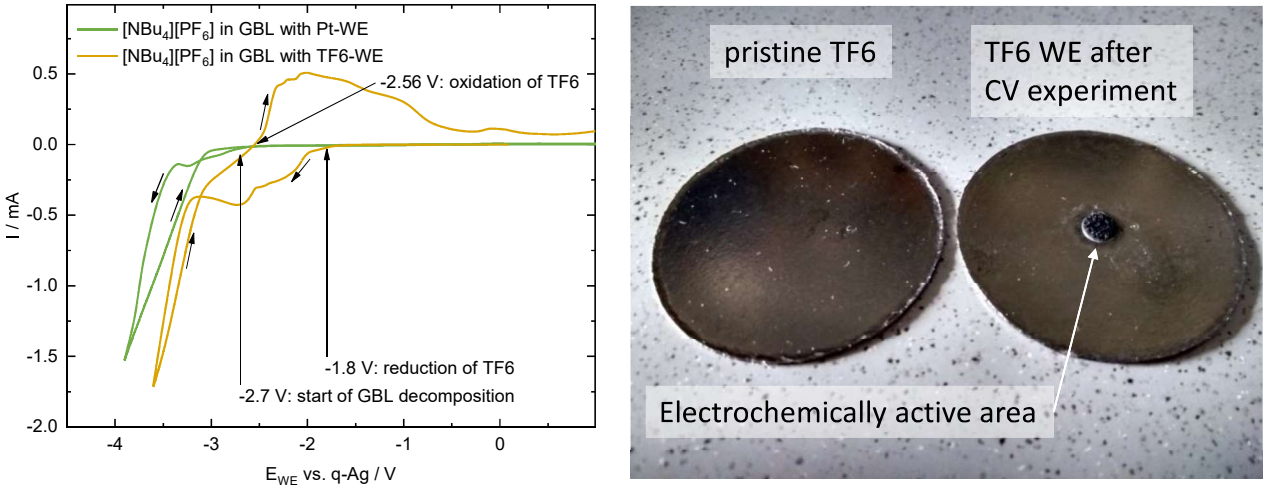

Figure S 30: left: CVs of a $[NBu_4][PF_6]$ solution in GBL (c = 0.1 mol L^{-1}) using a Pt-WE and a TF6-WE with a surface of 0.2 cm^2. The scan rate was 2 mV s^{-1} in both experiments. Pt foil was used as CE and an Ag wire was used as q - RE in both experiments. Right: Photograph of the TF6 electrode that was used in the CV experiment in comparison to a pristine TF6 electrode. The CVs were recorded in our homemade battery cells (v.s.).

Full Cell Battery Measurements with $[EMP]_2[Mn^{II}Cl_4]$ in GBL

Figure S 31 shows the voltage profiles and the CE of the TF6|Mn full-cell with $EL_{GBL\text{-}EMP\text{-}Cl\text{-}58}$ / $EL_{GBL\text{-}EMP\text{-}C\text{-}58}$* and compares the results with the same cell using $EL_{GBL\text{-}BMP\text{-}Cl\text{-}55}$ / $EL_{GBL\text{-}BMP\text{-}Cl\text{-}55}$*.

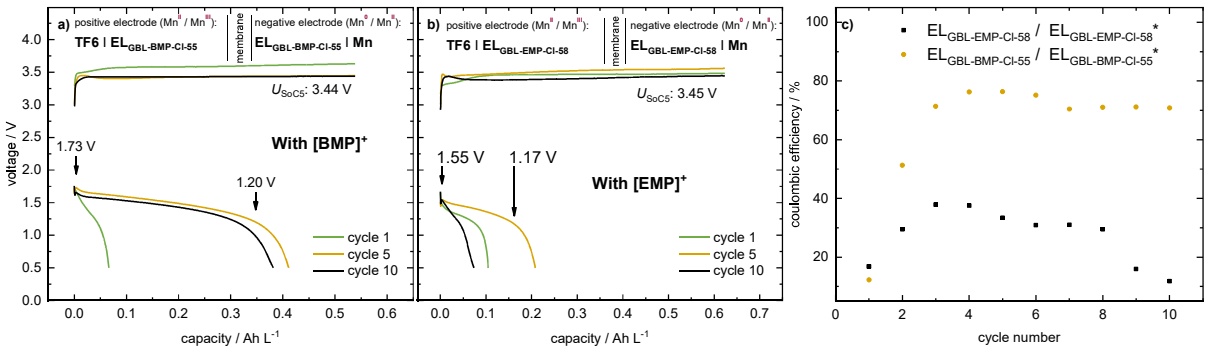

Figure S 31: a) Voltage profiles of the SoC5 cycling with $EL_{GBL\text{-}BMP\text{-}Cl\text{-}55}$ / $EL_{GBL\text{-}BMP\text{-}Cl\text{-}55}$*, b) with $EL_{GBL\text{-}EMP\text{-}Cl\text{-}58}$ / $EL_{GBL\text{-}EMP\text{-}Cl\text{-}58}$* and c) the corresponding coulombic efficiencies. Both experiments were conducted with a current density of 0.25 mA cm^{-2}.

Energy density

Figure S 32 shows the OCV measurements after charging a battery to SoC80 for GBL and MeCN based electrolytes. These measurements were conducted to obtain an experimental value for E_{cell}, which is needed for the calculation of the energy density. The OCV measurement does not deliver a stable potential, due to the measurement being conducted in static cells. Still in both measurements a plateau is reached, which allows us to estimate E_{cell}. For the cell with $EL_{GBL\text{-}BMP\text{-}Cl\text{-}55}$ at the positive electrode and $EL_{GBL\text{-}BMP\text{-}Cl\text{-}55}$* at the negative electrode a cell

potential of 2.59 V is obtained. With $EL_{MeCN\text{-}BMP\text{-}Cl\text{-}30}$ at the positive electrode and $EL_{MeCN\text{-}BMP\text{-}Cl\text{-}30}$* at the negative electrode a cell potential of 2.42 V is obtained. Since charging the battery to SoC80 takes 37 h we assume that $[MnCl_5]^{2-}$ is constantly present at the negative electrode due to cross contamination, making it impossible to measure a stable OCV.

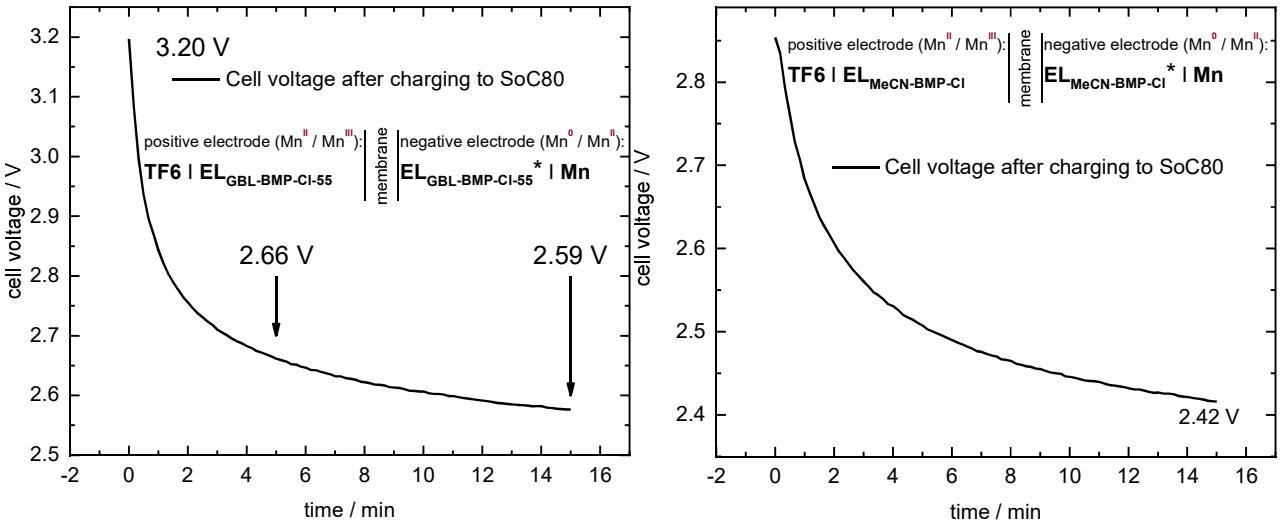

Figure S 32: Measurements of the OCV at SoC80 of the battery cells with TF6 as the positive electrode and a Mn-plate as the negative electrode. $EL_{GBL\text{-}BMP\text{-}Cl\text{-}55}$ was used at the positive electrode and $EL_{GBL\text{-}BMP\text{-}Cl\text{-}55}$* was used at the negative electrode (left). $EL_{MeCN\text{-}BMP\text{-}Cl\text{-}30}$ was used at the positive electrode and $EL_{MeCN\text{-}BMP\text{-}Cl\text{-}30}$* was used at the negative electrode (right).

Table S 19 shows a comparison of different battery systems conceivable for large scale EES systems and compares their practical energy density. For the all-MFB only the theoretical energy density is given, since it is still in its infancy.

Table S 19: Estimation of the theoretical energy density of an all-Mn battery (all-MFB), calculated with the aqueous E^0 values for the Mn^0/Mn^{II} and the Mn^{II}/Mn^{III} redox couple and concentrations between 1 and 2 mol L^{-1}. A density of 1.1 mol L^{-1} was assumed. For comparison, state of the art RFBs and a LIB with $LiFePO_4$ as material for the positive electrode are listed. All of them are considered suitable for large scale EES systems.

	ΔE^0 / V	Theoretical energy density / Wh Kg^{-1}	Practical energy density / Wh Kg^{-1}	Practical energy density / Wh L^{-1}
All-MFB	2.69	44 – 87	?	?
ZBFB[17,24]	1.85	440	60 – 85	50
VRFB[17,24]	1.1 – 1.6	-	15 – 25	25 – 35
VBFB[17,24][a]	1.29	-	25 – 50	35 – 70
LIB[25]	3.3	-	93 – 136	203 – 331

[a] VBFB = Vanadium-bromine redox flow battery (next generation VRFB)

Investigations in a Pumped Flow-Cell

Specifications of the flow-cell and the overall setup

Figure S 33,Figure S 34 andFigure S 35 shows an exploded view of the self-designed flow-cell, photographs of the single components and a schematic view of the entire system used for the measurements. The modular setup allows the utilization of up to three electrochemical cells connected in series. In this work we used the single cell setup only. Due to the short distance between the TF6 electrodes it was necessary to use graphite felt electrodes (GFA6 from SGL carbon) in the flow-cell in contrast to the static battery cells, because otherwise the membrane and the TF6 come into contact due to the deflection of the membrane caused by small differential pressure in both half-cells. Besides, the current densities without felt electrodes were extremely poor and not practical. Additionally, we had to use TF6 as electrode material for the negative electrode, since a solid manganese plate in the required size was too expensive. Ironically a solid manganese electrode is quite expensive due to the brittle nature of manganese. Therefore, the production of these pates is quite complicated causing the high price, although manganese itself is cheap. As already discussed (v.s.), pure manganese electrodes are anyway no option as electrode material, since they do not result in an improved manganese deposition. The temperature of the flow-cell can be kept at a constant level, using heating foil placed behind the current collectors. Figure S 34 shows photographs of the overall setup and Figure S 35 shows a schematic view. The cell was assembled under atmospheric conditions without any pretreatment of the membrane or the electrodes. Afterwards a pressure test was conducted to check, whether the cell was tight. An overpressure of 950 mbar nitrogen gas was applied and the pressure drop was observed with an integrated pressure sensor. If the cell was tight enough, it was connected to the tubing. The tightness of the entire system was then checked again, applying an overpressure of around 1 bar of argon. Afterwards the entire system was dried by applying vacuum and argon in alternation, to remove oxygen and residual water. To further remove trace water, the tubing and the flow cell were flushed with dry MeCN. Then the electrolyte tanks, filled under inert conditions in a glovebox, were coupled to the rest of the system, which was dried again by applying vacuum and argon in alternation before the measurements were started. All components - the battery cell, the pump, the electrolyte tanks and the whole tubing - are placed in a specially designed box. In the box, temperature is kept constant during the measurements using a heat exchanger. Additionally, to keep the atmosphere inert, a constant flow of nitrogen is passed through the box, permanently. Since we observed that the filling level of the catholyte tank decreased during cycling, accompanied by an increased filling level of the anolyte tank, a third tank with pure

solvent was introduced into the system that allows to adjust the filling level of the catholyte tank under inert conditions (not shown in the photographs).

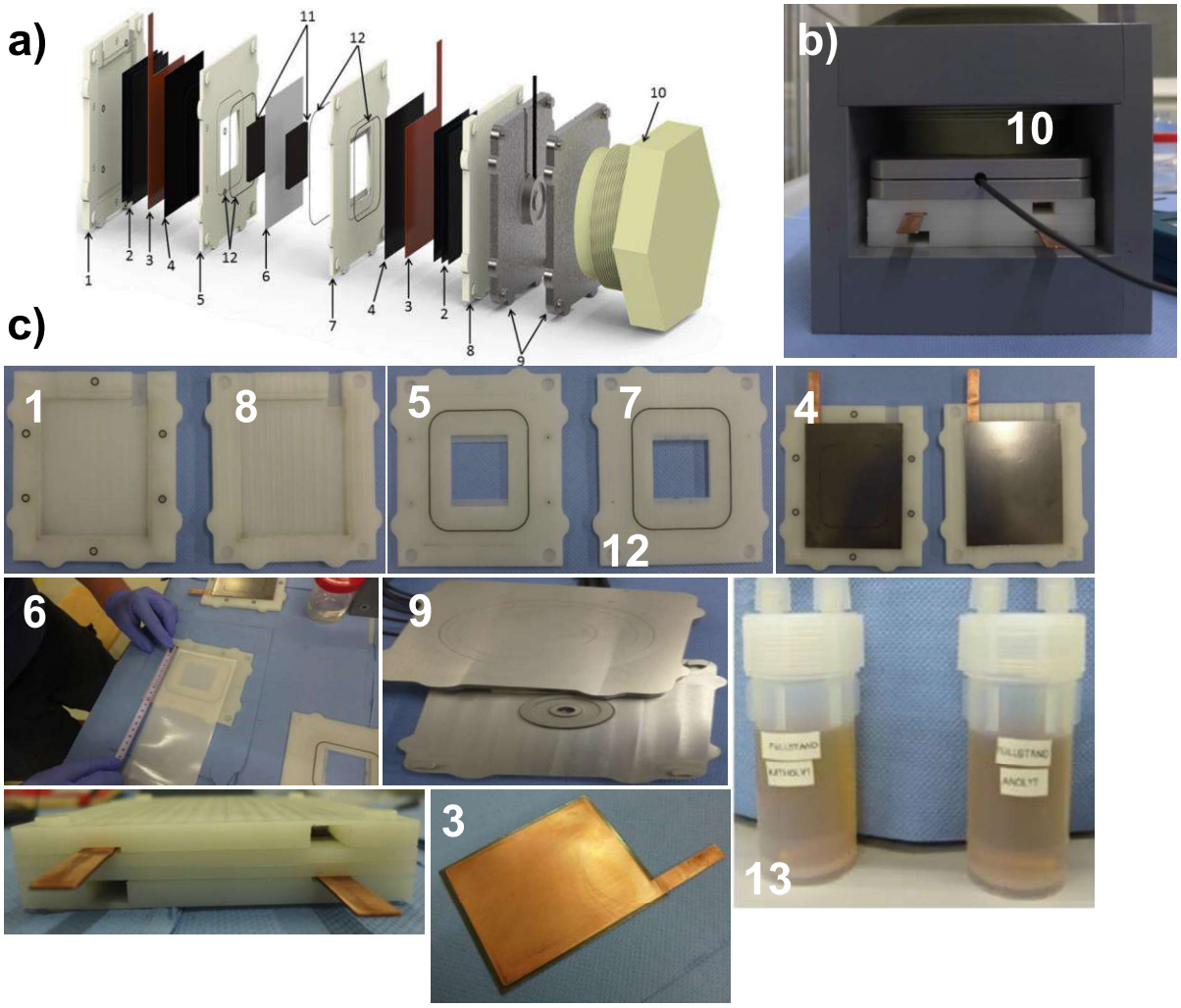

Figure S 33: a) Exploded view of the single cell setup. b) Assembled single cell setup with pressure sensor. c) Photographs of the single components of the flow cell: 1 and 8 = PVDF endplates with O-ring sealing, 2 = TF6 spacers that can be replaced with heating foil, 3 = copper current collector, 4 = TF6 electrodes, 5 and 7 = PVDF frames with O-ring sealing (12), 6 = membrane, 9 = pressure sensor between aluminum plates, 10 = PVC screw, 11 = graphite felt electrodes, 13 = electrolyte tanks.

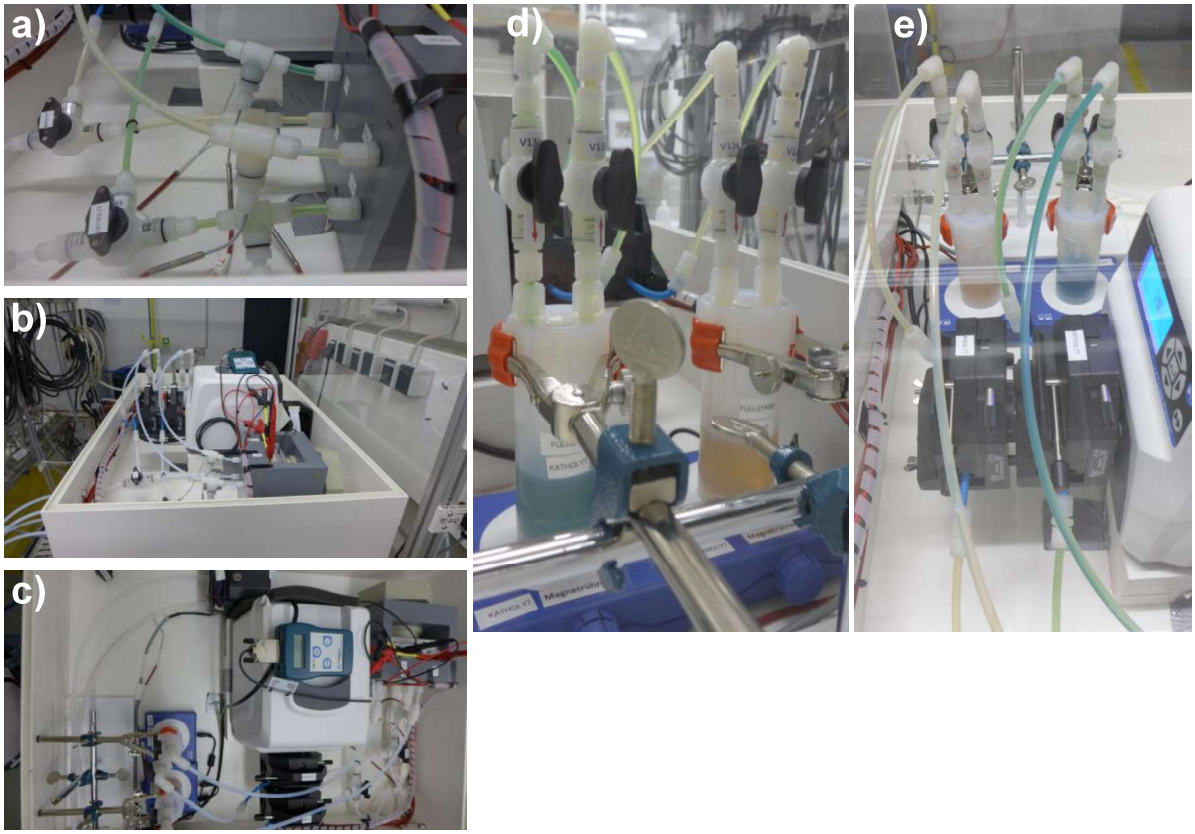

Figure S 34: a) Connection of the forward flow, as well as the return flow to the flow-cell. b) front view of the whole system. c) top view of the whole system. d) catholyte tank (green) and anolyte tank (yellow). e) tubing that shows the characteristic colors of the electrolyte.

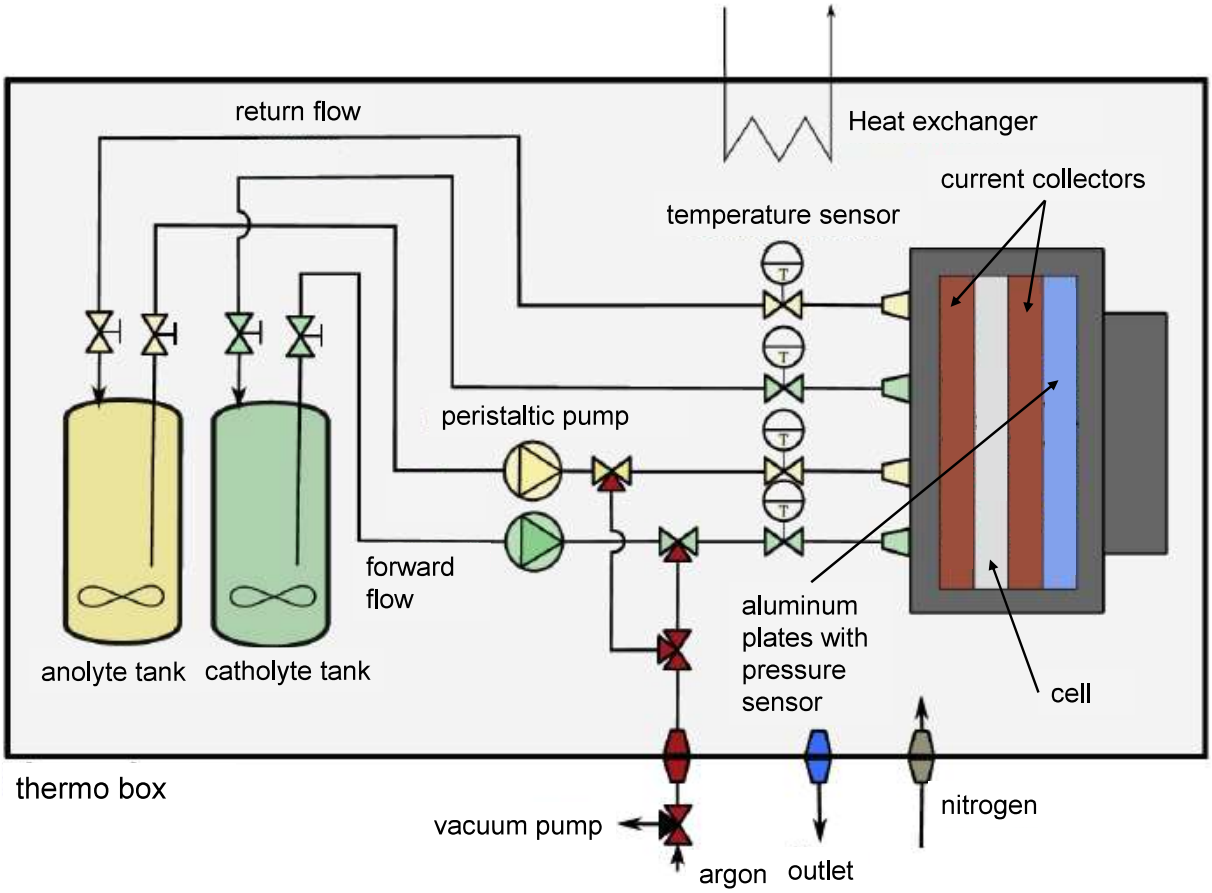

Figure S 35: Schematic representation of the overall setup used for the flow-cell experiments.

Methods used for the electrochemical characterization in the pumped flow-cell

OCV Measurements

OCV measurements were conducted to determine E_{cell}, an important parameter for the battery characterization. E_{cell} equals the OCV at a SoC of 100 %.

Battery cycling (cc-cycling)

The battery was charged and discharged galvanostatically, meaning that a constant current (cc) was applied. The resulting voltage (U_{cell}), present while charging or discharging the battery is given by Eq. [S 9],

$$U_{\mathrm{cell}} = U_{\mathrm{OCV}} + j \times ASR \qquad \text{[S 9]}$$

with j, being the current density and ASR the area specific resistance of the battery cell. j has a positive sign for charging, and a negative sign for discharging the battery. Since U_{OCV} is a function of the SoC, U_{cell} constantly increases, while charging and decreases while discharging the battery. Therefore, U_{cell} is a commonly used cut-off criteria for cc-cycling. Eq. [S 9] also shows that it is important to use a suitable current density. If the current density is too high, the

upper cut-off voltage comes into operation, before the whole capacity (SoC100) is utilized. The same is true for the lower cut-off voltage.

Polarization measurements (ASR determination)

Polarization measurements were conducted for the evaluation of the ASR. A pulsed method was used, applying short current pulses of 1 s, followed by an OCV measurement of 59 s. The range of the current densities was between – 15 mA cm^{-2} and + 15 mA cm^{-2}. Figure S 36 shows the measurement of a current pulse with 2.5 mA cm^{-2} and the respective voltage response. With U_{cell} and U_{OCV}, obtained from the measurement, the ASR can be calculated according to Eq. [S 10],

$$ASR = \frac{U_{\text{cell}} - U_{\text{OCV}}}{j} \qquad \text{[S 10]}$$

with *j* being the current density. For the current pulse in Figure S 36an *ASR* of 218.0 Ω cm^2 is obtained.

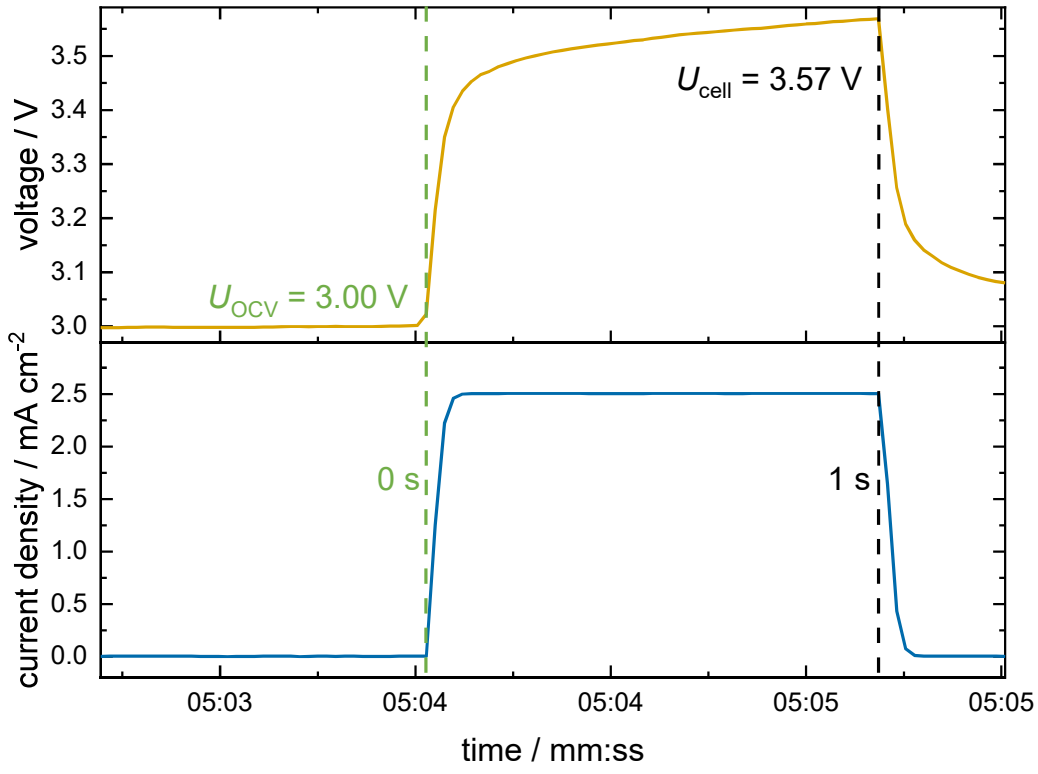

Figure S 36: Current pulse with 2.5 mA cm^{-2} and the respective voltage response. U_{OCV} and U_{cell} are required for the calculation of the ASR.

MeCN based electrolytes

Using MeCN as a solvent for the electrolytes had drastic consequences for the materials used in the flow-cell. Especially the pieces made from PVDF and PVC showed strong alterations after the experiments (Figure S 37). Therefore, new frames made of polyether ether ketone (PEEK) were manufactured, which was very expensive, but allowed longer measurements.

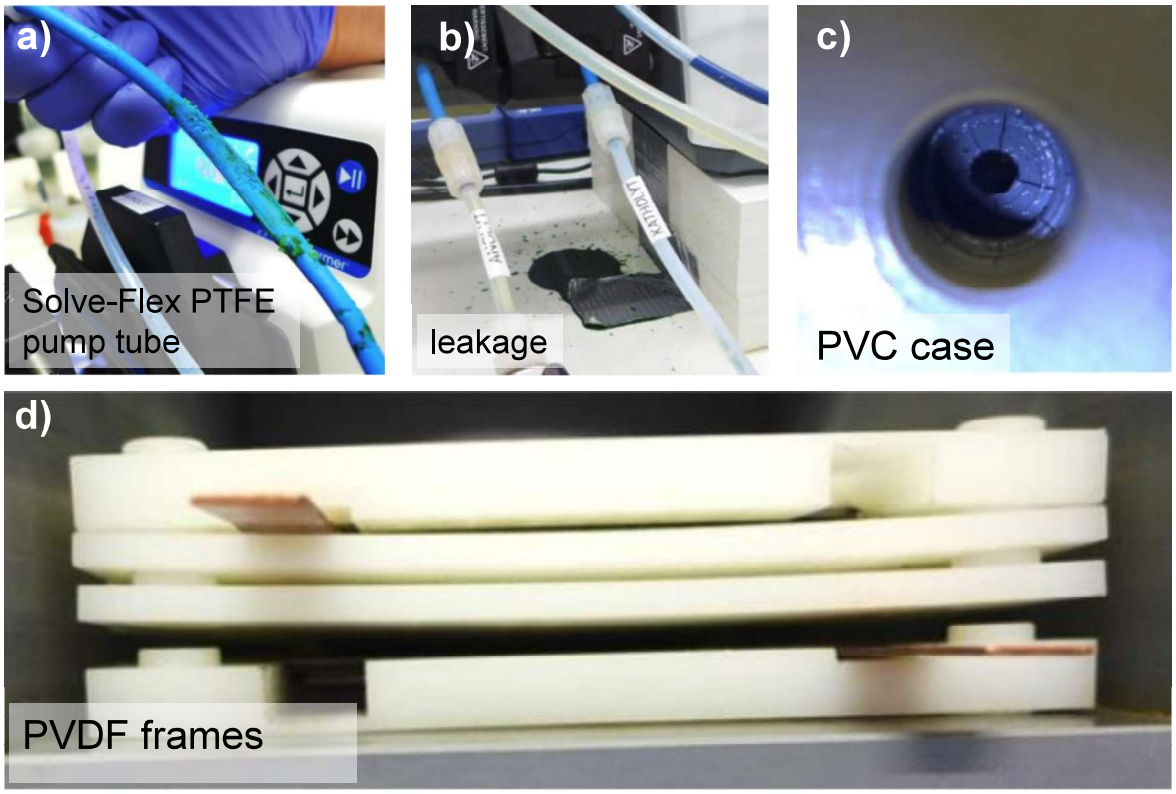

Figure S 37: Negative effects on the material used in the flow-cell caused by MeCN. a) Pump tube that was destroyed due to incompatibility with MeCN. b) Leakage. C) Cracks in the PVC case of the flow-cell. d) PVDF frames, that lost their original shape.

GBL based electrolytes

Table S 20 shows the protocol that was used for the measurements of $EL_{GBL\text{-}BMP\text{-}0.33}$ and $EL_{GBL\text{-}EMP\text{-}Cl\text{-}0.33}$ in the flow cell and $EL_{GBL\text{-}EMP\text{-}Cl\text{-}0.33}$ in a static cell. $EL_{GBL\text{-}BMP\text{-}0.33\text{-}F}$ was not discharged after charging to SoC50 like $EL_{GBL\text{-}EMP\text{-}Cl\text{-}0.33\text{-}S}$ and $EL_{GBL\text{-}EMP\text{-}Cl\text{-}0.33\text{-}F}$. Instead the self-discharge was observed by measuring the OCV (Figure S 38). At the end of the OCV measurement the starting point for the cycling can be compared to the starting point of $EL_{GBL\text{-}EMP\text{-}Cl\text{-}0.33\text{-}S}$ and $EL_{GBL\text{-}EMP\text{-}Cl\text{-}0.33\text{-}F}$, which were discharged galvanostatically.

Table S 20: Protocols for the measurements with $EL_{GBL\text{-}BMP\text{-}0.33\text{-}F}$ and $EL_{GBL\text{-}EMP\text{-}Cl\text{-}0.33\text{-}F/S}$.

Method	$EL_{GBL\text{-}BMP\text{-}0.33\text{-}F}$	$EL_{GBL\text{-}EMP\text{-}Cl\text{-}0.33\text{-}F}$	$EL_{GBL\text{-}EMP\text{-}Cl\text{-}0.33\text{-}S}$
Charge to SoC50[a]	1 mA cm^{-2}, 5 mL min^{-1}	1 mA cm^{-2}, 5 mL min^{-1}	1 mA cm^{-2}
OCV (15 min)	OCV_{SoC50} = 3.07 V	OCV_{SoC50} = 2.89 V	OCV_{SoC50} = 2.83 V
ASR	charge: 249 – 156 Ω cm^2 discharge: 258 – 226 Ω cm^2	charge: 201 – 179 Ω cm^2 discharge: 201 – 189 Ω cm^2	charge: 366 – 211 Ω cm^2 discharge: 652 – 284 Ω cm^2
Discharge from SoC50[b]	–	CE = 36 %	CE = 35 %
OCV	OCV after 6 h: 2.55 V	–	–
Cycling	1.5 mA cm^{-2}, 5 mL min^{-1} C_U: 11 % for 66 cycles C_U < 11 % for 60 cycles	1.5 mA cm^{-2}, 5 mL min^{-1} C_U: 10 % for 333 cycles C_U < 10 % for 170 cycles	1.5 mA cm^{-21} C_U: 10 % for 500 cycles

[a] A potential limit of 3.8 V was used. For $EL_{GBL\text{-}BMP\text{-}0.33\text{-}F}$ this limit was hit before SoC50 was reached. Therefore, the cell was further charged to SoC50, using a constant voltage of 3.8 V. [b] A potential limit of 0.0 V was used.

Figure S 38 shows the OCV measurement of $EL_{GBL\text{-}BMP\text{-}0.33\text{-}F}$ at SoC50. After 6 h the cell voltage is still at 2.55 V, supporting our estimation of the cell voltage of 2.59 V, at SoC100. However, during the following 66 h the cell voltage decreases constantly because of the $[MnCl_5]^{2-}$ leaching.

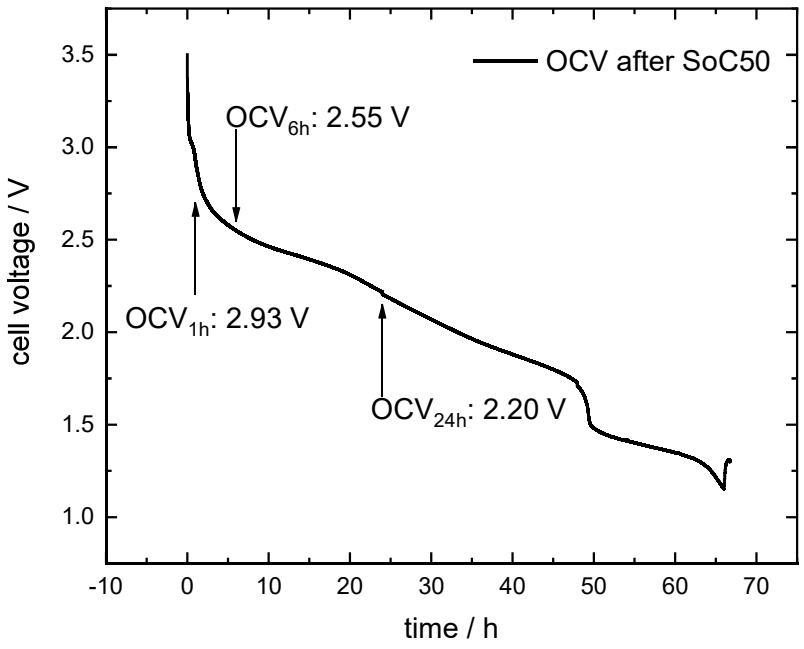

Figure S 38: OCV measurement of $EL_{GBL\text{-}BMP\text{-}0.33\text{-}F}$ at SoC50. During the whole measurement the electrolyte was pumped through the battery cell with a flow rate of 5 mL min^{-1}.

Cost estimations for a battery stack based on a 1 MW facility with a capacity of 8 MW h

For a 1 MW facility, 40 battery stacks are necessary. One stack consists of 42 cells with an electrode surface of 420 × 594 mm (DINA2). Using a current density of 50 mA cm^{-2}, each cell delivers 25 kW and 160 – 175 V. Stack costs in € / kW of different designs are shown in Figure S 39. The evaluation of the cost is based on the assumption, that the current density from the cycling experiment with $EL_{GBL\text{-}EMP\text{-}Cl\text{-}0.33\text{-}F}$ can be improved by one order of magnitude. The biggest potential for reducing the cost is obviously the material for the frame. This shows the importance of using a solvent that is compatible with a cheap material like for example PVC (design 3-–8). With a solvent, that is compatible with polypropylene (PP) it is also possible to change the more expensive TF6 bipolar plate to a cheaper alternative that uses PP instead of the fluoropolymer, used in TF6 (design 4 – 8). Design 1 is the closest to the cell we used for the cycling experiment with $EL_{GBL\text{-}EMP\text{-}Cl\text{-}0.33\text{-}F}$. Of course, this is too expensive from an economical point of view, but Figure S 39 shows that a reduction of the cost to 125 € / kW is possible with alternative cell designs and materials. The inset in Figure S 39 shows in detail the differences between the designs 1 – 8, concerning the used material and the stack design.

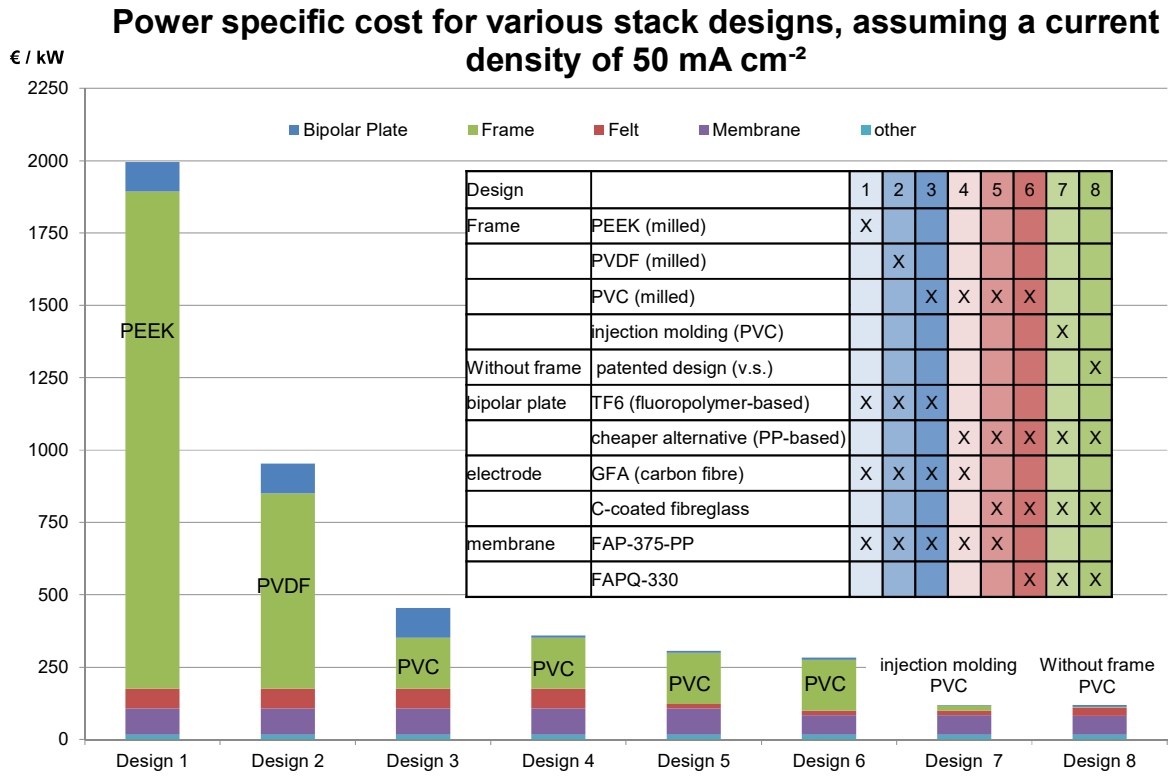

Figure S 39: Overview of the costs for a 1 MW facility, taking a current density of 50 mA cm^{-2} as a basis for the calculation of the required material. The material cost, based on the quantity for a 1 MW facility, were obtained from the respective manufacturers. Design 8, which does not use a frame, is based on a patent.[26]

The cost of the electrolyte is also relevant for an economical evaluation of the all-Mn battery. After consulting suppliers of the relevant chemicals, a cost of 6.5 – 8.0 € kg^{-1} is realistic for an electrolyte containing 45 wt % $[EMP]_2[MnCl_4]$ and 55 wt % GBL. For storing 8 MW h, approximately 183570 kg of electrolyte are needed. From this an electrolyte costs of 149 – 184 € $(kW\ h)^{-1}$ can be calculated. All of the calculated prices in this paragraph are based on a 1 MW facility, that can store energy up to 8 MW h. For bigger facilities the cost per kWh of the electrolyte as well as the stack costs are presumably further reduced.

Crystallographic details

Table S 21: Crystallographic details of the compound $[NEt_4]_4[MnCl_4][MnCl_5]$.

CCDC number	2031457
Empirical formula	$C_{32}H_{80}Cl_9Mn_2N_4$
Formula weight	949.93
Temperature [K]	100(2)
Crystal system	tetragonal
Space group (number)	$P4/n$ (85)
a [Å]	14.0370(4)
b [Å]	14.0370(4)
c [Å]	12.1648(4)
α [Å]	90
β [Å]	90
γ [Å]	90
Volume [$Å^3$]	2396.92(16)
Z	2
ρ_{calc} [g/cm^3]	1.316
μ [mm^{-1}]	1.055
F(000)	1006
Crystal size [mm^3]	0.16×0.16×0.13
Crystal colour	green
Crystal shape	octahedron
Radiation	MoK_α (λ=0.71073 Å)
2Θ range [°]	3.35 to 56.57 (0.75 Å)
Index ranges	-18 ≤ h ≤ 18, -18 ≤ k ≤ 18, -16 ≤ l ≤ 16
Reflections collected	59198
Independent reflections	2993 [R_{int} = 0.0297, R_{sigma} = 0.0120]
Completeness to θ = 25.242°	100.0 %
Data / Restraints / Parameters	2993/519/198
Goodness-of-fit on F^2	1.071
Final *R* indexes [$I \geq 2\sigma(I)$]	R_1 = 0.0569, wR_2 = 0.1391
Final *R* indexes [all data]	R_1 = 0.0629, wR_2 = 0.1430
Largest peak/hole [e$Å^3$]	1.21/-0.95

References

[1] *SAINT*, Bruker, SAINT, V8.34A, Bruker AXS Inc., Madison, Wisconsin, USA.

[2] *SADABS*, Bruker, SADABS, 2014/5, Bruker AXS Inc., Madison, Wisconsin, USA.

[3] G. M. Sheldrick, *Acta Crystallogr. C Struct. Chem.* **2015**, *71*, 3.

[4] G. M. Sheldrick, *Acta Crystallogr. A* **2015**, *71*, 3.

[5] D. Kratzert, J. J. Holstein, I. Krossing, *J. Appl. Crystallogr.* **2015**, *48*, 933.

[6] D. Kratzert, I. Krossing, *J. Appl. Crystallogr.* **2018**, *51*, 928.

[7] C. F. Macrae, I. Sovago, S. J. Cottrell, P. T. A. Galek, P. McCabe, E. Pidcock, M. Platings, G. P. Shields, J. S. Stevens, M. Towler, P. A. Wood, *J. Appl. Crystallogr.* **2020**, *53*, 226.

[8] *EC-Lab V11.21: 2018*, BioLogic **2018**.

[9] J. S. Avery, C. D. Burbridge, D.M.L. Goodgame, *Spectrochim. Acta* **1968**, *24*, 1721.

[10] H. G. M. Edwards, M. J. Ware, L. A. Woodward, *Chem. Commun. (London)* **1968**.

[11] F. A. Cotton, D. M. L. Goodgame, M. Goodgame, *J. Am. Chem. Soc.* **1962**, *84*, 167.

[12] G. Adamová, R. L. Gardas, M. Nieuwenhuyzen, A. V. Puga, L. P. N. Rebelo, A. J. Robertson, K. R. Seddon, *Dalton Trans.* **2012**, *41*, 8316.

[13] C. F. Bell, D. N. Waters, *J. Inorg. Nucl. Chem.* **1977**, *39*, 773.

[14] W. Levason, C. A. McAuliffe, *Dalton Trans.* **1973**.

[15] P. Alotto, M. Guarnieri, F. Moro, *Renew. Sust. Energ. Rev.* **2014**, *29*, 325.

[16] M. Skyllas-Kazacos, F. Grossmith, *J. Electrochem. Soc.* **1987**, *134*, 2950.

[17] Á. Cunha, J. Martins, N. Rodrigues, F. P. Brito, *Int. J. Energy Res.* **2015**, *39*, 889.

[18] K. Gong, F. Xu, J. B. Grunewald, X. Ma, Y. Zhao, S. Gu, Y. Yan, *ACS Energy Lett.* **2016**, *1*, 89.

[19] *Origin(Pro): 2018*, OriginLab Corporation, Northampton, MA, USA **2018**.

[20] S. Dorbritz, W. Ruth, U. Kragl, *Advanced Synthesis & Catalysis* **2005**, *347*, 1273.

[21] A. M. Fernandes, J. A. P. Coutinho, I. M. Marrucho, *Journal of mass spectrometry JMS* **2009**, *44*, 144.

[22] A. J. Bard, L. R. Faulkner, *Electrochemical methods: Fundamentals and applications*, Wiley, Hoboken, NJ **2001**.

[23] A. F. Holleman, E. Wiberg, N. Wiberg, *Lehrbuch der anorganischen Chemie*, de Gruyter, Berlin **2007**.

[24] E. Sánchez-Díez, E. Ventosa, M. Guarnieri, A. Trovò, C. Flox, R. Marcilla, F. Soavi, P. Mazur, E. Aranzabe, R. Ferret, *J. Power Sources* **2021**, *481*, 228804.

[25] *Supplier of 18650 LIB cells with LFP cathode material: Access: 11.11.2020, 16:58*, https://tyva-energie.com/en/lithium-en/our-secondary-battery-solutions/18650-li-ion-cells.html.

[26] K. A. Bromberger, T. Smolinka, J. Went, *ARRANGEMENT OF ELECTROCHEMICAL CELLS*, *H01M2/08;H01M2/14;H01M4/00;H01M8/18* **2014**.

D. Unpublished Compounds and Cyclic Voltammograms

Herein is the synthesis, NMR and ESI-MS data, elemental analysis, Raman spectrum, and solid state structure with the Cambridge Crystallographic Data Centre (CCDC) reference number to solid state structures that were left unpublished in the publication section.

Additionally, the cyclic voltammograms of $[N_{2221}][ClF_4]$, $[N_{2221}][BrF_4]$, and $[N_{2221}][IF_6]$.

D.1 *N*,*N*-diethyl-di(3-methoxypropyl)ammonium bromide, $[N_{22.(3O1)2}]Br$

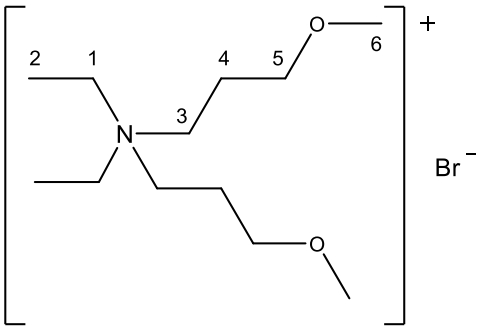

A slight excess of 1-bromo-3-methoxypropane, $BrCH_2(CH_2)_2OMe$, (32.8 g, 213 mmol, 2.2 eq.) was added dropwise over 30 minutes to a mixture of diethylamine (7.2 g, 98 mmol, 1.0 eq.) and potassium carbonate, K_2CO_3, (27.7 g, 201 mmol, 2.0 eq.) in 40 mL of MeCN. The mixture was stirred under reflux for 4 h. The work up was performed in a mixture of water and diethylether. The product was extracted in the ether phase and dried under vacuum at a temperature of 80 °C for 8 h, yielding a light brown solid. The yield was 19.0 % (5.6 g, 18.6 mmol). Colorless crystals were obtained at *r.t.* in MeCN.

^{1}H NMR (400 MHz, $CDCl_3$, 22 °C): δ = 3.53 (q, *J* = 7.2 Hz, 4H, 1-H), 3.47 (t, *J* = 5.3 Hz, 4H, 5-H), 3.44 (s, 6H, 6-H), 3.29 (t, *J* = 5.0 Hz, 4H, 3-H), 2.02 (tt, *J* = 5.3 Hz, 4H, 4-H), 1.36 (t, *J* = 7.0 Hz, 6H, 1-H) pPHM.

^{13}C{^{1}H} NMR (100 MHz, $CDCl_3$, 22 °C): δ = 68.47 (s, 5-C), 58.88 (s, 6-C), 56.01 (s, 1-C), 54.27 (s, 3-C), 22.89 (s, 4-C), 7.89 (s, 2-C) pPHM.

ESI+ = [M^+] 218.2073 m/z;

CHN: Calculated for $C_{12}H_{28}BrNO_2$: C 48.323 %, H 9.462 %, N 4.697 %; Found C 48.53 %, H 11.94 %, N 4.736 %;

FT-Raman (*r.t.*, crystal, res. = 2 cm^{-1}): $\tilde{\nu}$ = 3003(s,sh), 2996(vs), 2983(vs,sh), 2974(vs), 2964(vs), 2939(vs), 2907(s), 2884(vs), 2868(s), 2855(vs), 2831(vs), 2813(m), 2737(s), 1496(s), 1487(s), 1473(m), 1465(m), 1455(s), 1445(s), 1412(w), 1399(w), 1383(w), 1370(w), 1351(w), 1320(s), 1311(s), 1268(w), 1263(w,sh), 1239(m), 1180(m), 1174(w), 1156(w), 1141(w), 1136(m), 1117(m), 1076(m), 1055(vw), 1031(vw), 1025(vw,sh), 1017(m), 968(m), 931(w), 919(w,sh), 912(m), 873(w), 860(s), 823(vw,sh), 820(w), 776(w), 762(vw), 736(m), 581(vw), 574(w), 500(vw,sh), 495(w), 489(vw,sh), 423(w), 408(m), 396(vw,sh), 305(w), 289(w), 273(vw) cm^{-1};

CCDC: 2024864.

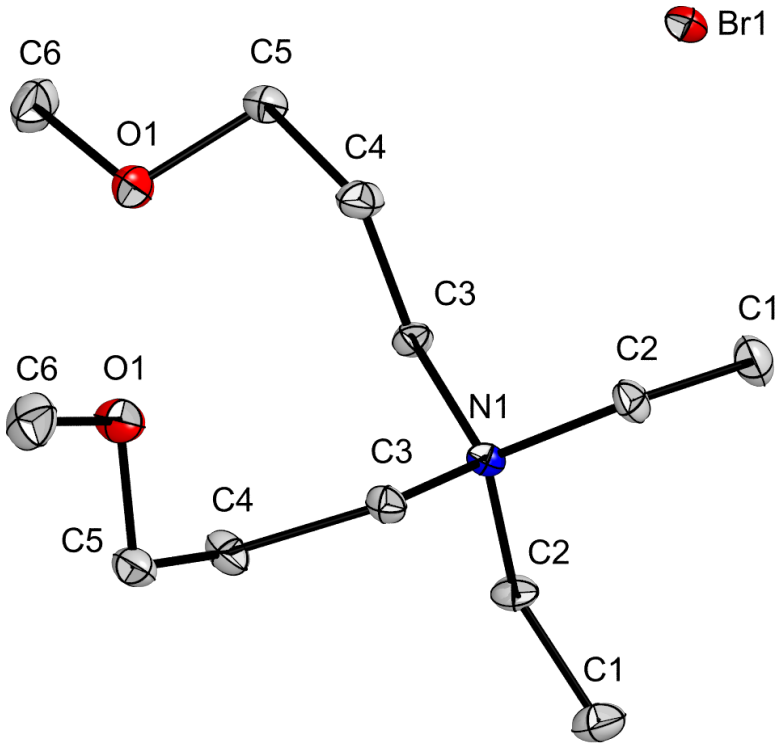

Figure 8. Solid state structure of $[N_{22.(3O1)2}]Br$. Thermal ellipsoids set at 50% probability.

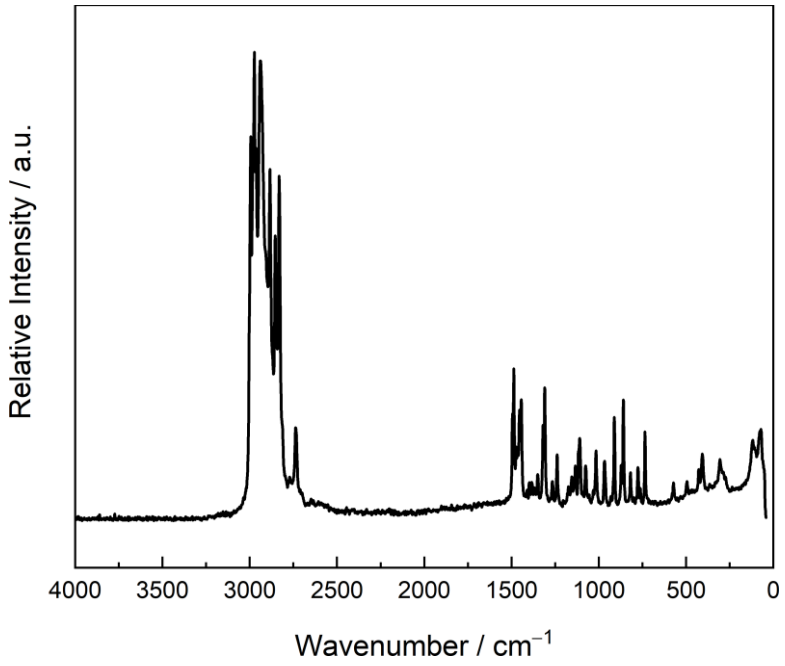

Figure 9. Raman spectrum of $[N_{22.(3O1)2}]Br$ single crystals using a Raman microscope at *r.t.*, resolution 2 cm^{-1}.

Table 3. Summary of crystallographic data and refinement results for $[N_{22.(3O1)2}]Br$.

CCDC number	2024864
Empirical formula	$C_{12}H_{28}BrNO_2$
Formula weight	298.25
Temperature [K]	100.0(1)
Crystal system	monoclinic
Space group	*P* 2/*n*
a [Å]	9.5781(12)
b [Å]	8.3383(14)
c [Å]	9.6266(15)
α [Å]	90
β [Å]	104.0(1)
γ [Å]	90
Volume [Å^3]	746.0(2)
Z	2
ρ_{calc} [g/cm^3]	1.328
μ [mm^{-1}]	2.745
F(000)	316.0
Crystal size [mm^3]	0.12×0.11×0.12
Crystal color	colorless
Radiation	MoK_α (λ=0.71073 Å)
2Θ range [°]	4.886 to 56.56 (0.75 Å)
Index ranges	$-11 \leq h \leq 12$, $-11 \leq k \leq 11$, $-12 \leq l \leq 12$
Reflections collected	15918
Independent reflections	1842 [R_{int} = 0.0563, R_{sigma} = 0.0293]
Completeness to θ = 25.242°	100.0 %
Data / Restraints / Parameters	1842/0/76
Goodness-of-fit on F^2	1.076
Final *R* indexes [$I \geq 2\sigma(I)$]	R_1 = 0.0244, wR_2 = 0.0485
Final *R* indexes [all data]	R_1 = 0.0299, wR_2 = 0.0498
Largest peak/hole [eÅ^3]	0.41/–0.36

D.2 Tetraphenylphosphonium (acetonitrile)tetrachloridomanganate(III), [PPh4][MnCl4(MeCN)]

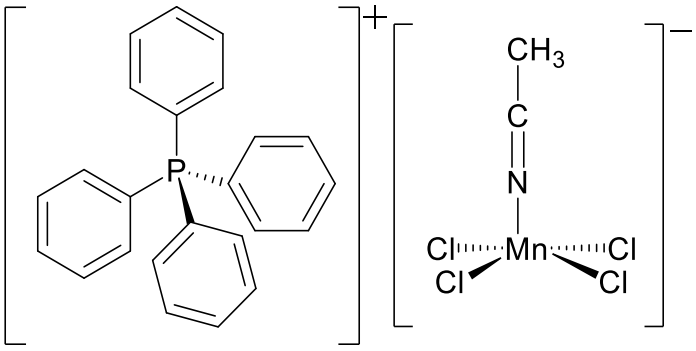

[PPh_4]Cl (97.1 mg, 0.26 mmol, 98 %, 2 eq.) was added to $MnCl_2$ (16 mg, 0.13 mmol, 1 eq.) in 4 mL of MeCN. The mixture was heated at 90 °C until a homogeneous yellow solution appeared, [PPh_4]$_2$[$MnCl_4$]. At *r.t.* the mixture was stirred, while Cl_2 was added to the mixture until stored under a Cl_2 atmosphere (1 bar). The solution turned black-green. Crystallization occurred at –40 °C into the anion [$MnCl_4$(MeCN)]$^-$ has a slightly distorted square pyramidal structure ($\tau = 0.15$)[1] and [PPh_4] [$MnCl_4$(MeCN)] is in the *P*4/*n* space group, producing black green crystals with a yield of 38.5 % (34 mg, 0.10 mmol).

NMR spectra were not obtainable due to a partial degradation in solution at T > –40 °C to the paramagnetic anionic reactant species $[MnCl_4]^{2-}$ (Mn^{+II}, S = 2).

ESI+ = [M^+] 339.1284 m/z;

ESI– = [M^-–(MeCN)] 198.7906 m/z;

CHN: Calculated for $C_{26}H_{23}N_1P_1MnCl_4$: C: 54.102%, H: 4.021%, N: 2.4324; Found: C: 53.82%, H: 4.695%, N: 2.454%;

FT-Raman (–196 °C, crystal, res. = 4 cm^{-1}):$\tilde{\nu}$ = 3082(m), 3060(vs), 3054(s,sh), 3041(w), 3018(vw), 3012(vw), 3008(vw), 3001 (m), 2993(vw), 2957(w), 2944(vs), 2915(m), 2327(w), 2254(s), 1589(m), 1376(w), 1189(w), 1186(m), 1168(vw,sh), 1162(w), 1109(w), 1100(w,sh), 1096(w), 1026(m), 998(s), 951(w), 920(w), 679(w), 614(w), 396(vw), 382(w), 302*(s) (ν_1, νMnN), 269*(m) (ν_7, $\nu_{as}MnCl_4$), 260*(w) (ν_2, $\nu_s MnCl_4$), 247*(s) (ν_4, $\nu MnCl_4$), 201*(m) (ν_8, δNMnCl), 189*(s) (ν_3, $\delta MnCl_{4,oop}$, out of plane deformation), 100*(vs) (ν_3, $\delta Cl_{4,ip}$, in plane deformation), 87*(s) (ν_5, $\delta Cl_{4,oop}$), 70*(vs) cm^{-1} (ν_9, $\delta MnCl_{2,ip}$). * Refers to anionic vibrations, and anionic vibrational assignment based upon a slightly distorted square pyramidal structure ($\tau = 0.15$)[1];

CCDC: 2024865.

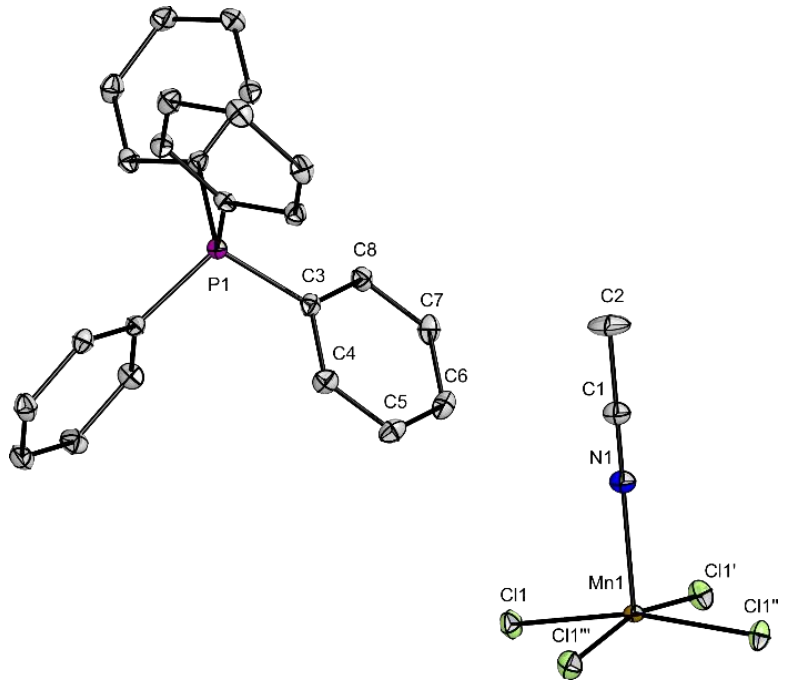

Figure 10. Molecular structure of $[PPh_4][MnCl_4(MeCN)]$. Thermal ellipsoids set to 50% probability.

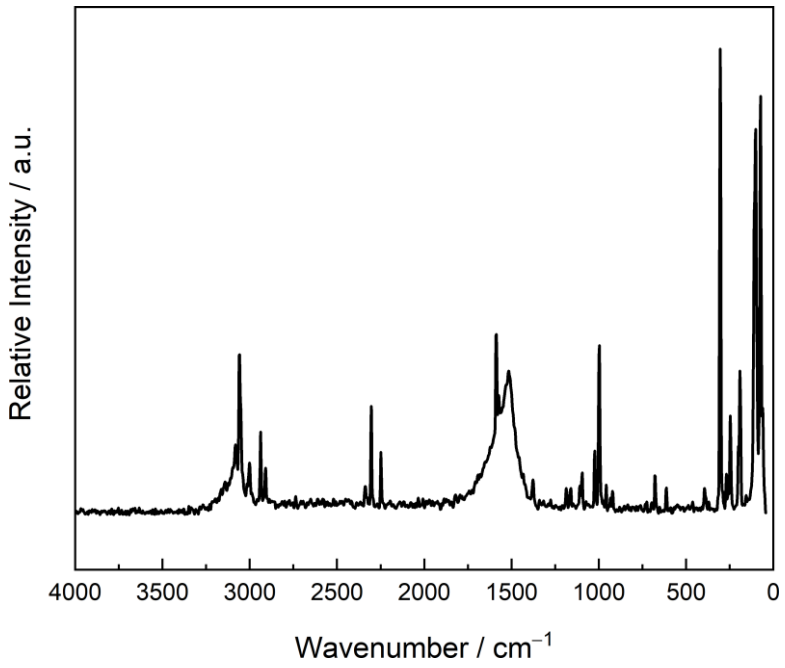

Figure 11. Raman spectrum of $[PPh_4][MnCl_4(MeCN)]$ single crystals using a Raman microscope at –196 °C, resolution 4 cm^{-1}.

Table 4. Summary of crystallographic data and refinement results for $[PPh_4][MnCl_4(MeCN)]$.

CCDC number	2024865
Empirical formula	$C_{26}H_{23}Cl_4MnNP$
Formula weight	577.16
Temperature [K]	100.0(1)
Crystal system	tetragonal
Space group (number)	*P* 4/*n*
a [Å]	12.6017(7)
b [Å]	12.6017(7)
c [Å]	7.9334(4)
α [Å]	90
β [Å]	90
γ [Å]	90
Volume [Å^3]	1259.85(15)
Z	2
ρ_{calc} [g/cm^3]	1.521
μ [mm^{-1}]	1.028
F(000)	1006
Crystal size [mm^3]	0.374×0.265×0.152
Crystal color	black green
Radiation	MoK_α (λ=0.71073 Å)
2Θ range [°]	4.572 to 56.608 (0.75 Å)
Index ranges	$-16 \leq h \leq 16$, $-16 \leq k \leq 16$, $-10 \leq l \leq 10$
Reflections collected	50732
Independent reflections	1561 [R_{int} = 0.0600, R_{sigma} = 0.0144]
Completeness to θ = 25.242°	100.0%
Data / Restraints / Parameters	1561/0/78
Goodness-of-fit on F^2	1.119
Final *R* indexes [$I \geq 2\sigma(I)$]	R_1 = 0.0220, wR_2 = 0.0520
Final *R* indexes [all data]	R_1 = 0.0240, wR_2 = 0.0530
Largest peak/hole [eÅ^3]	0.34/–0.30

D.3 Cyclic voltammograms of $[N_{2221}][ClF_4]$, $[N_{2221}][BrF_4]$, and $[N_{2221}][IF_6]$

The redox couples of the active species $[ClF_4]^-$ $[BrF_4]^-$, and $[IF_6]^-$ (with the cation $[N_{2221}]^+$) were examined additionally via cyclic voltammetry similar to the literature known $[N_{2221}][BrF_4]$.[2] The synthesis of the species was also similar to literature.[2,3] The cyclic voltammograms presented in **Figure 12** are of $[N_{2221}][ClF_4]$, $[N_{2221}][BrF_4]$, and $[N_{2221}][IF_6]$ (all 50 mM) taken in MeCN at T = 0 °C with a scan rate of 1000 mV·s^{-1}. The working electrode was a planar glassy carbon electrode (2 mm diameter) and the counter and reference electrodes planar platinum electrodes (1 mm diameter), and subsequently referenced against ferrocene as an internal redox couple. The cell was maintained semi-inert with Ar gas. The $E_{1/2}$ potential for the redox process (**I**) is given as the following approximation:

$$E_{1/2} = E_c + \frac{E_a - E_c}{2} \qquad (23)$$

where E_c and E_a are the peak or shoulder (inflection point) potentials of the cathodic and anodic waves, respectively.

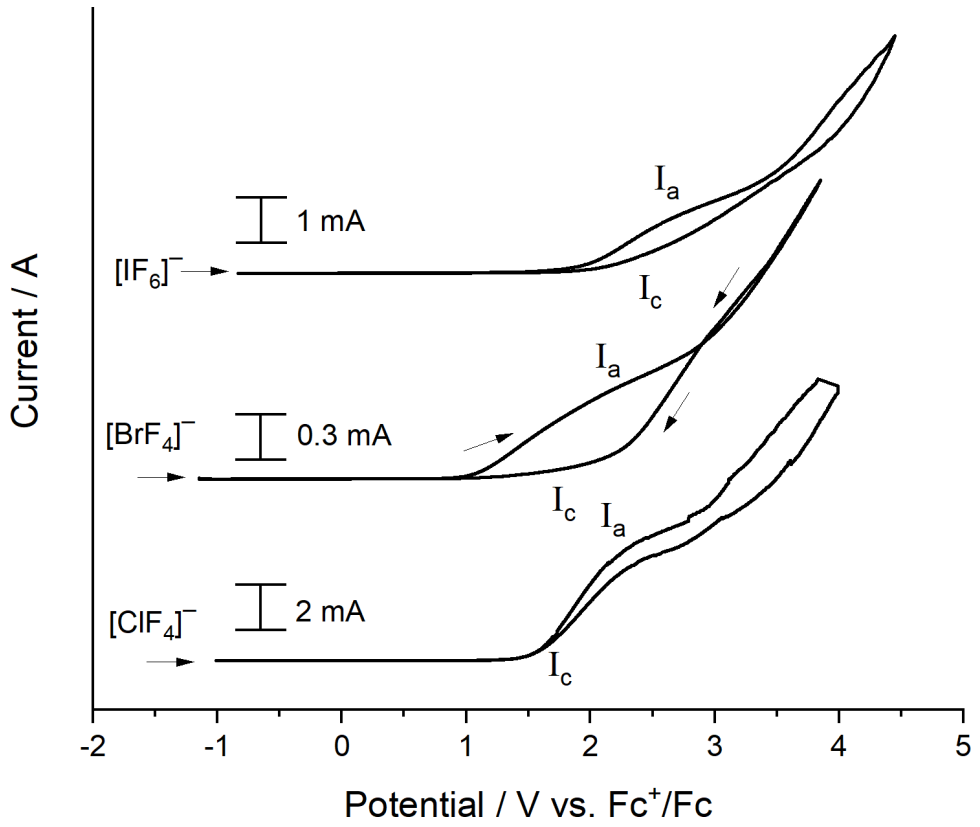

Figure 12. Cyclic voltammograms of $[N_{2221}][ClF_4]$, $[N_{2221}][BrF_4]$, and $[N_{2221}][IF_6]$ (50 mM) in MeCN at T = 0 °C with a scan rate of 1000 mV·s^{-1}. The working electrode is planar glassy carbon (2 mm diameter). The arrow on the far left represents the initial scan direction and zero current. The subsequent arrows on $[N_{2221}][BrF_4]$ represent the scan direction.

Additionally, after the initial cyclic voltammogram a small amount of substance was removed and measured via ^{19}F NMR to determine if the resulting species in the electrolyte solution. The resulting ^{19}F NMR signals are 67.79 ppm for $[ClF_4]^-$, –35.54 ppm for $[BrF_4]^-$,[2] and –27.9 ppm for $[IF_6]^-$, these values concur with literature values.[2-5] For $[IF_6]^-$ the ^{19}F NMR shift is slightly greater than that of literature (–27.9 ppm to literature –19 ppm[5]), the chemical shift of 9 ppm can be attributed to the difference in cation $[N_{2221}]^+$ versus the literature $[N_{1111}]^+$ and the temperature measured at room temperature versus 0 °C in the literature.[5] The shift, considering the experimental variables is negligible. Therefore, the active species is not destroyed

The $E_{1/2}$ values for the redox process **I** are calculated to be 1.90 V ($[ClF_4]^-$), 2.08 V ($[BrF_4^-$), and 2.50 V ($[IF_6]^-$). Whereby, the crossing that occurs for the measurement of $[BrF_4]^-$ is probably caused by a diffusion effect from the electrode surface and as such, the $\mathbf{I_c}$ peak value is less reliable compared to the $\mathbf{I_a}$ value of 2.21 V.

The redox process (**I**) for $[ClF_4]^-$, $[BrF_4]^-$ and $[IF_6]^-$ are proposed to undergo one of two chemical (C) or electrochemical (E) mechanisms, either a CEC or CECC mechanism similar to literature for $[BrF_4]^-$.[2] The CEC mechanism starts with the chemical equilibrium between $[XF_y]^-$ to XF_{y-1} and F^- (X = Cl, Br, or I, y = 4 or 6), see **Equation 24**, similar to that of $[X_3]^-$ to X_2 and X^-.[2] The second step is the subsequent oxidation of F^- to F_2 (**Equation 25**) followed by the chemical reaction between F_2 and XF_{y-1} to XF_{y+1}, see **Equation 26**. The reverse process would proceed by a similar mechanism.

$$[XF_y]^- \overset{C}{\rightleftharpoons} XF_{y-1} + F^- \quad X = Cl, Br, or I, y = 4 or 6 \qquad (24)$$

$$2\,F^- \xrightarrow{E} F_2 + 2\,e^- \qquad (25)$$

$$F_2 + XF_{y-1} \xrightarrow{C} XF_{y+1} \qquad (26)$$

The CECC mechanism would have the same first two steps as in the CEC mechanism, but would differ in the final two steps. The third step has F_2 react with $[XF_y]^-$ in the electrolyte near the electrode surface to $[XF_{y+2}]^-$, see **Equation 27**. The final step is the dissociation of $[XF_{y+2}]^-$ to F^- and XF_{y+1}, see **Equation 28**.

$$F_2 + [XF_y]^- \xrightarrow{C} [XF_{y+2}]^- \qquad (27)$$

$$[XF_{y+2}]^- \rightleftharpoons XF_{y+1} + F^- \qquad (28)$$

The proposed electrochemical component for all species is the oxidation of F^- to F_2. Therefore, the proximity of the electrochemical potential for all three interhalogen monoanions is plausible. The small differences in potential can be attributed to the differences in the halogen monoanion electrolyte, causing a slight variance at the electrolyte-electrode interface.

References

[1] A. W. Addison, T. N. Rao, J. Reedijk, J. van Rijn, G. C. Verschoor, *J. Chem. Soc. Dalton Trans.* **1984**, 1349.

[2] T. A. Gully, P. Voßnacker, J. R. Schmid, H. Beckers, S. Riedel, *ChemOpen* **2021**, *10*, 255-264.

[3] P. Pröhm, J.R. Schmid, K. Sonnenberg, P. Voßnacker, S. Steinhauer, C.J. Schattenberg, R. Müller, M. Kaupp, S. Riedel, *Angew. Chem. Int. Ed.* **2020**, *59*, 16002-16006.

[4] W. W. Wilson, K. O. Christe, *Inorg. Chem.* **1989**, *28*, 4172.

[5] A.R. Mahjoub, K. Seppelt, *Angew. Chem. Int. Ed.* **1991**, *30*, 323-324.